Author:
Hunt, Christopher J

Title:
WrapToR composite truss structures

analysis, manufacturing, characterisation, and optimisation

WrapToR Composite Truss Structures: Analysis, Manufacturing, Characterisation, and Optimisation

University of Bristol

January 2021

Christopher John Hunt

A dissertation submitted to the University of Bristol in accordance with the requirements for award of the degree of Doctor of Philosophy in the Faculty of Engineering, Department of Aerospace Engineering.

Word Count: 48,982

Abstract

The wrapped tow reinforced (WrapToR) truss combines the benefits of a truss geometry with the impressive material properties of composites to produce highly efficient structural members. While composite trusses are not a new concept, this work uses a novel manufacturing process to produce a unique wound truss configuration. Adapted from filament winding, the manufacturing process involves wrapping wetted fibre tow around rigid longitudinal members to form a truss geometry. This manufacturing method dramatically reduces labour demands compared with traditional trusses, which require assembling a large number of parts. The WrapToR truss concept therefore offers a low-cost method for producing structural members that could offer significant weight savings in a range of applications. To progress towards commercial application, the current work focuses on further developing and understanding the novel truss concept. The research is divided into two main themes: manufacturing and analysis.

The manufacturing work focused on developing and understanding the novel truss winding process. Prior to this work, WrapToR trusses were produced using a manual hand-winding process that is both inaccurate and labour-intensive. A key objective was to automate the process to improve consistency and throughput. This objective was achieved through the design and manufacture of a three-axis truss winding machine. Additional process development work found that twisting the shear member tow while winding significantly improved load-carrying capability.

The analysis work focused on developing tools that could predict truss behaviour under static loading scenarios. Models based on matrix structural analysis techniques were built and experimentally validated using a series of three-point bending tests. Initially, the models' ability to predict pre-failure response was investigated. This preliminary investigation revealed the necessity of modelling behaviour at the truss joints to capture overall truss deformations. Failure analysis was later conducted in which the key truss failure mechanisms were identified and predicted. The mechanisms investigated were member material failure, joint failure, and local and global buckling. The critical loading of these mechanisms was predicted by implementing failure criterion within the developed truss model. Again, the predictive capabilities were validated via a series of three-point bend tests.

An efficient design method was later developed that maximised truss structural efficiency by embedding the analysis tools within an optimisation algorithm. Results of this optimisation study showed huge weight-saving potential of the truss technology. Compared to conventional carbon fibre tubes, one truss configuration displayed over 50% mass reduction while offering equivalent strength and stiffness performance.

Through development of the manufacturing process and exploration of modelling techniques, this work has significantly advanced understanding of the Wrap-ToR truss technology. Combined with the demonstration of structural performance, the work lays the foundations for implementing the technology within commercial applications.

List of publications

Some of the work within this thesis has been published in journal articles or presented at conference.

Journal articles

[1] C. J. Hunt, M. R. Wisnom, and B. K. Woods, "WrapToR composite truss structures: Improved process and structural efficiency," *Composite Structures*, vol. 230, p. 111467, 12 2019.

[2] C. J. Hunt, Y. Zhao, M. R. Wisnom, and B. K. Woods, "WrapToR composite truss structures: Measurement and modelling of mechanical response," *Composite Structures*, vol. 254, no. July, p. 112834, 2020.

Conferences papers

[3] C. J. Hunt, M. R. Wisnom, and B. K. Woods, "Design, manufacturing and testing of an automated winding machine for WrapToR composite truss structures," in *18th European Conference on Composite Materials (ECCM18)*, (Athens, Greece), 2018.

[4] C. J. Hunt, M. R. Wisnom, and B. K. S. Woods, "Analysis of WrapToR composite truss structures," in *Royal Aeronautical Society, 6th annual structural design conference*, (Bristol, UK), 2018.

[5] C. J. Hunt and B. K. S. Woods, "Experimental and numerical exploration ofthe detailed mechanical response of WrapToR composite truss structures," in *SAMPE Europe Conference 2019*, (Nantes, France), 2019.

Magazine features

[6] C. J. Hunt, M. R. Wisnom, and B. K. Woods, "WrapToR composite truss structures: Improved process and structural efficiency,", *Advances in Engineering*, 2020.

Use of publications in thesis

Chapter 1: may contain work published in any of [1-5].

Chapters 2 & 3: based on publications [1,4] and also contains work from the author's 2017 AENGM0006 Extended Research Project (XP) Report, submitted as part of the CDT in Advanced Composites.

Chapter 4: based on work published in [2,4,5].

Chapters 5 & 6: work currently unpublished.

Declaration

I declare that the work in this dissertation was carried out in accordance with the requirements of the University's *Regulations and Code of Practice for Research Degree Programmes* and that it has not been submitted for any other academic award. Except where indicated by specific reference in the text, the work is the candidate's own work. Work done in collaboration with, or with the assistance of, others, is indicated as such. Any views expressed in the dissertation are those of the author.

SIGNED:..... DATE:.....

Acknowledgements

I would like to thank The Engineering and Physical Sciences Research Council (EPSRC) for funding the project, including a 3 months COVID extension which was invaluable for completing the work after repeated national lockdowns.

I am incredibly grateful to have had fantastic supervisory support throughout my studies. My primary supervisor, Dr Benjamin Woods, has continually provided both excellent technical support and friendship, which has made the past four years not only incredibly interesting, but also very fun. My secondary supervisor, Professor Michael Wisnom, provided invaluable expertise and was always promptly available when required. I would also like to thank the many academic staff who have provided equipment, knowledge, and general support. This includes but is not limited to, Dr James Kratz, Dr Carwyn Ward, Dr Ian Farrow, Dr Michael Dicker, and Professor Paul Weaver. I must also thank my fellow CDT cohort members. I hope once the current madness has ended, we will be able to meet in person once more. Other colleagues to whom I owe many thanks are the laboratory technical staff who supported my tinkering throughout the project. This includes Ian Chorley, Steve Rae, Allison McIntosh-Smith, Mark Fitzgerald, David Godoy Alonso, Guy Pearn, Pete Whereat, and the entire Queens and Hackspace workshop teams. Gratitude must also go to Dr Yian Zhao, who during his short visit provided fantastic contribution and friendship. I wish him the very best in his new job in Singapore.

I also offer much gratitude to those who supported me outside of the academic environment. I am very fortunate to have a fantastic network of friends around me who have guided me through. These are too many to list, but they know who they are. My housemates, Sam, Gunny, Jane, and Sherriff, deserve particular thanks for providing a comfortable working environment once the offices were shut down.

None of this would have been possible without the continual love and support of my close family. I am very lucky to have the most generous and hard-working parents imaginable. My mother's scientific background and my father's love of aircraft undoubtedly led me here. I am eternally grateful for everything they have done for me. To my late grandparents, Brenda, Gordon, Stan, and Betty, most of whom sadly passed during my studies. They taught me so much and are all greatly missed. While the loss of life experienced during the last 4 years has been very

upsetting, I have also been blessed with two new lives and the joy of becoming an uncle. During this time, my sister, Lucy, gave birth to two lovely children, Ianto and Mali, all of whom I look forward to seeing much more once the current restrictions are eased.

Last, but certainly not least, thanks must go to my partner, Neda. Without her patience, understanding, and most of all, her uncompromising belief in me, I would have never succeeded. Our adventures together have been the highlights of my time in Bristol. I am extremely excited for whatever comes next for us.

Contents

List of Figures

List of Tables

Acronyms

1D-LTCS one-dimensional lattice truss composite structures.

ACT advanced composite truss.

AFP automated fibre placement.

CAD computer aided design.

CFRP carbon fibre reinforced polymer.

CNC computer numerically controlled.

CP-ACT continuous printing of advanced composite trusses.

DIC digital image correlation.

DOF degree of freedom.

FEA finite element analysis.

FRP fibre reinforced polymer.

GA genetic algorithm.

GFRP glass fibre reinforced polymer.

HAPS high-altitude pseudo-satellite.

MAPE mean absolute percentage error.

MSA matrix structural analysis.

O-ACS open-architecture composite structures.

PVA polyvinyl acetate.

RSM response surface methodology.

RTM resin transfer moulding.

UD unidirectional.

UHMWPE ultra-high molecular weight polyethylene.

UTM universal test machine.

WPG winding program generator.

WrapToR Wrapped Tow Reinforced.

Nomenclature

Composite material properties

E	Young's modulus
E_{11}	Longitudinal modulus
E_{22}	Transverse modulus
G_{12}	In-plane shear modulus
G_{23}	Transverse shear modulus
ν_{12}	Longitudinal poisons ratio
ν_{23}	Transverse poisons ratio
S_{ij}	Compliance matrix terms
σ_1^*	Longitudinal strength
τ_{12}^*	Shear strength

Truss geometric features

$\varnothing_c$	External diameter of chord members
n_c	Number of chord members
t_c	Chord wall thickness
θ_w	Winding angle
θ_s	Shear web angle
n_b	Number of truss bays
$\varnothing_s$	Shear web diameter
H	Truss height
h	Truss height between centres of chord members
L	Truss length or span
l	Truss bay length

Matrix structural analysis terms

$\mathbf{k}$	Local stiffness matrix
$\mathbf{K}$	Global stiffness matrix
$\mathbf{P}$	External loading vector
$\mathbf{U}$	Nodal displacements vector
$\mathbf{F}$	Element internal force vector
$\mathbf{K_r}$	Reduced global stiffness matrix
$\mathbf{P_r}$	Reduced external loading vector
$\mathbf{U_r}$	Reduced nodal displacements vector
$\mathbf{K_e}$	Elastic stiffness matrix
$\mathbf{K_g}$	Geometric stiffness matrix
$\mathbf{K_t}$	Tagent stiffness matrix
$\mathbf{\Delta P}$	Incremental loading vector
$\mathbf{\Delta U}$	Incremental displacement vector
S	Current stiffness parameter
λ	Buckling eigenvalue
$\mathbf{v}$	Buckling eigenvector

Tow twisting parameters

α_R	Fibre twist angle yarn surface
α_r	Fibre twist angle at arbitrary radial distance r
h	Twist pitch
R	Twisted yarn radius
S_{ij}^{y}	Compliance matrix terms of twisted yarn

Structural terms

I	Second moment of area
I_{11}	Maximum principle second moment of area
I_{22}	Minimum principle second moment of area
J	Polar second moment of area
P	Applied load

M Applied moment

P_{crit} Critical buckling load

L Beam length or span

δ Beam deflection

A_s Shear area

AE Axial stiffness

EI Flexural rigidity

EI_{eff} Effective flexural rigidity of truss beam

σ_1 Normal, longitudinal stress

τ_{12} Transverse shear stress

ε_x Normal strain

ϕ_b^e Shape factor for stiffness in elastic bending

ϕ_b^f Shape factor for failure bending

Tapered truss geometric parameters

L_{2D} Truss length parallel to the centre line of 2D planar truss face

L_{3D} Truss length parallel to truss centre axis

h_{root} Height of truss root

h_{tip} Height of truss tip

h_n Height of nth truss bay root

γ_{2D} Taper angle of a 2D planar truss face

$\delta_{2D,n}$ Change in height of nth truss bay

Winding program generator terms

x_n Carriage translation for stage n

α_n Mandrel rotation for stage n

Other

CV Coefficient of variance

MUL Mass per unit length

Chapter 1

Introduction

1.1 Background and motivation

There is an ever-pressing need within engineering to reduce structural mass. In many applications, particularly within transportation, mass is coupled with fuel-burn, which is a primary contributor to operational costs and environmental impact. The desire to reduce mass is particularly pressing in the aerospace industry. For aircraft, the relationships between mass, lift, and drag means that fuel-burn is highly dependant on mass. For a typical civil airliner journey, it has been estimated that a 10% reduction in aircraft mass results in a 7% reduction in fuel usage [1]. Furthermore, reductions in structural mass can be traded for increased wingspan to improve aerodynamic performance giving fuel savings 2-3 times larger than that for reducing mass alone. For spacecraft, the benefits of reducing mass are even greater. Even for the most cost-effective modern spacecraft it still costs close to 3000 US$ for every kilogram of payload launched to lower earth orbit [2].

In addition to minimising fuel-burn, reducing mass has other key benefits, including reducing material cost and improving dynamic performance. Even engineering fields that have traditionally placed little value on mass are now looking to lightweight solutions to reduce transportation, installation, and maintenance costs. In civil engineering, for example, many designers and researchers are now considering using lightweight fibre reinforced polymer (FRP) bridges instead of traditional concrete, or metallic structures [3].

The increasing threat of global heating will continue to push the reduction of greenhouse gas emissions onto the international agenda. This will most likely manifest in tighter vehicle emission standards that will drive engineering decisions to target improved fuel-efficiency. Additional to this, emerging alternative power sources, such as lithium-ion batteries, provide much lower energy-densities than traditional fossil fuels. The adoption of these technologies in cars, aircraft, and other vehicles will only further the need for efficient structural solutions that minimise mass.

1.1.1 Structural efficiency

The term structural efficiency is commonly used within engineering, however, the term itself is often loosely or poorly defined. Unlike other commonly used efficiency terms, structural efficiency can not be described by a simple ratio value. While the efficiency of an engine, for example, can be quantified by determining the percentage of energy in the fuel that is converted into useful work, such an equivalent ratio to assess structural performance does not exist. Perhaps the most useful definition of structural efficiency is provided by Weaver and Ashby [4] as:

> *"the ability [of a structure] to carry the design loads safely, while minimising weight, or cost, or optimally meeting some other objective."*

Within the framework of this definition, it is not possible to compare the efficiency of two structures that are designed for different roles; no such parameter exists to universally compare structural efficiency. If two structures are designed for, and meet, the same set of requirements (loading, deflection, etc.) then the most efficient is that with the lowest mass, or cost. Assessing structural efficiency in terms of mass is relatively simple. Assessment in terms of cost, while perhaps often more important, is much more difficult as life cycle cost is affected by much more than just raw material cost. It is also necessary to consider manufacturing costs, operational costs, end-of-life disposal/recycling costs etc. Within this thesis, structural efficiency will only be considered in terms of mass minimisation.

From a structural design viewpoint, two options are available to improve structural efficiency: change the material used, and/or the geometry. Selection of the most appropriate combinations of material and geometry for various loading scenarios has been investigated in a series of studies [4–6]. Within these works various simple section shapes are assessed using dimensionless shape factors to provide an efficiency metric for that shape under a given loading condition. The higher the shape factor the more efficient that section's shape. A simple example of these factors comes from considering the bending shape factors of circular tubes. The shape factor for stiffness in elastic bending, ϕ_b^e, and for failure in bending, ϕ_b^f, are functions of section radius, r, and thickness, t, given by:

$$\phi_b^e = \frac{r}{t} \qquad (1.1) \qquad\qquad \phi_b^f = \frac{2r}{t} \qquad (1.2)$$

From Equations 1.1 and 1.2, it is seen that thinner tubes with larger radii are more efficient in bending; this is intuitive as such tubes move material further from the neutral axis. The presented studies all focus on simple section shapes such as solid shafts, tubes, and I-beams. The shape factors (and hence efficiencies) of such structural geometries are limited by both manufacturing and failure considerations.

Again considering the circular tube example, efficiency in bending increases as wall thickness decreases. At a certain point, however, the thickness is so small that either such a section could not be feasibly manufactured, or the thin wall would buckle when loaded. Such limits on the efficiency of simple sections has been explored by Weaver and Ashby in [7].

1.1.2 Lattice structures, space frames, and trusses

Lattice structures present geometric solutions capable of surpassing the efficiency limits imposed when using simple sections. These are structures formed of multiple individual elements connected at joints. By grouping material together into localised, discrete elements, they can move material further away from the axis of bending or torsion before reaching minimum material thickness constraints. Further efficiency gains are achieved as the elements that make up the structures then carry primarily axial loads, meaning material within each element is loaded equally [8]. The ASCE Task Committee on Lattice Structures have used to the following definition for a lattice structure [9]:

> *"a structural system in the form of a network of elements (as opposed to a continuous surface). Rolled, extruded, or fabricated sections comprise the member elements. Another characteristic of latticed structures is that their analytical solution is three-dimensional in nature."*

It is noted that this definition is similar to that given by the International Association for Shell and Spatial Structures for the term space frame [10]:

> *"a structural system assembled of linear elements so arranged that forces are transferred in a three-dimensional manner. In some cases, the constituent elements may be two-dimensional. Macroscopically a space frame often takes the form of a flat or curved surface."*

While the two terms are often used interchangeably, lattice structure is perhaps a more general term and can be applied to structures across length scales including those in the microscopic domain, sometimes referred to as lattice materials [11]. The term space frame tends to refer solely to larger-scale structures.

Trusses, like space frames and lattices, are structures formed by connecting many members. Technically in a truss, the joints are free to rotate, resulting in a structure where the individual members experience exclusively axial loading; this is often referred to as a two-force member structure as the individual members have only

two-forces acting on them, one at either end. In reality the term truss is often used more generally for structures with fixed joints whose elements will also experience bending moments, shear forces, and torsion. Despite this, the assumption of two-force member behaviour can greatly simplify structural analysis and still provide reasonable results [12].

In summary, while the terms truss, space frame, and lattice structure are arguably slightly different, they are very often used interchangeably. All three represent geometric configurations involving the connection of many discrete members and offer highly structurally efficient solutions.

1.1.3 Advanced composite materials

In the 1960s, the discovery of new fibre technologies lead to the rapid development of a new class of materials known as advanced composites [13]. The impressive properties offered by these materials initially attracted attention from the aerospace industry and has since spread. Advanced composite materials are formed of a fibre constituent, typically glass or carbon, that is embedded within a matrix, most often a polymer, but also can be a ceramic or metal. The resulting materials are anisotropic owing to the directionality of the embedded fibres. These materials can offer fantastic specific properties; however, their potential is greatest in applications where there are dominant stress directions, and where those directions are known. In such applications, the material anisotropy can be tailored, through fibre alignment, to maximise the material properties in the most highly stressed directions. In applications where resistance to loading in many directions is required, the efficiency gains of composite materials are lessened as fibres must be placed in various orientations.

1.1.4 Composite lattice structures

Composite lattice structures present a synergistic combination of material and geometry that offers incredibly high structural efficiencies. By producing lattice members from composites, the material anisotropy can be taken advantage of by aligning the fibres along the length of the primarily axially loaded members. While composite lattice structures have seen growing research interest in recent years, their use in industrial applications has been fairly limited. It is perhaps the notorious difficulties related to joining of composite parts that has limited their more widespread adoption in lattice structures, which traditionally require assembly of many individual members. Most of the composite lattice concepts now detailed within the literature use novel manufacturing processes that reduce or remove the need to assemble many individual members.

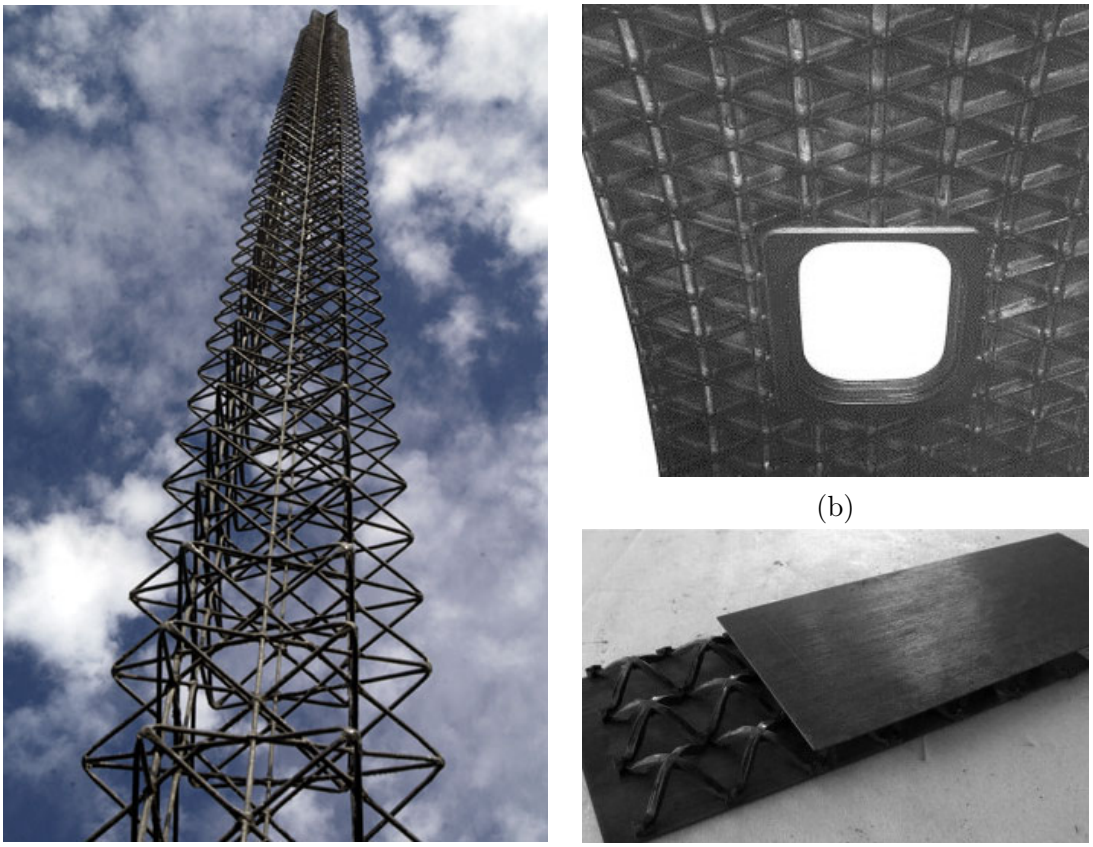

(a) (b) (c)

Figure 1.1: Examples of composite lattice structures: a) Isotruss® beam [14]; b) Anisogrid stiffened panel [15]; c) Hot pressed sandwich core [16].

Within the literature, there are a range of technologies that fall under the term composite lattice structure. A majority of these can be grouped into one of the following three categories:

- Composite grid stiffened panels
- Composite lattice sandwich cores
- Composite lattice beams

These three categories encapsulate the majority of composite lattice structures. There are, however, some manufacturing concepts which can be used to produce more general three-dimensional lattices and space frames which do not fit into one of the above three categories. Examples include, bolting of pultruded sections [17], hybrid metal-composite space frames in which composite members are bonded into metallic joints [18, 19], and a concept named coreless filament winding [20, 21] which involves winding fibres over a series of pins. There are also some deployable space structures that could be classed as composite lattices [22].

Each of the three lattice structure categories listed above will be discussed in the following three subsections, and an example of each is displayed in Figure 1.1. A much more detailed survey of composite lattice beams is given as this is the category that the WrapToR truss falls within.

1.1.4.1 Composite grid stiffened panels

Grid stiffened panels are the oldest category of composite lattice structure and have now been used commercially in both space launch vehicles and aircraft fuselages [15, 23]. These structures are formed by interlacing unidirectional (UD) fibre strips to produce a series of stiffeners (often referred to as ribs) arranged into a 2D planar grid pattern. The grid structure is normally bonded, or co-cured, to a composite skin to give a continuous surface. The planar grid is often curved, giving a cylindrical or conical surface. It could be argued that these structures do not fit the definition of lattice structure discussed in Section 1.1.2, as their arrangement is 2D rather than 3D. Never-the-less they are frequently referred to as lattices and are at least very closely related.

Isogrids are lattice grid arrangements in which the stiffeners form a pattern of repeating equilateral triangles resulting in isotropic stiffness within the lattice plane. Isogrids were originally machined from aluminium, but during the 1970s and 80s American companies began to investigate using filament winding to make them from composites [24]. Around the same time, Russian researchers were developing anisogrid structures; such as that seen in 1.1b. These are similar to isogrids, however the stiffeners are arranged to prioritise mechanical properties in specific directions; meaning they are anisotropic within the lattice plane. By tailoring the directionality of the mechanical properties, these structures can provide more structurally efficient solutions [25]. Kagome is a grid geometry in which the intersecting nodes are offset to reduce build-up of material, resulting in a pattern of repeating triangles and hexagons. The Kagome geometry has been used in grid stiffened sandwich panels, where the grid is sandwiched between two skins rather than being attached to a single outer skin [26–28]. Orthogrids are another lattice grid in which stiffeners run in two perpendicular directions forming a series of repeating squares. Due to the lack of angled stiffeners, orthogrids have severely reduced shear performance making their use less popular [29].

Composite grid stiffened panels are most commonly manufactured as cylinders using filament winding. A similar approach to traditional filament winding can be used, however a winding pattern that builds up discrete stiffener members, rather than a continuous surface, must be used. This can be done without a mould, with a sacrificial foam mould, or with an elastomeric removable mould [25]. Fibre placement, either manual or automated (AFP), is sometimes used to make grid stiffened

panels that are flat [30–32]. Another manufacturing method proposed by Han et al. [33] involves connecting pultruded sections by interlocking of a series of cut grooves to make flat orthogrids.

1.1.4.2 Composite lattice sandwich cores

Replacing conventional honeycomb or foam sandwich panel cores with 3D lattices formed of composite struts is an idea currently being explored by several research groups. Common lattice core geometries include 3D Kagome/octahedral [34–38], tetrahedral [39, 40], and pyramidal [16, 41–43].

A variety of manufacturing approaches have been investigated to form the lattice core geometries. 3D Kagome lattice cores are typically formed by stitching dry fibres between two separated composite plates. The stitched lattice is then impregnated by either resin submersion [35, 36] or spraying [37]. Various methods using hot pressing of either prepreg sheets or strips have also been used. Xiong et al. [16] laid-up strips of prepreg in a grid formation, then using an undulating mould the strips were pressed into the lattice geometry seen in Figure 1.1c. Hu et al.[44] used hot pressing to form corrugated CFRP laminates which were then cut into strips. The strips were woven to form a pyramidal lattice that was bonded between two skin panels. Xiong et al. [45] used a similar method of hot pressing to form a corrugated laminate. However, instead of cutting into strips, they used a computer numerically controlled (CNC) laser cutter to remove pieces leaving a near pyramidal lattice core.

Other methods used for fabrication of composite lattice cores includes placing rolled prepreg struts between two skin panels [39, 41, 46] and 3D printing [47, 48]. Another approach introduced by George et al. involved stitching either linear fibre braids [49], or braided nets [50] between two composite plates. When the plates were pulled apart, the braids formed a lattice geometry which was then impregnated and cured in place. In both studies, George et al. chose to use embedded foam inserts to improve impregnation and energy absorption resulting in a hybrid foam-lattice core.

A different foam-lattice core hybrid concept was investigated by Yin et al. [51, 52]. In this concept, the struts themselves were formed of very small foam core sandwich panels. This concept can be seen as a hierarchical-hybrid core as it features two orders of sandwich structure. Other researchers have investigated two-order hierarchical lattice cores in which the struts are formed of smaller-scale composite lattice beams [53, 54]. It is noted however that both studies only provided analytical consideration of the hierarchical concepts and any test samples were manufactured from 3D printed polymer.

1.1.4.3 Composite lattice beams

Composite lattice beams are three-dimensional arrangements of composite members that macroscopically form one-dimensional beam members. Such structures are highly efficient in flexure due to their ability to move aligned fibre material far from the beam neutral axis. This efficiency in bending, coupled with high axial stiffness and strength, also makes them attractive solutions as lightweight compression columns.

Lattice beams are typically formed of longitudinal (or chord) members that run parallel to the beam axis, and shear members that run diagonal to the beam axis. Note the shear members are sometimes formed via helical winding and hence are often called helical members or helicals. Within a lattice beam, the longitudinal members predominately carry the axial and bending loads while the shear members carry the shear and torsional loads. Depending on the loading scenario, the relative sizes or numbers of the longitudinal and shear members can be varied to maximise structural efficiency.

The first clear example of a composite lattice beam presented within the literature was detailed by Schütze in 1997 [55]. Schütze presented the truss beam concept seen in Figure 1.2a, which was produced through the assembly of individual members. Joining of the members was achieved via bonding where at each joint, nodal gusset plates were used to provide additional bond area. To the best of the authors' knowledge, this technology is the only example of a composite-lattice beam within the literature that is manufactured by joining many prefabricated members. While the standard choice for metallic trusses, this method is perhaps less popular for composites due to notorious difficulties in joining composite parts. Following the technology presented by Schütze, there has been a movement within the literature towards composite lattice beams that use novel fabrication methods to reduce or remove the required assembly stage.

The first and most prevalent example of such is the IsoTruss® technology which was initially developed and patented by researchers at Brigham Young University [56, 57]. Rather than assembling prefabricated members, manufacturing of IsoTrusses involves winding continuous fibres to form both the lattice geometry and the individual members simultaneously. The geometry of these structures is complex, and several variant configurations have been produced. The most researched form, referred to as the 6-node IsoTruss, is formed of six longitudinal members and two opposing sets of six helical members. This 6-node configuration is displayed in Figure 1.2b and for further visualisation purposes, the reader is referred to the images in [56, 58].

Other configurations of IsoTruss® that have been tested include an 8-node

[59, 60] and a "double shell" variant [61] that was tested by a separate research group based in China. This group have also published several studies investigating the manufacturing and structural mechanics of the IsoTruss® which they refer to as being part of a wider category of structures called one-dimensional lattice truss composite structures (1D-LTCS) [61–64]. Another configuration derived from the IsoTruss® is the rectangular section IsoBeam technology seen in Figure 1.2c. The IsoBeams rectangular section improves beam flexural stiffness at the cost of increasing manufacturing complexity [65].

IsoTruss® test samples produced for studies within the literature have so far been produced using filament winding [59, 66–68]. The geometry of the IsoTruss® is captive, meaning that when winding onto a rigid internal mandrel, the mandrel is geometrically trapped within the part. To avoid this problem, collapsible mandrels such as that detailed in [63], are required. In more recent publications, a continuous process has been presented which uses a 3D braiding machine to wind the fibre tows, and a robotised series of hooks that act as an external mandrel [69, 70]. While significantly more complex, this braiding process has several potential benefits, including enabling continuous truss production and increasing design freedom. While winding or braiding of IsoTrusses can be automated, the process requires an additional step in which the UD fibres are wrapped with a layer of Kevlar to provide member consolidation and joint reinforcement. In the published work, this is achieved by hand sewing [59, 60, 66] of the fibres, and it is currently unclear whether this labour-intensive step can be automated.

Researchers at Auburn University have used a modified braiding process to produce a cylindrical composite lattice beam concept referred to as O-ACS [71, 72]. These structures are manufactured via maypole braiding over a cylindrical mandrel, as seen in Figure 1.2d. Using a novel braiding pattern that was earlier proposed in [73], referred to as true triaxial, the resulting lattice beam has both axial members and two oppositely rotating sets of helical members. By altering the braid pattern, beams with different numbers of axial and helical members can be produced. The members themselves are formed of prepreg carbon tows that are encapsulated within a braided sleeve to aid both member consolidation and shaping.

In 2011 Ju et al. [74] published a study aimed at modelling the structural response of a glass fibre reinforced polymer (GFRP) truss concept. This structure features three longitudinal members that form the section shape of an equilateral triangle. The longitudinal members are connected by helically wound diagonal members, and vertical struts that run perpendicular to the beam longitudinal axis. Within the study, a 6 m truss-beam (seen in Figure 1.2e) was manufactured by what the author states is filament winding of prepreg tow; however, limited information on the manufacturing process is given.

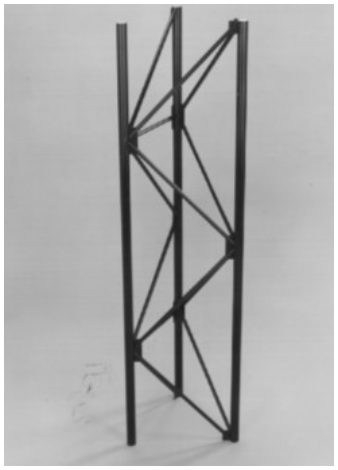

(a)

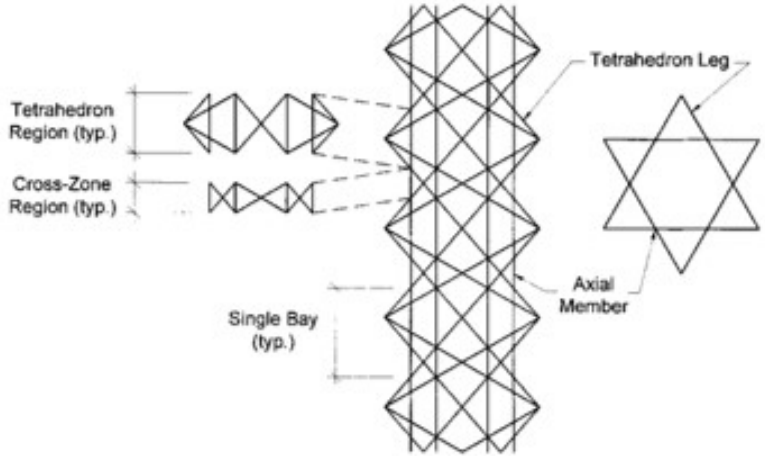

(b)

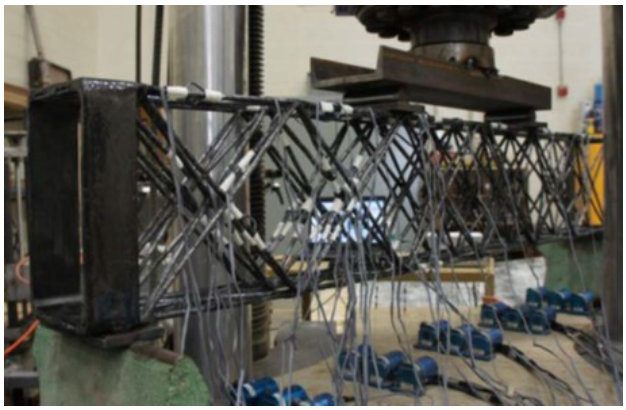

(c)

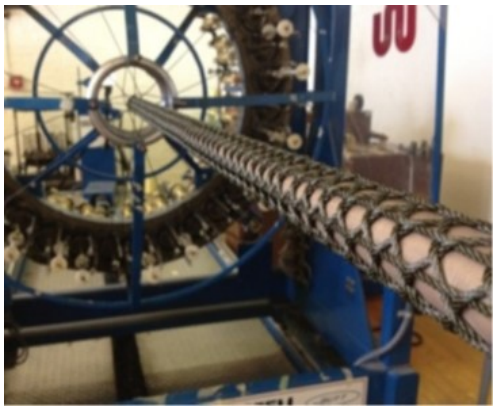

(d)

(e)

(f)

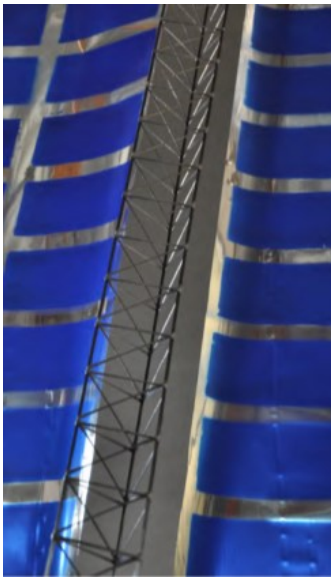

(g)

Figure 1.2: Composite lattice beam concepts: a) Schütze's assembled truss beam [55]; b) 6-node IsoTruss; c) IsoBeam [75]; d) Open-architecture composite structures (O-ACS) [76]; e) GFRP truss [74]; f) Advanced composite truss (ACT) [77]; g) Trusselator beam [78].

San Diego Composites, a company in the USA, are developing a continuous manufacturing process to produce lattice beams. The process is named continuous printing of advanced composite trusses (CP-ACT) and is intended for in-situ manufacturing of large space structures. The concept uses prepreg to form the longitudinal members, and wet winding to form the shear members, producing a co-cured structure. Within the published work [77], the continuous process is not detailed, and filament winding was used to produce test samples, an example of which is seen in Figure 1.2f.

A separate company, Tethers Unlimited, are developing a similar concept for in-situ manufacture of space structures. The company is developing an automated system, called SpiderFab™, for in-orbit manufacture and assembly of their lattice beam concept. The initial published work from this project introduces a truss printing machine named the Trusselator™ [78]. The functioning of this machine is not detailed; however, it is known that their lattice beams use thermoplastic matrix composites (carbon-PEEK). Thermoplastics are selected here for their superior performance, especially within the space environment. The later work on this project was largely focused on developing the system's in-orbit assembly capability [79]. An image of the thermoplastic composite lattice beam produced by the Trusselator™ is seen in Figure 1.2g.

1.1.5 WrapToR truss

In 2012 researchers at the University of Maryland published design work on the world record-breaking Gamera II human-powered helicopter [80]. To meet the demanding mass requirements for the helicopter airframe, designers developed a novel composite lattice beam (in 2009) that was manufactured using an adaptation of filament winding. Woods et al. later patented this technology [81] and published a study detailing the wound truss concept [82] which has since been named the Wrapped Tow Reinforced (WrapToR) truss.

The geometric configuration of the WrapToR truss shares similarities with several of the beams described in the previous section. The most commonly investigated WrapToR variant (seen in Figure 1.3) has an equilateral triangular section formed of three tubular chord members and features six helically wound shear members around the section. This geometry is very similar to the glass truss presented by Ju et al. [74] (seen in Figure 1.2e), only without the members perpendicular to the longitudinal axis.

The WrapToR technology is not defined by the final part geometry but instead by its manufacturing process; which can be used to create a variety of lattice beam geometries. The manufacturing process involves holding composite longitudinal mem-

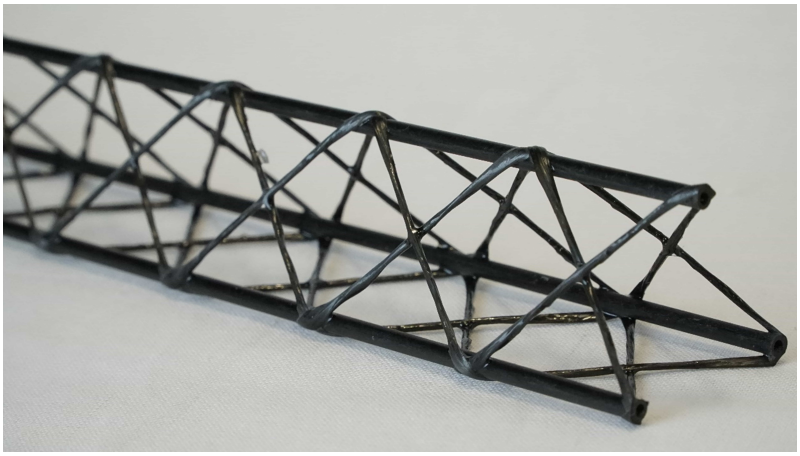

Figure 1.3: Three chord member, triangular section WrapToR truss.

bers (typically premade tubes) on a rotating mandrel while wetted fibre tow is wound around them. The wetted tow is then cured, forming shear members which are simultaneously co-cured to each other and co-bonded to the underlying longitudinal members. The WrapToR process is described in much greater detail in Section 2.1.3 and the potential alternative geometries are discussed in Section 2.1.4.

1.2 Aims & objectives

The work in this thesis has two main aims. The first is to develop and improve the WrapToR truss manufacturing process to increase the technology's industrial applicability. The second is to use the WrapToR truss as a vessel for developing understanding of how composite lattice beams behave and how that behaviour can be modelled in order to maximise their performance potential. The objectives assigned to reach these aims are as follows:

- Automate the WrapToR truss manufacturing process, which until now has involved manual hand-winding.
- Investigate the quality of parts manufactured via the automated process and investigate means of improvement.
- Compare the structural performance of the WrapToR truss to conventional composite configurations.
- Develop and experimentally validate analysis tools to predict both truss stiffness and failure to a level of accuracy suitable for use in preliminary component design.
- Demonstrate how the developed modelling tools can be used with optimisation algorithms to maximise structural performance.

1.3 Thesis structure

The thesis is divided into five contents chapters. Already given in the introduction was a literature survey that introduced the concept of a composite lattice beam and discussed the existing technologies that fall within the category. Further literature surveys are conducted within each chapter that detail the published work specifically related to the topic of that chapter. For example, published work relating to optimisation of composite lattice beams is reviewed in Chapter 6: Optimisation.

In Chapter 2, detailing of the WrapToR truss manufacturing process is given, followed by a discussion of the possible geometric configurations it could be used to produce. The core of the chapter is then focused on automating the previously manual process through the design and build of a CNC winding machine. Further development of the process to allow manufacturing of tapering trusses, and trusses with larger shear members, is then detailed.

The first half of Chapter 3 involves the characterisation of the constituent components of WrapToR trusses: chord members, shear members, and joints. This characterisation work provides member geometry and material property data that is used during the modelling work in later chapters. The second half of Chapter 3 details a three-point bend test that is frequently used throughout the thesis to characterise full truss beams. This three-point bend test is then used for two experimental investigations to evaluate truss structural performance.

Chapter 4 details the development of a truss analysis tool that is designed to predict pre-failure response. The analysis tool is verified against commercial software and then validated through a rigorous experimental investigation. Once validated, the analysis tool is used to conduct a parametric study that explores the design space of WrapToR trusses.

In Chapter 5, the capabilities of the analysis tool developed in the previous chapter are extended to include prediction of failure and nonlinear behaviour. Again an experimental investigation is conducted to assess the accuracy of the developed analysis methods.

Chapter 6 gives an introduction into how the developed analysis tools can be embedded within an optimisation algorithm for preliminary component design. Optimised truss configurations are generated for a series of load cases to demonstrate a design methodology for maximising truss structural efficiency.

In Chapter 7, the key conclusions of the thesis are summarised along with an assessment of how the work meets the aims and objectives set out in Section 1.2. Finally, discussed is the future work required to push the technology to industrial application, along with a discussion of what this application could be.

Chapter 2

Manufacturing

2.1 Introduction to WrapToR winding process

2.1.1 Background on filament winding

First conceived by Richard E. Young in the 1940s, filament winding is the oldest and most prevalent highly automated composite manufacturing process [83]. The process involves winding continuous fibre filaments, either dry or impregnated, onto a rotating mandrel. Winding and placement of the filaments relies on a repetitive and systematic set of movements that are typically automated using a filament winding machine, commonly referred to as a filament winder. In its simplest form, a filament winder has two axes: a mandrel rotation and a carriage translation. Earlier versions of these machines typically had two axes controlled by mechanical means, such as gears, chains, belts and pulleys. In the late 1970s, advancements in electronics and computers led to the development of computer-controlled machines that are commonplace today. This improved the speed, accuracy and ease of operation of the machines. The shift away from mechanical control methods also permitted the incorporation of more machine axes. Today machines with up to six axes are commercially available [84] with some researchers now using robotic arms to manipulate the delivery head [85], [86].

The most commonly used fibres for filament winding are carbon and glass, however, others such as aramid, ultra-high molecular weight polyethylene (UHMWPE) [87], and natural fibres [88] have also been used.

As well as laying down the fibres, the process also requires a method of impregnating the wound fibres. For impregnation, the following three methods are typically used:

1. *Dry winding*: dry fibres are wound onto the mandrel creating a preform. Impregnation is then achieved via an additional liquid composite moulding process such as resin transfer moulding (RTM). [89]

2. *Prepreg winding*: uses pre-impregnated fibre tows. It is noted here that some authors refer to prepreg winding as dry winding. [90]

3. *Wet winding*: uses a resin bath, typically mounted on the winder, to impregnate the tow in-situ.

Of the three methods wet winding is the most popular as, unlike dry winding, it only requires a single process stage and compared to prepreg winding it significantly reduces material cost. Thermosetting polymer resins, typically epoxy, polyester, or vinyl esters, are generally preferred in filament winding, largely due to their lower viscosity. In recent years, however, there have been developments in the field of thermoplastic filament winding. This includes filament winding using thermoplastic prepreg tapes [91, 92] and wet winding [93]. Also interesting to note is impregnation using co-mingled fibre tows [94, 95], a method that is not possible using thermosetting polymers.

Another key component within the filament winding process is the mandrel design. Often filament wound parts present a captive geometry making removal of a solid mandrel physically impossible. Even for prismatic parts such as straight-sided tubes, the inability to generate peel stresses between the tool and part can make it difficult to separate the two. In some parts, such as pressure vessels, a liner is necessary to seal the composite shell. In some cases, this liner may be thick enough to be used as the mandrel for the winding process. In any application where the part geometry is captive, and where a liner is not required or is not sufficiently stiff, a sacrificial or collapsible mandrel must be used. Sacrificial mandrels are suitable when the required part numbers are small. These can be made from low-temperature alloys, eutectic salts, soluble plasters or sand bonded with polyvinyl acetate (PVA) glue [96]. Collapsible mandrels are generally made from multiple metal pieces that can be deconstructed and removed from the part after curing. These have the advantage of being reusable, but can be complex and expensive.

Earlier mechanically controlled two-axis filament winding machines were largely limited to the production of cylindrical parts such as pipes and rocket motor cases. The arrival of machines with more axes coupled with the development of computer software for generating winding pathways, extended the capabilities of filament winding to produce parts with ever more complex geometries. With four-axis machines, it became possible to manufacture pressure vessels with integrally wound end closures, such as that seen in Figure 2.1. Such vessels provide lightweight fuel tanks that are extremely popular in aircraft and spacecraft today. Other common parts produced using filament winding include aircraft fuselages, bicycle wheels, yacht masts, and golf club shafts.

Filament winding has historically been, and currently is, a very popular com-

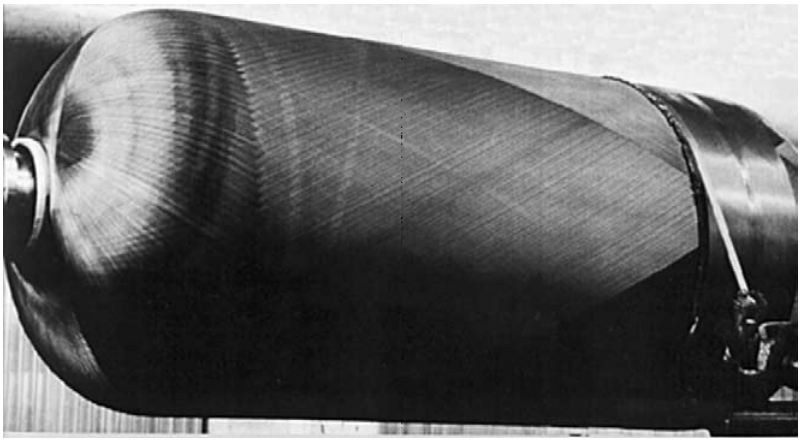

Figure 2.1: Filament wound pressure vessel. Reproduced from [97].

posite manufacturing technique. The advantages of filament winding [98] that have led to its popularity are discussed here:

- Using dry fibres and wet resin significantly reduces material cost when compared to processes that use prepreg material.
- The process is highly suited to automation. This has a several of benefits including reduced labour cost, manufacturing repeatability, and increased material deposition rates.
- High fibre volume fractions (above 55%) can be achieved resulting in good material properties.
- For pressure vessels fibres can be easily aligned with the primary loading direction, maximising structural efficiency.
- It produces relatively low material waste as no offcuts of material are generated.
- Within the part the fibres are continuous throughout meaning that there are minimal weakening joints.

2.1.2 Novel uses and adaptations of filament winding

The typical examples of filament wound parts mentioned in Section 2.1.1 all essentially involve manufacturing axisymmetric, closed-section, shell structures. This means that despite its many advantages, filament winding in its traditional form is largely limited regarding the components it can produce. There are now however emerging examples where filament winding has been adapted or used in innovative ways for novel purposes. Within this section, these examples are discussed.

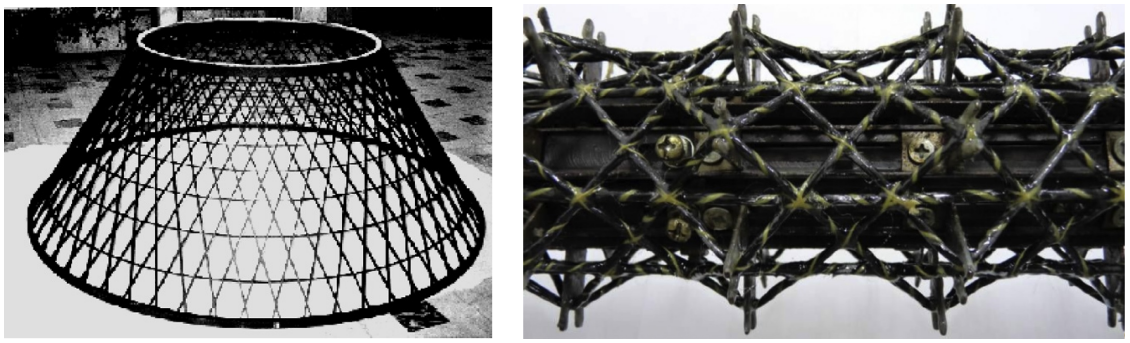

(a) (b)

Figure 2.2: Novel uses of filament winding a) Anisogrid; b) Isotruss®. Reproduced from [25, 63].

By using high degree of freedom (DOF) machines, researchers have been able to extend the capabilities beyond axisymmetric parts. For example, Xu et al. [99] have wound a pipe with a 90-degree bend using a winding machine incorporating a robotic arm. Using a similar 8 DOF machine, Scholliers and Brussel [100] were able to filament wind a T-piece.

Previously discussed in Section 1.1.4, the Anisogrid [25] and Isogrid [101] technologies use filament winding to create open-architecture cylindrical or conical grid structures, such as that seen in Figure 2.2a. Four variations of the filament winding process are used to create these grid structures. The first and most simple involves winding directly onto a mandrel using a winding pattern that places tows apart from each other. These tows are then layered up as the winder passes back and forth forming discrete elements rather than a surface. The second process is similar in concept with the difference that the tows are laid onto a foam core with machined grooves that guide the tow to produce better quality elements. The third uses an elastomeric mould that, unlike the foam mould, is reusable. In the fourth process, the tow is laid onto a metal liner which then forms a hybrid metal-composite structure. These structures have been successful in Russian spacecraft due to the combination of impressive structural weight savings and relatively simple and low-cost manufacturing methods.

Another novel use of filament winding that is discussed in Section 1.1.4.3 is the IsoTruss® technology. Here the filament winding process is adapted to produce open architecture lattice structures where the mandrel design allows the production of straight members rather than creating curved members on a cylindrical mandrel. Due to the captive geometry of the IsoTruss® configuration, collapsible mandrels such as the one seen in Figure 2.2b are used.

All the previously discussed examples use filament winding to produce parts that are used either as individual components, or that could be later assembled into a larger structure. One novel use of the process that has recently been investigated by

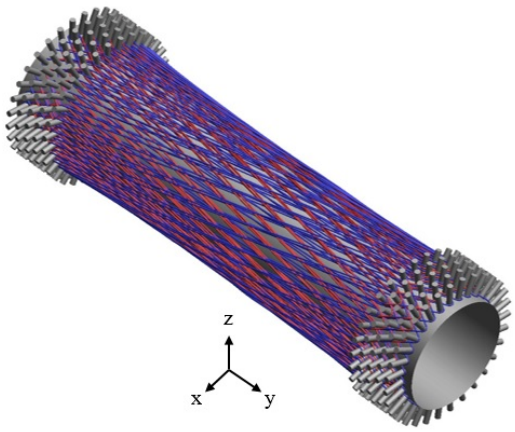

Figure 2.3: Novel hybrid filament wound joint. Reproduced from [102].

Jones et al. [102] involves using filament winding to create composite-metallic joints. This is done by creating two cylindrical metallic end plugs that feature a series of pins. By winding tows between the pins, the wound fibre is mechanically linked to the metallic parts. A computer model image of the concept is shown in Figure 2.3. The current published work is largely focused on simulation of the process and does not involve manufacturing of any demonstration parts.

2.1.3 The basic WrapToR process

Fundamental to the WrapToR technology is the manufacturing process. The process is adapted from filament winding and due to its close similarity, it shares many of the benefits. Within this section, the process is detailed for the manufacture of the "standard" WrapToR truss configuration. This refers to a triangular section, prismatic truss with three tubular chord members which is the primarily used configuration within this thesis. The process is then compared to traditional filament winding, and in Section 2.1.4, discussion is given as to how the process can be modified to produced trusses of varying configurations.

The initial stage of the process is the construction of the mandrel. The mandrel is typically constructed of a metal interior that supports three pre-made composite tubes. Further detail of mandrel design is given in Section 2.2.3. Once constructed the mandrel is rotated while a wetted fibre tow (typically carbon-epoxy) is wound around it following a helical winding pathway to form shear members that are evenly spaced. Six passages back and forth along the mandrel are required for completion of the winding pattern.

Once the winding is completed, the fibre tow is cut and tied-off. The truss is then left to cure either at room temperature or in an oven. As the wetted shear member tow is cured, it is simultaneously co-bonded to the chord members. Once the truss is fully cured the final step to the process is the removal of the mandrel.

While the truss geometry is not inherently captive, high mandrel-part friction and the inability to generate peel stresses between the two often means that a collapsible mandrel design is preferable.

While conventional filament winding and the WrapToR process are very similar, there are some key differences. In filament winding the fibre tow is wound around the mandrel many times using a winding pattern that creates a continuous surface with no gaps and often many fibre layers. In the WrapToR winding process, the helically wound tow is purposefully spaced out to form individual members. This means that where filament winding is used to produce shell structures, the WrapToR process produces lattice structures formed of many beam-type members. Another key difference relates to the role of the mandrel. After curing of a filament wound part, the mandrel is either wholly removed, or in the case of pressure vessels, a liner that formed either part or the entirety of the mandrel is left inside the part. Either way, the mandrel does not provide significant structural integrity to the final part. For the WrapToR process, the mandrel onto which the fibre is wound is in-part formed of three chord members that perform a key structural role in the final part.

One potential disadvantage of the WrapToR process, when compared to filament winding, is that it technically requires an extra step: the fabrication of the pre-made chord members. However, the members typically used for the chord members are pre-made composite tubes that are manufactured by either pultrusion, roll wrapping or pull winding which can be purchased from a wide range of suppliers at very reasonable prices. Indeed, pultrusions are the lowest cost form of cured composite available, due to the economies of scale and efficiency of this process.

2.1.4 The WrapToR process possibilities

While the trusses produced for the work in this thesis primarily used the standard, three chord member, prismatic truss configuration, the process is certainly not limited to this configuration. It can, therefore, be altered to produce a wide range of possible configurations. While a triangular section truss with three chord members is often favourable for structural reasons, it is theoretically possible to use any number of chord members from two up. As an example, a hexagonal sectioned (six chord members) wound truss is displayed in Figure 2.4. Tapering the section is also certainly possible and is later demonstrated in Section 2.3. With modifications of the mandrel and winding pathways, it is likely to be possible to create curved trusses using the process.

As well as being able to create a variety of truss geometries, a range of material choices are also available. Carbon fibre reinforced epoxy has been the favoured material for the work within this thesis. However, as is the case in filament winding,

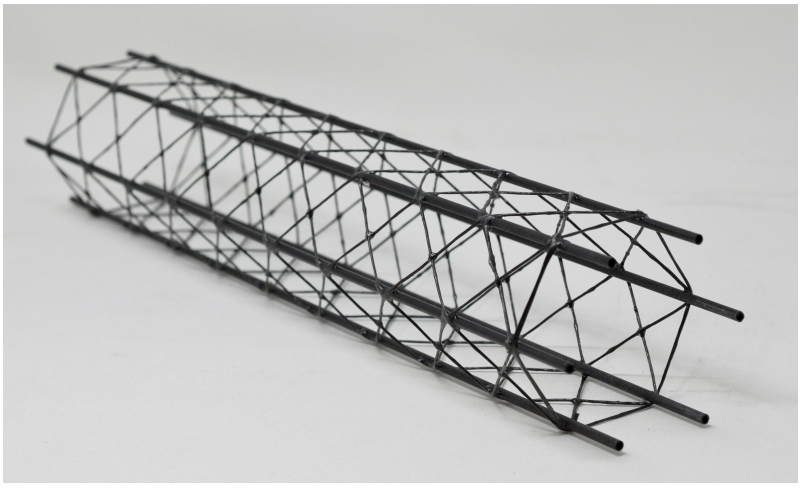

Figure 2.4: Hexagonal WrapToR truss with six chord members.

essentially any continuous fibre could be used for the wound tow that form the shear members. This could be glass, aramid, UHMWPE, or natural fibres such as jute. The chord members are also not restricted to pre-made composite tubes. Potential other options include bamboo canes, metallic rods, or pultrusions with different section shapes such as a V-section or rectangle. It may also be possible to adapt the process so that the chord members can be fabricated at the point of winding allowing the entire structure to be co-cured rather than co-bonded.

2.1.5 Tow twisting

As was stated in the previous section, a key difference between the WrapToR process and conventional filament winding is that the wound tow is used to form individual members rather than a continuous surface. In conventional winding, it is desirable to spread the fibres so that fibres cover maximum surface area when laid onto the mandrel and to aid impregnation. To achieve this, filament winding machines normally run the fibre tows over a series of rollers that progressively spread the tow. For the WrapToR process, the wound tow is used to create discrete shear members rather than a continuous composite surface. This change in function of the wound tow potentially means a different form is preferred. For discrete shear members, a spread tow is likely to be detrimental to the structural performance. The reason for this is due to the fact the shear members are required to carry compressive loads, meaning they are susceptible to buckling. If the tow is spread out, the section of the shear members will have a large difference between their minor and major second moments of area. The more spread out the tow, the lower its minimum second moment of area will be, and hence the lower the buckling resistance of the member will be. This, therefore, suggests that bundling the fibres together (rather than spreading it out) is desirable for the WrapToR process.

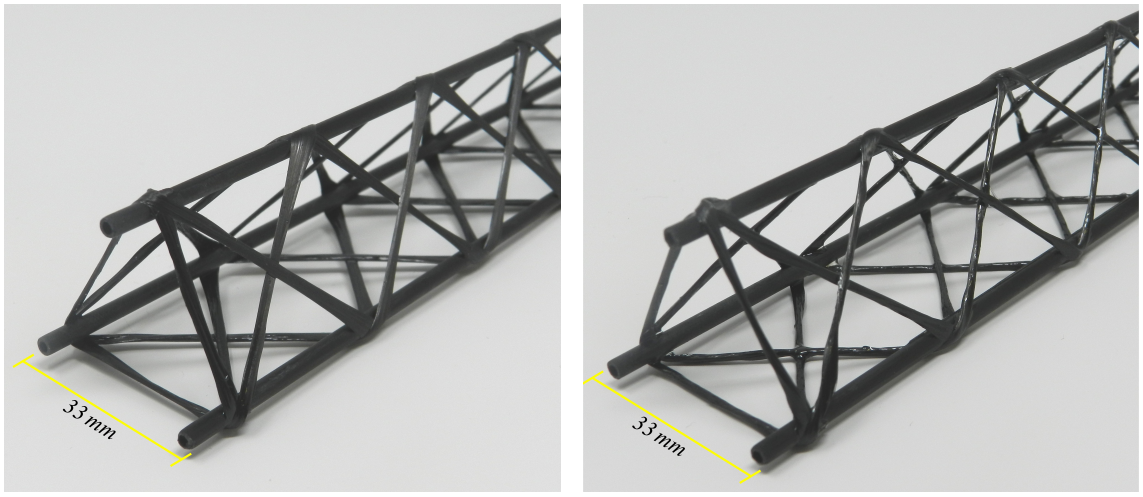

(a) (b)

Figure 2.5: Truss shear member configurations: a) truss where shear members are not twisted ('flat'); b) truss with twisted shear members ('twisted').

Even when not run over a series of rollers, there is a tendency for the fibre tow to spread out as it wraps around the mandrel. This can be seen by examining the shear members in the truss image in Figure 2.5a. One method to restrict the tow from spreading out is to twist the fibres together. When doing this the tow forms a near-circular section, as is seen in Figure 2.5b. A circular section is axisymmetric with respect to its second moment of area. This means that it has a larger minor second moment of area for a given amount of material than a spread tow shear member, therefore, making it more efficient at resisting compression buckling. Twisting the tow would therefore seem desirable from a structural perspective. From hereon the shear member configuration in which the tow is not twisted (Figure 2.5a) will be referred at as 'flat' and those where it is twisted (Figure 2.5b), as 'twisted'.

Later in Section 3.6, an investigation into how tow twisting affects structural performance is detailed. The study found tow twisting is indeed beneficial for truss structural performance and hence the majority of trusses produced by the winding machine have featured twisted shear members.

2.1.6 WrapToR truss geometric definition

For the WrapToR truss configuration there are a number of geometric parameters that define a particular truss. These parameters can be varied to change the structural characteristics and ideally optimise truss performance for a given role. In this section, these parameters and their relationship to one another are discussed for a prismatic truss with tubular chord members. These parameters are summarised in Table 2.1 and Figure 2.6. Additional parameters that are needed to define tapering WrapToR trusses are later described in Section 2.3.

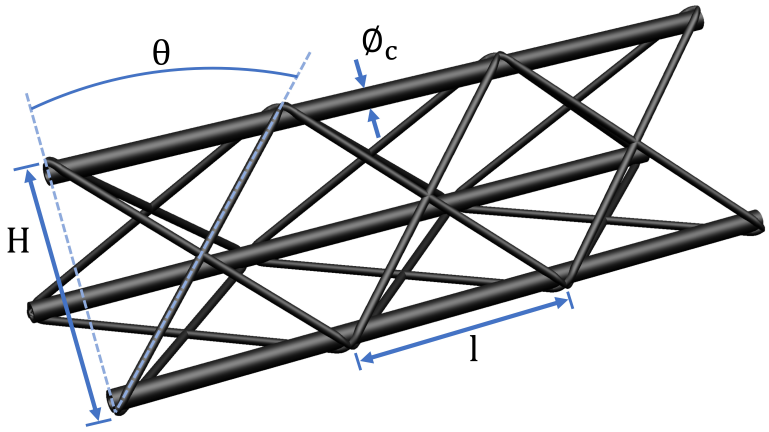

Figure 2.6: Geometric features of WrapToR truss.

Table 2.1: WrapToR truss geometric parameters.

Parameter	Symbol	Units
Winding angle	θ_w	degrees
Shear web angle*	θ_s	degrees
Number of truss bays*	n_b	-
Number of chord members*	n_c	-
Chord diameter*	$\varnothing_c$	mm
Chord wall thickness	t_c	mm
Shear web diameter	$\varnothing_s$	mm
Truss height*	H	mm
Truss length	L	mm
Truss bay length	l	mm

**input parameters for winding program generation*

The number of chord members used, n_c, defines the truss section shape. Within this thesis, all the tested trusses used the standard configuration of three chord members giving an equilateral triangle section. The tubular chord members themselves have an external diameter, $\varnothing_c$, and a thickness, t_c. For a truss with a twisted tow shear web, the shear members have a near-circular section with a diameter, $\varnothing_s$. A truss is formed of multiple repeating units represented by a repeating cross pattern. Each of these repeating units is referred to as a bay. The overall truss length, L, is the product of the bay length, l, and the number of bays, n_b. The truss height, H, is defined as the outside distance between chord members.

The angle of the shear members is another key defining feature. Within a prismatic truss, the angle of the shear members is required to stay constant across the length. Varying angle along the length is not possible as the tension forces within the shear tow would be unbalanced resulting in slipping of the tow on the mandrel. For the WrapToR truss, there are two useful parameters that can be used to define

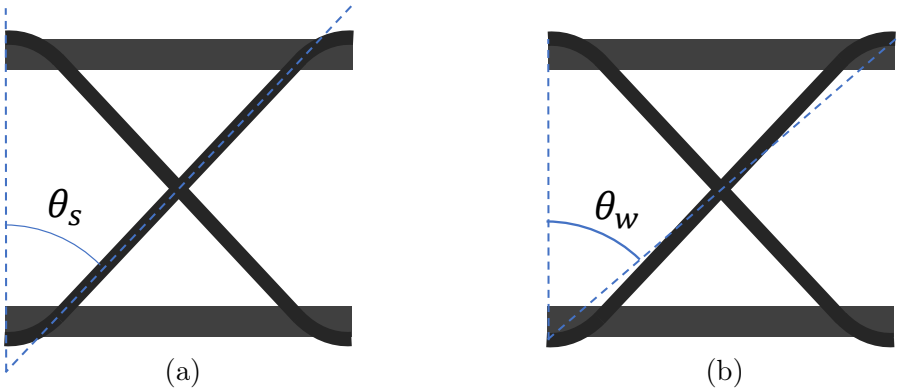

Figure 2.7: Face of individual truss bay depicting: a) shear member angle; b) winding angle.

the shear member orientation. These two angles are referred to as the shear member angle, θ_s, and the winding angle, θ_w. Both of these angular parameters are defined positive moving away from the vector perpendicular to the truss length, as is seen in Figure 2.6. To visualise the difference between these two angles schematics showing one face of a single truss bay are displayed in Figure 2.7. The shear member angle, θ_s, is the measured angle of the shear members to the perpendicular vector (seen in Figure 2.7a). The winding angle is the angle between the line connecting two opposite corners of a bay and the perpendicular vector (seen in Figure 2.7b).

Whilst the shear member angle better describes the physically observed angle, the winding angle allows for simpler expressions relating truss height and bay length. Due to the way the shear members curve as they contact the cylindrical chord members, the height, bay length and shear member angle do not form a simple trigonometric relationship. The winding angle is useful for the generation of winding programs and allows a more intuitive understanding of truss geometry. Using winding angle, the following expression can be used to link truss height and bay length:

$$\tan\theta_w = \frac{l}{H} \tag{2.1}$$

The difference between the winding angle and the shear member angle is dependent on the truss height and the diameter of the chord members. The ratio of the two angles is given Equation 2.2, the derivation of which can be seen in Appendix A. From this equation, it is seen that the winding angle and shear member angle are equivalent for a truss with chord members of zero thickness.

$$\frac{\tan\theta_s}{\tan\theta_w} = \frac{H}{H + \varnothing_c(\sqrt{3}-1)} \tag{2.2}$$

2.1.7 Constituent Materials

All the trusses manufactured for the work within this thesis used the same materials within the constituents components. For the shear members an intermediate modulus carbon fibre tow, Tenax IMS60 24k, was used. Due to supply issues, this was later changed to Tenax IMS65 24k tow which, as was assured by the supplier, has near-identical properties. The carbon tow was impregnated with SuperSap® CLV low-viscosity epoxy resin; a bio-epoxy derived from tree sap. For the chord members, pultruded carbon fibre reinforced epoxy tubes purchased from EasyComposites® were used.

2.2 Design and build of an automated truss winding machine

All WrapToR trusses produced prior to work in this thesis, including those in the Gamera II helicopter [80], were manufactured using a manual hand-winding process. This was achieved by rotating the mandrel using a speed regulated motor and guiding the impregnated fibre tow by hand. The initial work detailed within this thesis focused on automating the process by designing and building a CNC truss winding machine. The reasons for developing this machine were as follows:

- Demonstrate the WrapToR process to be automatable and therefore increase its commercial viability as a technology.
- Increase the manufacturing consistency of truss test specimens to improve the repeatability of any conducted tests.
- Reduce truss manufacturing time for the production of test samples.

The machine was sized for production of trusses with section radii up to 0.5 m and lengths of up to 2 m. As a piece of research equipment, the ability to later add additional features was necessary, making modularity a key design driver. Cost and ease of manufacture were also important design drivers due to budget and time constraints.

The truss winder layout was initially designed using computer aided design (CAD) software before purchase and assembly of the components. The machine design drew significant inspiration from the open-design movement which has grown rapidly in recent years allowing widespread production of homemade CNC machines. The following published studies on the design of small scale low-cost filament winders were also useful [103, 104].

2.2.1 Machine overview

The final machine design features three axes. Two of the axes are inherent to any filament winding machine: a rotational axis that turns the mandrel, and a longitudinal axis that translates the tow delivery unit along the length of the mandrel. The third axis is however unique to the WrapToR process and performs the function of twisting the shear web tow.

A CAD rendering of the machine design is shown in Figure 2.8 in which key components are labelled and detailed in Table 2.2. Both the machine supporting structure and carriage axis linear rail are made from V-slot aluminium extrusions. Most of the mechanical parts are off-the-shelf. For custom parts, laser cutting and 3D printing were used where applicable to minimise the number of machined parts.

The third machine axis is the key difference between the truss winding machine and conventional filament winders and results in a unique tow delivery unit design. Conventional delivery units generally have assemblies of pulleys and rollers that spread the fibre tow. Instead of spreading the fibres, the truss winder delivery carriage is designed to bundle the tow, by twisting it, to form circular section shear members. An image of the truss winder delivery unit is shown in Figure 2.9 where the key features are labelled in Table 2.2. Here the entire tow spool, located at the rear of the carriage, is rotated using a motor, belt and pulley system. The rate of

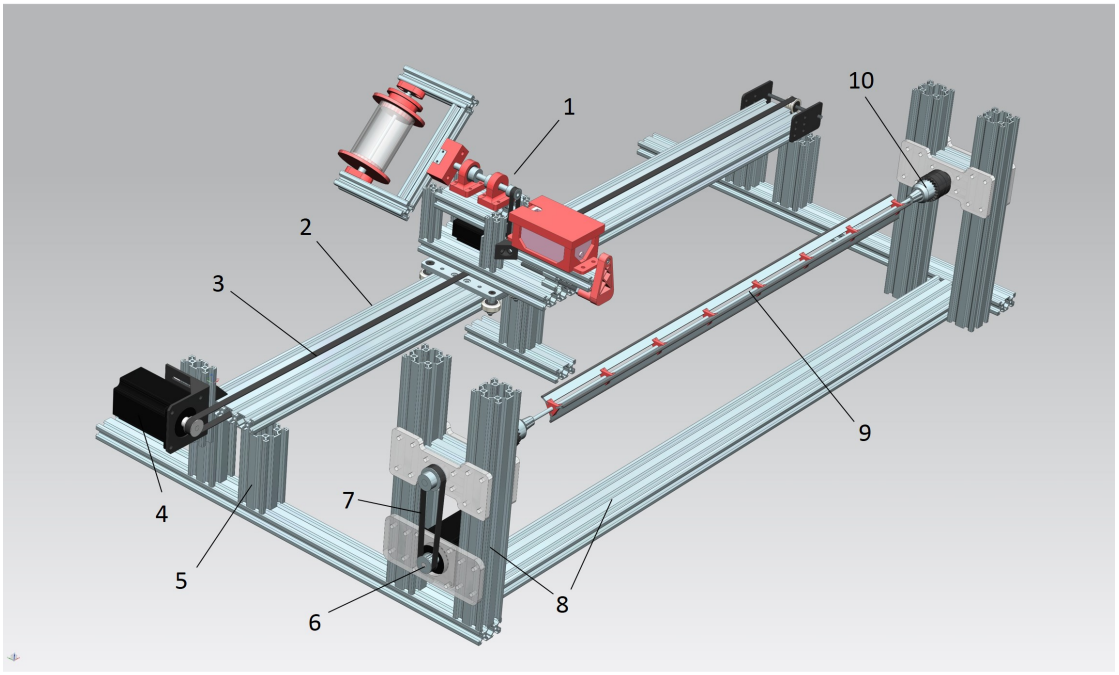

Figure 2.8: CAD image of truss winder design. Labelled features are detailed in Table 2.2.

Table 2.2: Description of machine features labelled in Figure 2.8.

Part label	Part name	Component description/construction
1	Delivery unit	Further detailed in Figure 2.9
2	Linear rail	Aluminium V-slot extrusion
3	Carriage axis belt	Glass fibre and rubber timing belt
4	Carriage axis motor	NEMA 23 stepper motor
5	Linear rail supports	Aluminium V-slot extrusion
6	Mandrel axis motor	NEMA 23 stepper motor
7	Longitudinal axis belt	Glass fibre and rubber timing belt
8	Mandrel axis supports	Aluminium V-slot extrusion
9	Mandrel	Detailed further in Section 2.2.3
10	Mandrel chucks	Keyed drill chucks

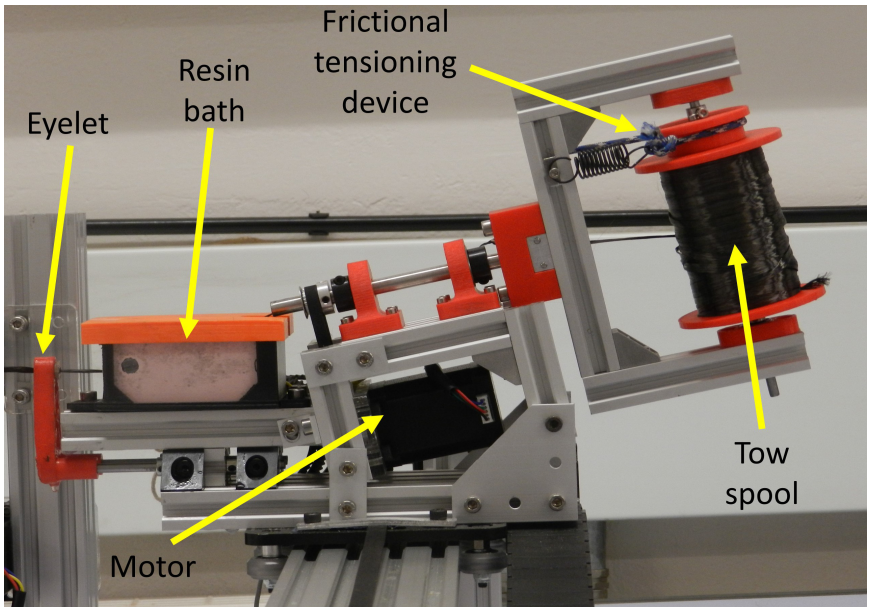

Figure 2.9: Tow delivery unit.

rotation is controlled to create a constant level of twist throughout the truss. While being twisted, the tow runs through a hollow shaft and into a silicone resin bath. The resin bath which is responsible for impregnating the tow with epoxy resin is detailed in Section 2.2.2.

For conventional filament winding, tow tension has been shown to influence both the fibre volume fraction and part mechanical properties [105, 106]. For the Wrap-ToR truss concept, tow tension also performs the role of straightening the shear members. For the truss winder, the simple and low-cost frictional device seen in Figure 2.9 was used to generate and control tow tension. Here a spring supplies tension to a string which is in contact with a surface on the side of the spool. The generated friction resists the unwinding of the spool creating tension in the tow. The tension in the tow can be controlled by adjusting the extension of the spring.

2.2.2 Resin bath and impregnation

The resin bath, seen in Figure 2.10, is formed of three parts, a main silicone body, a steel rod to change the tow direction, and an eyelet. Once impregnated, the tow exits the resin bath through the eyelet. The level of wetting within the truss is controlled by changing the eyelet size used. For earlier versions of the resin bath design, a cast silicone eyelet, was used for this role. This however created an issue that the eyelet hole would become enlarged after repeated use due to wear from the fibre tow. To avoid this problem, the design was later updated to incorporate ceramic eyelets (as seen in Figure 2.10) that were purchased from Ascotex Ltd.

To achieve the optimal level of wetting, a trial and error approach was adopted for eyelet selection. It was found that if the eyelet was too small, then the shear members and the joints would appear dry, as is seen in Figure 2.11a. When too dry, adhesion between the chord and shear members is poor, which is detrimental to the performance of the truss. When the eyelet is too large, excess resin accumulates on the truss. The excess resin tends to run along the chord members, as is seen in Figure 2.11b, resulting in the truss becoming bonded to the internal metal mandrel. Located here the excess resin has little benefit structurally but does add mass. At the preferred level of wetting (Figure 2.11c) the shear members appear well impregnated and minimal excess resin is found running along the chord members. At this level small pockets of resin form between the chord and shear members that increase the bond area, improving performance of the joints.

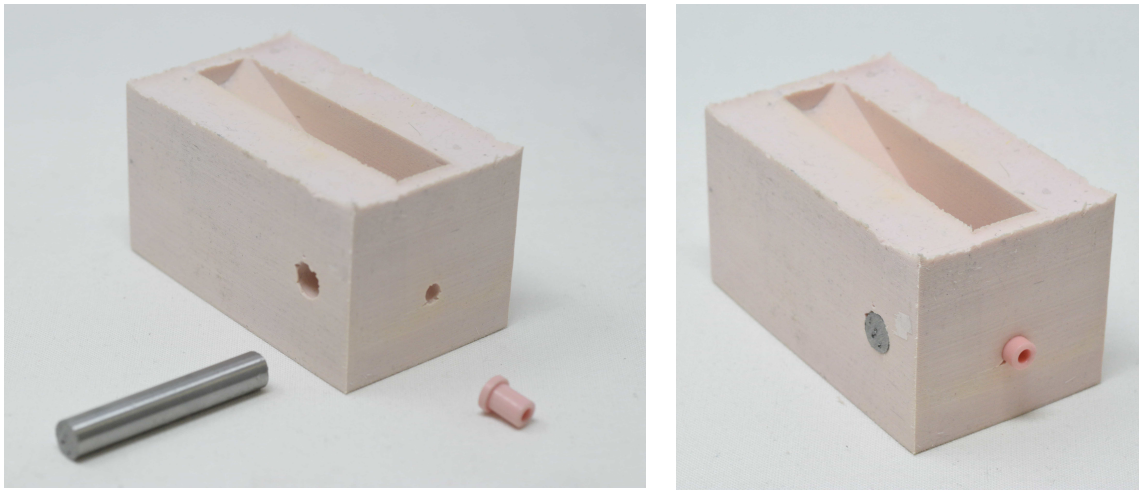

(a) (b)

Figure 2.10: Resin bath: a) disassembled; b) assembled.

(a) (b)

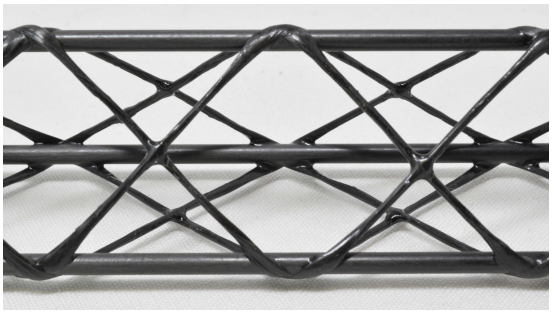

(c)

Figure 2.11: Levels of wetting in trusses: a) too dry; b) too wet; c) optimal.

Table 2.3: Optimal ceramic eyelet sizes.

Tow number	Eyelet internal diameter (mm)	Eyelet hole area (mm^2)
24k	1.7	2.3
48k	2.0	3.1
72k	2.3	4.2
96k	2.85	6.4

2.2.3 Mandrel Design

The mandrel design experienced a series of updates throughout the PhD, the final version of which is detailed here. The mandrel, displayed in Figure 2.12, is constructed from three steel flat bars which are attached to a steel hexagonal bar by several laser-cut acrylic mounts. A hexagonal bar is preferred here over a circular tube or rod as it allows torque to be mechanically transferred into the laser-cut mounts. The CFRP pultruded tubes that form the chord members of the trusses are then held on the flat bars using acrylic clips. At the truss ends, bolts are attached to the clips which act as end stops allowing the tow winding pattern to change direction at either end of the mandrel.

One key advantage of this design is that the laser-cut mounts could be designed within a CAD file that is parameterised to the truss design variables. This meant that for the manufacture of a new truss size, a mandrel could be created by simply specifying the truss parameters within the CAD model and laser cutting the resulting mandrel mounts and clips.

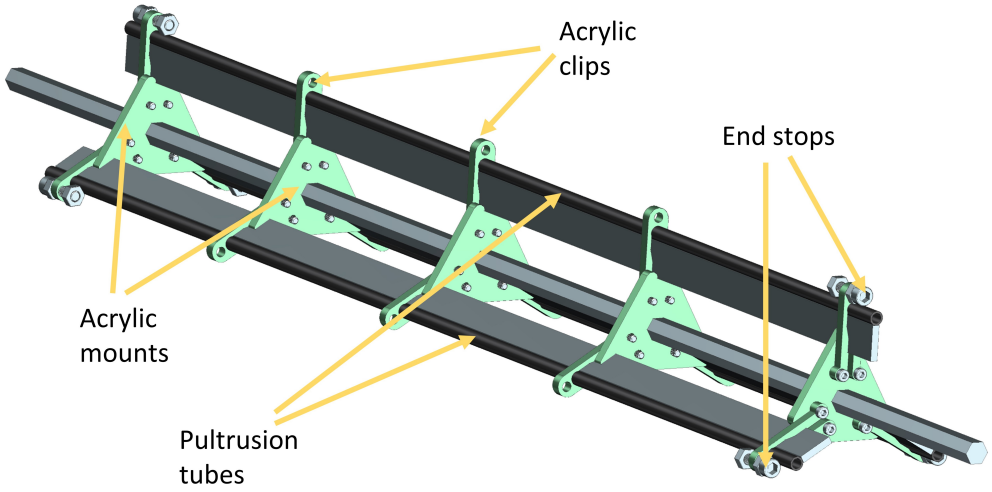

Figure 2.12: CAD image of truss mandrel design.

2.2.4 Electronics

Each machine axis is driven by a stepper motor allowing precise control of absolute positioning without the need for external position feedback. Each motor is powered by a Toshiba TB6600 stepper driver. Limit switches are used on the carriage axis to limit the travel of the tow delivery carriage. Relative motion of the three axes is controlled by an Arduino Mega microcontroller and the open-source G-code interpreting software: Grbl. This set-up provides a low-cost and easily modifiable control system.

2.2.5 Winding program generation

Similar to a conventional filament winder, the machine requires a winding program which controls the relative motion of each axis. However, the winding patterns required for the trusses vary significantly from that of conventional filament wound parts and are in many ways substantially simpler. This meant that commercial software, such as Cadfil® or CADWIND®, would be unsuitable and unnecessary for generating winding programs. Therefore, a custom WrapToR truss specific winding program generator (WPG) was written in MatLab. Within this section, an overview of the code's operation is given. A full explanation of the code's operation is given in Appendix B. While the overview of the code given here is specific to a standard truss with three chord members, it was coded for a general case of n_c chord members and has been demonstrated capable of producing hexagonal section trusses with six chord members.

The WPG uses information on truss geometry and process variables to produce a set of G-code commands that control the relative motion of the winders axes. Inputted into the WPG are several parameters defining the truss geometry. These

parameters are highlighted with an asterisk in Table 2.1. The process feed rate and twist rate are also inputted along with some machine parameters. Using the inputted parameters, the WPG calculates other geometric features of the truss, such as truss length and winding angle.

A flow chart summarising the operation of the WPG is seen in Figure 2.14. The first machine movement assigned by the WPG is required to twist the initial length of tow that runs between the fibre spool and the mandrel. Without this 'pre-twist' the initial section of the shear web would not be twisted. Following the pre-twist, the WPG starts to generate G-code commands that define the truss winding pattern. For a standard truss with three chord members, a full winding program consists of six passes along the length of the truss. Each pass consists of three individual movements, referred to here as stages. Each of the stages involves a carriage translation and mandrel rotation. The carriage translations, x_n, associated with these stages are depicted in Figure 2.13. The first stage involves the initial movement away from the start point to create the first shear member, as seen in Figure 2.13a. The second stage creates the remaining shear members along the length for the current pass and is depicted in Figure 2.13b. At the end of the second stage movement, the delivery head has moved past the truss end. To hook the end-stop, allowing a reverse pass, the third stage moves the eyelet back to the truss end-stops (Figure 2.13c). Depending on the specific truss geometry, a fourth stage is sometimes necessary to ensure a winding pathway is not traversed twice. This involves first checking if the hooked end-stop has been used as the starting point for a previous pass. If it has been previously used, then a mandrel rotation movement is undertaken to move to an unused end-stop.

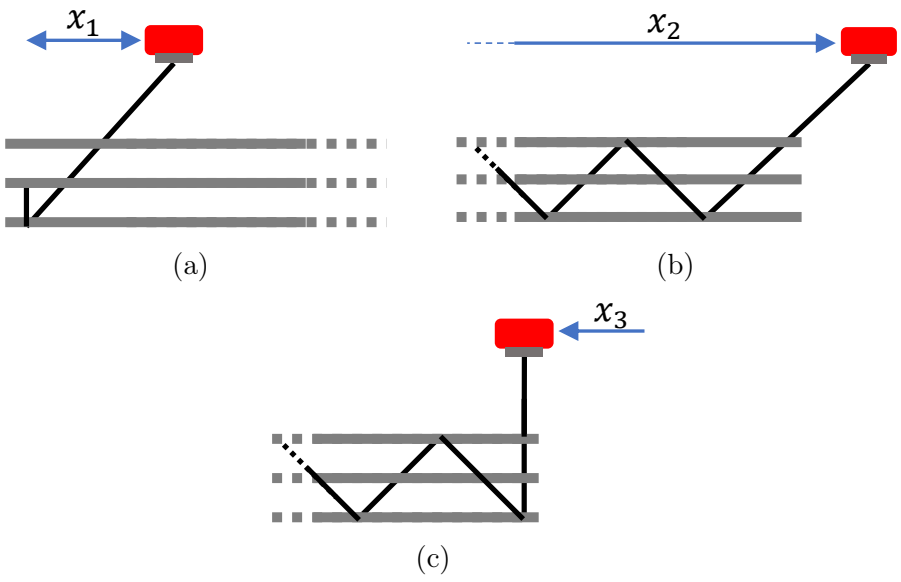

Figure 2.13: Schematics showing carriage translations, x_n, of : a) stage 1; b) stage 2; c) stage 3.

The four stages are repeated six times (three times in each direction of carriage translation) to create the full winding pattern. Once each pass's carriage translations and mandrel rotations are determined the WPG then uses the inputted process parameters to determine the twist axis commands and feed rate for each movement. Once complete the code outputs a G-code file that can be loaded onto the machine.

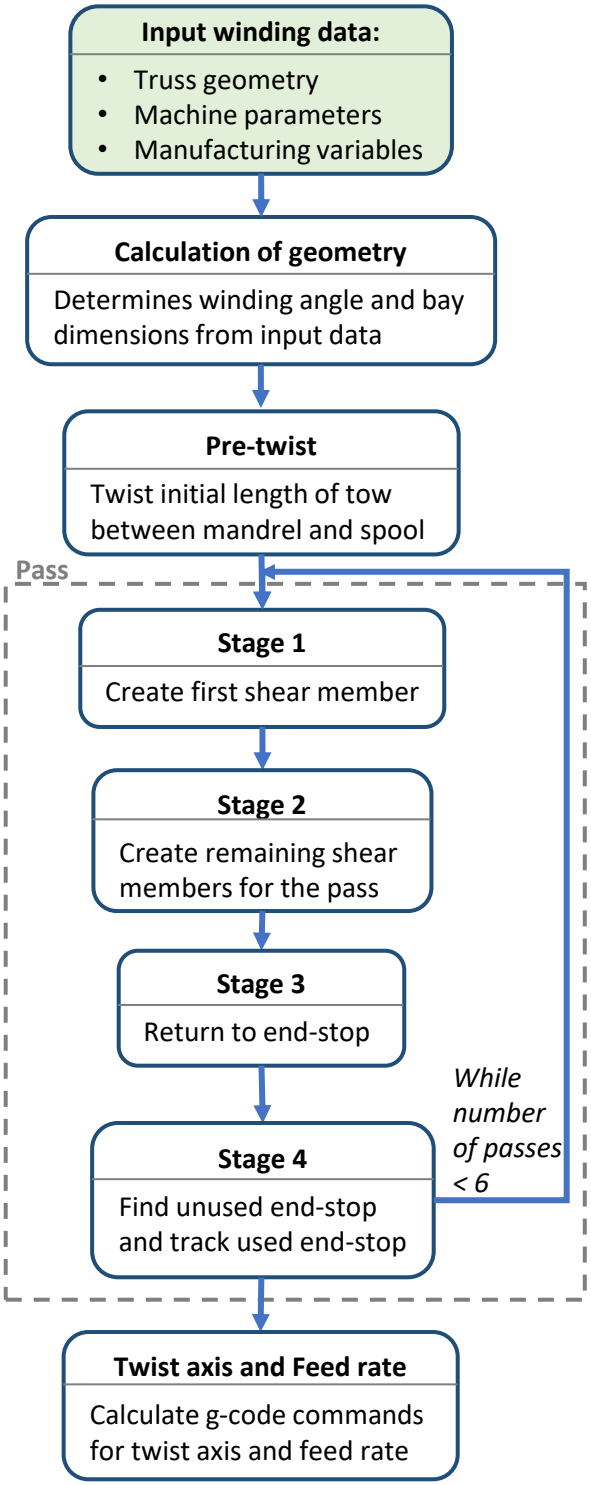

Figure 2.14: Summary of winding program generator operation for prismatic truss with three chord members.

2.2.6 Machine operation

Once operational, the WrapToR winding machine was used frequently to manufacture truss test samples. A variety of truss configurations were manufactured, a selection of which are shown in Figure 2.15. While this included a small number of tapered trusses and one hexagonal truss, the majority were of the standard three-chord member, prismatic arrangement. Detailing of all the standard arrangement truss configurations produced using the machine are detailed in Appendix C. Also detailed in Appendix C are the winding times and average masses for each truss configurations. Throughout the work in this thesis, a constant tow federate of 2 m/min was used. This resulted in winding times between 4 minutes 13 seconds and 4 minutes and 41 seconds for 1 m long trusses. While no controlled timing of the previously used hand-winding technique has been conducted, it is highly likely that these sub-5-minute machine winding times are a significant improvement. The level of repeatability is also likely to be significantly improved. The machine is capable of running at much higher feed rates, however, doing so is likely to be detrimental to tow impregnation due to a reduction of time submerged within the resin bath. While solutions exist to improve impregnation allowing higher feed rates, increasing feed rate was not a primary objective for this work and hence it is not investigated within this thesis.

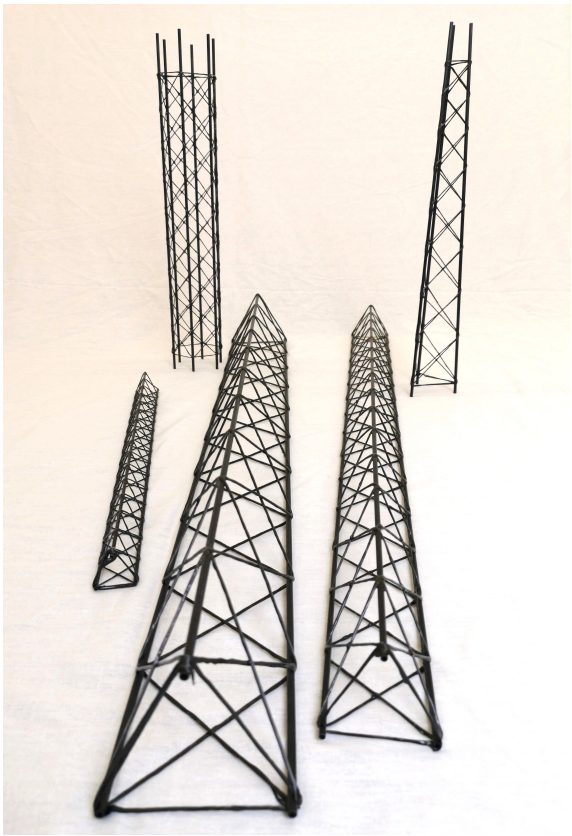

Figure 2.15: Selection of truss configurations produced using the winding machine.

2.3 Tapered truss manufacture

Often beam members used in real-world applications have a tapering of their section along the length. When a beam is used in a cantilever loading case, a tapering cross-section offers a more structurally efficient solution because the section properties scale along the beam length with the bending moment. For these reasons, the ability to manufacture tapered trusses will likely be beneficial for certain applications.

To enable the manufacture of tapered trusses, no modifications to the machine hardware were required meaning the constructed three-axis machine was suitable. While a fourth axis that allows translation of the delivery head eyelet would simplify the winding program, it is still possible with just three axes; this does, however, require significant alterations to the winding program generation process.

Two main alterations were made to the WPG to produce tapered winding patterns. Firstly, as the dimensions of the truss bays vary along the length, the relationship between the truss length, truss radius, number of truss bays, and winding angle is not trivial. Therefore, an extra step is required to determine the winding angle from given truss length, section dimensions, and number of bays. The additional parameters required to define tapered trusses and their relationship to one and other is detailed in Section 2.3.1. The second alteration is due to the change in length of each coincident shear member. This means that a single G-code instruction is required for the creation of each individual shear member and results in winding programs containing many more G-code instructions. In Section 2.3.2, an overview of how the WPG is altered is to account for truss tapering is given. A full detailing of the code's operation is given in Appendix B. As well as altering the WPG, tapered truss manufacture also required modification to the mandrel design; this is detailed in Section 2.3.3.

2.3.1 Geometric definition

The key difference when defining tapered truss geometry is that the truss height and bay lengths vary along the truss length. Five inter-related parameters are used to define the external geometry of a tapered truss; these are the root height, tip height, length, winding angle, and number of bays. With any four of these parameters being known, the fifth can be calculated. In the tapered WPG code a tapered truss is defined by the root height, tip height, length, and number of bays. From these inputs, the truss winding angle and then bay dimensions are calculated. As with a prismatic truss, the shear member angle must be kept constant, otherwise, the tow would slip along the chord members. Additional to stopping tow slippage, keeping a constant winding angle also greatly simplifies the process of determining tapered truss geometry.

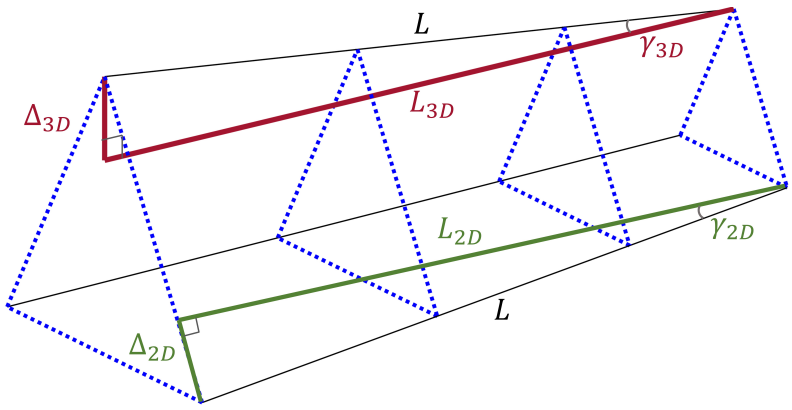

Figure 2.16: Geometry definition of tapered truss.

To determine the winding angle and the dimensions of each truss bay, it is first necessary to find a relationship between the truss length, section heights, number of bays, and winding angle. The first step to achieving this is the definition of three truss lengths. The first, L, is the inputted truss length which is defined as the length of the truss from root to tip along a chord member. The second, L_{3D}, is the length of the truss parallel to the truss centre axis in 3D space i.e. along the mandrel centreline. The third, L_{2D}, is the length of the truss parallel to the centre line of a 2D planar truss face. An example tapered truss showing these lengths is displayed in Figure 2.16. Also shown in Figure 2.16 is the taper angle of the truss, γ_{3D}, and the taper angle of a 2D planar truss face, γ_{2D}.

The length of the truss parallel to the centre line of a 2D planar truss face, L_{2D}, is useful for determining the geometry of individual truss bays, and is found as follows:

$$L_{2D} = \sqrt{L^2 - \delta_{2D}^2} \tag{2.3}$$

where δ_{2D} is half the change in truss height from root to tip, i.e.:

$$\delta_{2D} = \frac{h_{\text{root}} - h_{\text{tip}}}{2} \tag{2.4}$$

The taper angle is then given by:

$$\gamma_{2D} = \sin^{-1}\left(\frac{\delta_{2D}}{L_{2D}}\right) \tag{2.5}$$

To determine the truss winding angle, θ_w, from the given inputs, it is useful to consider the general 2D planar truss side seen in Figure 2.17. Here height and length dimensions for each bay is denoted using a subscript relating it to its relevant bay. A tapered truss is defined to have n_b bays where bay 1 is the root bay and bay n_b is its tip bay. Here the height of each bay, h_n, is defined as the section height at the bay root. The length of the bay parallel to the centre line of the planar truss face is denoted by l_{2D}.

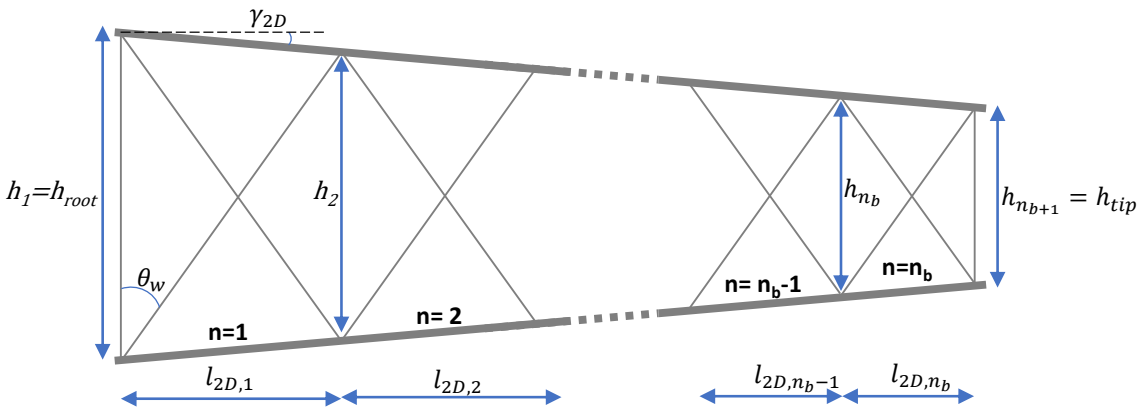

Figure 2.17: Planar side of general tapered truss with n_b truss bays.

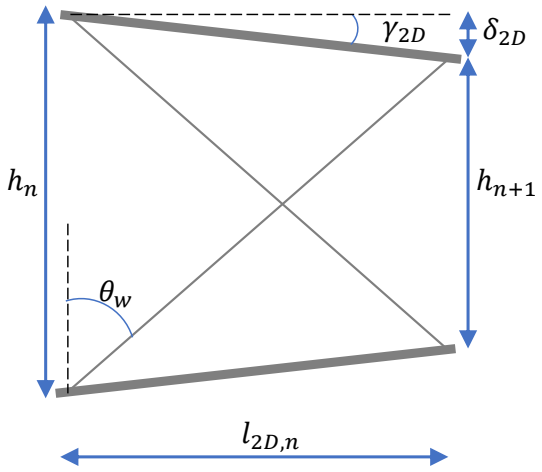

Figure 2.18: General dimensions of nth tapered truss bay.

By considering the planar face of a general tapered truss bay (Figure 2.18) the following three relationships can be drawn:

$$\delta_{2D,n} = \frac{h_n - h_{n+1}}{2} \quad (2.6) \qquad \tan\gamma_{2D} = \frac{\delta_{2D,n}}{l_{2D,n}} \quad (2.7) \quad \tan\theta_w = \frac{l_{2D,n}}{h_n - \delta_{2D,n}} \quad (2.8)$$

Rearranging Equation 2.8 and substituting into Equation 2.6 gives:

$$\delta_{2D,n} \cot\gamma_{2D} = (h_n - \delta_{2D,n}) \tan\theta_w \tag{2.9}$$

Rearranging this for $\delta_{2D,n}$ gives:

$$\delta_{2D,n} = \frac{h_n \tan\gamma_{2D} \tan\theta_w}{1 + \tan\gamma_{2D} \tan\theta_w} \tag{2.10}$$

Equating Equations 2.6 and 2.10 and then rearranging gives:

$$h_{n+1} = h_n \left(1 - \frac{2\tan\gamma_{2D} \tan\theta_w}{1 + \tan\gamma \tan\theta_w}\right) \tag{2.11}$$

From equation 2.11 it is seen that for any bay n, the height at its tip, h_{n+1}, is equal to the height at its root, h_n, multiplied by a constant. Considering Equation 2.6 for any truss bay n, the bay height is related to the truss root height such that:

$$h_n = h_{\text{root}} \left(1 - \frac{2\tan\gamma_{2D} \tan\theta_w}{1 + \tan\gamma_{2D} \tan\theta_w}\right)^{n-1} \tag{2.12}$$

Applying this equation to the tip bay gives the following relationship:

$$h_{tip} = h_{root} \left(1 - \frac{2\tan\gamma_{2D} \tan\theta_w}{1 + \tan\gamma_{2D} \tan\theta_w}\right)^{n_b} \tag{2.13}$$

In Equation 2.13 all parameters, except θ_w, are known. It is therefore possible to rearrange and solve for θ_w:

$$1 - \sqrt[n_b]{\frac{h_{tip}}{h_{\text{root}}}} = \frac{2\tan\gamma_{2D} \tan\theta_w}{1 + \tan\gamma_{2D} \tan\theta_w} \tag{2.14}$$

Referring to the LHS of this equation as Q, such that:

$$Q = 1 - \sqrt[n_b]{\frac{h_{tip}}{h_{root}}} \tag{2.15}$$

and rearranging to find θ_w gives:

$$\cot\theta_w = \tan\gamma_{2D}\left(\frac{2}{Q} - 1\right) \tag{2.16}$$

Once θ_w is calculated it is possible to determine the height of each bay using Equation 2.12. By substituting Equation 2.7 into Equation 2.8, the following equation relating bay length and height is found, in which the term inside the brackets is the ratio of the bay length to height:

$$l_{2D,n} = h_n\left(\frac{1}{\cot\theta_w + \tan\gamma_{2D}}\right) \tag{2.17}$$

By using the equations derived above the parameters defining the geometry of a tapered truss and its individual bays can be calculated. These parameters are used within the tapered truss WPG which is discussed in the following section.

2.3.2 G-code generation alterations

To enable manufacturing of tapered trusses using the three-axis winding machine, several alterations to the WPG were made. An overview of how the tapered WPG operates and how it differs from that of a prismatic truss is given within this section. A detailed explanation of the code‘s operation can be seen in Appendix B.

A flowchart summarising the operation of the tapered WPG is displayed in Figure 2.19. The first step involves using the equations derived in Section 2.3.1 to calculate the dimensions of each truss bay. Once the geometry of each bay is determined, it is then possible to calculate the necessary movements of the machine axes to create the desired winding pattern. The WPG process seen in Figure 2.19 is slightly different than that for a prismatic truss. This is because each bay has a different height and length, and therefore at each bay, the relative rate of the longitudinal and mandrel axes has to change. This means that the creation of each shear member requires an individual G-code instruction. As is seen in Figure 2.19, the movements in each pass are determined by repeating stage 1 n_b times. Determining the G-code instructions for each bay is achieved using similar formulations to stage 1 for the prismatic truss, however, it is applied to every truss bay and has alterations to account for the taper.

Following the completion of Stage 1, the WPG process is then identical to that of a prismatic truss. Tapered WPG stages 2 and 3 are equivalent to stages 3 and 4 for prismatic trusses. The method for determining feed rate and the twist axis movements are also equivalent.

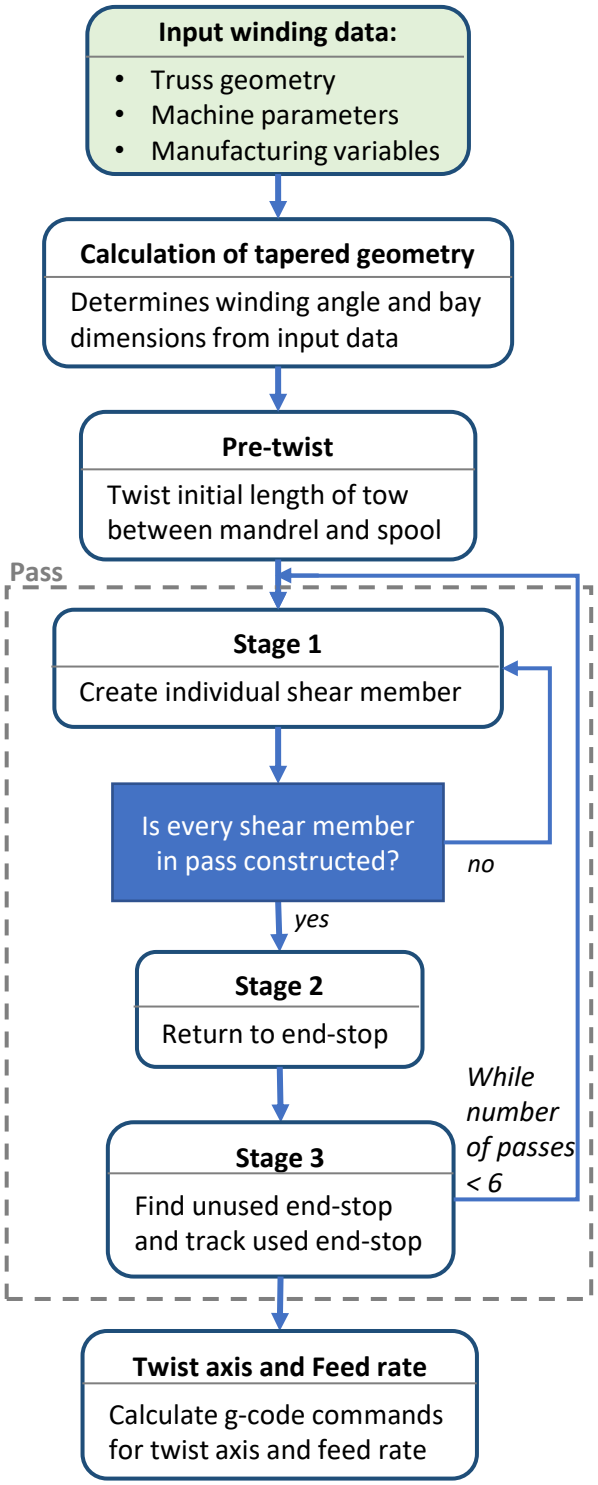

Figure 2.19: Summary of winding program generator operation for tapered truss with three chord members

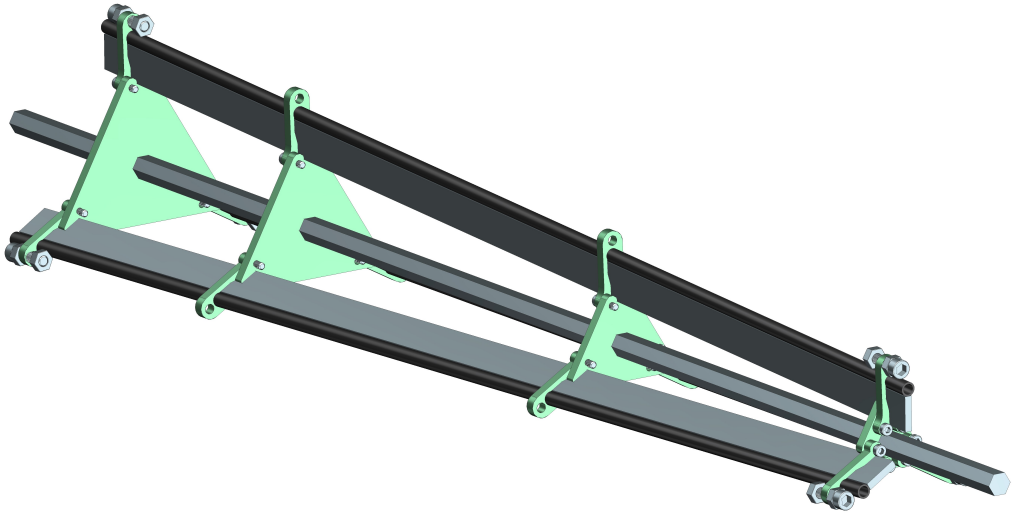

Figure 2.20: CAD image of tapered mandrel generated using parameterised CAD file.

2.3.3 Tapered mandrel construction

The prismatic truss mandrel detailed in Section 2.2.3 required modification to enable the manufacture of tapered trusses. The tapered mandrel construction features the same components as the prismatic version, that is a central hexagonal bar, laser-cut acrylic mounts, steel flat-bars, CFRP pultruded tubes, and laser-cut clips. The key difference is that the laser-cut mounts vary in size along the length of the truss.

For efficient production of tapered mandrels, a parameterised CAD assembly was created that automatically generates the geometry of the laser-cut acrylic parts from input truss geometry. Inputted into this file is the truss length, root height, and tip height which it then uses to calculate the size and location of each acrylic mount. A CAD image of a tapered mandrel generated using the parameterised file is shown in Figure 2.3.3.

Due to the tapering, the longitudinal axis of the pultrusion tubes is not perpendicular to the 2D plane of the acrylic mounts. To accommodate this, the acrylic clips have to bend. As the clips can only bend so far before breaking, the taper ratio achievable with this design is limited.

2.3.4 Results and discussion

To test the tapered truss manufacturing process, a demonstration truss was manufactured using the methodology outlined in the previous subsections. The tapered truss geometry used for the demonstrator is given in Table 2.4 and the final cured part is displayed in Figure 2.21.

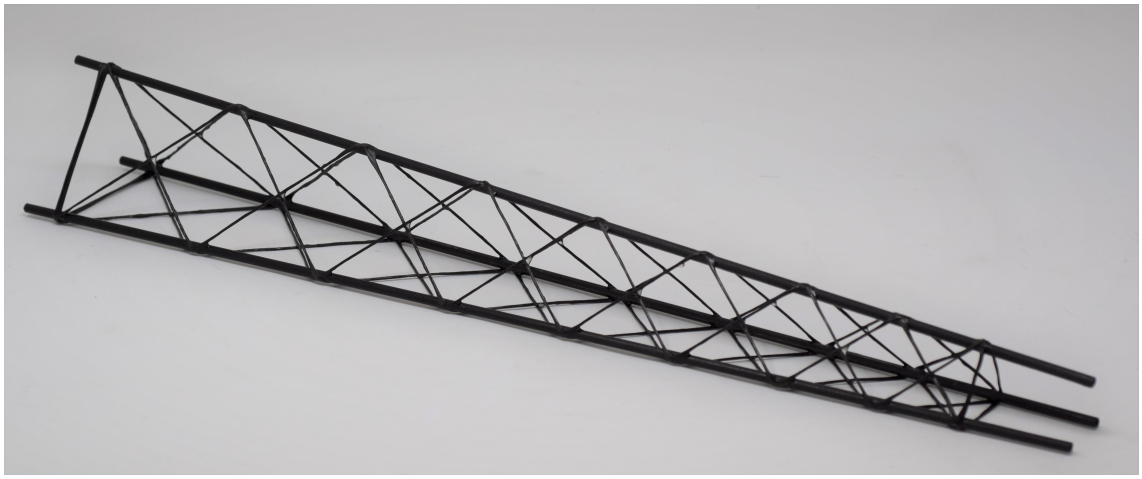

Figure 2.21: Tapered truss sample.

While producing the tapered truss demonstrator, one limitation of the process was identified. Due to the variation in truss section dimensions along the length, the distance between the mandrel and the carriage eyelet increases when moving from root to tip. This meant that when executing stage 2 of the winding program at the truss tip, the eyelet was sufficiently far from the mandrel that slack was generated within the tow upon returning to the end-stop. For this demonstration, the problem was elevated by manually rotating the tow spool to remove any generated slack. To remove this issue, any future machine design could either incorporate a fourth machine axis that allows movement of the carriage eyelet perpendicular to the truss length, or a spool clutch device that reverses tow unwinding when slack is present.

Table 2.4: Dimensions of demonstration tapered truss seen in Figure 2.21.

Root height (mm)	Tip height (mm)	Winding angle (°)	Bay number	Truss length (mm)
66	34	46.0	8	400

2.4 Concept scaling

Developing the ability to produce larger scale trusses would allow the WrapToR technology to be utilised in a wider range of applications. During the work within this thesis, three key challenges of up-scaling the technology were identified. Within this section, these challenges are detailed and their developed or potential solutions discussed.

2.4.1 Development of multi-spooling device

The machine design detailed in Section 2.2 is limited to producing trusses with shear members made from only a single tow. As carbon fibre tows are typically only available in sizes up to 48k, having only one spool limits the potential shear member size. Limiting the shear member size will limit the size of the truss section that would be structurally useful. This is because the section size can only be increased so far before the stability of the shear members becomes critical. It was therefore identified that developing the ability to produce larger diameter shear members would be a key challenge when attempting to scale the process for larger truss manufacture.

To expand the capabilities of the machine to enable the production of trusses with larger shear members, a multi-spooling device was developed. This device, which is pictured in Figure 2.22, holds four tow spools. The spools are rotated to twist the fibres together creating a shear web wrap formed of up to four tows. A key design feature of the multi-spooling device is that the tows are held separate until they enter the resin bath. This is done so that the individual tows get some level of impregnation before they are twisted together to form a larger tow bundle. If the tows were to combine before entering the bath, it would be more difficult for the resin to propagate into the centre of the larger fibre bundle. The effectiveness of this device to impregnate the fibre bundles is investigated via optical microscopy in Section 2.5.

For all truss specimens manufactured, a consistent tow size of 24k with a 7 μm fibre diameter was used. Using the multi-spooling device, trusses with shear members of the following fibre numbers were manufactured: 24k, 48k, 72k, and 96k.

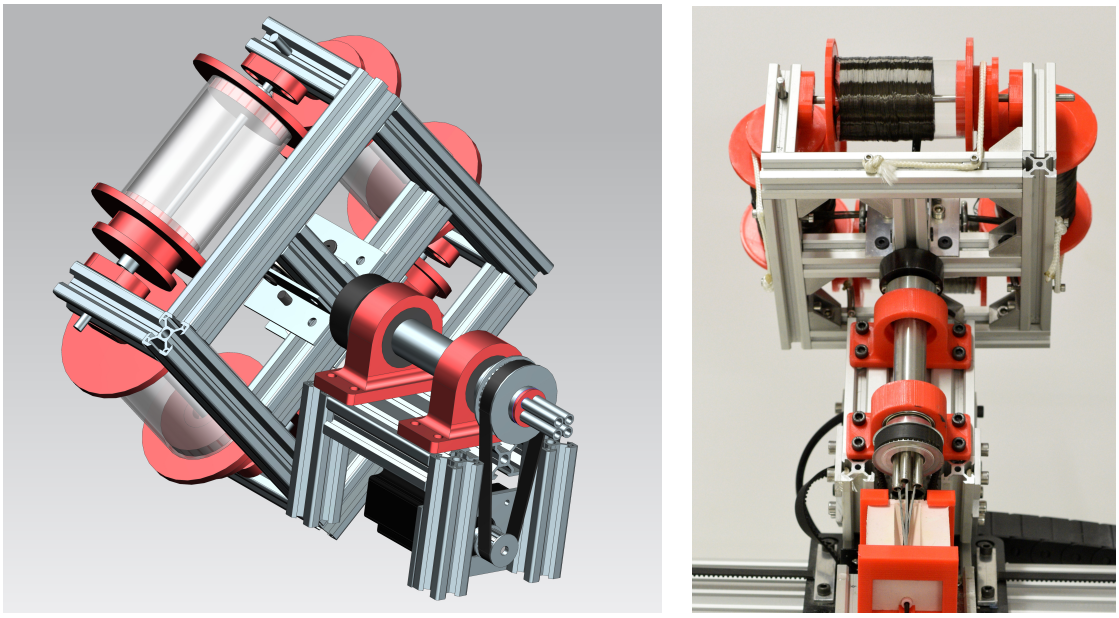

(a) (b)

Figure 2.22: Images of multi-spooling device. a) CAD rendering; b) in operation.

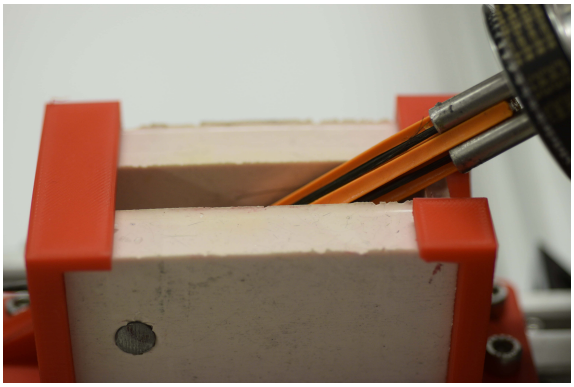

Figure 2.23: Cone added to multi-spooling device to separate tows.

Upon testing of the multi-spooling device, it was found that when using two tows, the individual strands did not combine until they were well within the resin bath. This was the intended behaviour to maximise impregnation. However, when using three or four tows, it was found that the point at which the tows combined would move to the very top of the resin bath. This meant that the separate stands had little or no time within the resin to be impregnated. As this was not the desired behaviour, an additional plastic cone was added to keep the tows separate until they reached far into the resin. This additional piece, seen in Figure 2.23, provided a means of separating the tows without totally redesigning the multi-spooling device.

2.4.2 Joint slippage

During manufacturing of trusses with larger shear member sizes, a phenomenon was observed whereby the truss joints would "slip" during the curing stage. The phenomenon can be observed by studying the images in Figure 2.24. Figure 2.24a shows a truss joint in which slipping has not occurred where the shear member tows cross on the top of the connecting chord member. For the slipped joint, displayed in Figure 2.24b, it is seen that the crossing point of the shear member tows has moved to the side of the chord member. It is suspected that the joints migrate to the slipped position because it presents a lower energy state for the tensioned tows.

Joint slipping was found to be worst in the largest shear member trusses produced (96k), and it is suspected that the problem would worsen at larger sizes. Three factors were observed that influenced the level of joint slipping. These were the level of twist, the fibre tension, and the curing configuration. Key to minimising the problem was keeping the trusses stationary while curing. Any attempt to cure the trusses on a rotating mandrel consistently resulted in significant slipping. The most effective method was found to be hanging the truss mandrel vertically for curing. Reducing the level of twist or fibre tension was also observed to lessen the problem.

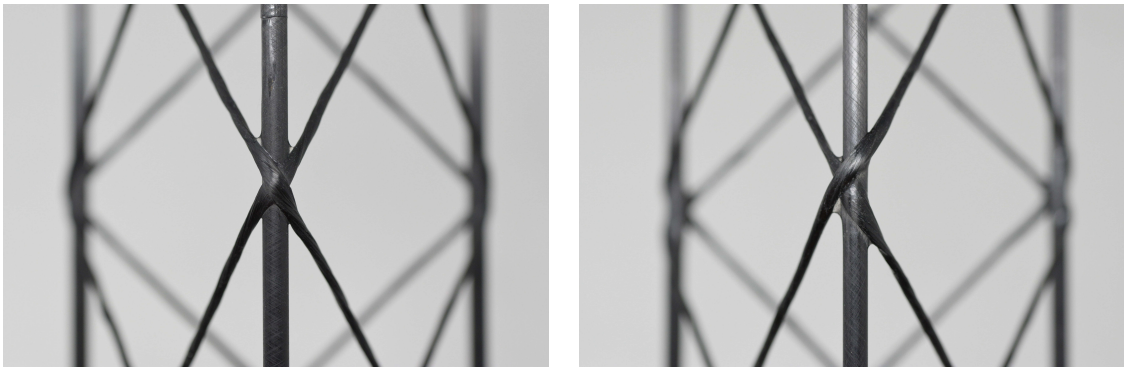

(a) (b)

Figure 2.24: 96k shear member truss joint: a) no slipping; b) significant slipping.

2.4.3 Mandrel stiffness

When attempting to increase truss aspect ratio (truss length over section height), at a certain point flexibility of the mandrel will become an issue. For the work in this thesis, this problem was not encountered as the manufactured trusses had sufficiently low aspect ratio, and hence the problem was not investigated. Mitigation of this problem in any future work will likely require redesigning of the mandrel to improve its bending resistance.

2.5 Investigation of shear member impregnation

The truss shear members are created during the winding process by pulling a carbon fibre tow through an epoxy resin bath and winding it onto the mandrel. While this method is commonly used in conventional filament winding, for truss winding the configuration of the fibre tow as it passes through the resin bath is different due to it having been twisted. Often conventional filament wound parts are consolidated using a vacuum bag and are cured in either an oven or autoclave. The truss winding process however has no consolidation stage. These differences between conventional filament winding and the WrapToR process mean that the impregnation and the quality of the produced wound shear members are of interest. Impregnation of the shear members is of particular concern in larger shear members made using the multi-spooling device as for larger tow, the resin has a larger distance to propagate to reach the centre of the tow. Within this section, the shear member impregnation is investigated by taking and analysing optical micrographs of the member sections.

2.5.1 Methodology

Section micrograph images were obtained for four shear member sizes: 24k, 48k, 72k, and 96k. These samples were cut from fully wound trusses where the truss

samples with shear members consisting of more than one fibre tow (48k, 72k, and 96k) were produced using the multi-spooling device detailed in Section 2.4.1. For each shear member size, at least four samples were imaged using a Zeiss Imager M2 microscope and a 2MP Camera. Note here that for the single tow configuration the micrograph images from the tow twisting investigation in Section 3.6.3 were used. Micrographs were visually inspected for a qualitative assessment. For a quantitative assessment of the shear member quality, the micrographs were analysed using a self-coded Matlab script that detects voids via analysis of pixel colour. The code also detects the outline of the sample and calculates the section area. From the determined sample area and the area of the void regions, the code then calculates void content. By analysing the void regions, the code is also able to determine void numbers and average void size.

2.5.2 Results and discussion

Two micrographs for each tow size are displayed in Figures 2.25 to 2.28. From a qualitative assessment of these images, a substantial quantity of voids is observed in all the samples. A significant variation in the void quantity, size, and distribution is seen. Variance is also seen in the sectional shape of the samples.

In Figure 2.29 the average area and void content of each configuration is displayed. Here the sample area is normalised by the number of combined 24k tows to allow more direct comparison of the different sized samples. Overall sample area variability and void content are relatively high compared to parts made using typical composite processes. This is to be expected given their forming method and the fact that no consolidation stage is used within the process. Minimal change in normalised area and void content is seen between shear members with one and two tows. When adding an additional tow (72k), little change in void content occurs but a lower normalised area is observed; this suggests a drop in resin content. The four tow (96k) shear members had a larger observed void content and normalised area 15% lower than that of the single tow configuration. This suggests that there must be a substantial drop in resin content. Visually comparing Figures 2.25 and 2.28 it is seen that fewer resin-rich regions are present for the 96k tow and that the fibres seem to be more closely packed. Two possible causes for this decrease in resin content are given. Firstly, it is possible that individual tows separated using the plastic cone (Figure 2.23) do not impregnate as effectively. This is possible as the cone reduces the numbers of fibres directly exposed to the resin. The second possible reason is that the larger tow diameter results in a larger twist angle within the fibres. The larger twist angle then results in larger consolidation forces as tension in the tow radially pulls the fibres together.

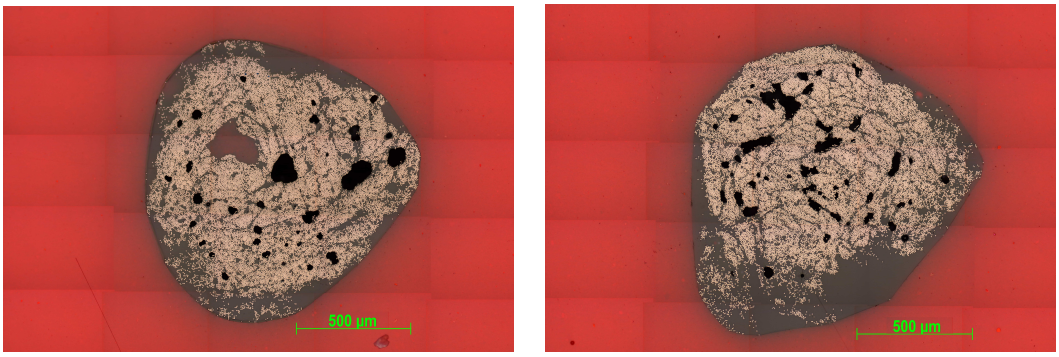

Figure 2.25: 24k shear member sections.

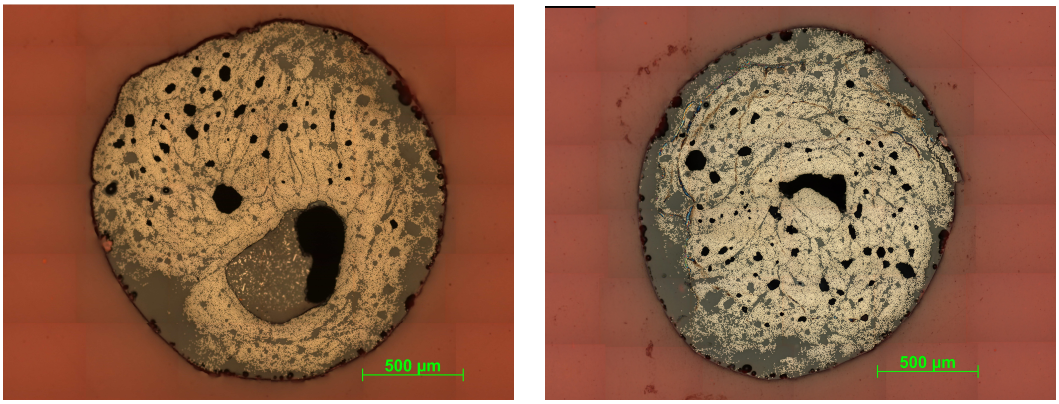

Figure 2.26: 48k shear member sections.

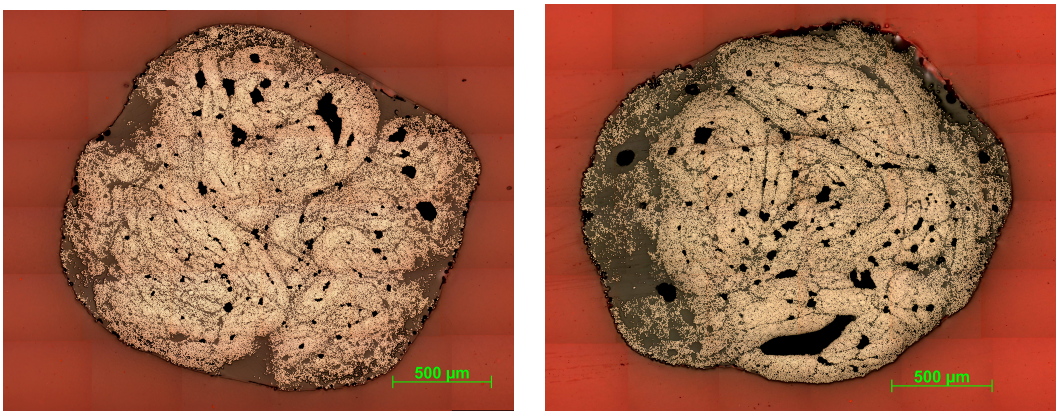

Figure 2.27: 72k shear member sections.

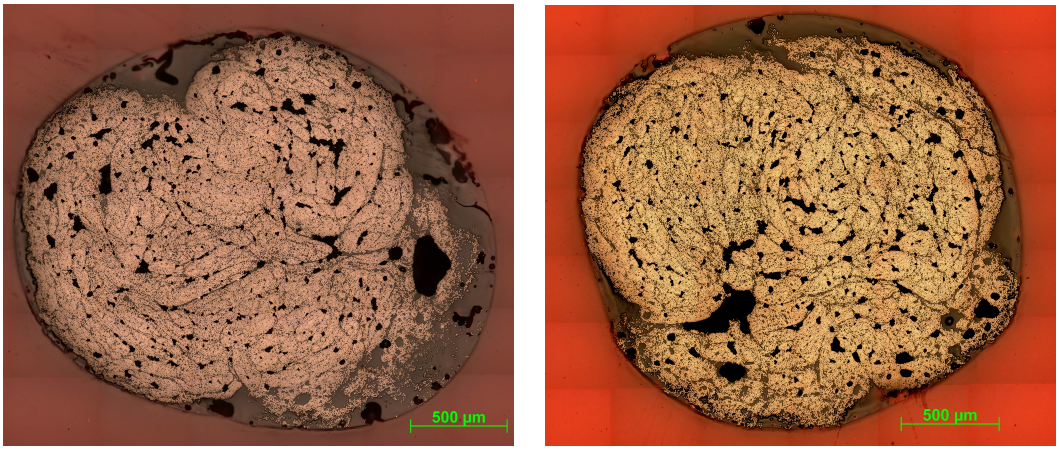

Figure 2.28: 96k shear member sections.

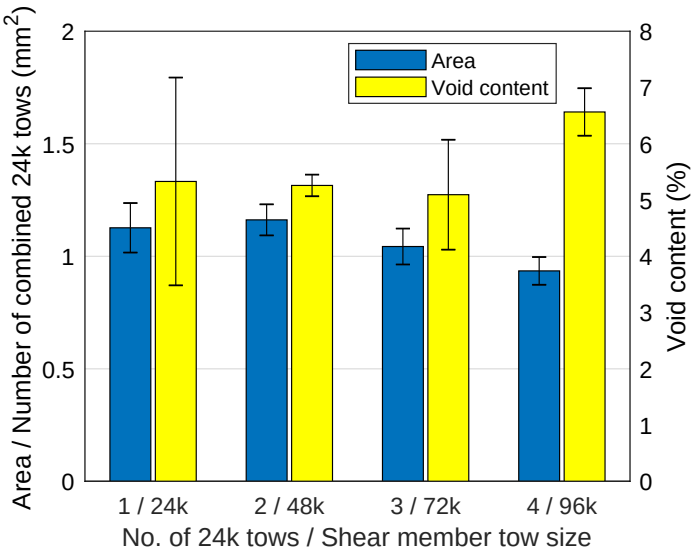

Figure 2.29: Shear member section average area and void content. Error bars denote one standard deviation.

For a more detailed investigation of void distribution within the samples, in Figure 2.30 the average number of voids per sample and the average void size are plotted. The average number of voids per sample is normalised to the sample area for comparison across configurations. These results again show that shear members with one and two tows have similar internal architecture. Again, this changes as the number of tows is increased beyond two, where the number of voids increases but the size of voids decreases (i.e. a higher number of smaller voids). This may also be the result of higher consolidation forces generated from a higher twist angle.

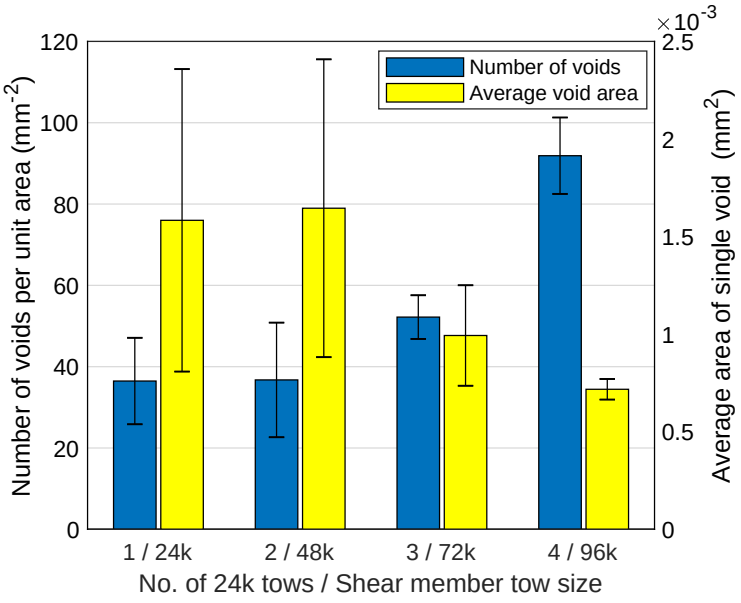

Figure 2.30: Average number of voids per sample and average void size. Error bars denote one standard deviation.

It is uncertain at this stage as to whether the observed drop in resin content and increase in void content for larger shear members has a significant effect on structural performance. Further experimental investigation would be required to determine this. If it were found to be detrimental to performance, redesign of the multi-spooling device could be considered. An improved design would allow the separated tows to be submerged in resin for longer before being combined. Any redesign however, would need to consider the trade-off between improving shear member quality and increasing process complexity or cost.

2.6 Conclusions & further work

The core of the WrapToR technology lies within the manufacturing process. This chapter details the progress made in developing the process from labour-intensive hand-winding to highly automated CNC winding through the design and construction of a three-axis winding machine. The successful operation of the first-ever WrapToR winding machine demonstrated the automatability of the truss manufacturing process. It also improved the production rate and repeatability of the process which proved to be an extremely valuable tool when manufacturing test samples for the experimental work detailed within this thesis. Another benefit of moving to CNC winding was that it enabled the manufacture of a new truss configuration in which the shear web tow is twisted to form near-circular section shear members. The structural benefits of tow twisting will later be demonstrated in Section 3.6.

Increasing truss size is desirable for extending the potential applications of the technology. Producing trusses with larger shear members was identified as a key challenge associated with up-scaling of the technology. To enable manufacturing of larger diameter shear members, a device was developed for combining multiple fibre tows. This device was designed to increase the capabilities of the WrapToR winding machine to allow manufacturing of trusses with shear members formed of up to four 24k tows. The device has been successfully demonstrated through the production of trusses with 24k, 48k, 72k, and 96k shear members. Investigation of impregnation within the produced shear members via optical microscopy showed a drop in resin content and an increased void content when combining more than two tows. Further work is needed here to determine if this has a detrimental effect on the shear member structural performance and if so, how to improve the tow impregnation.

Another challenge identified when attempting to produce trusses with larger diameter shear members was the avoidance of joint slipping. For the truss sizes manufactured, this problem was mitigated by limiting movement of the mandrel while curing. This problem is expected to worsen when producing even larger trusses and will require further work to understand its causes and to develop solutions.

Chapter 3

Truss & constituent characterisation

3.1 Introduction

A key objective of the project was to develop analytical tools to predict the structural behaviour of the WrapToR trusses. To meet this objective, two bodies of experimental characterisation work were required. Firstly, characterisation of the material properties of the truss's constituent members was needed to provide necessary input parameters for the developed analysis tools. Secondly, experimental characterisation of truss structural response was required to validate the predictive capabilities of any developed model.

A WrapToR truss can be conceptualised as the formation of the following three constituent components:

- Chord members: formed of pultruded UD CFRP tubes.
- Shear members: formed of carbon fibre tow impregnated with epoxy.
- Joints: the epoxy bonds that connect the chord and shear members.

Within this chapter, the experimental characterisation of these constituent components is detailed. For the chord and shear members, Young's modulus was determined via tensile testing. As the chord members are purchased in a pre-fabricated form, they were tested in their as-purchased state. Testing of the chord members tubes is detailed in Section 3.2. The shear members are formed during the winding process and, therefore, it is possible that parameters within the process affect the properties of the members. To investigate the effects of varying process parameters on shear member properties, multiple shear member configurations were tested in Section 3.3.

The determined chord and shear member properties were used within the truss structural models (detailed in Chapter 4) to predict truss deflections and member stresses and strains. To assess the accuracy of these models, the truss mechanical

response was experimentally characterised via structural testing. Within the literature, a number of approaches have been used for characterisation of composite lattice beams. The approaches taken by other researchers are detailed and discussed in Section 3.5.1. Within this thesis, all the truss structural characterisation work was conducted using a three-point bend loading configuration. This three-point bend test was used to interrogate both pre-failure and failure behaviour of a variety of truss configurations. The three-point bend test and its development is detailed within Section 3.5.

The developed three-point bend test method is used throughout this thesis for both validation of structural models and for experimental investigations. In this chapter, the test method is first used in Section 3.6 to experimentally investigate the effects of tow twisting on truss structural performance. Truss three-point bend test results from this investigation are then used for two additional purposes: in Section 3.7 to assess the accuracy of a previously developed analysis tool, and in Section 3.8, to compare the structural performance of the WrapToR truss to a conventional composite beam configuration.

3.2 Chord member characterisation

The WrapToR trusses manufactured for the work in this thesis had chord members formed of UD pultruded carbon fibre tubes purchased from EasyComposites™. In Table 3.1, the manufacturers quoted dimensions of the three pultrusion tube sizes used are given. Within this section, these tubes are characterised to find their sectional area, density and tensile modulus.

Table 3.1: Pultrusion tube sizes tested (manufactures quoted dimensions).

External diameter (mm)	Wall thickness (mm)
3	0.5
4	0.5
5	1

3.2.1 Mass and density

A minimum of 6 samples per tube size were measured and weighed to find the mass, section dimensions, and density. The external diameters of the tube section was measured with a micrometre, and the internal diameter was measured using pin gauges. All the tubes were found to have external diameters between 0.04-0.08 mm lower than the manufacturers stated value. The tubes mass per unit length (MUL), external diameter, sectional area, and density are displayed in Table 3.2.

Table 3.2: Chord member pultrusion tube section dimensions and mass properties.

External diameter, manufacturers data (mm)	Measured Diameter (mm)		Area (mm^2)	MUL (g/m)	Density (g/cm^3)
	External	Internal			
3	2.96	1.95	3.73	5.88	1.56
4	3.95	2.95	5.19	8.44	1.52
5	4.92	2.95	11.46	17.97	1.57

3.2.2 Tensile test method

For tensile testing of the pultruded tubes, the "ASTM D3916 – 08: Standard Test Method for Tensile Properties of Pultruded Glass-Fiber-Reinforced Plastic Rod" [107] was used. While this test method is specifically designed for GFRP rods, it was used in this study as no such standard exists specifically for CFRP pultruded tubes. The method uses aluminium clamps that grip the pultrusions for load introduction. Loading the CFRP tubes to failure using the clamps was not possible as they provided insufficient grip to reach required loads. The tests conducted here, therefore, were only used to measure the material tensile modulus. The tube sizes tested are those seen in Table 3.2. The length of each test sample was 30 cm and the gauge length was 20 cm. Testing was conducted on an Instron 8872 test machine with a 25 kN load cell. Samples were loaded at a crosshead displacement rate of 5 mm/min. Strain measurements were recorded using an Imetrum Video Gauge™. An image of the test set-up is displayed in Figure 3.1.

3.2.3 Tensile test results

Results of the pultrusion tube tensile testing are displayed in Table 3.3. Here the axial stiffness (section area multiplied by Young's modulus) was determined from the slope of the load versus strain graph. The Young's modulus was then determined by dividing the axial stiffness, AE, by the measured tube section areas in Table 3.2. The results show that the 3 and 4 mm tubes have near-identical Young's moduli. The 5 mm tube however has a modulus that is 9% lower than the two smaller sized tubes.

Table 3.3: Axial stiffness and Young's moduli of chord member pultrusion tubes

Tube outer diameter (mm)	No. samples tested	Axial stiffness (kN)		Young's Modulus (GPa)
		Average	Standard deviation	
3	5	529.8	25.3	137.1
4	5	741.9	14.5	136.9
5	6	1433	74.4	125.1

Figure 3.1: Tensile testing of chord member pultrusion tubes.

3.3 Shear member characterisation

The WrapToR trusses manufactured for the work in this thesis had shear members formed of intermediate modulus carbon fibre tow impregnated with low viscosity epoxy resin. Within this section, samples for several shear member configurations are manufactured by varying process parameters. These samples are then tested using, the "ASTM D4018 -17 Standard Test Methods for Properties of Continuous Filament Carbon and Graphite Fiber Tows" [108] to determine both tensile properties and resin content.

3.3.1 Sample configurations

The WrapToR shear members are created during the winding process, and therefore their properties are likely to be affected by the process variables. To investigate any such effects, eight shear member tow configurations were produced by varying the following manufacturing variables: level of twist, feed rate, resin type, tow size, and resin bath exit-hole size. The chosen configurations are detailed in Table 3.4 with the baseline configuration (BL) being the most commonly used shear member

Table 3.4: Shear member tow test sample configurations.

Config. ID	Investigated variable	Tow size	Resin type	Degree of twist (mm^{-1})	Bath exit-hole size (mm)	Feed rate (mm/min)
BL	Baseline	24K	Epoxy	0.0303	2	2000
R	Resin type	24K	Vinyl-ester	0.0303	2	2000
F (flat)	Twist (none)	24K	Epoxy	0	2	2000
HT	Twist (high)	24K	Epoxy	0.05	2	2000
48k	Tow size	48k	Epoxy	0.0303	2.8	2000
SH	Bath exit-hole	24K	Epoxy	0.0303	1.5	2000
Q (quick)	Feed rate (high)	24K	Epoxy	0.0303	2	2800
S (slow)	Feed rate (low)	24K	Epoxy	0.0303	2	1200

configuration for truss manufacture. Tenax® IMS60 24K carbon fibre tow was the tested reinforcement material which had a measured mass of 0.87 g/m. The test samples were manufactured on the truss winding machine using a large mandrel that allowed sample lengths of 220 mm. For each configuration, eight samples were manufactured and weighed to find the mass and resin content; and four samples were tensile tested. All configurations used SuperSap® CLV epoxy resin for the matrix, except for configuration R which used a medium viscosity vinyl-ester resin (ATLAC® premium 100). For configuration 48k a larger, 48k tow size was formed by combining two 24k tows together. For this configuration, the resin bath exit-hole was increased to provide a tow-to-exit-hole area ratio that was similar to that of the baseline configuration.

3.3.2 Mass, resin content, and density

Using the method described in the test standard [108], fibre tow was weighed before and after impregnation to determine the mass per unit length (MUL) and resin content. The values found for each configuration are displayed in Table 3.5. The Students T-test was used to investigate if the configurations had statistically significant variation from the baseline. Configurations that had less than 5% probability of being in the same data set as the baseline are deemed to vary significantly and are highlighted in the table with an asterisk.

Table 3.5 shows how many of the alterations in process parameters affect the tow resin content. Samples containing the vinyl-ester resin had a slightly higher resin content compared to the baseline. In the vinyl-ester samples, beading of the resin along the tow was witnessed (seen in Figure 3.3) which likely accounts for the increased resin content. This beading was not witnessed for any of the epoxy samples. Changing the level of twist was seen to have an effect on resin content where the untwisted samples (configuration F) had higher resin content than twisted baseline samples (configuration BL). As is discussed in Section 3.6, untwisted tow spreads out during winding. This spreading may promote wetting by increasing the

Table 3.5: Configuration MUL and resin content.

Config ID	MUL (g/m)			Resin content (% mass)		
	Average	Standard deviation	% difference	Average	Standard deviation	% difference
BL	1.56	0.07	baseline	43.9	2.30	baseline
R*	1.70	0.07	8.40	48.5	2.11	9.9
F *	2.03	0.10	26.9	57.0	2.12	26.2
HT	1.57	0.07	0.70	44.4	2.38	1.0
48k*	2.59	0.03	54.5	32.6	0.76	-25.0
SH*	1.30	0.04	-14.3	33.0	1.91	-25.4
S*	1.65	0.07	5.00	46.9	2.36	6.9
Q	1.52	0.08	-2.50	42.3	3.09	-3.9

**configuration's MUL and resin content vary significantly from the baseline.*

tow surface area. It is also possible that the spread tow forces the flexible silicone resin bath exit-hole to expand, allowing a greater flow of resin. It is worth noting here that the machine design was later updated to use an inflexible, ceramic bath exit-hole (detailed in Section 2.2.2) which would likely remove this effect.

As would be expected, switching the resin bath exit-hole to a smaller size resulted in a lower resin content. Using the larger tow (configuration 48k), also resulted in lower resin content. When winding the 48k tow samples, the hole diameter was increased to match the area change of the larger tow meaning that the reduction in resin content can not be attributed to a change in relative size between the tow and exit-hole. It is, therefore, likely that this lower resin content is caused by reduced propagation into the larger diameter tow. Winding feed rate was also seen to affect resin content. Slowing the feed rate relative to the baseline increased the resin content, likely because it gives resin more time to permeate into the tow. Following this trend, increasing the speed appears to reduce the resin content; however, the small observed change was not statistically significant.

3.3.3 Tensile test method

Tensile testing of the shear member material was conducted in accordance with the ASTM-D4018 [108] standard. Within the standard, three options are proposed for sample end-tabbing. All three of these options were trialled on the WrapToR shear member tow to determine the most appropriate method. The methods where:

1. Un-tabbed samples with rubber grips
2. GFRP tabs with epoxy resin
3. Un-tabbed samples with aluminium grip plates

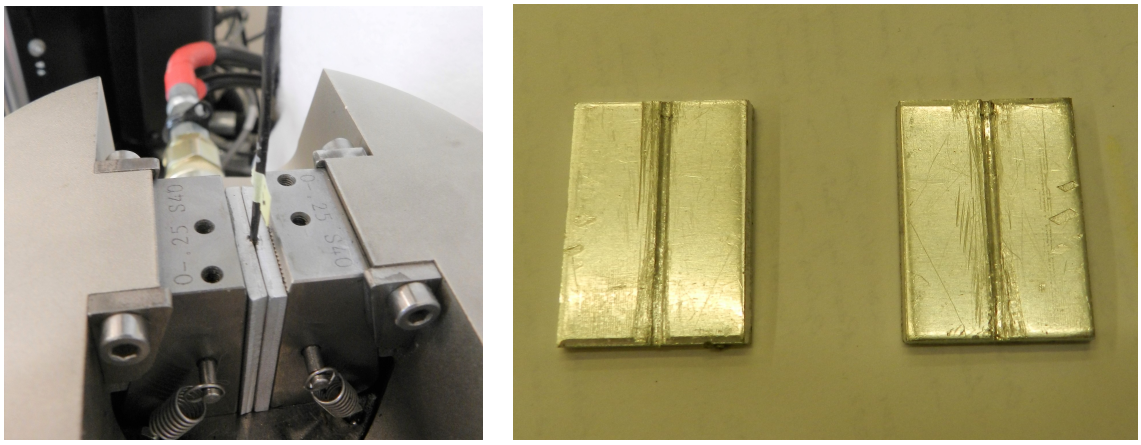

(a) (b)

Figure 3.2: Aluminium plate end-tabbing method: a) plates in test machine; b) Plate surfaces.

The rubber grips in method 1 were found incapable of holding the samples at higher loads and therefore were deemed unsuitable. With method 2, it was possible to load the samples to failure without slipping; however, getting suitable alignment when bonding the end-tabs was difficult and very time-consuming. Additional to this problem, each sample tested with the bonded GFRP end-tabs was seen to fail within the tabs. When using the aluminium plate grips (method 3), it was possible to load the samples to reasonably high loads before observing slipping. For some samples testing to failure was achieved; however, failure would always occur within the grips. Due to it being easier to achieve sample alignment and being less time-consuming, method 3 was chosen as the most suitable method. Images showing the aluminium plate grips used for end-tabbing are displayed in Figure 3.2.

Due to failure being consistently observed within the grips, it was concluded that measuring tensile strength via these tensile testing methods would not be possible. The tests were therefore conducted with the purpose of determining only the modulus. As will be discussed later in Section 5.3, tensile failure of the shear members is unlikely to occur in WrapToR trusses and hence determining tensile strength is of minimal importance. Tensile modulus, however, is a key input for the structural models developed in Chapter 4.

Again, tensile testing was conducted on an Instron 8872 test machine with a 25 kN load cell. A crosshead displacement rate of 2 mm/minute was used. Samples had a gauge length of 150 mm and a total length of 220 mm. Strain measurements were taken using an Imetrum Video Gauge^{TM}. Due to the small sample width, the video gauge was unable to reliably track markings on the sample surface. To improve tracking, marked tape was attached to either end of the sample. An image of the set-up is displayed in Figure 3.3.

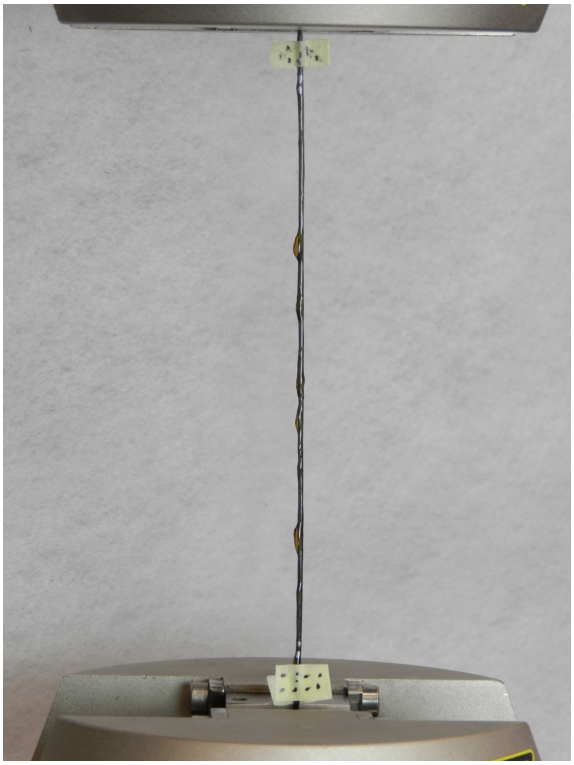

Figure 3.3: Shear member tow sample in test machine.

The axial stiffness, AE, of the tow samples is determined from the gradient of the load versus strain graph. To determine the Young's moduli of the impregnated tow, accurate measurement of the section area is required. Due to the small and inconsistent sectional shape of the impregnated tow samples, determining the area is difficult. For comparison of the configurations Young's moduli, an estimate of the impregnated tows sectional area was found by taking measurements of diameter at three locations along four samples and assuming a circular-section. Note here that the diameters could not be determined for configuration F samples, due to the assumption of a circular-section being invalid, and the R configuration samples, due to resin beading (seen in Figure 3.3) creating an inconsistent cross-section.

For the developed analysis methods in Chapter 4, accurate values for the members' sectional properties and Young's modulus were required. More accurate measurements of the cross-sectional areas were later acquired for the baseline configuration during the optical microscopy investigation detailed in Section 2.5. These area measurements were therefore used to provide more accurate predictions of the Young's modulus for implementation of the structural model. This refinement in the estimation of Young's modulus is detailed in Section 3.3.5.

3.3.4 Tensile test results

Tensile testing results showing the average axial stiffness, AE, for each configuration are displayed in Figure 3.4. Again, the results were investigated using the Students T-test to determine any statistically significant variance from the baseline configuration. The highest stiffness is seen in configuration 48k, whose stiffness is 98% larger than the baseline. This range of increase is expected as the number of fibres is doubled. The only other sample with a significant variation from the baseline is the non-twisted configuration, F, which has a stiffness that is 6% larger. This increase in stiffness is most likely caused by greater fibre alignment with the member longitudinal axis.

The measured diameters and correspondingly calculated section areas and Young's moduli for each configuration are displayed in Table 3.6. Here the measurements for configuration SH show that decreasing the resin bath exit-hole size decreases the area of the produced members. This suggests that the resin constant and members section geometry can be manipulated by altering the exit-hole size. A strong correlation is observed here between a configurations Young's modulus and its resin content. To display this correlation, the two properties are plotted in Figure 3.5. Here it is seen that configurations with higher resin content have lower modulus, and vice-versa. This inverse relationship between resin content and Young's modulus suggests that the level of wetting is the dominant cause in the variation of modulus between the configurations.

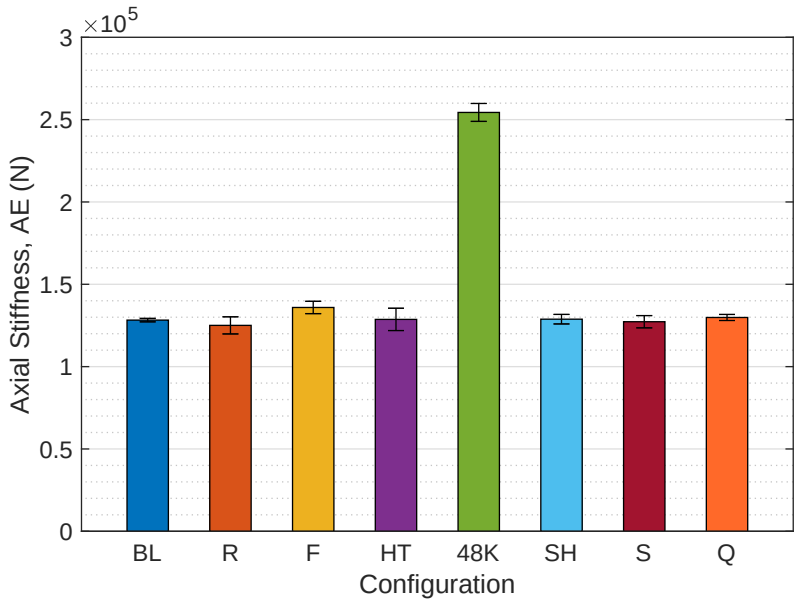

Figure 3.4: Shear member tow average axial stiffness. Error bars equal to one standard deviation.

Table 3.6: Shear member tow configuration average section diameter, area, and Young's modulus

Config ID	Tow diameter (mm)	Area (mm^2)		Young's Modulus (GPa)	
		Value	% difference	Value	% difference
BL	1.23	1.19	baseline	107.8	baseline
R	-	-	-	-	-
F	-	-	-	-	-
HT	1.22	1.17	-0.7	110.0	2.0
48k	1.52	1.83	22.3	139.0	25.3
SH	1.08	0.92	-11.8	140.0	26.0
S	1.24	1.21	0.8	105.2	-2.4
Q	1.20	1.13	-2.46	114.9	6.4

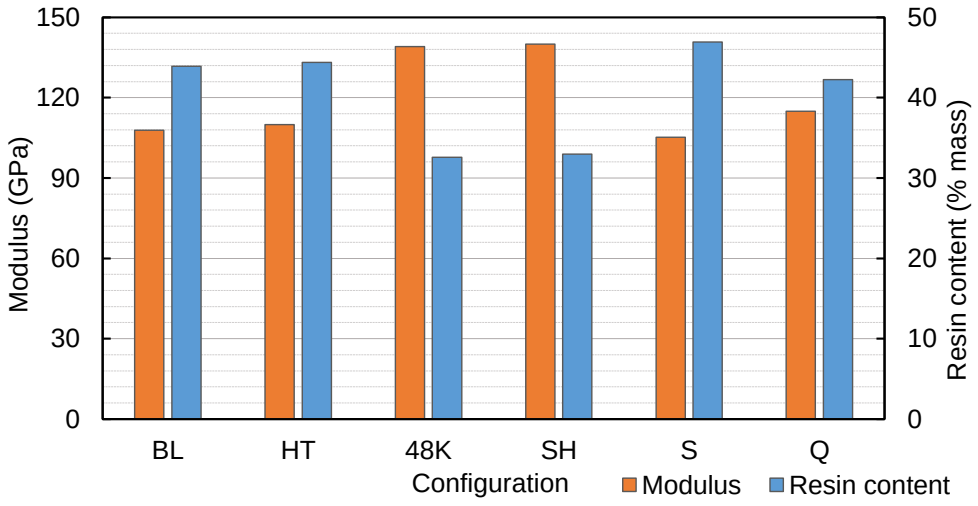

Figure 3.5: Relationship between resin content and modulus.

3.3.5 Refinement of Young's modulus estimation

During a later conducted investigation into the effects of tow twisting (detailed in Section 2.5), a more accurate method of measuring the shear member cross-sectional area was developed. This method involved analysing section micrographs using a Matlab image analysis script to determine section area. The shear members analysed during this study were taken from actual truss samples rather than being wound specifically for shear member tensile testing. The process parameters used for the manufacture of these trusses were identical to those used in the baseline configuration, BL. Using the shear member cross-sectional area determined via microscopy, a refined estimate of shear member Young's modulus was calculated and is displayed in Table 3.7. Here, Young's modulus was calculated assuming that member axial stiffness, AE, was 128,250 N; consistent with that found for the baseline configuration in Section 3.3.4. These refined values were used within the later developed structural models.

Table 3.7: Refined baseline configuration properties.

Section area (mm^2)	Radius (mm)	Modulus (GPa)
1.0891	0.589	117.76

3.4 Joint characterisation

The WrapToR joints are the co-bonded connections between the shear and chord members. They are formed during the winding process when the wetted shear member tow is wrapped over the pre-cured chord members. At each joint, four shear members, formed of two tow strands, intersect at a single chord member tube. When the joints are viewed from above (Figure 3.6a), the shear member tow forms a cross on the chord member surface. Additional to the connection of the contacting tow and pultruded tube, surface tension in the resin results in the formation of menisci; these can be seen in Figure 3.6. These menisci increase the contact area, and are likely to improve the integrity of the joint.

Unlike the chord and shear members, the joints can not be easily isolated and tested to determine mechanical properties. Such characterisation of the joints would require the development of custom test methods and was therefore deemed beyond the scope of this thesis. Instead, certain aspects of the joint geometry were characterised as these were suspected of having a significant effect on their mechanical performance. Understanding how the truss geometric parameters affect the joint ge-

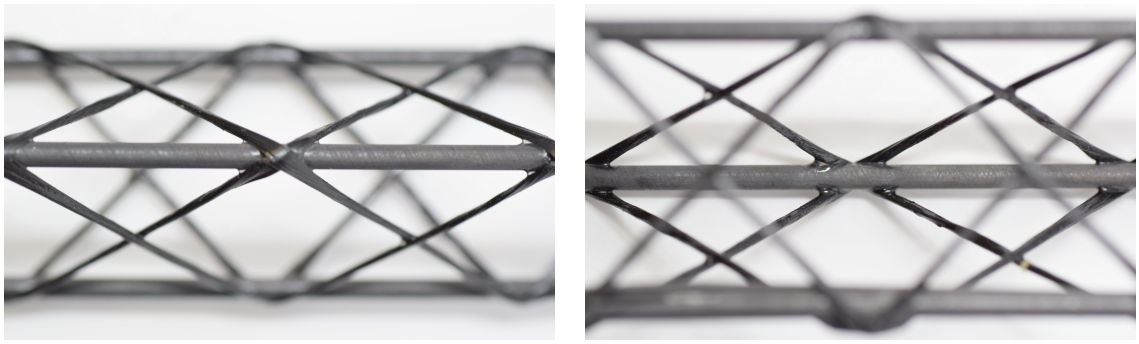

(a) (b)

Figure 3.6: WrapToR truss joints: a) top view ; b) underside view. Note formation of resin menisci.

ometry will therefore be useful for design purposes. Furthermore, accurate modelling of the truss behaviour will rely on the ability to predict joint geometry.

WrapToR joints are reasonably complex, and full characterisation of the geometry would be a difficult task. For simplification purposes, estimating the contact area between the shear member tow and the chord member tubes was the main focus in this investigation. This contact area, hereon referred to as the joint area, is likely to be a key parameter governing the performance of the joint. The joint area was measured for a variety of truss configurations using a custom image analysis technique. The results of this investigation are later used in Section 5.5.2 to validate a geometric model that was developed for prediction of joint area. This model is then later used for strength analysis of the truss structures.

3.4.1 Joint configurations

Joint geometry, and specifically area, will be dependant on some of the truss geometric parameters earlier discussion in Section 2.1.6. The external diameter of the chord members and shear members will have an effect, where larger diameters provide larger contact areas. The winding angle will also have an effect, where it would be expected that increasing the winding angle would increase the joint area. Truss height would also have an effect, although likely less significant, due to the relationship between the actual shear member angle, winding angle and height (detailed in Section 2.1.6). To investigate how each of these parameters effect the area, eight joints configurations were measured which are taken from trusses with varying chord member diameters, shear member tow sizes and winding angles. The configurations investigated are detailed in Table 3.8.

Table 3.8: Joint configurations used for joint area measurement investigation.

Joint configuration ID	Tube diameter (mm)	Tow size	Winding angle (°)	Height (mm)	Shear member angle (°)
3_24k	3	24k	45	33	42.2
3_24k_56.3	3	24k	56.3	33	52.8
4_24k	4	24k	45	66	43.1
4_48k	4	48k	45	66	43.1
4_72k	4	72k	45	49.5	42.5
5_24k	5	24k	45	36	40.8
5_48k	5	48k	45	36	40.8
5_72k	5	72k	45	49.5	41.9

3.4.2 Area measurement methodology

For joint area measurements, a technique was developed based on analysis of images taken with a DSLR camera. In this section, a summary of the method is given. Full detailing of the method and the accompanying mathematics is given in Appendix F. Joint images for each configuration are also displayed in Appendix F.

Joint sections consisting of chord members and shear web members in the vicinity of a joint were first cut from fully wound trusses using a diamond saw. The shear member tow was then separated from the chord member by manually inducing shear failure in the joint, leaving a fracture surface on the chord member, marking the region where the joint has failed. This fracture surface, an example of which can be seen in Figure 3.7a, generally takes the form of an irregular, cross-like shape. For the joint area measurements taken here, it was assumed that the joint area is equal to the area of the exposed fracture surface. As these fracture surfaces tend to extend over halfway around the circumference of the tube, two images, one of each joint half, were required to capture an entire joint. Once imaged, the half joint fracture surface was manually outlined. An example of this manual outlining is shown by the red line around the joint region in Figure 3.7b.

The half joint image presents a two-dimensional projection of the three-dimensional fracture surface. Therefore, the two-dimensional projected area had to be transformed back into the three-dimensional, curved space of the tube surface to give the relevant joint area. This transformation was conducted using a custom-written Matlab script. This script first identifies the pixels that are within the manually outlined joint region. It then identifies the tube edges and determines the corresponding tube centre line. By determining each pixel distance from the tube centre line, it calculates the corresponding surface area on the cylindrical tube. The detailing of the mathematics behind this transformation is detailed in Appendix F. For each joint, the areas measured from each half were summed to give the total joint area. This process was conducted for at least five joints per configuration.

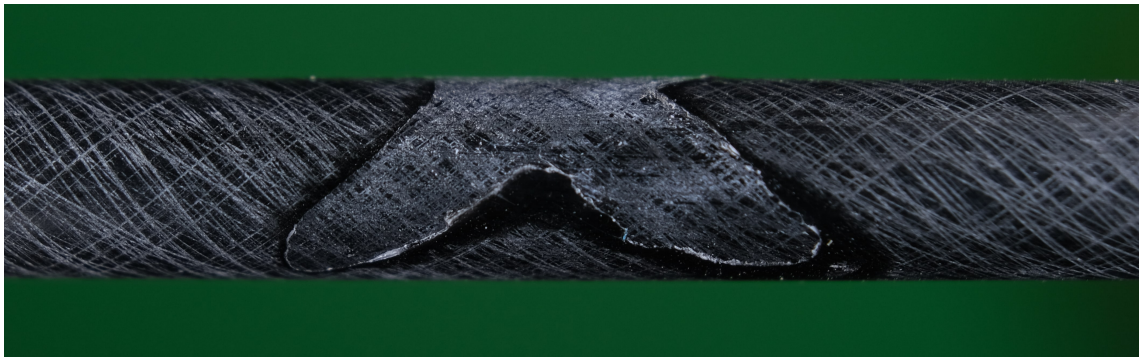

(a)

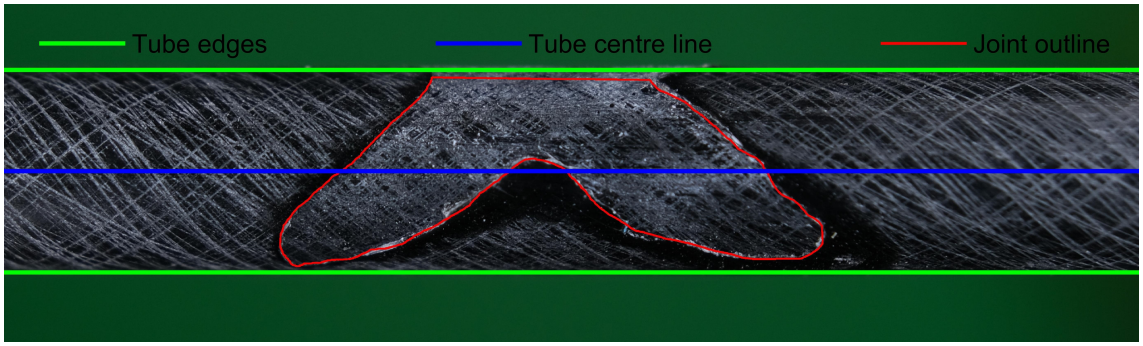

(b)

Figure 3.7: Image of half joint fracture surface: a) unprocessed image ; b) processed image. Joint outline is manually traced. Tube edges and centre line are computer detected.

3.4.3 Results

Averaged joint area results for each configuration are displayed in Table 3.9. The results here show several expected trends: increasing the chord member tube size and the shear member tow size are both seen to increase the joint area; increasing the winding angle also significantly increased the joint area. Variation between samples was seen to be reasonably high, with the coefficient of variance ranging between 4-11%. Between the different samples, the visually inspected joint shape was seen to vary significantly, explaining the variance in the area measurements. These results therefore show that the consistency of the joints is perhaps less than ideal. As these joints are a key structural component of the WrapToR truss, this will likely result in significant variance of the structural performance of the truss beams, particularly in loading scenarios where the joints are critical. Improvement of the joint consistency will therefore be an important step in future development of the WrapToR technology.

Table 3.9: Measured joint areas.

Configuration ID	No. of joints imaged	Tow size	Winding angle (°)	Joint area (mm^2)	
				mean	CV (%)
3_24k	11	24k	45	39.1	6.8
3_24k_56.3	6	24k	56.3	52.4	10.6
4_24k	7	24k	45	70.9	7.5
4_48k	5	48k	45	82.5	7.9
4_72k	5	72k	45	85.8	7.2
5_24k	5	24k	45	82.1	8.8
5_48k	6	48k	45	107.8	10.5
5_72k	6	72k	45	120.5	4.0

3.5 Truss characterisation

Composite lattice beams present novel configurations for which no standardised approaches of mechanical characterisation are available. Various approaches have therefore been used by researchers to investigate lattice beam behaviour; an overview of these approaches is given in Section 3.5.1. For characterisation of the WrapToR truss beams, a three-point bend test was developed which is detailed in Section 3.5.2. Flexural loading via three-point bending was selected for three main reasons. Firstly, as is discussed previously, WrapToR trusses are likely to be most useful as lightweight beam members. Therefore, loading under flexure is most relevant for application of the technology. Secondly, the developed method is extremely convenient as it requires minimal sample preparation. Thirdly, this loading scenario can be easily represented within the later developed structural models. A key challenge in the development of this test method was determining the most appropriate method of introducing the loads into the structures. For this, an experimental investigation was conducted, which is detailed in Section 3.5.4.

3.5.1 Background: Testing of composite lattice beams

Within the literature, authors have used a variety of experimental methods to investigate the structural response of composite lattice beam structures. Table 3.10 presents a summary of the published experimental characterisation work related to the composite lattice beam technologies introduced in Section 1.1.4.3. As was discussed previously, due to impressive flexural resistance, composite lattice beams are highly suited as lightweight beam members or compression columns. This, therefore, explains why most of the published work has investigated response under either flexural or compressive loading. Some authors, however, have also investigated response under torsion [76, 82, 109, 110] or axial tension [110, 111].

Cantilever, three-point, and four-point methods have been used for probing the

flexural response of the lattice beams. Flexural rigidity of the beams is commonly determined during these tests to gauge the resistance to bending loads. It should be noted that the flexural rigidity found via such experimental means is not the true value because the measured experimental deflection will be a combination of both bending and shear deformations. This is discussed further in Section 3.5.3. Composite lattice beams present novel configurations in which the members are often locally fragile, meaning that introducing load into the structures requires careful consideration. Methods used include casting the beam ends in a low melting temperature alloy [110] or polymer [63]; inserting metallic or polymer plugs [77]; and attaching custom end plates [82].

As is seen in Table 3.10, testing of composite lattice beams has been conducted to examine both pre-failure and failure behaviour. Most studies have focused on static loading scenarios (as is the case for the work in this thesis); however, two published studies have experimentally investigated dynamic response. McAllister et al. [77] performed dynamic tests to determine the natural frequencies of an ACT beam. Schütze and Goetting [112] performed dynamic testing of an assembled truss beam to test the functionality of a novel active vibration suppression device. This device consisted of a piezo-electric actuator that was embedded into one of the truss member tubes and was controlled via a closed-loop system. The experimental work showed the device extremely effective at reducing vibrations within the structure.

Results of the discussed experimental investigations are predominately used for one of three purposes. Often, they are used to provide results for validation of structural models. These validated models can then be used for design purposes.

Table 3.10: Summary of composite lattice beam mechanical tests within the literature.

Technology	Loading configuration(s)	Static/dynamic/ fatigue	Loaded to failure?	Ref
Schütze truss	Cantilever	Dynamic	No	[112]
IsoTruss® / 1D LCTS	Axial compression & tension, torsion	Static	Yes	[110]
	Axial compression	Static	Yes	[59]
	Axial compression	Static	Yes	[63]
IsoBeam	3 & 4-point bend	Static	Yes	[65]
	4-point bend	Static	Yes	[75]
Ju et al. truss	3-point bend	Static	Yes	[74]
O-ACS	Axial compression, torsion & cantilever	Static	No	[76]
	Axial tension	Static	No	[111]
	Torsion	Static	No	[109]
WrapToR	3-point bend & torsion	Static	Yes	[82]
ACT	Cantilever	Dynamic & static	Yes	[77]
Trusselator™	Cantilever	Static	No	[78]

Some authors have used results of such tests to compare the performance of their lattice beam technology to more conventional solutions. Such comparisons are discussed in Section 3.8. Experimental tests are also sometimes used to determine the structural effects of varying the manufacturing process. For example, Lai et al. [63] used compressive tests to assess the structural benefits of consolidating the members of 1D-LCTS beams by wrapping them with Kevlar fibres. The three-point bend method developed in the following section (Section 3.5.2) was used for all three of these purposes: in Chapters 4 and 5, for validation of the developed structural models; in Section 3.6, to assess the effect of tow twisting on truss structural performance; and in Section 3.8, to compare the WrapToR structural performance to conventional pultruded tubes.

3.5.2 Three-point bend test method

The three-point bend test described within this section was used for all testing of WrapToR beams within this thesis. The set-up, displayed in Figure 3.8, uses a custom test rig built from modular aluminium extrusions. This rig allows easy modification for testing of different size trusses at a range of spans. Two steel tubes form the end supports and load is introduced to the lower-central truss joints using a 6 mm steel pin. The custom rig was placed within an Instron 8872 universal test machine (UTM). Load was measured with a 5 kN load cell and was applied at a displacement rate of 4 mm / min. Due to the high stiffnesses of the trusses, precise measurements of displacement were required. Two Micro-Epsilon® ILD1700-100 laser sensors were used to measure displacement at the two lower central truss joints. Deformations within the rig were measured by positioning two potentiometers at the supports.

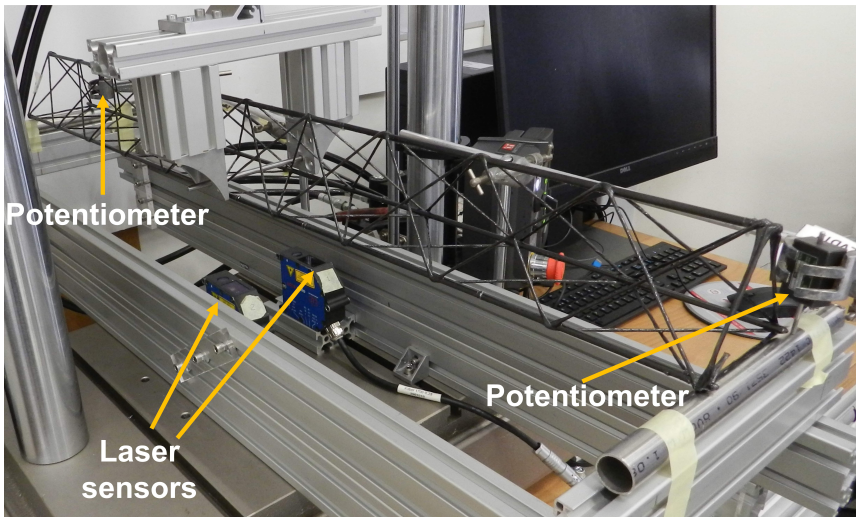

Figure 3.8: WrapToR truss three-point bend test setup.

3.5.3 Effective flexural rigidity

When tested in the devised three-point bend configuration, the trusses act as beams, primarily resisting bending loads. A useful parameter for comparing the resistance of these truss beams to bending deflections is the flexural rigidity, EI. For a prismatic, monolithic beam member, the second moment of area, I, can be determined through integration of the section shape. This can then be multiplied by the material Young's modulus, E, to give the flexural rigidity. For the WrapToR truss beams, this calculation cannot be used as they do not have a constant section and do not carry bending loads in the same manner. The flexural rigidity can, however, be determined experimentally by measuring the beam deflection under three-point bending and using the following deflection equation for a simply supported beam:

$$\delta = \frac{PL^3}{48EI} \tag{3.1}$$

in which L is the beam span, P is the applied load, and δ is the measured deflection.

This method has been used by other researchers to determine the flexural rigidity of other composites lattice beams such as the O-ACS [76] and the Isobeam [113]. However, the flexural rigidity obtained using this method will not be the "true" value as the measured beam deflections will be a combination of flexural and shear deformations. As will be seen in Section 4.4.2 these shear deformations are non-negligible, especially in trusses with lower aspect ratios. While not the true flexural rigidity, the measured value determined using this method is still useful for comparing trusses of different sizes and spans. Within this thesis it will, therefore, be referred to as the effective flexural rigidity, EI_{eff}, and is determined using the following equation:

$$EI_{eff} = \frac{P}{\delta}\frac{L^3}{48} \tag{3.2}$$

where P/δ is the gradient of load-displacement graph. Note that when non-linear behaviour was observed, the gradient was taken from the linear portion of the graph.

3.5.4 Investigation of loading introduction method

To determine the most appropriate method for introducing load into the trusses, an experimental investigation comparing three different methods was conducted. Any loading method used for testing must not create excessive stress concentrations at loading points or supports that may promote failure. Ideally, the loading method would also apply load directly at the truss joints as this would allow direct compari-

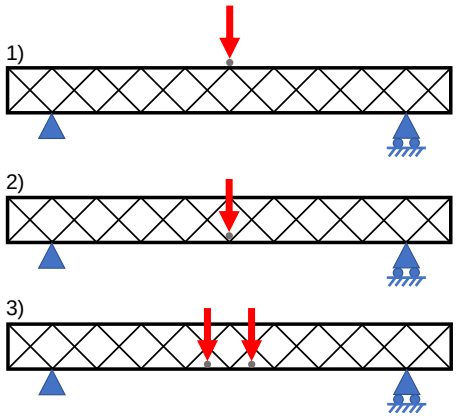

Figure 3.9: Candidate loading configurations.

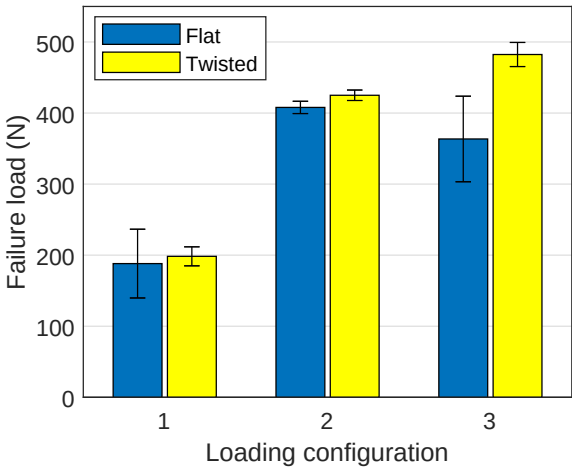

Figure 3.10: Average failure load for different loading configurations. (Error bars denote 1 standard deviation).

son to the analysis tool in which loads and boundary conditions can only be applied to element nodes.

Three candidate loading configurations were selected and experimentally tested. Four small section trusses, two flat and two twisted, were tested to failure using each loading configuration. For each configuration, load was applied at the locations shown in Figure 3.9 using 6 mm steel rods. The average failure loads when using the different loading configurations are displayed in Figure 3.10. Here loading configuration 1 is seen to result in failure loads much lower than the other two configurations. The samples tested with this method failed at the load application point due to debonding or failure of the upper chord member. When using this configuration, the load is applied to the most highly stressed region of the truss, which appears to promote failure within that region. Configurations 2 and 3 displayed similar failure loads that were higher than those observed for configuration 1. For both methods, no failure at the loading points or supports was observed. Configuration 3, however, does not apply loads directly at the joints and therefore, in order to allow for more direct comparison to analysis results, loading configuration 2 was selected.

3.6 Tow twisting investigation

Before the work in this thesis, all of the WrapToR trusses produced and studied used a 'flat' shear member configuration in which the fibre tow was not twisted. In this configuration, the tow is wound in its as-purchased form where the fibres are spread out widthways. In Section 2.1.5, reasoning was given as to why this tow spreading may be detrimental to the structural performance of the shear members

and that twisting the tow during winding may produce more structurally efficient members. The development of the truss winding machine (Section 2.2) made it possible to produce these trusses with consistently twisted shear members; a task that is practically impossible with the previously used hand-winding technique. Within this section, the technique of tow twisting is investigated analytically and experimentally to determine if it is structurally advantageous. For images of trusses with both twisted and flat shear members, the reader is referred back to Figure 2.5 in Section 2.1.5.

The purpose of the tow twisting technique is to alter the shear member cross-sectional shape to increase member buckling resistance. There are however some potential detrimental effects that tow twisting could have on structural performance. It is possible that tow twisting could reduce the bond area between the shear and chord members resulting in weakened bonds. Tow twisting also results in a misalignment of the fibres from the tow longitudinal axis. This misalignment is expected to have a detrimental effect on the longitudinal stiffness of the members, which in turn would reduce truss structural stiffness.

To assess the benefit of tow twisting, all of these potential effects are investigated, as well as studying the member cross-sectional shape via microscopy. The effect of fibre misalignment on member stiffness is investigated using an analytical method in Section 3.6.1. Then using the test method developed in Section 3.5, trusses with flat and twisted shear members are loaded to failure to assess any influence of twisting on member buckling resistance and joint strength.

3.6.1 Analysis the effects of tow twisting

When twisting a fibrous yarn, such as a tow of carbon fibre, the angle of the twisted fibres to the yarn longitudinal axis, α, will vary radially throughout the yarn. This angle will vary from zero at the yarn centre to its maximum at the yarn surface. Assuming that the fibres follow an ideal helix, the angle at any radial distance, r, from the tow centre, α_r, can be found using the following equation [114, 115]:

$$\tan \alpha_r = \frac{2\pi r}{h} \tag{3.3}$$

where h is the length of a single twist, referred to as the twist pitch, which is equal to the inverse of the level of twist. The fibre angle at the tow surface is then found using:

$$\tan \alpha_R = \frac{2\pi R}{h} \tag{3.4}$$

In [114], Naik and Madhavan present an analytical method for predicting the effect of fibre twist on moduli in impregnated twisted yarns. The method is derived by integrating the compliance matrix terms radially across a twisted tow according to:

$$S_{ij}^{y} = \int_{0}^{\alpha} \frac{S_{ij} 2\pi r}{\pi R^2} \mathrm{d}r \tag{3.5}$$

where S and S^y are the non-twisted and twisted tow compliance terms, respectively.

To estimate the effects of tow twisting on the longitudinal modulus of a single truss shear member, Naik's and Madhavan's method was implemented using a set of generic material properties for carbon-epoxy composite and the measured shear member radius (values displayed in Table 3.11). Predictions from the analytical model are displayed in Figure 3.11 which shows the reduction in longitudinal modulus as the level of twist increases. The level of twist used in the truss samples manufactured within the following section was 30.3 twists per meter, corresponding to a twist angle at the tow surface of 6.4°; the same level of twist used in the baseline tow configuration in Section 3.3. The model predicts that this level of twist for the 24k tow will result in a reduction in longitudinal modulus of 15%. This prediction seems to be inconsistent with experimental results obtained in Section 3.3 which found only a 6% reduction in stiffness at this level of twist, some of which was attributed to a reduction in resin content. It should be noted here that the method derived by Naik and Madhavan [114] was not experimentally validated within the study and is based on the assumption that fibres within a tow follow a perfect helical path. A later experimental study by Shioya et al. [115] found much more modest reductions in modulus at the levels of twist used here. Results of truss testing later detailed in Section 3.6.4 also suggest that any reductions in stiffness caused by tow twisting are likely to be more modest than this analysis predicts.

Table 3.11: Input parameters for Twisting model.

Model input parameter	Symbol	Value
Longitudinal modulus (GPa)	E_{11}	140
Transverse modulus (GPa)	E_{22}	10
Shear modulus (GPa)	G_{12}	4.5
Transverse shear modulus (GPa)	G_{23}	3.45
Longitudinal poisons ratio	ν_{12}	0.3
Transverse poisons ratio	ν_{23}	0.45
Member radius (mm)	R	0.59

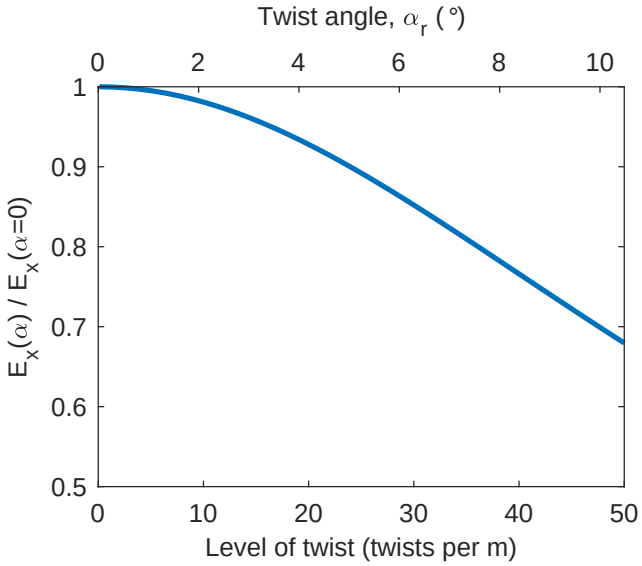

Figure 3.11: Decay of shear member longitudinal modulus with increasing twist. Estimated using Naik's and Madhavan's method.

3.6.2 Methodology and sample manufacture

Using the CNC winding machine, truss beams were manufactured for testing to failure using the three-point bend test previously detailed in Section 3.5. The constituent components were formed of the materials detailed in Section 2.1.7. The aim of the investigation was to determine whether twisting the shear member tow, to form circular section shear members, is beneficial to structural performance. As stated previously, to test this hypothesis it is necessary to investigate how tow twisting effects both shear member buckling and the bond strength at the truss joints. To probe each of these two failure mechanisms, trusses were manufactured in two sizes which create different relative amounts of loading in the shear members and at the joints. These truss sizes were selected using a combination of analysis (Chapter 4), engineering intuition, and experimental trial and error. The dimensions of the two chosen truss sizes are detailed in Table 3.12.

The first, larger truss size was selected to probe shear member buckling. It has a larger cross-section with long, slender shear members which should be susceptible

Table 3.12: Dimensions of selected truss sizes for tow twisting investigation.

Geometric property	Symbol	Units	Truss size	
			Large	Small
Truss height	H	mm	66	33
Chord tube diameter	$\varnothing_c$	mm	4	3
Chord tube wall thickness	t_w	mm	0.5	0.5
Winding angle	θ_w	deg	45	45
Shear member length	L	mm	23.3	46.7

Table 3.13: Average mass of truss test samples for tow twisting investigation.

Configuration ID	Number of samples	Mass per unit length (g/m)	
		Mean	Standard deviation
Large Flat (L-F)	3	42.2	0.8
Large Twisted (L-T)	3	41.2	0.4
Small Flat (S-F)	6	33.5	0.8
Small Twisted (S-T)	6	34.2	0.6

to buckling. Trusses of this size were manufactured at a length of 1 m and tested at a span of 792 mm, corresponding to twelve truss bays. The second truss size has half the section height and was selected to probe joint debonding. Shear members in these trusses have a lower aspect ratio to reduce the likelihood of buckling, moving the critical region to the joints. A smaller pultrusion size was also selected for the chord members to reduce the bond area. Trusses of this size were manufactured at a length of 1 m, cut in half, and tested at a span of 396 mm, corresponding to twelve truss bays. As the same number of large and small trusses were manufactured, cutting the small trusses in half resulted in double the number of small truss test samples.

For each truss size, samples with both flat and twisted shear member configurations were manufactured and tested. Twisted samples had a level of twist of 30.3 twists per metre, corresponding to one twist per shear member for the smaller truss size and two per shear member in the larger size. This level of twist was chosen qualitatively as it provided a satisfactory level of tow bundling along the shear member but also was low enough to allow the tows to spread out at the joints. The two truss sizes and two shear member arrangements result in four test configurations. These configurations are given a label of two letters. The first letter corresponds to the truss size, either 'L' for the larger size or 'S' for the smaller. The second refers to the shear member twist level, either 'F' for flat or 'T' for twisted. The averaged mass per unit length of each configuration is given in Table 3.13 where twisting of the fibre tow was seen to have no significant effect on truss mass.

3.6.3 Microscopy

Shear member cross-sections for both flat and twisted samples were investigated via optical microscopy to determine the effect of twisting on shear member shape and impregnation. Ten micrographs per configuration were obtained using a Zeiss Imager M2 microscope and a 2MP Camera. Visual inspection of these images allowed a qualitative assessment of the shear member shape. For a quantitative assessment of the shear member quality, the Matlab script detailed in Section 2.5.1 was again used to determine cross-sectional area and void content.

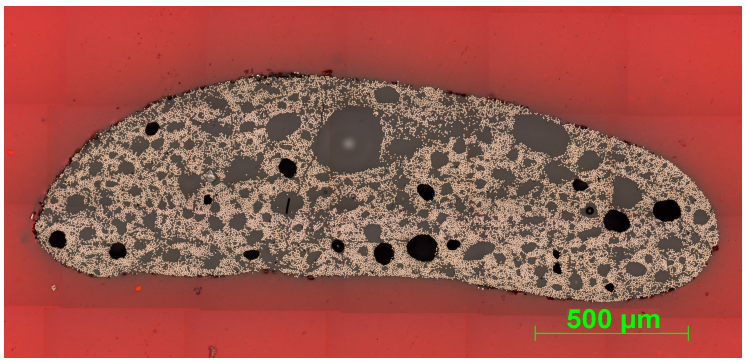

(a)

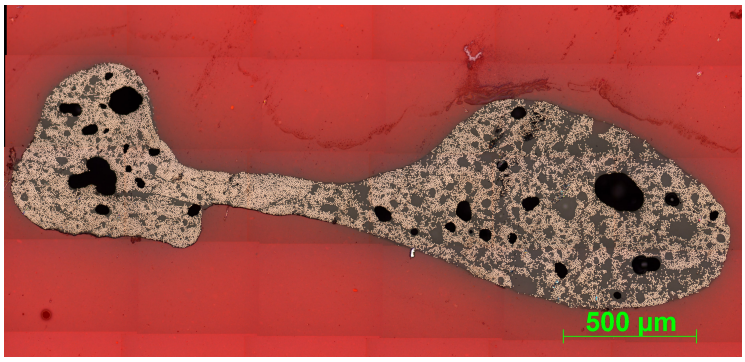

(b)

Figure 3.12: Section micrographs of flat shear member configuration: a) representative section; b) unusual section.

Typical micrographs for each tow configuration are displayed in Figures 3.12 and 3.13. For the twisted tow samples (Figure 3.13) near-circular sections were observed. Section shapes in the flat samples were much less consistent. Most imaged flat sections resembled that seen in Figure 3.12a but as is seen in Figure 3.12b, some vastly different shapes were also observed. In the micrographs displayed, significant void content is observed. This was common in all the obtained micrographs and is likely to stem from the lack of consolidation method employed during the manufacturing process. The averaged cross-sectional area and void contents are displayed in Table 3.14. Here it is seen that the flat samples had an average area of 18% larger than the twisted samples. Analysis of the void content results using the Students T-Test [116] shows that the small difference between the flat and twisted samples is not statistically significant.

Table 3.14: Flat and twisted shear member section area and void content.

Shear member configuration	Area (mm^2)		Void content (%)	
	Mean	Standard deviation	Mean	Standard deviation
Flat	1.3	0.2	4.9	2.1
Twisted	1.1	0.1	5.3	1.8

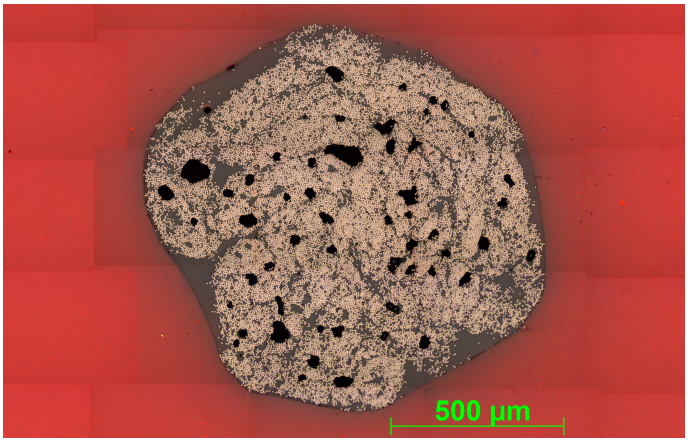

Figure 3.13: Section micrograph of twisted shear member configuration. Two further micrographs from this test case can be seen in Figure 2.25.

By performing numerical integrations of the section micrographs, the principle second moments of area of the flat and twisted shear members were determined. The principle second moments of area then give an indication of the improvement in buckling resistance of the members. The averaged principle second moments of area are displayed in Figure 3.14 where tow twisting is seen to reduce the variance of the section properties and that crucially, the average minor second moment of area is increased by 56%. As it is the minor second moment of area value that is critical for column buckling, this suggests an increase in buckling resistance.

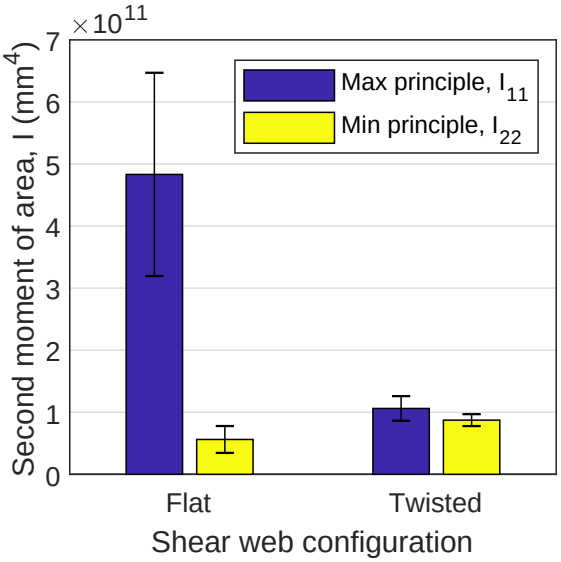

Figure 3.14: Average principle second moments of area for shear member configurations.

3.6.4 Results and discussion

The slender shear members of the larger trusses were susceptible to buckling resulting in all the large truss samples failing due to shear member buckling. Images of the buckled shear member in both flat and twisted samples can be seen in Figure 3.17. The load-displacement graphs in Figure 3.15 show the structural responses of all the large section trusses. Here, a stiffness reduction is observed at higher loads, prior to failure. This is observed to a lesser extent in the load-displacement graphs of the S-F configuration (Figure 3.16a) and is not observed for the S-T configuration (Figure 3.16b). The reduction in stiffness is likely a geometric non-linearity caused by a bowing outward of the shear members at higher loads. Bowing of the shear members was more prominent and occurred at lower loads in the flat samples whose shear members had a lower minor second moment of area. This non-linear response is investigated using numerical analysis in Section 5.4. A non-linearity is also witnessed in some samples at the start of testing which was caused by a slight unevenness of the samples on the supports resulting in an initial bedding-in phase.

From the averaged results in Table 3.15 it is seen that twisting the tow improved load-carrying capability of the larger section trusses by 51%. It is interesting to note that this increase closely matches the increase in section minimum second moment of area of 56%. This would be expected as, according to Euler buckling theory, critical loading should scale linearly with second moment of area. For the smaller trusses, the twisted configuration seems to display a small increase in load-carrying capability. However, statistical analysis of the test populations using the Students T-test shows that no conclusive improvement can be drawn from the results. Investigation of the failure mechanisms of the small truss samples found debonding of the shear and chord members to occur in all samples. Figure 3.18 shows images of the most common failure mechanisms in the test samples, which for configuration S-F was debonding (Figure 3.18a), and for S-T was debonding coupled with chord compression failure (Figure 3.18b). As all the small samples failed due to debonding and no degradation in load-carrying capability was observed in the twisted samples, it can be concluded that for these samples tow twisting was not detrimental to joint bond strength.

Table 3.15 also shows average effective flexural rigidity, EI_{eff}, which was estimated using the methodology outlined in Section 3.5.3 for the linear portions of the load-displacement graphs. The linear portions used were between 1.5-2.5 mm of deflection for the L-F configuration and 1.5-3.5 mm for the L-T configuration. Tow twisting was seen to improve stiffness in the larger section trusses where flexural rigidity increased by 10% and for the smaller section trusses no significant variation was observed. The increase in stiffness that is observed for the larger section

trusses is likely caused by the improved bending resistance of the circular section shear members. As was discussed previously, the stiffness results here further suggest that the analysis method used in Section 3.6.1 to predict effects of tow twisting on stiffness, is not appropriate for WrapToR shear members.

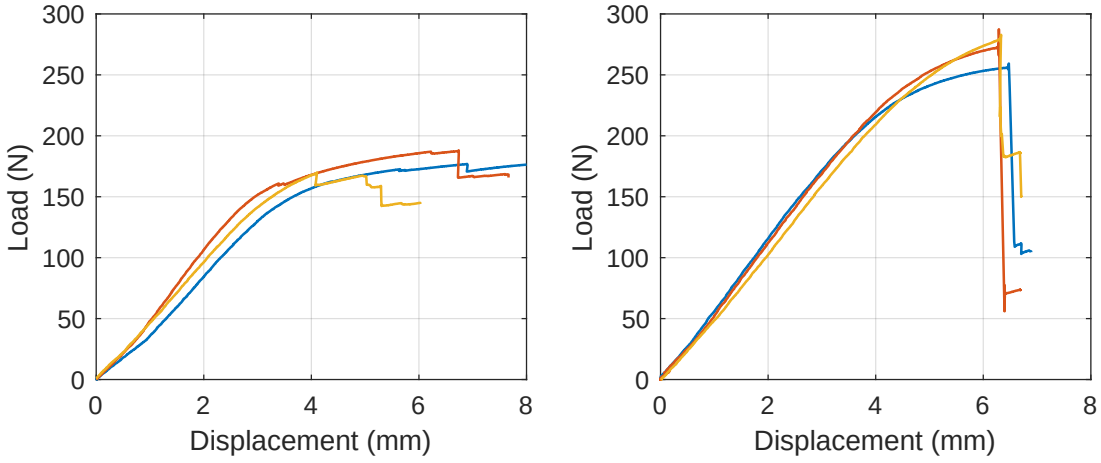

Figure 3.15: Load-displacement graphs for large section trusses of the two configurations: a) L-F; b) L-T.

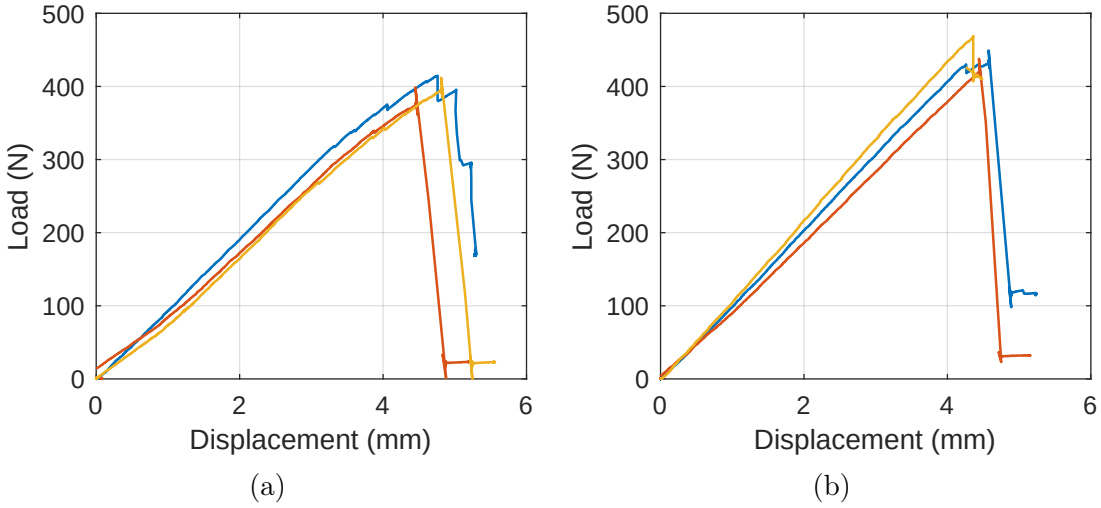

Figure 3.16: Load-displacement graphs for small section trusses of the two configurations: a) S-F; b) S-T. (Three of six samples are plotted)

Table 3.15: Three-point bend test results for the flat and twisted truss configurations. Sample average results and coefficient of variation (CV).

Configuration	Flexural rigidity (Nm^2)		Failure load (N)	
	Mean	CV (%)	Mean	CV (%)
L-F	528.9	6.3	178.3	5.2
L-T	579.4	1.5	269.0	4.4
S-F	119.0	5.0	407.8	8.6
S-T	128.3	7.1	434.9	11.0

(a) (b)

Figure 3.17: Failure in large section truss configurations: a) L-F; b) L-T.

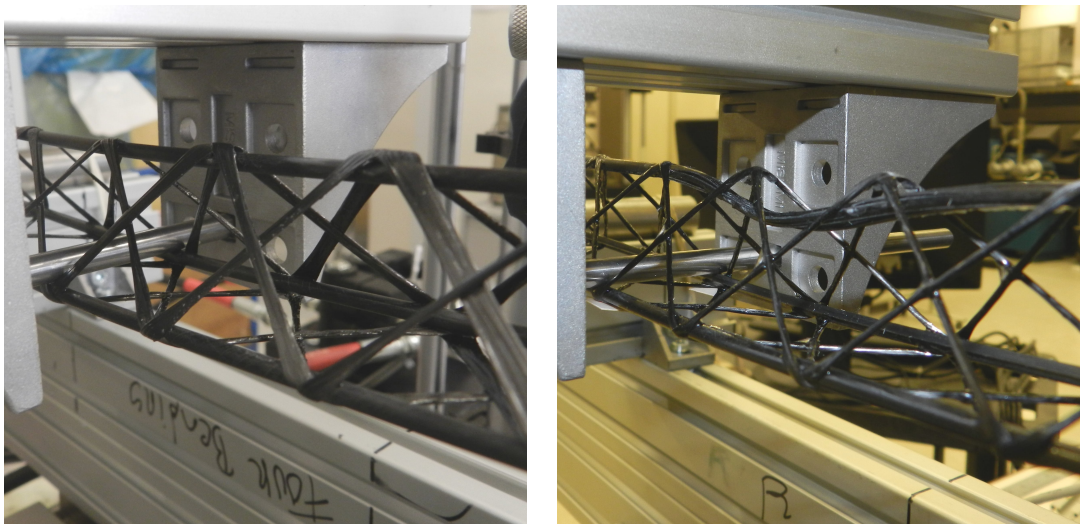

(a) (b)

Figure 3.18: Failure in large section truss configurations: a) S-F; b) S-T.

3.6.5 Conclusions

Tow twisting is a simple modification to the manufacturing process that requires virtually no increase in cost or time and only a small increase in complexity. This section of work aimed to determine if this twisting technique is structurally advantageous. Investigation of the shear member sections via optical microscopy revealed several differences between the twisted and non-twisted ('flat') shear members. Firstly, from a qualitative assessment, the twisted samples had a much more consistent sectional shape, which for all samples was near-circular. Analysis of the section shapes suggested the twisted members would be more resistant to buckling. This was then demonstrated experimentally through the testing to failure of trusses with twisted and flat shear members. Results showed that twisting increases the load-carrying capability of a particular truss configuration that is susceptible to shear member buckling by 51%. Testing of a truss configuration that is critical in debonding of the shear and chord members showed that twisting had negligible effect on the bond strength.

While analysis predicted that longitudinal modulus would be 15% lower in twisted shear members, experimental results showed no decrease in truss stiffness when twisting. In fact, for the larger truss configuration, twisting was observed to increase truss stiffness. Results within this section, therefore, show that tow twisting can improve both stiffness and strength of the trusses, providing a simple method of further increasing their structural efficiency.

3.7 Comparison to low-fidelity truss analysis

In previous work, Woods et al. developed a low-fidelity analysis tool to predict the structural response of WrapToR trusses. The tool, detailed fully in [82], is based on a simple matrix structural analysis (MSA) method that uses a two-force member assumption, meaning that each member is assumed to carry only axial loads. This method is analogous to finite element analysis (FEA) using truss (or bar) elements. While the two-force member assumption is not physically accurate for the WrapToR trusses, the assumption significantly simplifies the analysis and can provide reasonable predictions in highly stretch dominated lattices. In the study, Woods et al. found predictions from the tool correlated well with displacement results from both three-point bend and torsional tests of a single truss configuration. To further test the accuracy of this tool, in this section, the experimental results found during the truss beam characterisation in Section 3.6.4 are compared to predictions from the tool.

In Table 3.16, effective flexural rigidities predicted using the truss analysis tool

Table 3.16: Comparison of previously developed low-fidelity analysis tool to truss characterisation results.

Truss configuration	Effective flexural rigidity (Nm^2)		
	Experimental	Analytical	% error
S-T	129.9	172.0	32.4
L-T	579.4	920.9	58.9

are compared with the experimental results of the two twisted truss configurations from Section 3.6. Results here show significant inaccuracies in the low-fidelity analysis, with the model over-predicting beam stiffness in each configuration. The two-force member assumption used in the analysis is likely invalid for the WrapToR members as they are connected via bonded joints allowing the transfer of bending moments, as well as axial forces. The invalidity of this assumption, however, does not explain why the analysis tool provided reasonable predictions in the previously published work [82] but provides inaccurate predictions to the results from Section 3.6. Two possible reasons for this are suggested. Firstly, the truss configuration tested by Woods et al. had a larger aspect ratio than those tested here; with section height identical to the small truss configuration but with over double the span. It will later be seen in Section 4.5 that predictions from varying fidelity analysis methods tend to converge at higher aspect ratios. The second potential reason is that the member material properties used for the analysis in [82], were not determined experimentally. Instead, either manufacturer's data or generic values were used.

3.8 Comparison to conventional CFRP beams

To demonstrate the potential of composite lattice beams, some researchers have attempted to compare their beam concepts to more conventional configurations using either analytical or experimental means. Schütze stated that their assembled truss beam concept weighed approximately half that of an aluminium equivalent [55]. There was, however, no information given in the study as to how this was determined. Initial analysis works on the IsoTruss® concept compared the technology to conventional steel beam configurations [56]. The study analytically approximated the strength of four IsoTruss® configurations and then compared their mass with that of equivalent strength steel I-beams and solid shafts. The study found large potential mass savings, with the IsoTruss® configurations weighing between 1.2-19.5% of an equivalent strength steel beams. The steel beams were much stiffer in axial and flexural loading but more compliant in torsion. Ju et al. [74] used FEA to compare the bending stiffness per unit weight of their GFRP truss concept to trusses of identical geometry but made from CFRP, steel, or aluminium. Results of

this study found the glass, steel and aluminium trusses had similar bending stiffness per unit weight and that the CFRP performed far better. The usefulness of this study is, however, limited due to the lack of consideration of failure.

The WrapToR truss has previously been compared to conventional composite beams using low-fidelity analysis methods. Woods et al. [82] compared optimised WrapToR trusses to conventional CFRP tubes, such as pultruded and roll wrapped tubes, of equivalent linear mass. Results of the analytical study showed that in some cases, the WrapToR trusses offer a two-order of magnitude increase in stiffness. The work however used low-fidelity modelling with limited consideration of failure and hence is likely to have some inaccuracies. To further investigate whether the WrapToR trusses offer improvements in structural performance over conventional composite beams, in this section the trusses are experimentally compared to UD pultruded tubes.

3.8.1 Methodology

Two sizes of UD pultruded CFRP tubes were selected that had similar masses to that of the S-T truss configuration tested in Section 3.6. These tubes, purchased from EasyComposites^{TM}, larger versions of the tubes used for the WrapToR chord members. The selected tube sizes and the corresponding mass per unit length are displayed in Table 3.17. Three tubes of each diameter were tested to failure using the three-point bend test detailed in Section 3.5. For a direct comparison of stiffness and load-carrying capability to the S-T truss configuration, the tubes were tested at the same span of 396 mm.

Table 3.17: UD CFRP tube mass and dimensions.

Configuration	Diameter (mm)		MUL
	External	Internal	(g/m)
7 mm tube	7	5	32.1
8 mm tube	8	6	38.0
ST- truss	-	-	34.2

3.8.2 Results and discussion

Displayed in Figure 3.8 are the average flexural rigidities and failure loads for the small-twisted truss configuration and the two pultrusion tube sizes. The results of these tests clearly show the potential benefits of the WrapToR configuration. Compared to the 7 mm tube the truss has 7% more mass but achieves a 1006% stiffness increase and a 181% increase in load-carrying capability. Compared to the 8 mm tube, the truss offers a mass saving of 9%, a stiffness increase of 537%, and

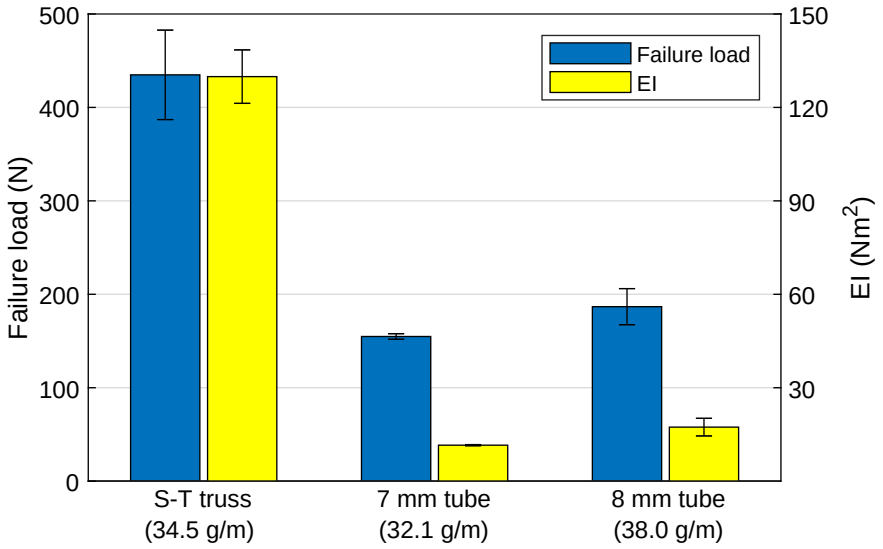

Figure 3.19: Average failure loads and flexural rigidities of small-twisted truss configuration and pultruded tubes. (Error bars denote one standard deviation).

a 133% increase in load carrying capabilities. As both the tubes and the trusses are formed of carbon fibre reinforced epoxy, this impressive increase in stiffness demonstrates how the WrapToR configuration uses geometry to drastically improve structural performance. It should be noted here that the truss configuration was not optimised for the loading scenario meaning that further improvements in structural efficiency are likely to be achievable with alteration of the truss geometry.

3.9 Conclusions

Detailed within this chapter is experimental work relating to structural characterisation of the WrapToR trusses. Initially, the individual truss components were characterised to provide stiffness and sectional properties that are vital inputs for the structural models developed in later chapters. These tests revealed how shear member resin content and stiffness is influenced by winding process parameters such as feed rate and level of twist. Following component characterisation, a three-point bend test was introduced that was developed specifically for structural characterisation of the WrapToR trusses. This convenient test method is used throughout the thesis for experimental investigations of structural performance and validation of the analysis methods developed in later chapters.

The developed three-point bend test was used within this chapter to experimentally investigate the structural benefits of tow twisting during the WrapToR winding process. This simple alteration to the manufacturing process was investigated as a means of increasing the truss structural performance through suppression of shear

member buckling. The investigation found tow twisting improved structural performance of the shear members where results showed greater sectional consistency and buckling resistance. There is scope for further research here to determine the optimal twist level for various size shear members.

Three-point bend test results from the tow twisting investigation were then used for two additional purposes. First, the results were used to assess the accuracy of a previously developed low-fidelity analysis tool. Comparison of the experimental and analytical results highlighted significant inaccuracies in the models' predictive capabilities, prompting the need for the higher-fidelity analysis tool that will be developed in the following chapter. Following this, the results were used to compare the WrapToR truss configuration to a more conventional composite beam configuration: pultruded CFRP tubes. Compared to the larger of the two tube sizes tested, the WrapToR truss offered a 9% reduction in mass, a stiffness increase of 537%, and an increase in failure load of 133%. These results demonstrated that within the size range tested, the WrapToR truss configuration provides substantial improvements in structural efficiency when compared to conventional composite beams.

Chapter 4

Pre-failure analysis & validation

4.1 Introduction

As was seen in the structural comparison work in Section 3.8, WrapToR trusses, as well as other composite lattice beam technologies, offer significant improvements in structural performance. Indeed, implementation within lattice structures has been highlighted as a means to maximise the potential of composite materials [117]. However, to fully unlock the potential of these technologies, the ability to both understand and accurately predict their mechanical response will be needed. This must be achieved through the development and detailed validation of structural models.

Undoubtedly contributing to the historical popularity of lattice structures, are the relatively simple techniques available for analysis of their structural behaviour. Before the advent of computers, the response of a truss could be predicted by applying the assumption that the structure is formed of two-force members that only carry axial loads [12]. The advent of modern computers led to the development of matrix structural analysis (MSA) methods which do not require such assumptions to reduce computational expense. By forming structural problems in a systematic manner that is ideal for computer implementation, MSA methods made it possible to conduct analyses of large and highly redundant lattice structures that were previously unfeasible to compute by hand [118]. These methods, which can be viewed as a simple form of FEA, allow analysis of structures formed of one-dimensional truss or beam elements. From MSA methods, modern FEA methods have since been developed that can be applied to more general one-, two-, and three-dimensional elements. As will be seen in Section 4.2, it is these modern FEA methods that have been the preferred choice for researchers when structurally analysing composite lattice beams.

The aim of this chapter was to develop an analysis tool capable of accurately pre-

dicting the pre-failure mechanical response (namely stiffness) of WrapToR trusses. In Chapter 5 the tool is updated to incorporate failure criterion allowing prediction of failure. The ability to predict both truss deflections and failure loads would provide an aid for structural design to improve structural efficiency through selection of the most suitable truss configuration. To maximise the potential efficiency of the trusses, the analysis tool is implemented within an optimisation framework in Chapter 6. The pre-failure analysis tool developed in this section is based on MSA methods and was built in Matlab. The development of the tool is detailed in Section 4.3 and its validation, through comparison with experimental results, is detailed in Sections 4.4 and 4.5. Finally, in Section 4.6, the validated analysis tool is used to investigate how the various truss design parameters impact truss stiffness.

4.2 Background: Analysis of composite lattice beams

Developing accurate modelling techniques is a critical step in realising the full potential of composite lattice structures. There are now numerous studies involving development, implementation, and validation of analytical methods for the various composite lattice technologies. This section will discuss the methods used by authors to analyse composite lattice beam technologies. A summary of the published works relating to the modelling of composite lattice beams is displayed in Table 4.1. It is noted here that there is also a large body of research investigating analysis methods for composite lattice core sandwich panels. These works tend to use analytical expressions derived from beam theory and consideration of the lattice geometry to predict through-thickness stiffness and member stress [16, 49, 119]. This section will, however, focus on the works associated with composite lattice beam structures, due to their relevance to the WrapToR technology.

To predict pre-failure structural response, both static and dynamic, finite element analysis (FEA) has been the most popular method. The repetitive nature of the lattice structures makes their input into commercial FEA packages cumbersome. To alleviate this, some researchers have used commercial tools that allow parametrically driven geometry generation, such as ANSYS Parametric Design Language (APDL) [56, 61, 64, 120]. Others have chosen to write custom FEA codes in languages such as Matlab [71, 76] or Python [111].

The discussed lattice beams feature complex geometries that must be accurately numerically idealised to conduct meaningful structural analysis. The open-architecture composite structures (O-ACS) present a range of particularly complex geometric configurations formed of braided tows that follow curved paths. Shen and Branscomb [111] derived and validated a model that geometrically idealises these structures based on the braiding process parameters. This model was then used to

feed into an FEA solver for structural analysis. More recent work on the O-ACS technology found modelling the torsional stiffness of the O-ACS joints to be crucial in predicting beam response under axial loading [109]. In the study, O-ACS member joints were modelled using beam elements that were only permitted to deform in torsion. By varying joint torsional stiffness, they were able to determine the most appropriate value empirically.

For all the lattice beam technologies discussed in Section 1.1.4.3, the members will carry both axial and bending forces due to their end attachments not being free to rotate. As can be seen in Table 4.1, most researchers have therefore chosen to use beam elements within their models; with shear-flexible Timoshenko formulations most prevalent. In previous work on the WrapToR truss technology, Woods et al. [82] developed a low-fidelity analysis tool based on MSA methods in which the WrapToR members are modelled using truss (or bar) elements. While not physically accurate, this method reduces the computational cost and is known to provide reasonable predictions in highly stretch-dominated lattices. The study found the truss analysis matched experimental results for a high-aspect-ratio truss. In Section 3.7 predictions from this previously developed truss analysis tool were compared to experimental load-displacement results for two lower aspect ratio WrapToR beams. Here significant inaccuracy of the truss analysis method was highlighted, prompting the need for the higher-fidelity method that is developed in the following section, which uses shear-flexible beam elements.

Most published studies, as is the case for the analysis work within this thesis, have focused on static analysis. An exception to this is the study by Sui et al. [64], who generated a series of FEA models to investigate how varying the geometric parameters of IsoTruss® beams effects their vibrational responses. The study found that short beams with a high helical inclination vibrate as a cylindrical shell and that longer beams with lower inclinations vibrate as a beam. They then derived analytical expressions to predict the natural frequency of these two modes and found good agreement with the FEA models. McAlister et al. [77] have also investigated dynamic response, comparing predictions from FEA to experimental results for the advanced composite truss (ACT) technology.

The majority of published studies have used linear analysis methods. However, nonlinear behaviour has been observed during testing of several lattice beams. For example, linear FEA of the IsoBeam [75] matched experimental results at low loadings, but when close to failure, nonlinearities created significant disparities. Nonlinear functionality of commercial FEA packages has been used to capture both stiffening [111] and softening [74] geometric nonlinearities in composite lattice beams. In the previous WrapToR work by Woods et al. [82], the truss analysis tool incorporated incremental loading capabilities to model geometric nonlinearities; however,

within the tested load range, no significant nonlinear behaviour was observed. In Section 3.6.4, nonlinear softening behaviour was observed in the structural response of WrapToR trusses when approaching failure loads. To capture these nonlinear phenomena, the WrapToR analysis tool is later further developed in Section 5.4 to include incremental loading and updating of the tangent stiffness matrix.

Table 4.1: Summary of composite lattice beams analysis work. FEA element coding: Unspecified beam (B); Timoshenko/shear flexible beam (TS); Euler-Bernoulli beam (EB); Truss/bar (T).

Technology	Analysis method used	Loading scenarios	Static / Dynamic	Linear / Non-linear	Ref
Schütze truss	-	-	-	-	-
IsoTruss® /	FEA commercial (B)	Flexure, torsion, axial	Static	Linear	[56]
1D LCTS	Analytical – equivalent section geometry	Torsion, axial	Static	Linear	[110]
	FEA commercial (TS) & dynamic equivalent models	N/A	Dynamic	Linear	[64]
	FEA (B)	Axial	Static	-	[59]
	Analytical calculations	Axial	Static	Linear	[63]
	FEA commercial (TS)	Axial	Static	Linear	[61]
	FEA commercial (B) & analytical calculations	Axial	Static	Linear	[62]
IsoBeam	FEA commercial (TS)	Flexure	Static	Linear	[65]
	FEA & "hand calculations"	Flexure	Static	Linear	[75]
Ju et al. truss	FEA commercial (TS)	Flexure	Static	Non-linear	[74]
	FEA commercial (TS)	Flexure	Static	Non-linear	[120]
O-ACS	FEA self-coded (TS)	Flexure, torsion, axial	Static	Linear	[76]
	FEA commercial (TS)	Axial	Static	Non-linear	[111]
	FEA self-coded (TS)	Torsion	Static	Linear	[109]
WrapToR	MSA self-coded (T)	Flexure, torsion	Static	Non-linear	[82]
ACT	FE-commercial (Shell elements)	Flexure	both	Linear	[77]
Trusselator™	-	-	-	-	-

4.3 Analysis development

To structurally analyse the WrapToR trusses, a Matlab code based on MSA was developed. MSA encompasses several numerical structural analysis techniques in which problem equations are mathematically organised using matrix algebra. The equations are organised in this manner as it makes them convenient for computer implementation. First developed in the 1950s, MSA methods are well understood and are well documented in an extensive range of textbooks; the following of which were frequently used when building the analysis tool detailed within this chapter [118, 121, 122]. There are two variants of MSA: the force method, and the stiffness method. Within the lesser-used force (or compatibility) method, the element forces are taken as the primary unknowns which are first determined through solving of the compatibility equations. The stiffness (or displacement) method uses the nodal displacements as the primary unknowns which are found by initially solving the equations of equilibrium. Element forces are determined using compatibility considerations and member force-displacement relationships. Due to its relatively simple implementation in computer codes, the stiffness method is more suitable for large and highly redundant structures, resulting in its more widespread use. These advantages also make the stiffness method the most appropriate for analysing the WrapToR truss structures, and hence, is the method used here.

Within Section 4.3.1 an overview of the stiffness method is given with highlighting of any particular aspect adopted for the WrapToR analysis tool. An extensive detailing of the method is not given due to the vast number of texts available for this purpose. A key stage in the implementation of the stiffness method was the idealisation of the truss geometry. Two geometric idealisation approaches were investigated which are detailed in Section 4.3.2. Once developed, the functionality of the analysis code was tested by comparison with a commercial FEA program; this verification work is discussed in Section 4.3.4.

4.3.1 Stiffness method

When using the stiffness method, a structure is first geometrically idealised into a series of discrete one-dimensional elements that are connected at nodes. The locations of the nodes are stored as a series of x, y, and z coordinates stored within a matrix. An element connectivity matrix is then used to reference each elements connecting nodes. Geometric idealisation of structures is rarely trivial and often requires careful consideration. For the WrapToR truss analysis, two methods of geometric idealisation were used, which are later detailed in Section 4.3.2.

Once the structure geometry is mathematically defined, the next step is determining the force-displacement relationships of the individual elements. In the

stiffness method, an elements force-displacement relationships are defined by its local stiffness matrix, $\mathbf{k}$. These relationships depend on the type of element used. For the WrapToR analysis, shear-deformable beam elements, were selected to represent the truss members. Beam elements were chosen because the WrapToR members are bonded at their ends, meaning that the members will carry axial, bending, and torsional loads. As WrapToR truss members can have aspect ratios well below 10, it was necessary to use a formulation that considers shear deformations. The local stiffness matrices for these elements were found using Equation 4.1 which is derived in [122] through solving the differential equations of Timoshenko beam theory.

$$\begin{bmatrix}
\frac{EA}{l} & & & & & & & & & & & \\
0 & \frac{12EI_z}{l^3(1+\Phi_y)} & & & & & & & & & & \\
0 & 0 & \frac{12EI_y}{l^3(1+\Phi_z)} & & & & & & & & & \\
0 & 0 & 0 & \frac{GJ}{l} & & & & & & & & \\
0 & 0 & \frac{-6EI_y}{l^2(1+\Phi_z)} & 0 & \frac{(4+\Phi_z)EI_y}{l(1+\Phi_z)} & & & & & & & \\
0 & \frac{6EI_z}{l^2(1+\Phi_y)} & 0 & 0 & 0 & \frac{(4+\Phi_y)EI_z}{l(1+\Phi_y)} & & & & & & \\
\frac{-EA}{l} & 0 & 0 & 0 & 0 & 0 & \frac{EA}{l} & & & & & \\
0 & \frac{-12EI_z}{l^3(1+\Phi_y)} & 0 & 0 & 0 & \frac{-6EI_z}{l^2(1+\Phi_y)} & 0 & \frac{12EI_z}{l^3(1+\Phi_y)} & & & & \\
0 & 0 & \frac{-12EI_y}{l^3(1+\Phi_z)} & 0 & \frac{6EI_y}{l^2(1+\Phi_z)} & 0 & 0 & 0 & \frac{12EI_y}{l^3(1+\Phi_z)} & & & \\
0 & 0 & 0 & \frac{-GJ}{l} & 0 & 0 & 0 & 0 & 0 & \frac{GJ}{l} & & \\
0 & 0 & \frac{-6EI_y}{l^2(1+\Phi_z)} & 0 & \frac{(2-\Phi_z)EI_y}{l(1+\Phi_z)} & 0 & 0 & 0 & \frac{6EI_y}{l^2(1+\Phi_z)} & 0 & \frac{(4+\Phi_z)EI_y}{l(1+\Phi_z)} & \\
0 & \frac{6EI_z}{l^2(1+\Phi_y)} & 0 & 0 & 0 & \frac{(2-\Phi_y)EI_z}{l(1+\Phi_y)} & 0 & \frac{-6EI_z}{l^2(1+\Phi_y)} & 0 & 0 & 0 & \frac{(4+\Phi_y)EI_z}{l(1+\Phi_y)}
\end{bmatrix} \tag{4.1}$$

where:
$$\Phi_y = \frac{12EI_z}{GA_{s_y}l^2} \tag{4.2}$$

and:
$$\Phi_z = \frac{12EI_z}{GA_{s_z}l^2} \tag{4.3}$$

Once the local element stiffness matrices of each element have been found, these matrices are then combined into a global stiffness matrix, $\mathbf{K}$, which defines the force-displacement relationships of the entire structure. To do this, each element's local stiffness matrix must first be transformed from its local coordinate system to a common datum system using a transformation matrix derived by considering member orientation. The global stiffness matrix is then formed by positioning each transformed local matrix within a larger single framework and summing any overlapping terms (i.e. terms related to shared nodes). Boundary conditions are applied by eliminating rows and columns associated with fixed constraints from of the global stiffness matrix, giving a reduced stiffness matrix, $\mathbf{K}_r$. Any external loads on the

structure are formed in a matrix, $\mathbf{P}$, which is similarly reduced to account for fixed boundary conditions, giving $\mathbf{P}_r$. Using the external loading matrix and the global force-displacement relationships, the nodal displacements, $\mathbf{U}_r$, are found according to:

$$\mathbf{U}_r = {\mathbf{K}_r}^{-1}\mathbf{P}_r \tag{4.4}$$

From the determined nodal displacements in the global coordinate system, member forces and moments can be determined using the transformed elements stiffness matrices. Using these forces and moments with knowledge of element sectional properties, member stress and strains can then be found.

Matlab's matrix-based environment proved to be extremely convenient for the implementation of the discussed matrix method. For example, Equation 4.4 could be easily implemented using Matlab's matrix division capabilities. Using Matlab was also beneficial due to extensive in-built optimisation capabilities that were used for the optimisation work later detailed in Chapter 6.

4.3.2 Geometric idealisation

As stated previously, the first stage of the stiffness method is the idealisation of the structural geometry into a matrix based format that is suitable for computer implementation. When attempting to idealise the WrapToR truss configuration into a series of beam elements, an issue is encountered at the truss joints. As the shear member tow is wrapped over the pultruded chord members (and does not run through their centres), placing beam elements along the centre line of the truss members results in an eccentricity where the shear and chord elements do not connect at a node. To deal with this joint eccentricity, two methods of geometric idealisation were investigated. The first, referred to as the concentric model, simply alters the angle of the shear members to remove the eccentricity at the joints, as is depicted in Figure 4.1a. The change in angle between the physical truss and the geometrically idealised model is typically less than 2 degrees to create concentric joints. The second method does not alter the geometry of the truss members and deals with the eccentricity using an additional beam element at the joint. This method, depicted in Figure 4.1b, is referred to as the eccentric model. As well as representing the actual truss geometry more closely, this method has the benefit of being able to model displacements within the joints. The major disadvantage of the eccentric model approach is that representative stiffness properties are needed for the additional joint element. Determining these properties is not trivial and is discussed in Section 4.3.2.

(a) (b)

Figure 4.1: Joint geometric idealisation methods: a) Concentric; b) Eccentric.

4.3.3 Element properties

After idealising the structure into a series of elements and nodes, the stiffness properties and sectional geometry of the individual elements need to be assigned. For the WrapToR truss configuration, three sets of element properties are required: chord, shear, and for the eccentric model, joint members. For the chord and shear members, element moduli and sectional geometries found during the characterisation work in Sections 3.2 were used (summarised in Table 4.2). In Section 3.3 properties were only determined for 24k tow shear members. For analysis of trusses with 48k, 72k, and 96k tow shear members, it was assumed that the areas would be 2, 3, and 4 times larger, respectively. For the elements' transverse shear modulus, G, a typical value for carbon-epoxy of 4.5 GPa was used [98].

In the eccentric model, stiffness properties are also required for the beam elements that represent the joints. Properties required are the joint elements' moduli and cross-sectional area. Accurately determining joint stiffness values via localised joint testing would be extremely difficult for the given truss configuration. Additional to this, the region represented by the joint element has an inconsistent geometry. It was therefore concluded that an empirical fit of the model and experiment data would be the most appropriate method of determining joint element properties.

For the empirical fit, first, it was assumed that only shear deformations would occur within the joint elements and that axial, bending, and torsional deformations are negligible. This greatly simplifies the problem and is likely a reasonable assumption given that the joint members typically have an aspect ratio below one and tend to be subject to primarily shear loads. The Young's modulus, E, and polar second moment of area, J, of the joint elements were therefore increased to an arbitrarily large value (1000 GPa and 1 m^4, respectively) such that changes in either had a negligible effect on the model deformations. This essentially switches-off the joint elements' axial, bending, and torsional deformations, meaning that they behave as shear springs. The only term then that needs to be found is the element shear

Table 4.2: Chord and shear member Young's moduli and sectional geometry.

Truss component	Member	Young's modulus (MPa)	Diameter (mm)	
			External	Internal
CFRP tube: 3 mm	Chord	137.0	2.96	1.95
CFRP tube: 4 mm	Chord	137.0	3.95	2.95
CFRP tube: 5 mm	Chord	125.1	4.92	3.10
Impregnated CFRP 24k tow	Shear	107.8	1.178	-

stiffness, GA_s. Two fitting methods were used to find the joint shear stiffness. Both the methods used iterative searches to find shear stiffness values that minimised the mean absolute percentage error (MAPE) across all the truss configurations tested. The difference between the methods is that the first method uses a consistent shear stiffness value across all the configurations, but in the second, each configuration has its own shear stiffness value. While the second method should provide a lower MAPE, it presents an issue from a design perspective as to model any new truss configuration a shear stiffness value would need to be experimentally determined. To overcome this issue, a multivariate linear regression was used to find an expression that relates truss geometric parameters to joint stiffness. This expression can then be used for modelling of new truss configurations and is particularly useful for optimisation studies. Results relating to the joint stiffness empirical fitting are discussed in Section 4.5.1.

4.3.4 Analysis verification

To verify the coded MSA analysis tool, equivalent linear FEA models for three truss configurations were built in Abaqus using shear deformable beam elements (B32). A single element was used for each truss member with geometric idealisation being conducted using the concentric method (explained in Section 4.3.2). Results comparing the models for a span of 792 mm and a load of 400 N are shown in Table 4.3. Here it is seen that the MSA model predictions of deflection are within 1% of those from FEA and predictions of member loads are within 0.1%. The primary advantage of the Matlab coded MSA tool is that truss geometry is parametrically defined within the code, such that the user can generate new truss configurations and define new analyses by simply specifying the parameters of the truss configuration and the applied loading/boundary conditions. The run time of the Matlab tool is also very fast. For the truss configurations investigated in this study, a full solution from geometry generation to results output took between 0.17-0.25 seconds on a desktop computer with a 3.4 GHz processor and 16 GB of RAM. This makes the analysis convenient for the optimisation work later detailed in Chapter 6.

Table 4.3: MSA and commercial FEA comparison for concentric idealisation method. Truss configurations detailed in Table 4.4.

Truss config.	Load point displacement (mm)			Max element axial force (N)			Min element axial force (N)		
	MSA	FEA	% diff.	MSA	FEA	% diff.	MSA	FEA	% diff.
H33_1	20.62	20.65	-0.14	1435	1436	-0.04	-2943	-2944	-0.04
H66_2	5.286	5.296	-0.20	665.5	665.6	-0.02	-1411	-1412	-0.02
H99_1	-2.284	-2.304	-0.88	417.9	418.2	-0.06	-917.4	-918.1	-0.07

4.4 Model validation: Experimental methodology

4.4.1 Sample configurations

For validation of the analysis methods over a range of truss geometries, seven configurations were investigated. All configurations have an equilateral triangle cross-section formed of three chord members. For each configuration, three trusses were manufactured using the automated winding machine previously developed and detailed in Section 2.2. Tow feed rate was fixed to 2 m / min resulting in winding times between 4 minutes 13 seconds and 4 minutes 41 seconds (winding times of individual configurations are detailed in Appendix C). Curing of the shear web epoxy matrix was conducted at room temperature. The test samples were manufactured at a length of 1 m and were tested at multiple spans to investigate any effects of varying aspect ratio. The seven tested configurations are detailed in Table 4.4.

Table 4.4: Truss sample geometric configurations for pre-failure response investigation. For definition of truss geometric parameters see Section 2.1.6.

Truss configuration ID	Truss height, H (mm)	Chord tube diameter, (mm)	Chord tube wall thickness (mm)	Winding angle, θ (°)	Shear member tow size	Mass per unit length (g/m)
H33_1*	33	3	0.5	45	24k	33.0
H33_2	33	3	0.5	56.3	24k	31.1
H66_1	66	4	0.5	45	24k	41.2
H66_2*	66	4	0.5	45	48k	56.2
H99*	99	5	1	45	96k	102.0
H50_D4	49.5	4	0.5	45	72k	64.2
H50_D5	49.5	5	1	45	72k	92.5

**Configurations tested in both global stiffness and strain tests.*

4.4.2 Global stiffness tests

For a comprehensive validation of the models' ability to predict global truss deflection, three trusses from each of the seven configurations were tested at multiple spans using the three-point bending method detailed in Section 3.5. The spans tested were between the range of 396 and 990 mm. At each of the tested spans the effective flexural rigidity, EI_{eff}, was determined using the method detailed in Section 3.5.3 for comparison with predictions from the truss analysis tool. Testing the seven truss configurations at multiple spans gave a total of 41 unique test configurations. Each was repeated 3 times resulting in 123 tests.

As well as comparison with experimental data, models are also compared to flexural rigidity estimations from parallel axis theorem. These predictions were made by assuming that only the chord members contribute the beam second moment of area. This very simple method has been used by some authors to estimate IsoTruss® flexural rigidity for global buckling predictions [59, 61]. The following formula for parallel axis theorem was used to determine truss second moment of area, which was then multiplied by the chord member modulus to approximate flexural rigidity:

$$I = \sum I_i + A_i \bar{y}_i^2 \tag{4.5}$$

where I_i is the second moment of area of each member about its own neutral axis, A_i is the member cross-sectional area, and $\bar{y}_i$ is the distance of the member centroid to the beam neutral axis.

4.4.3 Member strains and local deformations

To investigate the mechanical response to a higher level of detail, and to further validate the models, a second round of testing was conducted in which member strains and local deformations were measured. For these tests, three of the seven truss configurations (highlighted in Table 4.4) were again tested in three-point bending at spans of 792 and 396 mm. The three-point bend method used here was slightly different to that detailed in Section 3.5. For these tests, the load was applied using hanging weights, rather than a UTM, to provide sufficient space around the structure for positioning of measurement equipment. For configuration H33_1, maximum loads of 10 and 15 kg were applied for 792 and 396 mm span, respectively. All remaining configurations and spans were loaded to 30 kg. For each truss configuration, a variety of instruments were used to measure strains and local deformations, including digital image correlation (DIC), strain gauges, and extensometers. Figure 4.2 shows a summary of where strains and local deformations were measured. Detailing of each of these measurements is given within the following subsections.

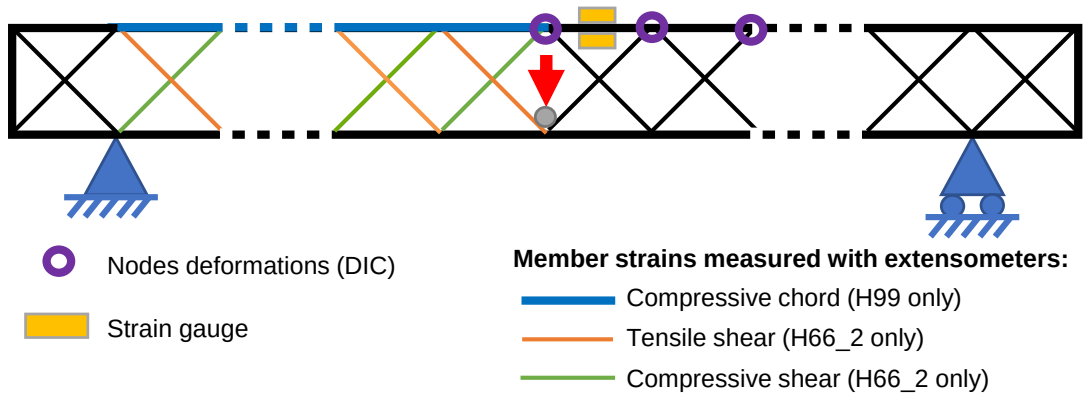

Figure 4.2: Summary of strain and local deformation measurement methods and locations.

4.4.3.1 Chord member strains

Two strain gauges were attached to one of the central upper-compressive chord members, as is seen in Figure 4.3a. This member was chosen because the analysis predicts it to be the most highly strained region of the truss. Strain gauges were placed at the centre span of the member on both the upper and lower surfaces so that bending and axial strain in the member could be determined. To determine the bending moment distribution within the upper (compressive) chord members, the largest truss configuration, H99, was subjected to a series of measurements using clip extensometers (Figure 4.3b). Again, by taking readings on the top and bottom surfaces of the tube, both the axial and bending strain could be determined. Using the measured bending strain, ε_x, the moment, M_Z, at each measurement point was calculated using the following rearranged form of the engineer's bending equation:

$$M_Z = \frac{\varepsilon_x E_x I_z}{y} \tag{4.6}$$

where E_x is the longitudinal Young's modulus and y is the member section height.

Using this method, the bending moment at one-quarter and three-quarters length of each upper chord member was determined. As loads are only introduced into members via the joints at their ends, the distribution of bending moment across a member is expected to be linear. This means that by measuring the moment at two places within a member, the moment distribution across the length of that member can be determined. By doing this in each upper chord member along half the truss span and assuming a moment distribution that is symmetric about the truss centre span, the moment distribution throughout the entire upper compressive chord member was determined.

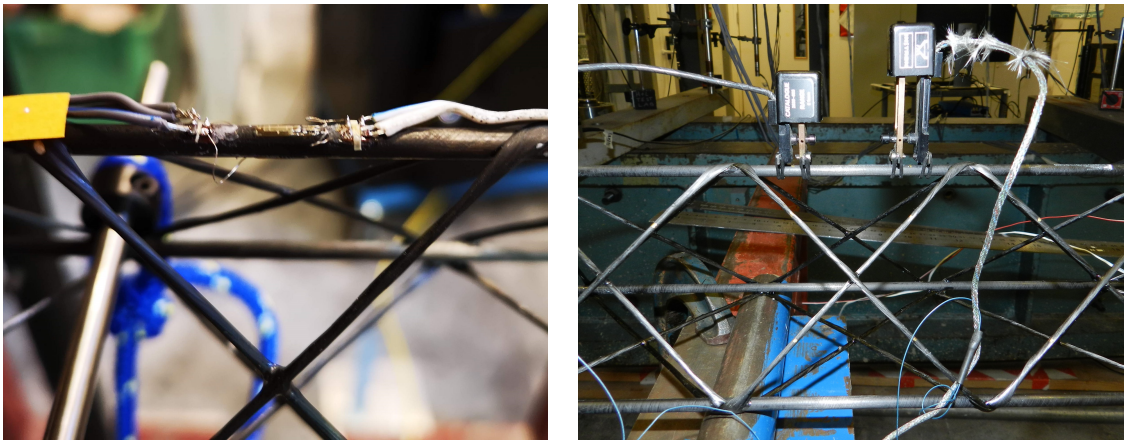

(a) (b)

Figure 4.3: Strain measurements in chord members: a) strain gauge; b) clip extensometers.

4.4.3.2 Shear member strains

The shear members of the WrapToR truss configuration form a repeating cross pattern. Each cross contains two shear members which are connected at their crossing-point via an epoxy bond that is formed during winding. Using clip extensometers, strain was measured in each shear member above and below this crossing point. Again, to determine axial strain within the member, it was necessary to account for bending by measuring the strain on opposing sides of the members. Strains in the shear members were only measured in configuration H66_2 as the smaller configurations were too small to fit the extensometers and the strains in the larger configuration truss were too small to be reliably measured by these devices.

4.4.3.3 Local joint deformations

To investigate deformations within the joints that connect the shear and chord members, three joints on each of the trusses were inspected during testing using a 5 MP 3D DIC system. Specifically, DIC was used to track the displacement fields of the joints along the truss length relative to the neighbouring chord members. Those inspected were the upper central joint and the two adjacent upper joints (as seen in Figure 4.2). This method was used to get a qualitative interpretation of deflections within the joints.

4.5 Model validation: Results and discussion

4.5.1 Empirical fit of joint shear stiffness

As discussed in Section 4.3.3, shear stiffness values for the joint elements within the eccentric model were determined through an empirical fit using the three-point bending experimental data. Two fitting methods were conducted, both of which performed iterative searches to minimise the MAPE of the models. The first assumed a constant joint shear stiffness value throughout all the configurations. The shear stiffness found using this method was 15,218 N, which produced a MAPE across all configurations of 8.2%. For the second method, separate shear stiffness values were found for all seven configurations. The values that produced the minimum MAPE in the second method are displayed in Table 4.5.

Once the individually fitted values were found, a multivariate linear regression was used to determine a linear expression that relates truss geometric parameters to the joint element shear stiffness. Statistical analysis of the linear regression was conducted to determine the truss variables that had a significant effect on joint shear stiffness; this is detailed fully in Appendix D. The determined linear expression takes the form of Equation 4.7 where it is seen that the primary influencing variables are the chord member diameter, shear member diameter, truss height and the winding angle. The coefficients, b_n relating to these variables are given in Table 4.6. The coefficients in Table 4.6 give some indication of which variables have the greatest effect on the joint stiffness. The configuration shear stiffnesses given by the linear expression are compared to the experimentally determined values in Table 4.5.

$$GA_s = b_1 + b_2 \varnothing_c + b_3 \varnothing_s + b_4 H + b_5 \theta_w \tag{4.7}$$

In Table 4.7 the errors in predicting truss effective flexural rigidity of the eccentric model using both shear stiffness fitting methods are compared with that of the concentric model. Here it is seen that the eccentric model, regardless of fitting method, provides much more accurate predictions than the concentric model (discussed further in the following section). Also seen is that the method using the empirically fit linear expression for shear stiffness, provides more accurate results than using a constant value. Due to its improved accuracy, this linear expression is used for the eccentric model results in the following sections and the later optimisation work. When using this method, however, some caution must be exercised due to several reasons. While the linear expression provides good approximations of the fitted shear stiffness values (as is seen in Table 4.5), this is not particularly surprising due to the relatively large number of variables in the equation relative to the number of data points. The statistical analysis detailed in Appendix D shows the linear

Table 4.5: Individually fitted joint shear stiffness values and linear model approximations.

Config.	Shear stiffness, GA_s (N)		
	Fitted value	Linear expression approx.	% error
H33_1*	10655	10430	-2.2
H33_2	20430	20430	0.0
H66_1	8823	8322	-6.0
H66_2*	9792	11265	13.1
H99*	14033	13596	-3.2
H50_D4	20630	19974	-3.3
H50_D5	31495	31770	0.9

Table 4.6: Joint shear stiffness linear expression coefficients.

Related variable	Coefficient	Value
Intercept	b_1	-64566
Chord diameter, $\varnothing_c$	b_2	11175165
Shear diameter, $\varnothing_s$	b_3	6116754
Section height, H	b_4	-403340
Winding angle, θ_w	b_5	1052

expression provides a good level of fit to the experimental data, but also suggests some potential overfitting. Another reason for caution is that other truss variables, most notably chord member wall thickness, are also likely to influence joint shear stiffness. The dataset provided from the seven truss configurations was, however, not sufficient to determine any significant link. It is expected that this model will be useful for new truss designs with geometric parameters which fall within the range of those tested (interpolation), but extrapolating significantly beyond that range should be avoided.

Confidence in the linear model could be improved through further testing of new truss configurations, or perhaps through detailed local modelling of the joint regions. For the work within this thesis, it was concluded that approximating the joint shear stiffness using the linear expression provides an appropriate level of accuracy. Also, it is worth noting that while the joint shear stiffness has a significant effect on truss deflections, its effect on member strains are small.

4.5.2 Global stiffness tests

In Figure 4.4 the experimentally determined effective flexural rigidities of each truss configuration are compared with predictions from the concentric and eccentric models. For each truss configuration, experimentally determined effective flexural rigidity is seen to increase with span; a trend that also features in the model results.

Table 4.7: Errors in predicting effective flexural rigidity of various models and joint shear stiffness fitting methods. Mean absolute percentage error (MAPE) and maximum error across all configurations displayed.

Model / Shear stiffness fit method	MAPE (%)	Maximum % error
Concentric	89.1	313.2
Eccentric / Constant	8.1	22.8
Eccentric / Individually fit	2.6	13.7
Eccentric / Linear expression	3.1	16.5

This increase with span is due to the changing of relative contributions of shear and bending deflections to the overall measured deflection. At shorter spans, the contribution of shear deflection is more significant and therefore, lower effective flexural rigidities are observed. As the span increases, shear deformations become less significant, and the bending rigidity approaches a constant value.

Also plotted in Figure 4.4 are flexural rigidity predictions determined using parallel axis theorem assuming contributions solely from the chord members (method discussed in Section 4.4.2). In all test cases, parallel axis theorem is seen to over-predict flexural rigidity. However, for the smaller section beams (Figures 4.4a and 4.4b) the model and experimental results appear to approach the predictions of parallel axis theorem at larger spans. In fact, model results approach predictions from parallel axis theorem for all configurations if the beam aspect ratio is sufficiently high. When running the eccentric model for a high beam aspect ratio (span divided by height) of 120, the determined effective flexural rigidity is found to be within 1% of that predicted by parallel axis theorem for all seven configurations. Again, this can be explained by the relative contributions of bending and shear deformations. At higher beam aspect ratios, bending deflections dominate meaning parallel axis theorem can provide reasonable predictions. Parallel axis theorem has been used in this way by other authors to predict IsoTruss® flexural rigidity [59, 61]. Results here, however, suggest this method may only be appropriate for high aspect ratio composite lattice beams.

When comparing experimental results of the different test configurations, Figure 4.4 demonstrates how the WrapToR trusses take advantage of the nonlinear scaling laws of stiffness to achieve impressive stiffness increases with only relatively small mass penalties. When comparing configurations H33_1 and H66_1 at the largest span, a 25% increase in mass corresponds to a 200% increase in stiffness. This is possible because the truss configuration can move material further away from its neutral axis using relatively small amounts of additional material.

Variance in the measured stiffness was observed between samples within the same configurations; this is evidenced by the error bars in Figure 4.4. One issue faced during testing was the difficulty in precisely levelling the trusses so that all four

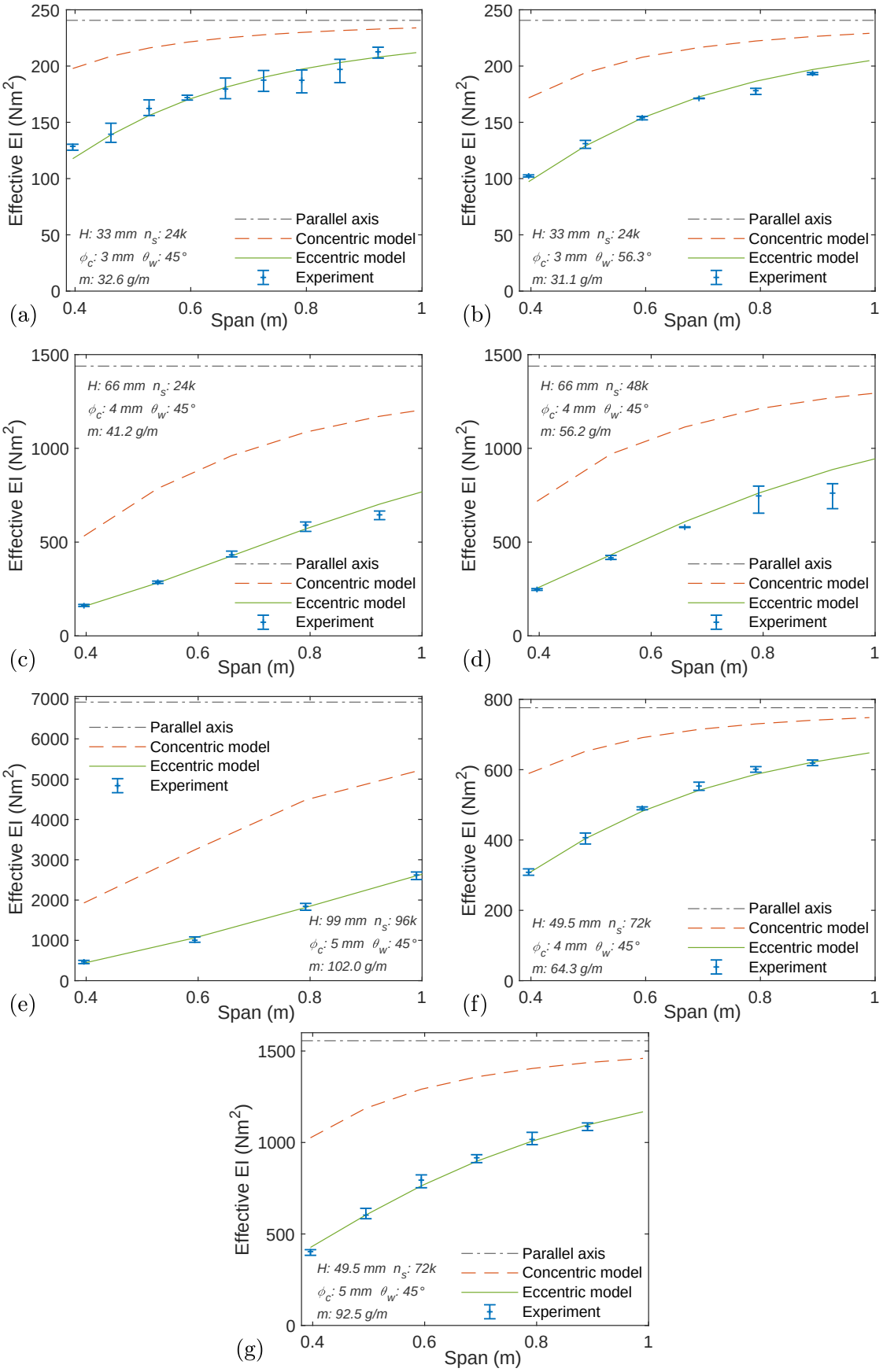

Figure 4.4: Effective flexural rigidites: a) H33_1; b) H33_2; c) H66_1; d) H66_2; e) H99; f)H50_D4; f) H50_D5. (Error bars denote the range of three values)

support points and both load points were in contact with the testing rig. This was particularly challenging in the configurations with larger shear members as the truss joints protruded further. This issue may account for some of the variance observed between samples. Manufacturing inconsistencies between samples is also likely to be a contributing factor, particularly the variation of resin content within the shear member tow. It should be noted here that due to the high stiffness of the structures, the measured displacements were very small. For example, the H99 truss at 396 mm span had a maximum displacement of 1.34 mm at 405 N. At these low displacements, small measurement errors can have a large effect on the calculated stiffness.

Figure 4.4 also displays the predictions from the analysis tool when using both the concentric and eccentric geometric idealisation approaches. When comparing the two geometric idealisation methods, large differences in predictive capabilities are observed. The total model MAPE values across all configurations displayed in Table 4.7 show that the eccentric model produces significantly more accurate predictions of the global truss stiffness. The key difference between the models is the insertion of an additional element at each joint. The results in Figure 4.4 and Table 4.7, therefore, indicate that the joint mechanics have a significant effect on overall truss deflections. The first possible reason for this is due to displacements within the joint. The epoxy joints are the only elements within the trusses that do not have fibres directly aligned with their primary loading direction meaning that although they are small relative to the truss members, their deflections may be significant. The second possible reason is that the eccentricity of the joint affects how forces are transferred between members. These reasons are investigated and discussed further in the following experimental sections.

4.5.3 Member strains and local deformations

4.5.3.1 Chord member strains

Within Figure 4.5 readings from strain gauges are compared to the model predictions for each truss configuration. Readings were taken on the upper and lower surfaces of the central upper-compressive chord member on each truss (location depicted in Figure 4.2). These two readings are plotted in Figure 4.5 as the minimum and maximum values. The average of the two readings gives the axial strain within the member which is also plotted in the graph. The difference between the axial and the minimum and maximum values represents the bending strain within the member. Note that the gradients of the strain vs load graphs (strain per unit load) are plotted here. The results show that the two geometric idealisation methods are effective at predicting axial strains within the members, with the average error for the concentric method being 4% and the eccentric method being 5%. While

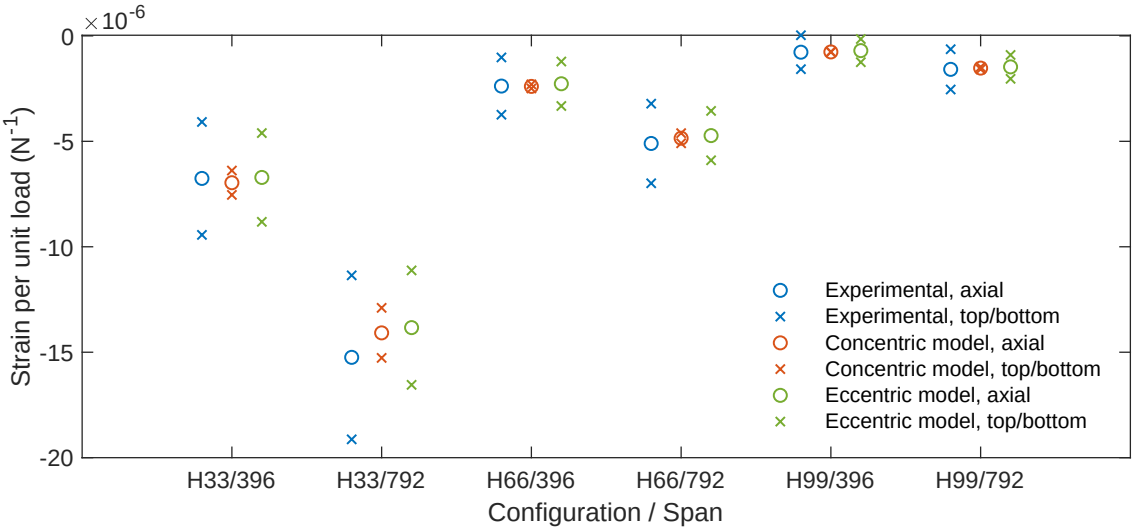

Figure 4.5: Measured chord member strains compared to predictions from concentric and eccentric models.

both the models predict axial strain effectively, they produce substantially different predictions of the bending strain within the central upper chord member. The results in Figure 4.5 show the concentric model underpredicts the magnitude of the bending strain for all configurations and spans tested. Meanwhile, the eccentric model provides a more accurate prediction of the bending strain.

To further assess the abilities of the models to predict member bending behaviour within the trusses, predicted bending moments in the upper compressive chord members are compared to experimental readings in Figure 4.6. As stated in Section 4.4.3.1, the experimental data points shown here were determined using clip extensometers positioned at two points per member. By assuming a linear distribution, the bending moment across the length of the member is then found by interpolating and extrapolating the data from the measured points. The results show that bending moments predicted by the eccentric model (Figure 4.6b) are larger and show closer agreement with the experimental results than the concentric model (Figure 4.6a). Within the eccentric model, forces are transferred from the shear to the chord elements via a joint element. The length of this joint element creates a moment arm, meaning that axial forces within the shear elements impart a moment on the chord elements at the joints. This explains why large step changes in bending moment are observed at the joints. This is a phenomenon also been witnessed by Tousignant and Packer [28], who found that modelling of the joint eccentricity was necessary for capturing bending moments within the chord members of hollow section metallic trusses. The vastly different bending moment distributions predicted by the two models provide some reasoning for the difference in their predictions of beam stiffness.

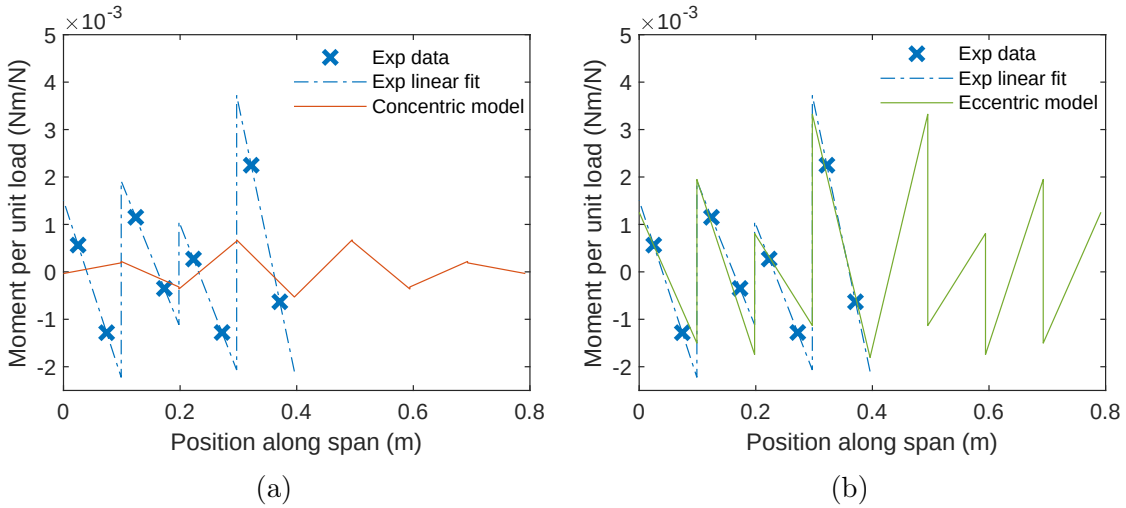

Figure 4.6: Bending moment distribution in upper chord members of H99 at 792 mm span. Experimental data and: a) concentric model; b) eccentric model.

4.5.3.2 Shear member strains

Shear member axial strains measured using clip extensometers are displayed for the tensile and compressive shear members in Figure 4.7. The experimental range plotted for each shear member represents the range of two readings: one above the shear member cross-point and one below. To determine the axial strain within the member, it was necessary to account for bending strain by averaging extensometer readings taken on opposite sides of the shear members.

For the tensile shear member results in Figure 4.7, both models provide similar predictions of axial strain. Compared to the average of the experimental results, the models perform well for the first two bays (less than 3% error) but show some error for the latter three (15-21% error). For the compressive members, a larger difference between the two models is observed. A larger error is also observed when comparing the models to the compressive experimental data where the concentric model gives an average error of 26% and the eccentric model 20%. This suggests again that, as was seen for the chord members in Section 4.5.3.1, the two models provide similar levels of accuracy when predicting axial strains. The results here potentially show inaccuracies in the models' ability to predict axial strain within the shear members. However, it should be noted here that acquiring the strain readings in these members was a difficult task. Firstly, the members are very small and have an uneven surface. This made it difficult to take readings on directly opposite sides of each member. Secondly, the strains being measured were very small and were close to the lower limit of what can be measured with the clip extensometers.

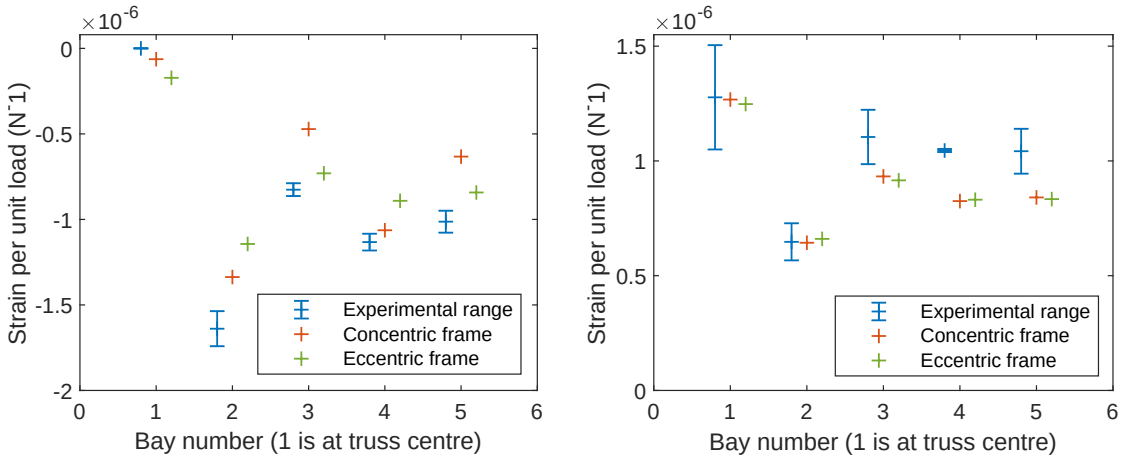

Figure 4.7: Axial strain per unit load in the shear members for configuration H66_2 at 792 mm span. a) Tensile members; b) Compressive members. (Error bars denote the experimental range of two readings)

4.5.3.3 Local joint deformations

Tracking the local displacements of the three upper joints (positioning detailed in 4.2) revealed an interesting phenomenon. Figure 4.8a shows the displacements transverse to the loading direction of a single joint measured using DIC. The specific joint shown is adjacent to the upper central joint on configuration H99 during testing at a span of 792 mm. Within Figure 4.8b, the joint region displays larger displacements transverse to the loading direction than the neighbouring chord members. This shows that the joint deforms at a local level. For the image in Figure 4.8a, the load point is to the left (in the negative x-direction) of the joint and the loading direction is in the image z-axis. When the truss is loaded, the shear members on the left of the image are in tension and on the right are in compression. This means a resultant force acting towards the centre of the truss is experienced, which causes the joint to be pulled towards the truss centre. Transverse joint deflections relative to the chord members were not witnessed at the central upper joint. This would be expected as for the central joint all connected shear members are in tension, meaning no resultant transverse force is exerted on the joint.

To further investigate this phenomenon, displacements were extracted from the DIC data along a segment of the top chord member that includes a joint. The yellow line on the image in Figure 4.8b shows the segment of the truss from which the displacement data was extracted. This data was extracted for three joints on each truss configuration, and in Figure 4.8b is plotted for configuration H99. The results here show that for the non-central joints (joints 1 and 2), there is a larger magnitude transverse displacement observed in the joint region than the adjacent chord member; something that is not observed for the central joint (joint 0). Also

interesting to note here is that the joint displacements in joint 1 appear to be more substantial than those in joint 2. Inspection of the analysis for this truss configuration revealed that transverse loading within joint 1 is predicted to be 79% larger than in joint 2.

The joint displacements observed in this section potentially provide reasoning as to why the concentric model fails to predict global displacements correctly, as without deformable joint elements these local displacements cannot be captured. It should be noted here that while only results for configuration H99 are displayed, the discussed joint deformations were consistently observed across all configurations.

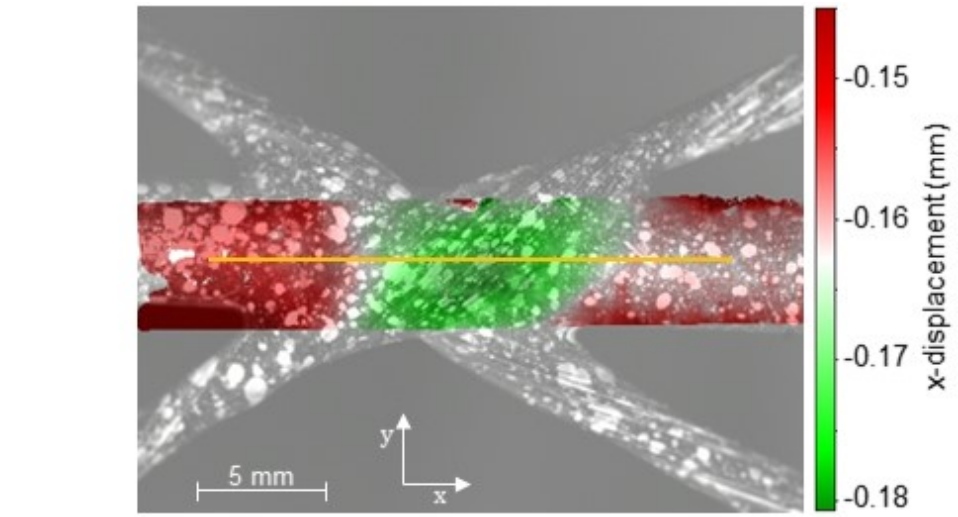

(a)

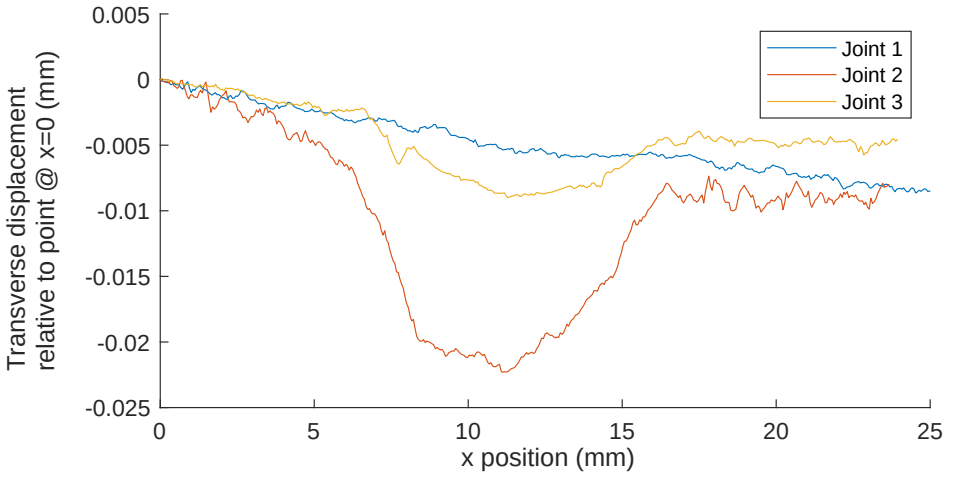

(b)

Figure 4.8: Transverse displacements in truss joints for configuration H99 at 792 mm span and 294 N loading. a) DIC image of joint 2; b) Displacements along yellow line in Figure a.

4.6 Parametric study

Development and validation of the truss analysis tool detailed in the previous sections demonstrated its ability to predict truss pre-failure response to a reasonable, useful level of accuracy. In this section, the validated tool will be used to investigate how truss geometric parameters influence truss beam stiffness. The purpose of this parametric investigation is to give useful insight into how truss geometry can be designed to maximise structural performance. The standard configuration WrapToR truss has five geometric parameters (or design variables) that can be altered to maximise structural performance for a particular role. These five geometric parameters are:

1. Shear member diameter, $\varnothing_s$
2. Chord member diameter, $\varnothing_c$
3. Chord member wall thickness, t_w
4. Truss section height, H
5. Shear member angle or winding angle, θ_s or θ_w

To investigate how each of these parameters influences truss stiffness, the analysis tool was run while sweeping across a range of values. The effective flexural rigidity was used as a metric to gauge beam bending resistance. To account for any change in mass that may occur when varying the parameters, the metric of 'specific flexural rigidity' was also used. This metric is determined by dividing the effective flexural rigidity by the truss mass per unit length (MUL). To determine truss MUL, a simple mass estimation module was added to the analysis code. This module estimates the truss member volume and uses the densities measured in Chapter 3 to find the mass. The mass estimation module is further detailed in Appendix E. Specific flexural rigidity can be viewed as a measure of structural stiffness efficiency. It has been used by Gurley et al. [76] for comparison of O-ACS beams with conventional beam configurations. Its usefulness as a measure of structural efficiency is, however, limited because flexural rigidity would not be expected to scale linearly with mass. It also does not account for any failure considerations. As was seen in Section 4.5.2, truss span, or length, has a significant effect on flexural rigidity. To account for this effect, sweeps of each parameter were performed at various spans, specified as an integer number of bays. This section will investigate how these five geometric parameters influence solely beam stiffness. Their effect of beam failure will later be investigated in Section 5.7.

4.6.1 Shear member diameter, $\varnothing_s$

The WrapToR trusses manufactured for the work within this thesis have shear members formed of intermediate modulus carbon tow that is impregnated with epoxy resin. The shear member diameter can be varied by changing the carbon tow size used during winding. To investigate the effect of the shear member diameter on the truss stiffness, the analysis tool was run for a range of diameters while keeping all other geometric parameters fixed. Shear member diameter was varied between 0-3 mm and all other parameters were fixed to that of configuration H33_1 (detailed in Table 2.1). As was seen in Section 4.5.2, truss span, or length, has a significant effect on truss flexural rigidity. It is noted here that in reality, a continuous selection of shear member diameters is not available as carbon fibre is generally purchased in a discrete selection of sizes. Through different combinations of various tow sizes, a wide selection would however be possible.

In Figure 4.9a, it is seen that increasing shear member size increases the beam stiffness. This is expected as the amount of material within the structure to resist the load is increased. This extra material, however, adds mass. In Figure 4.9b, it is seen that at a certain point the gains in stiffness are outweighed by the increases in mass meaning that the specific flexural rigidity increases to an optimal value before it decreases. For trusses with a larger number of bays (or length), the optimal diameter is smaller than for shorter trusses. Shorter trusses, and therefore lower aspect ratios, have more significant contributions from shear deformations. As it is the shear members that primarily resist these shear loads, lower aspect ratio trusses benefit from more shear member material. The longer, higher aspect ratio trusses have relatively less contribution from shear deformations, therefore requiring less shear member material.

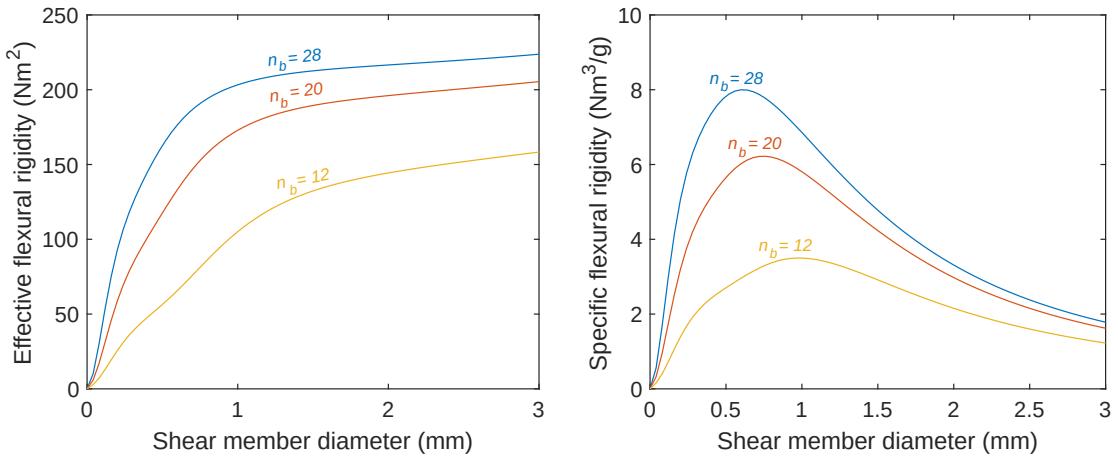

(a) (b)

Figure 4.9: Flexural rigidities at varying shear member diameters, $\varnothing_s$: a) effective; b) specific. All other parameters fixed at those for configuration H33_1.

4.6.2 Chord member diameter, $\varnothing_c$

The pultrusion tubes used in trusses tested within this thesis were supplied by EasyComposites®. These tubes are available in diameters ranging from 1 to 12 mm. Tubes with outer diameters less than 5 mm have a thickness of 0.5 mm while those with diameters of 5 mm or above have a wall thickness of 1 mm. When running the analysis over a range of chord member diameters, this was accounted for by incorporating a step change in thickness at 5 mm diameter. Also investigated were the flexural rigidities for tubes where the thickness is held constant at 0.5 mm across all diameters. Results of the constant diameter tubes are plotted as dashed lines in the Figure 4.10 graphs.

The flexural rigidities for varying chord member diameters are plotted in Figure 4.10. Here chord member diameter is varied between 1-12 mm with all other parameters fixed to that of configuration H66_2 (detailed in Table 2.1). The effects of varying chord member diameter show some similarity to those observed when varying shear member diameter in the previous section; increasing the diameter results in more material leading to an increase in effective flexural rigidity, as seen in Figure 4.10a. Again, the corresponding increase in mass creates an optimal size when considering the specific flexural rigidity. The pattern between optimal tube size and truss length is, however, opposite to that observed for the shear member diameter investigation. Here the optimal size increases with length, meaning longer trusses have a larger optimal chord member size. Again, this can be attributed to the relative contributions of shear and bending deformations. As the chord members predominately carry the bending loads, larger tubes are more beneficial in longer

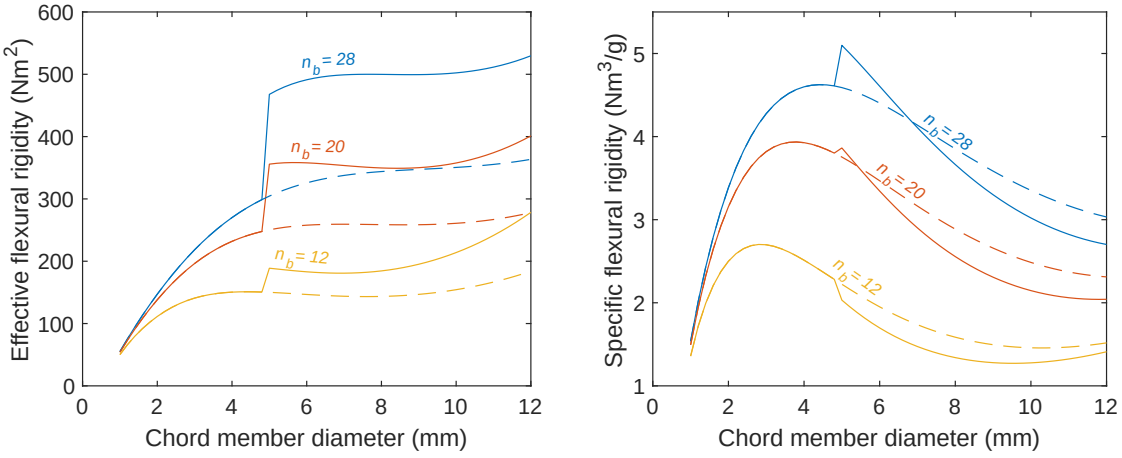

(a) (b)

Figure 4.10: Flexural rigidities at varying chord member diameter, $\varnothing_c$: a) effective; b) specific. Solid lines show tubes with step change in thickness at 5 mm. Dashed line shows tubes with a constant thickness of 0.5 mm. All other parameters fixed at those for configuration H66_2.

trusses which experience larger bending moments. Also interesting to note is that the step change in thickness has a positive effect on specific flexural rigidity at longer lengths, but is detrimental for shorter trusses. Again, the longer span truss here benefits from more chord member material to resist the larger bending moments.

4.6.3 Chord member wall thickness, t_w

While the purchased tubes used within this thesis had fixed thicknesses, tube thickness could be varied by using different suppliers or by manufacturing custom tubes. Further design flexibility around tube thickness is likely to contribute to further efficiency gains. To investigate the effect of chord member tube thickness, flexural rigidities were found over a sweep of thickness values. In Figure 4.11 flexural rigidities are plotted for three external tube diameters against the tube radius-to-thickness ratio, where 1 is a solid section rod (i.e. radius is equal to thickness). All other parameters were fixed to that of configuration H66_2, and the truss length used was 1.06 m, corresponding to 16 bays.

As would be expected, in Figure 4.11a decreasing tube thickness is seen to decrease the truss stiffness. When observing the specific flexural rigidity in Figure 4.11b, a more complicated relationship is observed. Varying the tube thickness has several structural effects. When decreasing thickness, member axial stiffness will be reduced, along with the mass. Decreasing thickness will also reduce the chord member bending stiffness; however, it will likely improve the member bending stiffness efficiency (thin-wall tubes are more efficient at resisting bending than thick-wall tubes). These effects have varying levels of contribution for the different tube sizes meaning that no overall trend is observed. In the 3 mm tube case, a solid section

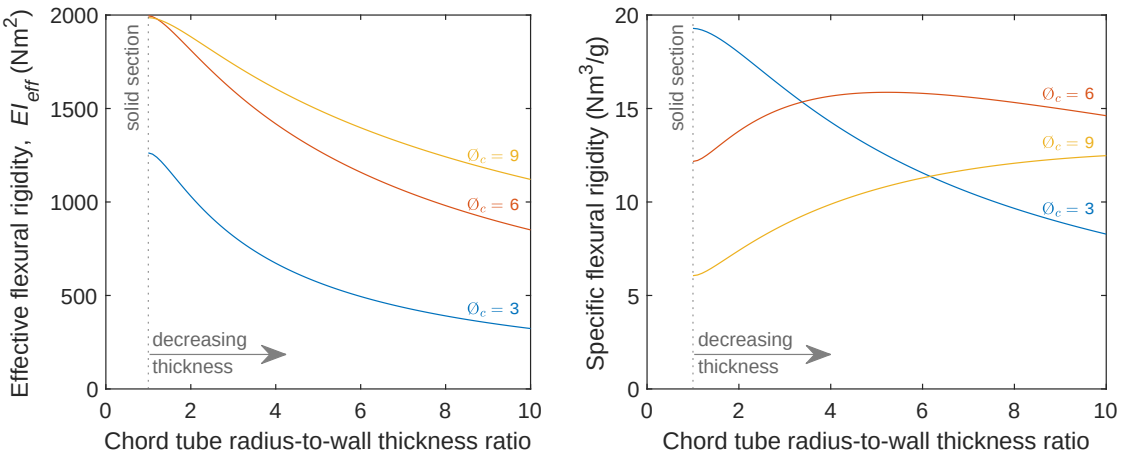

Figure 4.11: Flexural rigidities at varying chord member wall thickness, t_w: a) effective; b) specific. All other parameters fixed at those for configuration H66_2.

tube gives the highest specific flexural rigidity, which then decreases as wall thickness is reduced. For the 6 mm tubes, a solid section gives the lowest value. Then when decreasing thickness, specific flexural rigidity rises until an optimal value is reached before decreasing again. The 9 mm tubes follow a similar pattern, however, the optimal thickness ratio is outside the range of the graph. Figure 4.11b therefore shows that the effects of varying parameters are interrelated and that simple independent design rules relating geometric parameters to stiffness are likely to be insufficient. This provides motivation for the optimisation study later detailed in Chapter 6.

4.6.4 Truss height, H

Truss height will have a significant influence on truss stiffness as it dictates the distance of the chord members from the truss beam's effective neutral axis. Unlike the other geometric parameters investigated so far, performing a sweep of continuous height values while keeping other parameters fixed is not possible; this is because of the relationship between height, winding angle and number of bays (or length). For this reason, in Figure 4.12, four discrete truss heights are plotted at varying truss lengths. All other parameters are fixed to those of configuration H33_1.

The trends observed in Figure 4.12 for both the effective and specific flexural rigidity are near identical. This is because altering truss height, while fixing winding angle, results in only a minimal change in mass. A small mass change occurs due to the small change in length of the shear member close-outs (the vertical shear members at the truss ends); the amount of material used in the diagonal shear members remains constant. The graphs show that at larger truss lengths, increasing

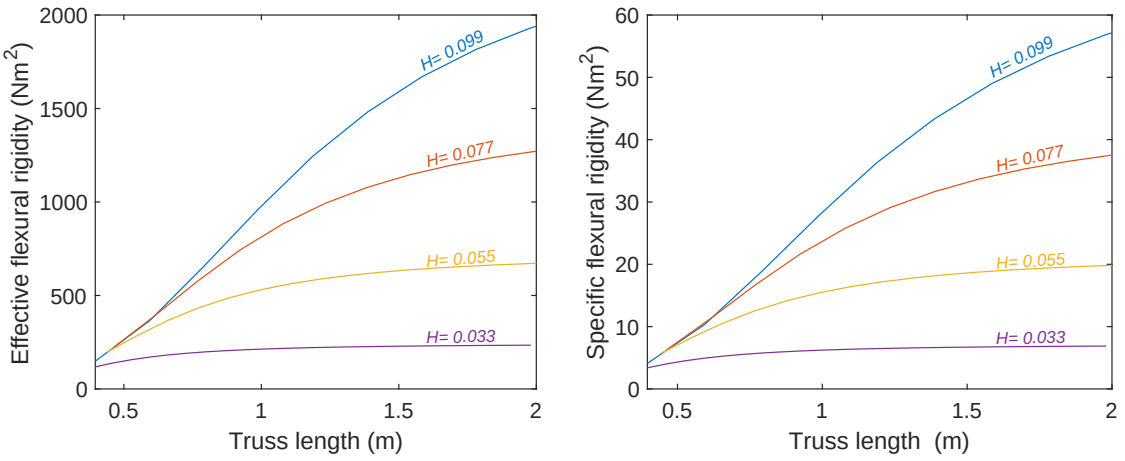

(a) (b)

Figure 4.12: Flexural rigidities for four truss heights, H, at varying truss length: a) effective; b) specific. All other parameters fixed at those for configuration H33_1.

the height is an effective means of increasing the stiffness efficiency. This is because it increases the distance of the chord members from the neutral axis, with a negligible increase in mass. This increase in stiffness will, however, increase the unsupported length of the members, making them more susceptible to buckling. At lower spans, truss height has minimal effect on stiffness because the truss deflections are primarily driven by shear loading. Therefore, changing the height, which primarily changes the bending resistance, has a negligible effect on the flexural rigidity.

4.6.5 Winding angle, θ_w

Both winding angle and shear member angle are truss parameters that describe the orientation of the wound shear members. As is detailed in Section 2.1.6, the difference between the two angles is subtle and generally small (often less than 2°). Winding angle was used during this section to investigate the effects of shear member orientation as its simpler relationship with the other parameters makes its use more straightforward. The effect of winding angle on the flexural rigidities is plotted in Figure 4.13 for three truss lengths. All other parameters were fixed to those of configuration H33_1. As is detailed in Section 2.1.6, the angle of the shear members is defined away from the axis perpendicular to the beam axis; such that a truss with a winding angle of 90°would have shear members aligned with the chord members. Changing the shear member angle, while fixing truss length, requires altering of the number of bays. A larger winding angle requires a lower number of bays. Altering these parameters has several structural effects. Increasing shear member angle reduces the amount of shear member material, subsequently lowering mass. An increase in shear member angle will also reduce the number of truss joints. The angle also determines how well the shear members are aligned with the beam shear forces; with an angle close to 45°most appropriate for alignment with these forces.

The effective flexural rigidity results seen in Figure 4.13a show that for most of the plotted range, a lower winding angle results in a higher stiffness. This is due to the increased number of joints and amount of shear member material. When the angle gets very small, i.e. the orientation of the shear member approaches being perpendicular to the beam axis, effective flexural rigidity drops. A likely reason for this is that the effects of misalignment of the shear members with beam shear loads begin to outweigh the positive effects of increasing joint numbers and amount of shear member material. At these low angles, the shear members have to carry the shear loads as internal bending moments rather than as axial forces.

When investigating the specific flexural rigidity in Figure 4.13b, again the trade-off between the structural effects and the truss mass results in an optimal angle. For

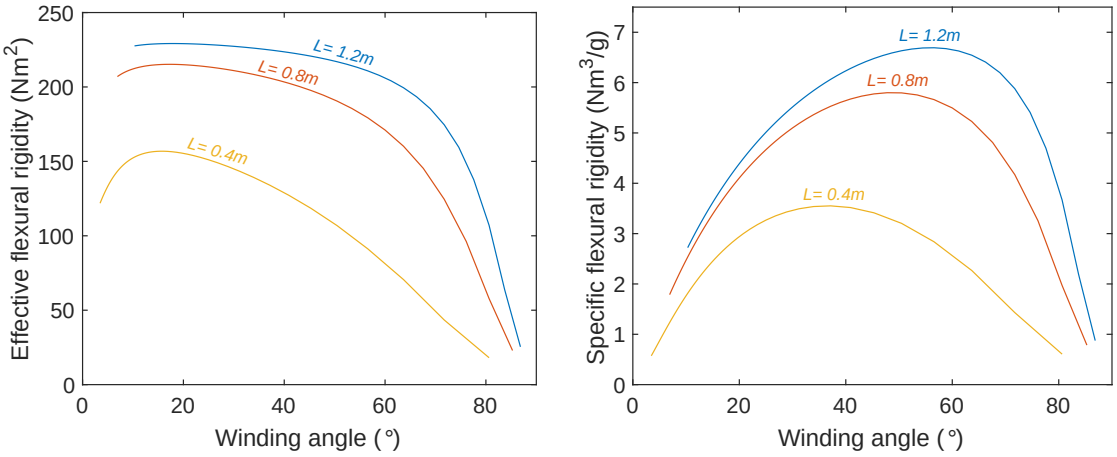

(a) (b)

Figure 4.13: Flexural rigidities at varying winding angle, θ_w: a) effective; b) specific. All other parameters fixed at those for configuration H33_1.

the three truss lengths, this optimal angle is between 37 and 57°. For shorter span trusses, the optimal winding angle is lower. At lower spans, shear deformations and member joint deformation effects will have a greater contribution to overall deflections, therefore, having more shear member material and joints is beneficial. The opposite is the case for the longer trusses.

4.7 Conclusions

This chapter aimed to develop an analysis tool capable of predicting the pre-failure mechanical response of WrapToR trusses. The analysis could then be later developed to include failure criterion providing a useful tool for design and optimisation studies. The developed analysis tool was coded in Matlab and is based on the stiffness method, a variant of matrix structural analysis (MSA). Two models were generated using different approaches for geometrically idealising the trusses. The first concentric model represents the shear and chord members using beam elements. The second, eccentric model additionally features joint elements that represent the connections between the chord and shear members. To validate the models, and to determine the most appropriate method of geometric idealisation, the mechanical response of the trusses under flexural loading was investigated to a high level of detail; measuring both global deflections and member strains.

The experimental validation work demonstrated large improvements in accuracy when using the eccentric model. These results highlighted the importance of modelling effects of the truss joints using dedicated joint elements when predicting truss deformations and member bending strains. The investigation provided two reasons as to why inclusion of joint elements improves model accuracy. Firstly, the eccen-

tricity at the joint has a significant effect on how forces are transferred between members, specifically that axial forces within the shear members impart bending moments in the adjacent chord members. Secondly, investigation using digital image correlation (DIC) showed that displacements occur within the joints themselves. Without the use of joint elements within the model, neither of these physical effects can be captured. When modelling the truss without using joint elements, the model significantly overpredicts truss stiffness and underpredicts member bending strains. These results, therefore, clearly show that physical effects associated with the joints have a significant effect on the overall mechanical response.

One issue faced when developing the eccentric model was that properties for the dedicated joint elements were required which could not be feasibly determined through experimental means. Joint properties were therefore determined through model fitting with the experimental data. An expression relating truss parameters to the stiffness properties of the joint elements was found using a linear regression of the fit values. This method provides an approximate means to model the behaviour of the truss joints and is suitable for the analysis and design work within this thesis. Further understanding and more accurate prediction of the joint behaviour would require more detailed modelling of the local joint region. Such modelling could provide a more accurate means of determining joint properties.

The work in this chapter shows that when incorporating joint elements, the developed WrapToR analysis tool can predict the detailed mechanical response to a reasonable, and very useful level of accuracy. This includes predicting global bending behaviour, local deflections, and member strains. These predictive capabilities are demonstrated across a range of truss configurations with varying section sizes, member dimensions, and truss aspect ratios.

The developed analysis tool was finally used to investigate the effects of varying truss geometric parameters on overall beam stiffness. By independently varying the truss parameters, the underlying trends were shown, and optimal values were identified for specific configurations. Finding the optimal combination of parameters for maximising structural efficiency would not be possible using this method. Furthermore, the parametric investigation did not incorporate failure consideration. The following chapter will focus on incorporating and validating failure criterion within the model. Following this, in Chapter 6, the model will be implemented within an optimisation framework to provide a powerful design tool capable of identifying the optimal combination of truss geometric parameters for any given application.

Chapter 5

Failure analysis & validation

5.1 Introduction

In the previous section, an analysis tool was developed that was shown to be capable of predicting WrapToR truss deflections and strains to a reasonable level of accuracy. While assessment of truss stiffness is important, without the ability to predict failure, the usefulness of the developed tool for component design will be limited. This chapter is therefore focused on developing the capabilities of the tool to predict failure. Prediction of failure within composite materials is notoriously difficult. The complexity of their internal structure results in a more complicated internal stress distribution and a wider range of potential failure mechanisms than more conventional materials. Such mechanisms include fibre breakage, delamination, fibre micro-buckling, matrix cracking and interfacial debonding [123, 124]. Significant research has investigated the prediction of failure in composites, with even the most developed methods providing varying levels of accuracy across different loading scenarios [125].

Composite lattice beam structures present novel configurations that may well be prone to failure mechanisms unlike those of conventional laminated composites structures. The complex nature of composite failure, combined with the novel and poorly understood structural mechanics of composite lattice structures, means that highly accurate prediction of failure in these trusses is likely to be difficult. In Section 5.2, the published literature relating to failure of other composite lattice technologies is discussed; this includes both mechanisms observed during mechanical testing, and the prediction methods used. In Section 5.3, failure mechanisms in WrapToR trusses are discussed; this includes those that have been previously observed and others that could exist. Detailed in later sections are the attempts made to predict the loads at which these failure mechanisms will occur.

This chapter aims to develop the WrapToR analysis tool to incorporate ap-

proximate failure prediction capabilities that can be used within an optimisation algorithm for the purpose of preliminary component design. The chapter does not aim to provide a detailed investigation of the failure micro-mechanics within WrapToR trusses, nor does it aim to provide highly accurate failure predictions. Instead, the crucial failure mechanisms are identified, and simple methods are employed to approximate their critical load values. The accuracy of these methods is then assessed through experimental validation in Section 5.6. With the end focus being implementation within an optimisation algorithm, any failure prediction method used was required to be computationally inexpensive. This, therefore, presents a trade-off between the method's accuracy and computational cost. This consideration meant that any developed failure prediction method would ideally be implementable within the Matlab coded tool. Not only would this aid in reducing computational expense, but it also would make implementation within an optimisation algorithm more straight-forward. High-fidelity methods, such as three-dimensional FEA, which would provide a high level of accuracy, were deemed too computationally expensive for the task. Where appropriate maximum stress criterion were utilised, and where such simple methods were inappropriate, more complex methods were utilised. In order to capture the experimentally observed non-linear behaviour, in Section 5.4 the code is developed to include incremental loading analysis.

5.2 Background: Failure of composite lattice beams

Summarised in Table 5.1 are the failure mechanisms observed during mechanical testing of composite lattice beams from studies documented within the literature. The most commonly observed mechanism is local buckling of the lattice members. Local buckling of the members has been observed in four different lattice beam technologies, including the IsoTruss® [59, 63], Isobeam [65, 75] and in previously published work on the WrapToR truss [82]. Local buckling has been observed when testing lattice beams under multiple loading configurations, including axial compression [59], flexure [65, 75], and torsion [82]. Failure in the glass FRP truss presented by Ju et al. [74] was characterised by a non-linear softening of the structure, prior to what was referred to in the paper as buckling. This failure mechanism is very similar to that observed during the tow twisting investigation in Section 3.6. While the authors of the paper refer to the failure mechanism as buckling, there is some debate as to whether this gradual increase of displacement can be defined as buckling. A more accurate description of the failure mode would be that the large nonlinear deformations result in sufficient strains to cause material failure; this is discussed further in Section 5.4. Global buckling has also been observed by Rackliffe et al. [59] when testing IsoTruss® beams under axial compression. The study showed that beams

with high aspect ratio and small bay lengths were susceptible to global buckling and that shorter beams with longer bay lengths were more susceptible to local buckling.

Lai et al. [63] observed two failure modes when testing 1D-LTCS under axial compression loading. Most commonly observed was material failure in the longitudinal members. Delamination of the members, originating from the interwoven joints, was also witnessed in some samples; this is the only published example of joint failure within a composite lattice beam published prior to work in this thesis. Testing of Isotruss® beams to failure under a range of loading scenarios was conducted by Weaver et al. [58]. During this testing, member buckling occurred, as well as what was described as member "shattering", which is suspected to be material failure. Failure of an ACT beam under cantilever bending was observed to occur due to cracking in the tensile longitudinal member, however, the exact mechanism was not identified [77].

Attempts within the literature to predict failure of composite lattice beams have generally focused on buckling and member material failure. To predict material failure in the members, some researchers use FEA to get member stresses then couple this with a maximum stress criterion, where the material strengths are taken from manufacturers data or material testing [56, 65, 82]. Others predict member stresses using analytical methods that make certain assumptions about member contributions. For example, Weaver et al. [58] assumed that under axial loading, the IsoTruss longitudinal members carry the majority of the load and that stress in the helical members is negligible. This assumption was shown reasonable using strain gauge measurements which showed negligible strain within the helical members. Lai et al. [63] presented an analytical method that considered contributions of the helical members based on relative member stiffness and the member inclination angle. From this, they too concluded that the helical members provide little contribution under axial loading.

Some studies have used a similar method to predict local buckling where the member loads are compared to a critical value derived from Euler buckling formula. When doing this, selection of an appropriate end condition factor is required. Some researchers have opted to use a conservative value [58], others have estimated using experimental comparison [82], and some have used analytical means to determine an appropriate value [59, 61, 62]. One potential issue when using Euler buckling column formula for this purpose is that lattice beam members are not pure columns. Having bonded ends, each member will experience moments as well as compressive forces, meaning they are in fact beam-columns.

Global buckling of lattice beams under axial compression loading has also been analysed either using Euler column theory or using FEA buckling analysis. When using Euler formula for global buckling, selection of appropriate flexural rigidity, EI,

Table 5.1: Failure mechanisms observed in other composite lattice beam technologies.

Technology	Loading configuration(s)	Observed failure modes	Ref.
IsoTruss® /1D-LTCS	Axial compression & tension, torsion	Buckling, "shattering"	[58]
	Axial compression	Local & global buckling	[59]
	Axial compression	Material, delamination	[63]
IsoBeam	3 & 4-point bend	Local buckling	[62]
	4-point bend	Local buckling	[75]
GFRP truss	3-point bend	Non-linear yielding/buckling	[74]
WrapToR	Torsion	Local buckling	[82]
ACT	Cantilever	Authors unsure	[77]

is required. In [59, 61] flexural rigidity was estimated using parallel axis theorem with the assumption that only longitudinal members contribute. Sui et al. [61, 62] derived equations for various buckling modes of 1D-LTCS which were verified using FEA buckling analysis. Using these equations, along with consideration of strut fracture, interesting failure maps were generated showing how various beam parameters affected the predicted failure mode.

One failure mechanism that has been continually overlooked in the published analysis works is that of failure at the joint between members. Joint failure is likely to occur in all the discussed lattice beam technologies but would be expected to be more prevalent in those where the joints are not fibre reinforced, such as the ACT, O-ACS, and the WrapToR truss. A potential reason as to why joint failure analysis is often neglected is that the three-dimensional stress state generated at the intersection of multiple members is likely to be difficult and computationally expensive to model.

While there are several studies attempting to predict composite lattice beam failure, none of the published works consider a comprehensive range of failure mechanisms. Additional to this, validation of the failure prediction methods used is not stringently conducted. Within this chapter, failure prediction methods are determined for a practically comprehensive range of failure mechanisms within WrapToR truss structures. In Section 5.6, experimental work will aim to validate the accuracy of these methods.

5.3 Failure of WrapToR trusses

Like other composite lattice beams, the WrapToR truss has a range of potential failure mechanisms. The failure mechanism that occurs within a truss will be dependant on the truss geometry, material selection, loading configuration, as well as factors such as manufacturing defects. Some of these mechanisms have already

been observed in previously published work and in earlier investigations within this thesis. In this section, these failure mechanisms are discussed. Also discussed are other mechanisms which are yet to be observed, but are also suspected to be possible. Note that failure mechanisms related to static loading are considered; those related to impact or fatigue are not. A focus is given to mechanisms that are likely to result from flexural or column compression loading as these have been identified as the most relevant scenarios. The failure mechanisms which are likely to be most prevalent are identified, and in Section 5.5 the development of methods to predict the loads at which these mechanisms occur is detailed.

5.3.1 Chord members

Under flexural loading of a WrapToR truss, at least one chord member will experience axial tension forces and at least one axial compression. Figure 5.1 shows two possible flexural loading scenarios and depicts the resulting axial loads experienced by the chord members. In Figure 5.1a, the applied moments result in a single compressive member and two tensile members. This is the scenario that occurs when using the three-point bend test outlined in Section 3.5. The axial force within the single compressive member must equal the force of the two tensile members, therefore each tensile member experiences half the magnitude of load of the compressive member. When considering that the compressive strength of CFRP is typically between 50-70% [126–128] of the tensile strength, it is clear that failure of the compressive member is much more likely during the flexural scenario in Figure 5.1a. If the moment direction is reversed, as in Figure 5.1b, this effect will be reversed and the single tensile member will have double the loading of each compressive member. Under operational conditions where the moment direction is consistent, or is larger in one direction, this second scenario provides a more efficient solution as the stress will be higher in the tensile member utilising the higher tensile strength. Applications where this may be useful include aircraft wings, which experience dominant loading upward at the tip, and wind turbine blades, which bend predominantly downwind. The discussion here suggests that under flexural loading, chord members may break by either compression or tension, however tension failure is less likely. In previous testing, only the flexural loading case in Figure 5.1a has been tested and hence only compressive failure of the compressive chord member has been observed (Section 3.6).

The chord members are made from UD pultruded CFRP tubes. When a truss is loaded, these members experience not only axial loading, but also internal bending moments. Under such loading, the tubes can fail via conventional composite mechanisms, such as fibre micro-buckling and fibre failure. Within this work, the precise

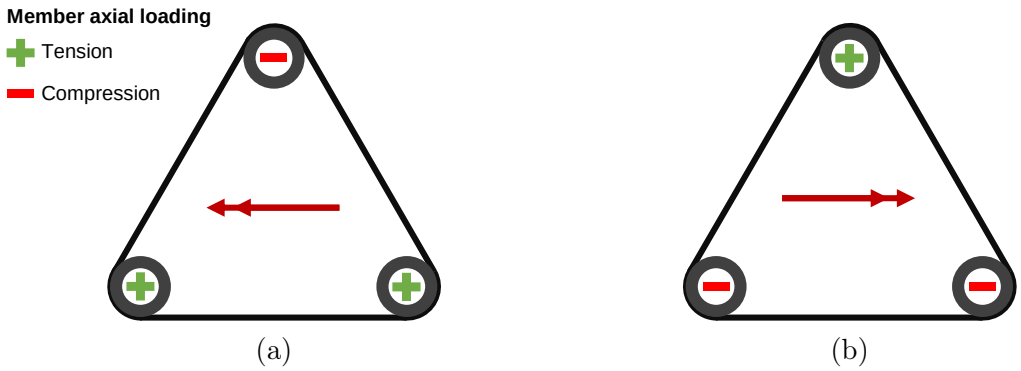

Figure 5.1: Chord member axial loading under beam flexural loads. Note bending moment notation follows right hand rule.

failure mechanism was not investigated, and these conventional failure mechanisms are grouped under the term 'material failure'. Additional to conventional mechanisms, UD tubes are also known to fail in a few unique ways. Under bending loads, ovalisation of the tubes can result in a catastrophic stiffness loss, or tube splitting due to the generated circumferential stresses [129]. Under compression loading, a mechanism can occur that is sometimes referred to as 'Chinese lantern failure'; this is characterised by longitudinal splitting around the tube circumference and a respective outward bowing of the fibre strands [130, 131]. It is also possible that individual members under compressive loading could locally buckle, leading to a global failure of the beam. Chord buckling will be most prevalent in truss configurations where the members have a high aspect ratio. Under tensile loading, the tubes are likely to fail via conventional composite mechanisms, such as fibre breaking. These conventional mechanisms will again be referred to as material failure.

5.3.2 Shear members

When a WrapToR truss is loaded under flexure, the shear members will experience both axial loads and bending moments. The axial load will be tensile in some members and compressive in others. Which members are in tension and which are in compression will depend on the flexural loading scenario. In Figure 5.2 the shear member axial load signs are shown for the flexural loading scenario in Figure 5.1b. Ignoring the shear members on the lower truss face, half the shear members experience axial tension, and half, axial compression. Investigation of the shear member axial load using the analysis tool shows that the axial force in a tension member is roughly equal and opposite to that in an adjacent compressive member. A similar pattern is observed when loading in torsion: half the shear members are in tension and half in compression, with near equal magnitude forces. Due to compressive strength being lower than tensile strength, it can be concluded that

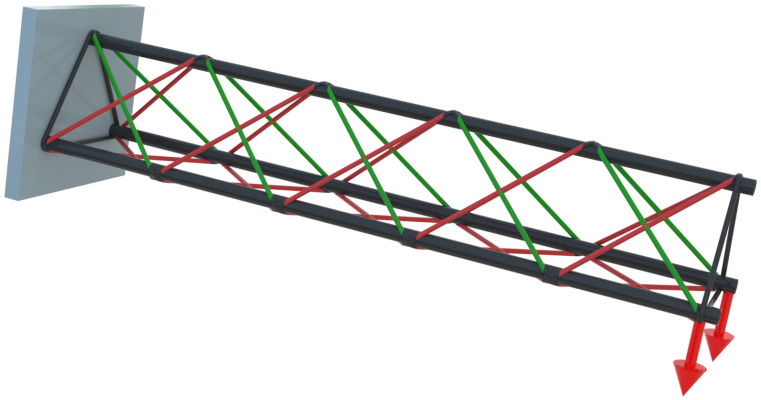

Figure 5.2: Axial loading in shear members under cantilever loading. Green members in tension, red are in compression.

tensile failure of the shear members is unlikely. Note that in Figure 5.2, the members along the lower surface are in compression because the applied load pulls the lower chord members together. The axial load experienced in these members is much lower than in the upper face members.

Failure of the compressive shear members was observed in work by Woods et al. [82] when testing trusses under torsional loading. During this study, it was stated that the members failed by buckling. During the tow twisting investigation detailed in Section 3.6, failure of the compressive shear members was witnessed when testing of multiple truss configurations. During these tests, two response types were observed prior to failure. In the truss configuration S-T, which had lower aspect ratio members, the response was fairly linear until failure (Figure 3.16b). In the configuration with higher aspect ratio shear members, L-T, significant non-linearity was observed prior to failure (Figure 3.15b), that corresponded with an outward bowing of the shear members. In both cases, fracture of one or more compressive shear members occurred and it was suggested that this resulted from either buckling or material failure. It should be noted however, that the shear members do not act as pure columns due to the presence of internal bending moments. In the high aspect ratio members, these internal moments meant that rather than a sudden change of shape (i.e. buckling) a gradual outward bowing occurs. Eventually, the large strains resulting from the non-linear softening cause fracture in the members. This is similar to the failure observed by Ju et al. [74] in their GFRP truss.

5.3.3 Joint failure

Joint failure was also witnessed while testing trusses to failure in Section 3.6. Joint failure mostly occurred in conjunction with member failure, however, some samples were seen to fail solely at the joints; an example of which is displayed in Figure 5.3. For the WrapToR configuration, a joint consists of two strands of carbon fibre tow

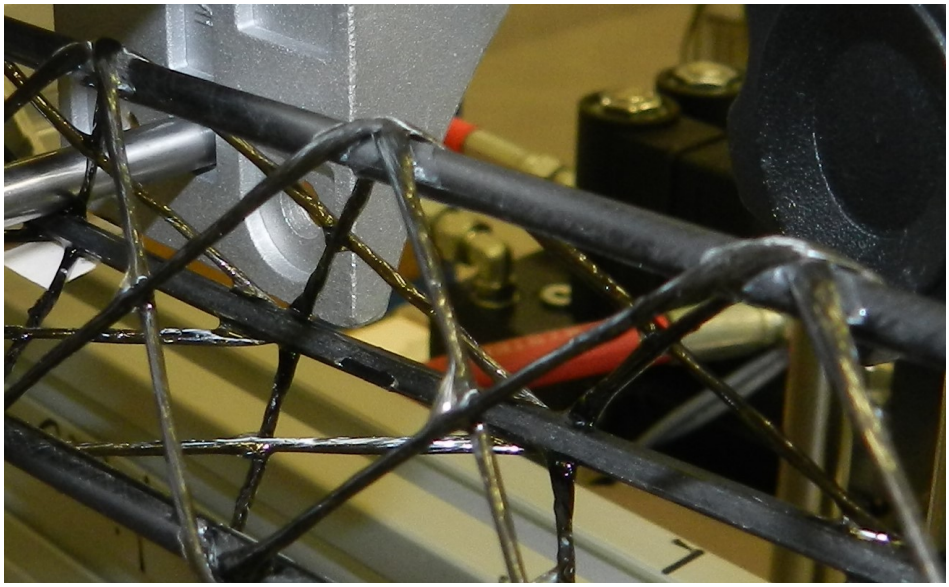

Figure 5.3: Joint failure observed during testing in Section 3.6.

running over one CFRP tube, all of which is connected via a co-bonded epoxy bond. Structurally this can be considered as the connection between four shear members and two chord members. Each of these members will be carrying both axial loads and internal bending moments, resulting in a complex three-dimensional stress state at the joints. This complex stress state, coupled with the detailed local joint geometry, is likely to make accurate prediction of failure difficult. A simplification of the stress state can however be made by assuming the WrapToR to be a highly stretch dominated lattice and therefore considering only the member axial forces.

During testing to failure in Section 3.6, joint failure was only seen to occur in joints along the upper compressive chord tube; as is the case in Figure 5.3. When considering the forces within a single joint along the upper tube, it is seen that on one side of the joint the shear members are in compression and on the other side in tension. This can be visualised by considering the upper chord member joints in Figure 5.2. As these forces are roughly the same magnitude, the resultant force experienced by the joint is predominately shear. The positioning of the members following joint failure seen in Figure 5.3 suggests that the joints have failed in shear. While the joints along the lower chord members could also fail due to combined shear and peel stress, this failure mechanism was not observed during the testing in Section 3.6. Member loads extracted from the analysis tool suggest that the generated peel forces under flexural loading are low relative to the shear forces. It is therefore possible that while a variety of complex failures at the joint are likely to occur, it may be appropriate to only consider failure due to shear loads in a majority of cases.

5.3.4 Global and local buckling

WrapToR trusses are formed of a series of slender members which when subject to compression loading can fail via local buckling. Global buckling of the entire truss is also possible when loaded as a compression column. Global column buckling will be more prevalent in high aspect ratio trusses and will be influenced by end conditions. Local buckling modes which involve more than just an individual member are also likely. Such modes have been identified in buckling of the Isotruss® and 1D-LTCS [59, 61, 62]. To predict both global and local buckling modes in WrapToR trusses, in Section 5.4 linear eigenvalue analysis is performed.

5.4 Nonlinear analysis

During the investigation into the effects of tow twisting Section 3.6, a nonlinearity was witnessed in the load-displacement responses of the test samples (see Figure 3.15b). Within lattice structures, nonlinearities can arise from either material or geometric effects. Material nonlinearities include plastic deformations and inelastic interaction between internal forces. Nonlinear elastic behaviour can also occur in carbon fibres [132]. Geometric nonlinearities arise primarily due to P-Δ effects, whereby member deflections are large enough that they alter the interaction of axial, shear, and bending loads [121]. The nonlinearity witnessed during testing is expected to be caused primarily by large deformations within the slender shear members as a significant bowing of the members was observed. This bowing effectively lowers the axial stiffness of shear members resulting in an overall truss stiffness reduction.

The WrapToR truss models developed so far within this thesis, both those in the MSA tool and commercial FE, use linear analysis. They therefore assume that only small deformations occur which do not alter geometry enough to have a significant effect on member stiffness or overall behaviour. Modelling of nonlinear behaviour using both MSA [121, 122, 133] and FEA [134] techniques is well established. Within Section 5.4.1, the development of the WrapToR analysis tool to predict nonlinear behaviour is detailed. The methodology used for this task is based on incremental loading application, and updating of the tangent stiffness matrix. Following this in Section 5.4.3, FEA models are built using Abaqus's nonlinear functionality and are used to verify the Matlab coded analysis tool. Predictions from the nonlinear analysis tool are later compared to experimental results in Section 5.7.3.

5.4.1 Incremental loading analysis

To incorporate nonlinear effects due to large deformations within the MSA tool, an incremental loading method was used. A few variations of this method are detailed

in different textbooks [121, 122, 133] but the method used and detailed here was primarily taken from McGuire [121]. As the nonlinear analysis techniques are well documented within the literature, only a brief overview of the specific method used is given here.

The method takes account of large deformations by applying load in multiple incremental steps. At each step, the stiffness matrix is updated to take account of geometric changes due to structural deformations, and changes to member stiffness due to internal loading. For each incremental load $\mathbf{\Delta P}$:

$$\mathbf{\Delta P} = \mathbf{K_T \Delta U} \tag{5.1}$$

where $\mathbf{\Delta U}$ is the vector of nodal displacements of an increment and $\mathbf{K}_T$ is the tangential stiffness matrix. The tangent stiffness matrix can be defined as the sum of the elastic stiffness matrix, $\mathbf{K}_e$, and the geometric stiffness matrix $\mathbf{K}_g$. The elastic stiffness matrix is calculated using Equation 4.1 for the geometry at the start of a loading increment. The geometric stiffness matrix is dependent on both member geometry and internal member loads at a chosen point within the loading increment. The local geometric stiffness matrices of all the individual members, $\mathbf{k}_g$ are calculated using Equation 5.2 and then assembled into the global geometric stiffness matrix $\mathbf{K}_g$. Note that in Equation 5.2, F and M are element internal axial forces and bending moments, respectively. The first subscript indicates the direction of the internal load component in the local element coordinate system. The second subscript indicates the nodal location of the load component.

$$\begin{bmatrix}
\frac{F_{x2}}{l} & 0 & 0 & 0 & 0 & 0 & -\frac{F_{x2}}{l} & 0 & 0 & 0 & 0 & 0 \\
 & \frac{6F_{x2}}{5l} & 0 & \frac{M_{y1}}{l} & \frac{M_{x2}}{l} & \frac{F_{x2}}{10} & 0 & -\frac{6F_{x2}}{5l} & 0 & \frac{M_{y2}}{l} & -\frac{M_{x2}}{l} & \frac{F_{x2}}{10} \\
 & & \frac{6F_{x2}}{5l} & \frac{M_{z1}}{l} & -\frac{F_{x2}}{10} & \frac{M_{x2}}{l} & 0 & 0 & -\frac{6F_{x2}}{5l} & \frac{M_{z2}}{l} & -\frac{F_{x2}}{10} & -\frac{M_{x2}}{l} \\
 & & & \frac{F_{x2}I_\rho}{Al} & -\frac{2M_{z1}-M_{z2}}{6} & \frac{2M_{y1}-M_{y2}}{6} & 0 & -\frac{M_{y1}}{l} & -\frac{M_{z1}}{l} & -\frac{F_{x2}I_\rho}{Al} & -\frac{M_{z1}+M_{z2}}{6} & \frac{2M_{y1}+M_{y2}}{6} \\
 & & & & \frac{2F_{x2}l}{15} & 0 & 0 & -\frac{M_{x2}}{l} & \frac{F_{x2}}{10} & -\frac{M_{z1}+M_{z2}}{6} & -\frac{F_{x2}l}{30} & \frac{M_{x2}}{2} \\
 & & & & & \frac{2F_{x2}l}{15} & 0 & -\frac{F_{x2}l}{10} & -\frac{M_{x2}}{l} & \frac{M_{y1}+M_{y2}}{6} & -\frac{M_{x2}}{2} & -\frac{F_{x2}l}{30} \\
 & & & & & & \frac{F_{x2}}{l} & 0 & 0 & 0 & 0 & 0 \\
 & & & & & & & \frac{6F_{x2}}{5l} & 0 & -\frac{M_{y2}}{l} & \frac{M_{x2}}{l} & -\frac{F_{x2}}{10} \\
 & & & & & & & & \frac{6F_{x2}}{5l} & -\frac{M_{z2}}{l} & \frac{F_{x2}}{10} & \frac{M_{x2}}{l} \\
 & & & & & & & & & \frac{F_{x2}I_\rho}{Al} & \frac{M_{z1}-2M_{z2}}{6} & -\frac{M_{y1}-2M_{y2}}{6} \\
 & & \text{Symmetric} & & & & & & & & \frac{2F_{x2}l}{15} & 0 \\
 & & & & & & & & & & & \frac{2F_{x2}l}{15}
\end{bmatrix} \tag{5.2}$$

Considering the tangent stiffness matrix as the sum of elastic and geometric stiffness matrices, Equation 5.1 then becomes:

$$\mathbf{\Delta P} = (\mathbf{K}_e + \mathbf{K}_g)\,\Delta\mathbf{U} \tag{5.3}$$

As this is an incremental process, for any step, i, Equation 5.3 can be expressed as:

$$\Delta\mathbf{P}_i = [\mathbf{K}_e\,(\mathbf{U}_{i-1}) + \mathbf{K}_g\,(\mathbf{U}_{i-1}, \mathbf{F}_{i-1})]\,\Delta\mathbf{U}_i \tag{5.4}$$

where $\mathbf{U}_{i-1}$ and $\mathbf{F}_{i-1}$ are the vectors of nodal displacements and internal loading, respectively, at the end of the previous loading step (i.e. the start of the current step).

Unlike the linear MSA analysis detailed in Section 4.3, the incremental analysis does not provide a unique exact solution and the solution will be dependent on the step sizes. To approximate the solution, either single-step, higher-order, or iterative methods can be used. Trialling of multiple solution approaches found the second-order Runge-Kutta mid-point approach to provide a good balance of computational efficiency and accuracy. In this approach, the tangential stiffness at the mid-point of the load increment is used to determine deflections and forces resulting from that increment.

To determine the size of each load increment, a method based on scaling the load increment with the level of nonlinearity was used [121]. This method uses the 'current stiffness parameter' which is a simple scalar term used to measure the level of nonlinearity at any given load step. The current stiffness parameter, S_i, is the ratio of the current stiffness to the stiffness found for the initial load increment. The load applied at each step is then found using:

$$\Delta\mathbf{P}_i = \Delta\mathbf{P}_1\,|S_i|^{\gamma} \tag{5.5}$$

where $\mathbf{\Delta P}_1$ is the initial load increment used for the first step and an exponent, γ, of 2 is used.

McGuire et al. [121] suggest using an initial load increment that is 10-20% of the expected failure load. An initial loading step that was 15% of the critical value predicted by the eigenvalue buckling analysis (later detailed in Section 5.5.4), was therefore used. The iterative process was halted once the current stiffness parameter drops below 0.1 (stiffness is less than 10% of the initial value), as this marks the point at which the truss stiffness is tending towards zero.

5.4.2 Effects of mesh density

Within the linear analysis detailed in Section 4.3, each member within the truss was represented by a single beam element. This coarse mesh was used as it minimised computational expense without affecting the accuracy of the analytical predictions. For the nonlinear analysis, the details of the local structural deformations are important and will affect the accuracy of the predictions. Therefore, using a finer mesh (higher mesh density) is necessary to capture the nonlinear response accurately. Increasing mesh density will, however, increase the number of calculations and therefore increase computational cost. Once again, a trade-off is presented between accuracy and computational expense.

The analysis was run at a range of mesh densities to determine an appropriate value for modelling of the nonlinear behaviour. In Figure 5.4a, the load-displacement graphs from the nonlinear analysis are plotted for mesh densities varying from 1 to 4 elements per member. In Figure 5.4b, the load at which the current stiffness parameter drops below 0.1 is plotted for the range of mesh densities, along with the corresponding analysis run time. Results here show how accuracy improvements from increasing mesh density are initially large, but are less significant at higher densities. The results in Figure 5.4b also show how increasing mesh density has an exponential effect on run time. From the results in the graphs, it was concluded that three elements per member provided a reasonable balance of speed and accuracy.

Figures 5.4a and 5.4b both show the effects of varying the mesh density of all the member types: shear, chord and joints. The joint members have a very low aspect ratio whose geometric nonlinearities are likely to be insignificant compared to those of the more slender chord and shear members. This, therefore, means

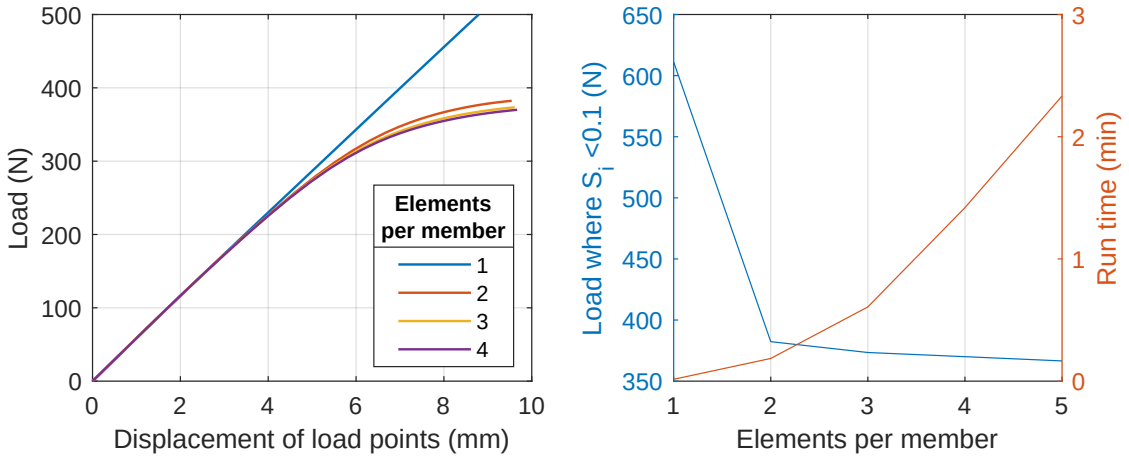

(a) (b)

Figure 5.4: Effect of mesh density on predicted nonlinear response. Configuration H66_1 truss at 792 mm span. a) load-displacement; b) maximum loading prediction and run time.

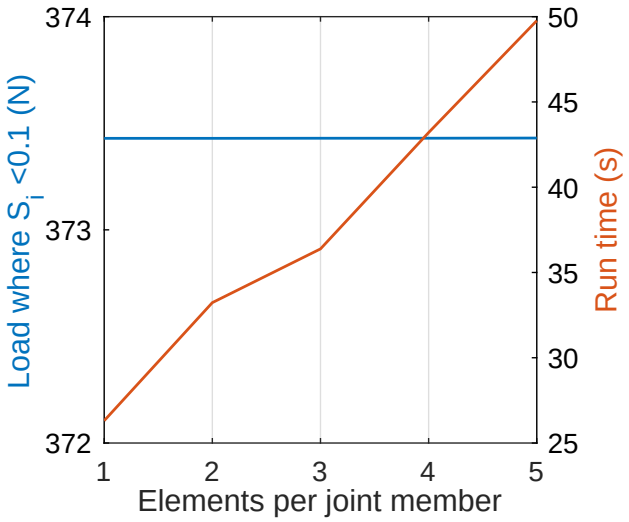

Figure 5.5: Effect of joint mesh density on nonlinear analysis accuracy and run time. Results generated for configuration H66_1 at 792 mm span.

that increasing the mesh density of the joints increases computational expense with minimal improvements to accuracy. To investigate the effect of joint mesh density, the nonlinear analysis was run using a mesh density of 3 elements per shear and chord member and a range of values from 1 to 5 for the joints. Results showing both the load where the current stiffness parameter approaches 0.1 and the run time are plotted in Figure 5.5. The results show the joint mesh density has essentially zero effect on accuracy but has a significant effect on run time. Therefore, using only one element per joint member is most appropriate.

Also worth noting from the results in Figures 5.4 and 5.5 is the significant increase in computational expense when attempting nonlinear analysis. For the linear analysis detailed in Chapter 4, the analysis run time was in the 10^{-1} seconds order of magnitude. The nonlinear analysis run times are seen to be two orders of magnitude larger than this. This large increase in run time therefore makes the implementation of the nonlinear analysis within an optimisation framework less attractive.

5.4.3 Verification with commercial FEA

To verify the correct functioning of the self-coded nonlinear analysis, equivalent models were built in the commercial FEA package, Abaqus. Again, the FEA models used shear deformable beam elements (B32). Abaqus' nonlinear geometry was enabled to allow prediction of nonlinear effects. For both the MSA and FEA models, mesh density was set at 3 elements per chord and shear member, and 1 element per joint.

In Figure 5.6, predictions from the nonlinear analysis tool are compared to those from equivalent models built in Abaqus. Here three of the truss configurations

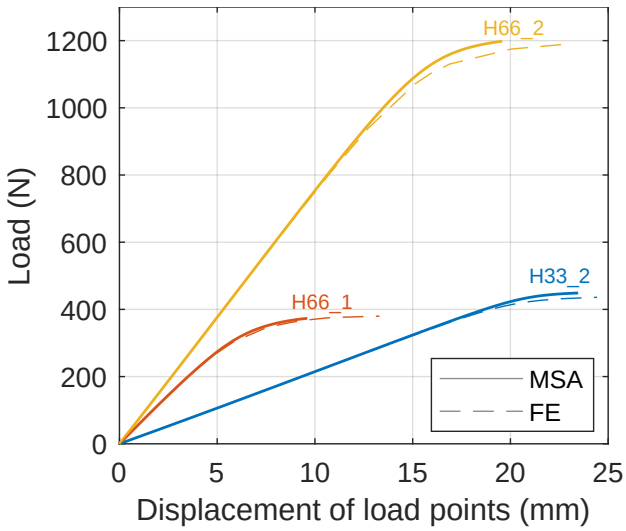

Figure 5.6: Comparison of nonlinear MSA tool with commercial FEA. All configurations modelled under three-point bending at a span of 792 mm.

from Section 4.4 are analysed under the three-point bending loading case at a span of 792 mm. For all configurations, the FEA and MSA tool show very similar results. The slight differences observed, particularly in configuration H66_2, may come from the different nonlinear solution methods used. Abaqus uses an iterative solver whereas the MSA uses a second-order Runge-Kutta solver. Results here show effective functioning of the nonlinear analysis tool. The key advantage of this tool over the commercial package is that it is designed to seek the load where stiffness tapers to zero and is therefore more useful for failure analysis.

5.5 Failure prediction

In Section 5.3 the likely failure mechanisms of WrapToR trusses were identified and discussed. Within this section, the methods developed and used to predict those failure mechanisms that are most likely to occur are detailed. These are grouped into member material failure, joint failure, and buckling. The methods used for member and joint failure both rely on an estimation of the critical stress (strength). The method used to predict the relevant strengths is detailed in Section 5.5.3.

5.5.1 Member material failure

As is discussed in Sections 5.3.1 and 5.3.2, failure of the WrapToR members, chord and shear, can occur through a variety of mechanisms. Developing models to predict each of these individual mechanisms would be a large task that is beyond the scope of this thesis. To simplify failure prediction, these mechanisms are grouped under the general term: material failure. Maximum stress criteria are then used to

approximate failure loads due to tensile, compressive, and shear stresses.

To assess failure using maximum stress criteria, the first step involves extracting member stresses from the analysis tool. Axial and shear stress were determined by dividing the relevant element force by the member area. Member stresses due to bending were determined using engineers bending equation:

$$\sigma_b = \frac{My}{I} \tag{5.6}$$

where M is the element's internal moment, and I is the relative axis second moment of area. y is taken as the point furthest from the element neutral axis, as this will be the point of maximum stress. In this scenario, y is equal to the member radius.

Failure due to loading interaction was investigated using the Tsai-Hill criterion. As the WrapToR members are treated as unidirectional fibre reinforced beam members, the transverse force can be neglected. Removing terms related to transverse stress, the Tsai-Hill criterion is reduced to:

$$\left[\frac{\sigma_1}{\sigma_1^*}\right]^2 + \left[\frac{\tau_{12}}{\tau_{12}^*}\right]^2 < 1 \tag{5.7}$$

where σ_1 and τ_{12} are the normal stress and in-plane shear stress, respectively. σ_1^* and τ_{12}^* are the corresponding material strengths.

Initial failure analysis using generic material strength values revealed that the shear stresses within the members are small relative to the normal stresses, meaning they have a small contribution to failure predicted by the Tsai-Hill criterion. In Table 5.2 material failure predictions using generic CFRP material properties [135] show how considering material failure interaction of normal and shear stress has minimal effect compared to consideration of normal stresses alone. As the truss members are slender beams, it is not surprising that the shear forces have minimal influence. From the results in Table 5.2, it was concluded that material failure due to interaction of shear and normal stresses could be neglected. Therefore, in the later failure analysis and optimisation work, member material failure will only consider normal stresses.

Determining of material strengths was also necessary for the implementation of the maximum stress criteria predictions. As is discussed in Chapter 3, determining the material strength properties of the WrapToR truss members through material testing was found to be difficult. Therefore, an alternative means of determining the member strengths was required. For the WrapToR member, where possible strengths were taken from experimental results using the method later detailed in Section 5.5.3. Where this was not possible generic material data was used.

Table 5.2: Comparison of member material failure criteria. Generic material strength data used : $\tau_{12}^{*} = 63\text{MPa}$; $\sigma_{1}^{*} = 1130\text{MPa}$ [135]. All configurations analysed under three-point bending at 796 mm span.

Configuration	Predicted truss failure load due to material failure (N)		
	Normal stress only	Normal and shear stress (Tsai-Hill)	% difference
H33_1	393.5	390.9	-0.7
H33_2	368.9	366.4	-0.7
H66_1	580.6	579.8	-0.1
H66_2	861.8	851.4	-1.2
H99	2121.7	2096.7	-1.2

5.5.2 Joint member failure

As discussed in Section 5.3.3, failure of the truss joints is likely to be difficult to accurately predict due to the complex geometry and stress state. To allow predictions of joint failure, assumptions were made relating to both the joint geometry and stress state. It was assumed that the forces experienced at the joint are primarily shear acting along the truss beam length axis. This assumption was made because while tested under bending, the attached shear members have similar magnitude axial forces that on one side are in tension and on the other in compression. Forces generated perpendicular to the beam axis therefore cancel and the resultant force acts along the beam axis creating shear stresses in the joint. To predict failure due to this shear loading, again a maximum stress criterion was employed. Estimation of the shear stress on the joint is however not straight forward, as the joint area that carries the shear loading is not clearly defined. To approximate the joint area, a geometric model was produced and validated against the joint area measurements taken in Section 3.4. The shear stress in the joint was then assumed to be equal to the joint area divided by the approximated shear force.

A geometric model of the joint region was developed to predict the joint area. Full detailing of this model is given in Appendix G, and in this section a summary of the model and its results are given. The geometric model developed to approximate joint area, referred to hereon as the joint area model, is based on approximating the joint region to a cross-shape formed of two overlaid parallelograms. This cross shape, seen in Figure 5.7, represents the overlapping of the shear member tows on the tube surface at a joint. The area of this approximated cross-shape depends on three parameters: winding angle, θ_w, the joint height, h_j, and the width of the tow, w_t. The joint height depends on the tube diameter and proportion of the tube circumference around which the joint extends. The width of the tow at the joint is approximated to be the diameter of the tow multiplied by a 'spread factor'. This factor represents how much the tow spreads out when it contacts the chord surface.

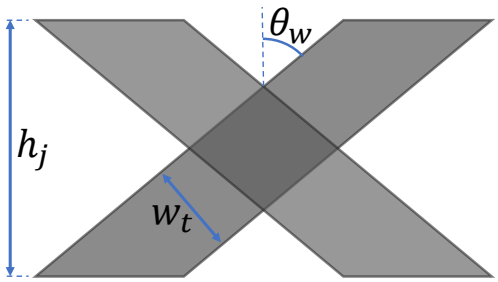

Figure 5.7: Cross-shape used in joint area model to approximate joint region.

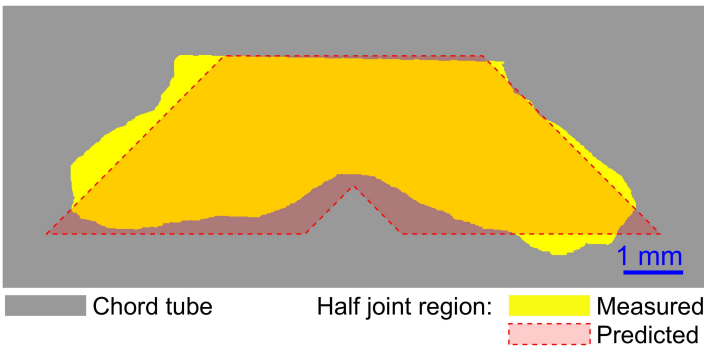

Figure 5.8: Surface area plot of half joint comparing measured region with prediction from joint area model. Configuration 3_24k displayed (detailed in Section 3.4.1).

Through experimental fit with the joint area measurements taken in Section 3.4, this factor was found to be 2.6. In Figure 5.8, the predicted joint region shape is overlaid onto the surface area of an example measured half joint.

In Section 3.4, the area of truss joints were measured for eight truss configurations using a digital imaging technique. To assess the efficacy of the developed joint area model, it was compared to the previously acquired area results. Across all the configurations the MAPE was found to be 6.9% with a maximum percentage error of -16.4%. In Figure 5.9 the mean measured joint areas are plotted with predictions from the model at varying winding angle and shear member diameter. In Figure 5.9a it is seen that the model predicts an increase in joint area with increasing winding angle that is similar to the measured results. It should be noted here however that significant variation is observed in the experimental results due to the large inconsistency in the observed joint architecture. Figures 5.9b and 5.9c show the effect increasing shear member radius on predicted joint area for 4 and 5 mm tubes, respectively. Here again, the model appears to capture the trends observed experimentally, however large variation in the measured joint areas makes a robust assessment difficult.

Once the area was predicted using the above described model, the shear stress in the joint was approximated by extracting the resultant shear force from the analysis tool developed in Chapter 4. The additional joint elements used in the eccentric

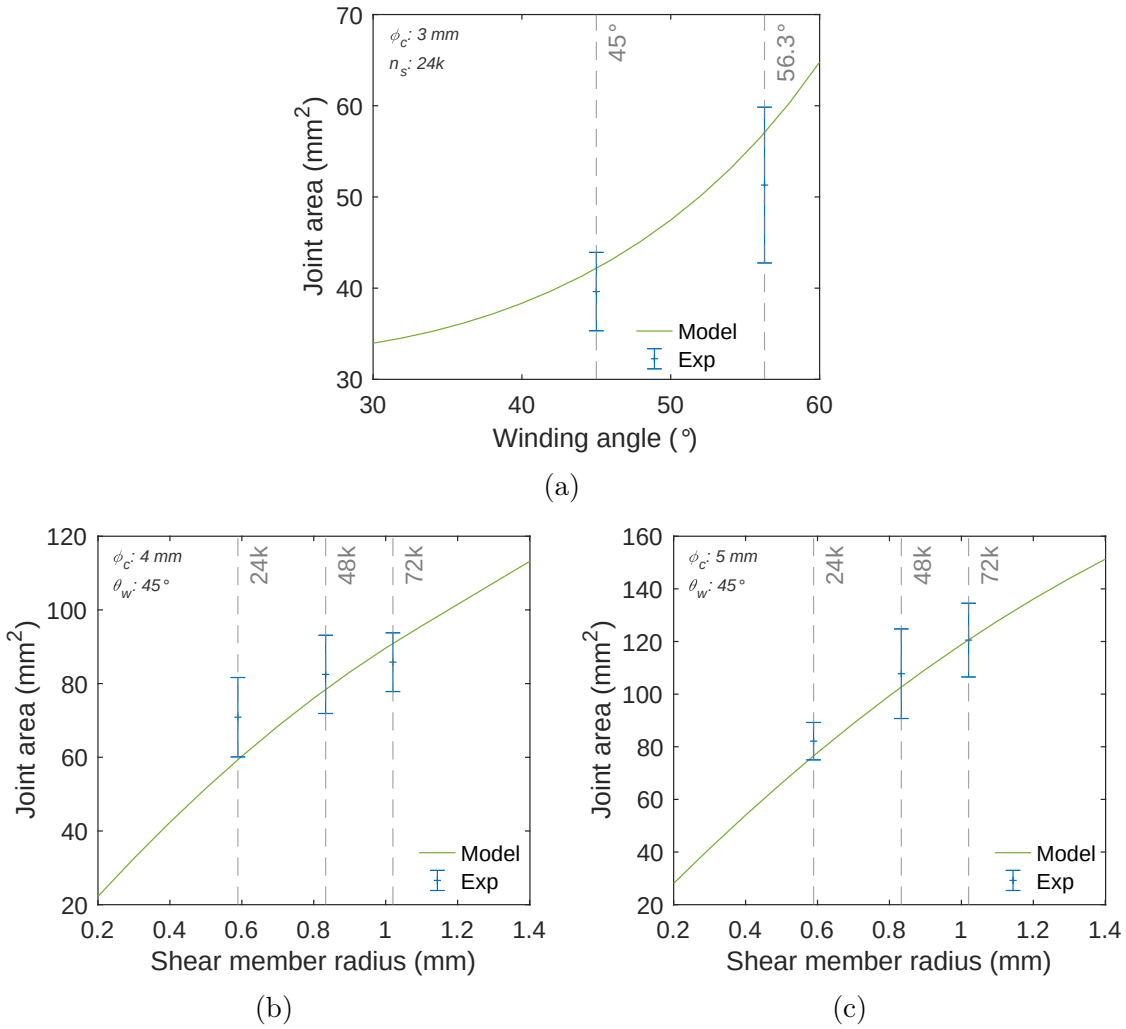

Figure 5.9: Joint area model predictions at varying: a) winding angle for 3 mm tube and 24k tow; b) shear member radius for 4 mm tube; c) shear member radius for 5 mm tube. Results are compared to areas measured in Section 3.4. Error bars denote one standard deviation.

model were useful here for identifying the forces specifically located at the joint. The shear force given by the analysis tool was divided by the predicted joint area to give the stress. This stress was then compared to a critical value to assess if failure would occur. The joint shear strength was again approximated from experimental truss test data using the method that is later detailed in Section 5.5.3.

5.5.3 Estimation of member and joint strengths

Prediction of member and joint failure using maximum stress criteria requires knowledge of the member and joint strengths. Where possible, for each failure mechanism strengths were approximated experimentally using the critical load data from full truss beam tests. The experimentally observed critical load were then fed into the analysis tool to estimate the stress in the members at failure. The predicted stress

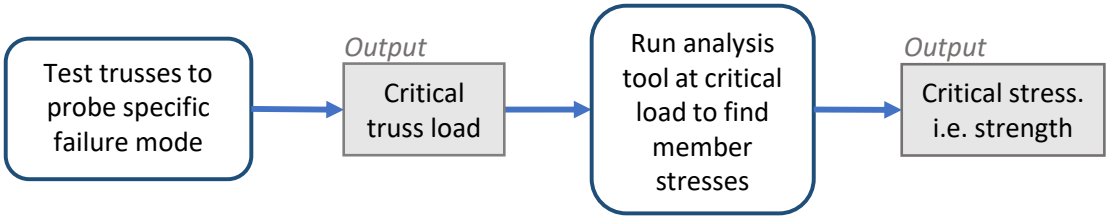

Figure 5.10: Function diagram showing method used to estimate member and joint strength values.

within the failed member was then taken to be the strength. A summary of this method is displayed in Figure 5.10. Multiple truss configurations were tested to target each strength value, with the mean being taken as the final strength value. Where it was not practical to determine the strength through experimental means, generic strength values for carbon fibre reinforced epoxy were used. The values determined using this method are presented and discussed with the results in Section 5.7.1.

5.5.4 Buckling

5.5.4.1 Linear eigenvalue buckling analysis

To predict both global and local buckling models, linear eigenvalue analysis was added to the MSA tool. Linear eigenvalue buckling analysis is well developed within the literature [121, 122, 136] and is based on solving of the following equation that is written in the standard eigenproblem form:

$$(\mathbf{K_e} + \lambda \mathbf{K_g})\mathbf{v} = 0 \tag{5.8}$$

where the eigenvectors, $\mathbf{v}$, relate to buckling mode shapes and the eigenvalues, λ, denotes the scalar factor by which the applied loading must be multiplied to induce that mode. The critical loading therefore relates to the minimum eigenvalue, λ_{min} and the applied reference loading, $\mathbf{P}^*$ such that:

$$\mathbf{P}_{crit} = \lambda_{min}\mathbf{P}^* \tag{5.9}$$

By determining the minimum eigenvalue associated with Equation 5.8 the critical buckling load can therefore be determined. Matlabs "Eigs" function was utilised to solve the eigenproblem in Equation 5.8, with the elastic and geometric stiffness matrices determined using the methodology detailed in Sections 4.3 and 5.4.1. To account for the boundary conditions, the rows and columns within the stiffness matrices associated with fixed DOFs are altered; the associated off-diagonal terms are set to zero, and the diagonal terms to one.

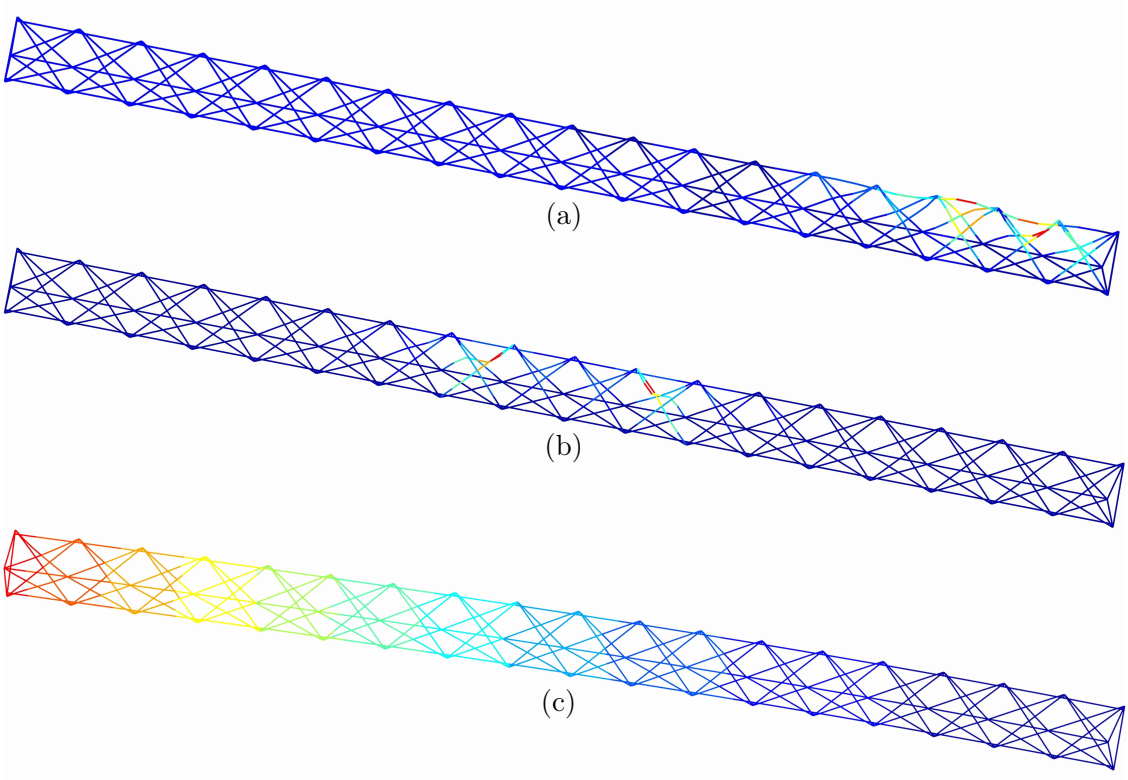

Figure 5.11: Buckling modes of 18 bay H66_1 truss under three loading scenarios: a) Three-point loading; b) Cantilever; c) Axial compression.

5.5.4.2 Effects of mesh density

To capture the buckling mode shapes, a finer mesh than the 1 element per member used in Section 4.3 was required. As is the case with the nonlinear analysis in Section 5.4, a finer mesh will result in more accurate predictions at the cost of computational expense. The analysis was therefore run at a range of mesh densities to determine the most appropriate value for capturing the buckling behaviour.

Again, as was observed for the nonlinear analysis in Section 5.4.2, the mesh density of the joint members did not affect the predicted response, but did have a significant effect on analysis run time. Mesh density of the joints was therefore held constant at 1 element per joint. To investigate the effect of chord and shear member mesh density on the buckling prediction, three test cases were selected that probe different buckling mode shapes. The three test cases involve the same 18 bay, H66_1 truss, loaded under three different scenarios. To target local buckling of the shear members, three-point bending was used. Cantilever loading was used to target local chord member buckling and axial compression to target global buckling. These three buckling mode shapes are plotted in Figure 5.11.

Plotted in Figure 5.12a are the critical buckling loads predicted for various mesh densities normalised by the value predicted for a fine mesh (10 elements per member). In Figure 5.12b the corresponding run times are plotted. The results show that 1

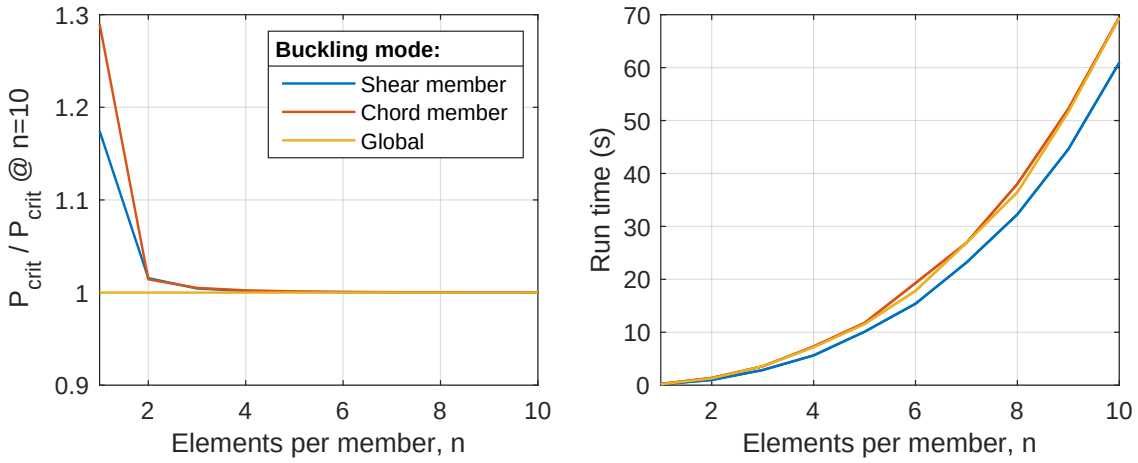

(a) (b)

Figure 5.12: Effects of mesh density on buckling predictions. Results for analysis of H66_1 truss at 1,188 mm span under three-point, cantilever and column compression loading.

element per member is insufficient to capture the buckling response. Increasing the mesh density has a large initial effect which quickly tapers off. The results also show that mesh density has an exponential effect on run time. From the sweep of mesh densities, it was again concluded that 3 elements per member provides a reasonable balance of accuracy and speed.

5.5.4.3 Verification with commercial FEA

The linear buckling analysis was compared to equivalent models built within Abaqus for verification of the Matlab code. Models were built for the same truss configuration and three load cases used in Section 5.5.4.2. Mesh densities of 3 elements per chord and shear member and 1 element per joint member were used in both the FEA and MSA models. Results displayed in Table 5.3 show that the MSA predictions are within 4% of that of the commercial FEA package, for all the tested scenarios. The mode shapes predicted were also seen to match those of the MSA tool displayed in Figure 5.11.

Table 5.3: Comparison of MSA linear buckling analysis function with commercial FEA. 18 bay H66_1 truss.

Buckling mode	Load case	P_{crit} (N)		
		MSA	FE	% diff
Shear member	Cantilever	128.0	125.55	-1.9
Chord member	Three-point	297.6	287.0	-3.6
Global	Axial compression	2353.8	2356.8	0.1

5.6 Experimental validation methodology

To validate the failure prediction methods discussed in the previous section, a range of truss test configurations were selected to probe the key failure mechanisms. These tests were all conducted using the three-point bending method detailed in Section 3.5. A majority of these tests used the truss configurations developed in Section 4.4 at spans specifically selected to target the various mechanisms. Previous test results acquired during the tow twisting investigation in Section 3.6 were also used for validation.

The test cases used for failure prediction validation are displayed in Table 5.4. For each configuration at least three truss samples were tested. During the tow twisting investigation in Section 3.6, testing of configuration H33_1 trusses at 396 mm span found a mixture of both joint and chord member failure. To probe each of these mechanisms individually, the same truss configuration, H33_1, was tested at three longer and three shorter spans. Four truss configurations previously used in Section 4.4 were tested to failure to probe the various mechanisms. To target chord member failure in larger tube sizes, configurations H50_D4 and H50_D5 were tested at a long span of 891 mm. H33_2 trusses were tested to target joint failure in a different joint configuration. Two new truss configurations, H36_1 and H36_2, were designed to probe shear member failure in 24k and 48k tow trusses. The geometric parameters of these two new configurations are detailed in Section 5.5. For detailing of the other truss configuration geometric parameters, see Table 2.1.

Table 5.4: Test cases for failure prediction validation. Failure locations are listed in order of frequency observed.

Truss	Test Span		Failure location	
configuration	(mm)	Bays	Targeted	Observed
H33_1	198	6	Joint	Joint, shear
H33_1	264	8	Joint	Joint, shear
H33_1	330	10	Joint	Joint
H33_1*	396	12	Joint	Joint, chord, shear
H33_1	594	18	Chord	Chord, joint, shear
H33_1	792	24	Chord	Chord, joint
H33_1	990	30	Chord	Chord, joint
H50_D4	891	18	Chord	Chord, joint
H50_D5	891	18	Chord	Shear, joint, chord
H66_1*	792	12	Shear	Shear (non-linear)
H33_2	297	6	Joint	Joint, shear
H36_1	288	8	Joint	Shear, joint
H36_2	288	8	Shear	Shear, joint

**configurations previously tested to failure in Section 3.6.*

Table 5.5: Truss configurations designed to target shear member failure.

Truss configuration ID	Truss height, H (mm)	Chord tube diameter, (mm)	Chord tube wall thickness (mm)	Winding angle, θ (°)	Shear member tow size	Mass per unit length (g/m)
H36_1	36	5	1	45	24k	69.4
H36_2	36	5	1	45	48k	82.2

Table 5.4, also shows the failure modes observed during testing of each configuration. While these results will be discussed in Section 5.7, it is worth noting here how for most configurations failure was observed in more than one member type and that trusses tended to fail in more than one location. This is unsurprising as once a critical member or joint fails, its load will be transferred to another region resulting in subsequent failure. During some of the tests, a Photron SA-Z high-speed camera was used to attempt to capture the location of initial failure. Due to the small field of view of the camera, capturing the exact failure location was difficult.

5.7 Results and discussion

In Table 5.4, the observed failure locations are given for each configuration. In a majority of tests, failure was seen to occur in multiple locations. Where multiple failure locations were observed, they are listed in order of the frequency that they occurred. As was predicted in Section 5.3, chord failure was confined to members that were subject to axial compression and joint failure predominately occurred in the upper truss joints. In the following section, the test results are initially used to estimate the component strengths. Failure results relating to joint and member failure are then compared to model predictions in Section 5.7.2. The nonlinear analysis code is then assessed against the experimentally observed nonlinear response of configuration H66_1 in Section 5.7.3.

5.7.1 Member and joint strengths

The critical truss loadings found from the failure tests were first used to approximate the strength of the truss members and joints using the method detailed in Section 5.5.3. The shear and chord member compressive strengths, and the joint shear strength were all found using this method. The targeted member stresses estimated by the WrapToR analysis tool at the observed failure loads are plotted in Figure 5.13. Also plotted in the graphs is the mean critical stress value that was used as the corresponding strength.

The mean stress observed for the chord members (Figure 5.13a) was 47% larger than that for the shear members (Figure 5.13b). The quality of the pre-assembled

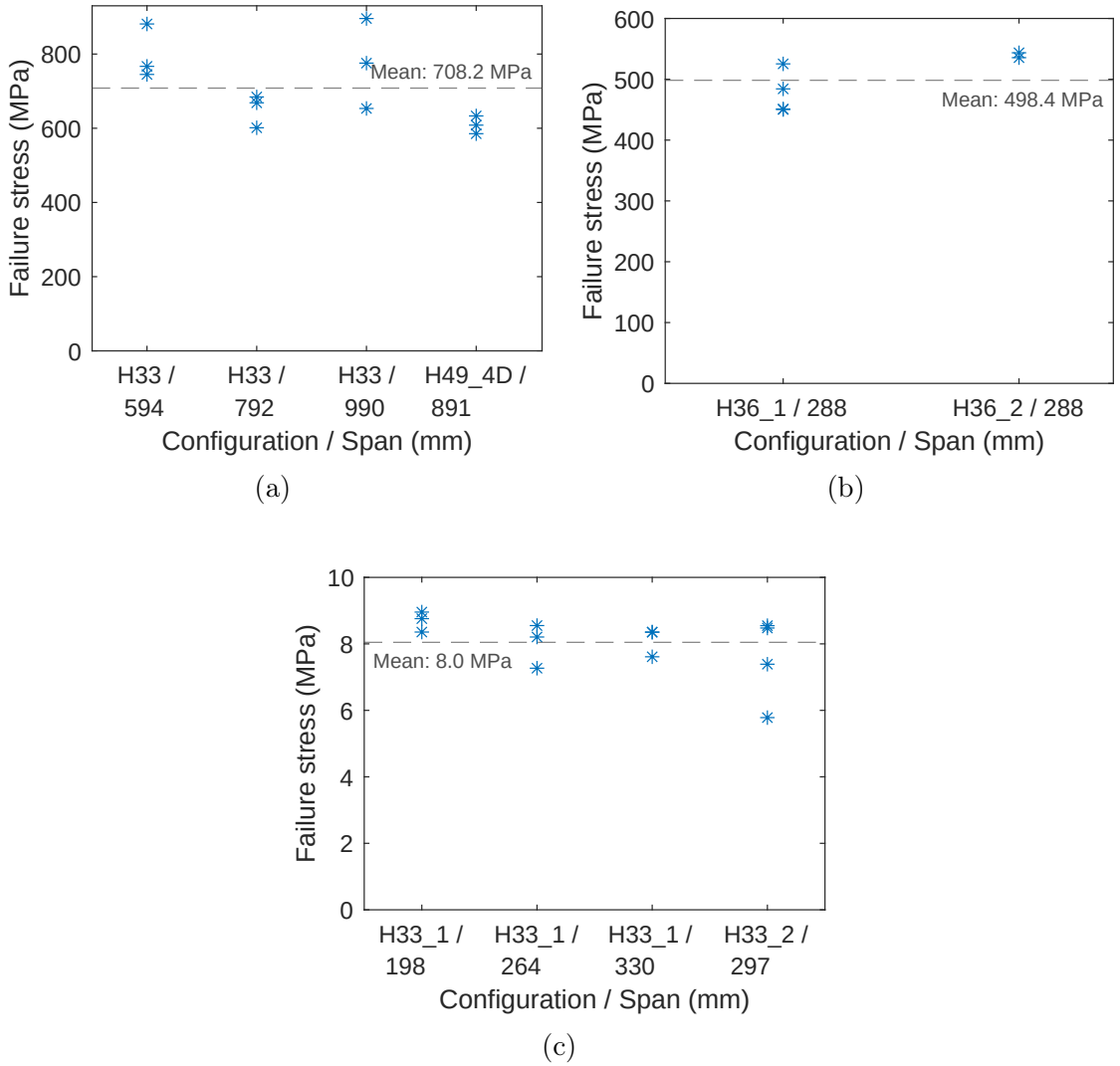

Figure 5.13: Predicted stresses at measure critical truss loading's in: a) chord members; b) shear members; c) joints.

chord member tubes is likely to be substantially better than the wound shear members which were observed in Section 2.5 to have significant void content and variability.

The mean critical shear stress measured in the joints in Figure 5.13c is seen to be on the lower end of what would be expected for an epoxy resin. The joint debonding witnessed during testing typically occurred at the interface of the chord member fibres and its outer layer of resin. This suggests the shear strength at this interface is lower than in the epoxy itself. Additionally, the method used to predict the shear stresses in the joints at failure assumes that only shear stress exist. While shear forces are suspected to be dominant, other stresses, such are tension or peel, are also likely to exist.

Where the stresses could not be determined from the experimental results, generic properties were taken from [135]. The strengths for which generic properties were

Table 5.6: Strength values used.

Member	Strength (MPa)		
	Tensile	Compressive	Shear
Chord	1270*	708.1	63*
Shear	1270*	498.4	63*
Joint	-	-	8.0

**generic properties taken from [135].*

used relate to failure mechanisms which are unlikely to occur in the trusses, such as tensile failure of the chord or shear members. The final strength values used within the model are summarised in Table 5.6.

5.7.2 Joint and member failure

A variety of failure mechanisms were observed during testing of the truss configurations detailed in Table 5.4. In Figure 5.14, images of the two main mechanisms observed in the chord members are displayed. These two chord member mechanisms consistently occurred in one or both of the central compressive chord members where axial stresses due to beam bending moments are highest. The first mechanism, shown in Figure 5.14a, was the most prevalent and is characterised by a longitudinal splitting of the unidirectional tube. As discussed in Section 5.3, longitudinal splitting occurs in unidirectional tubes under bending loads due to the relatively low transverse strengths. The second, shown in 5.14b, could be described as more typical composite compression failure. Several trusses were seen to fail due to a combination of the two mechanisms.

Example images of the observed shear member failure mechanisms are displayed in Figure 5.15. The most commonly observed was a clean fracturing of the compressive member, as is seen in Figure 5.15a. The second involved a collapsing of the member without complete fracture that was often coupled with a debonding of the shear members at the central cross-point; as is seen in Figure 5.15b. It is possible that the debonding of the central cross-point occurred first resulting in increased member length and bending moments causing the members to fail. This failure sequence was however not captured via high-speed camera as the exact failure location was unpredictable. The location of both the shear member failure mechanisms varied along the length but only ever occurred in axially compressed members.

Failure of the joints predominately occurred along the upper chord member in what appeared to be a shearing of the shear member tow from the tube surface. This mechanism, seen in Figure 5.16a, was observed at varying locations along the upper chord member and commonly occurred in multiple joints. The high frequency of occurrence of joint failure highlights the importance of joint integrity to struc-

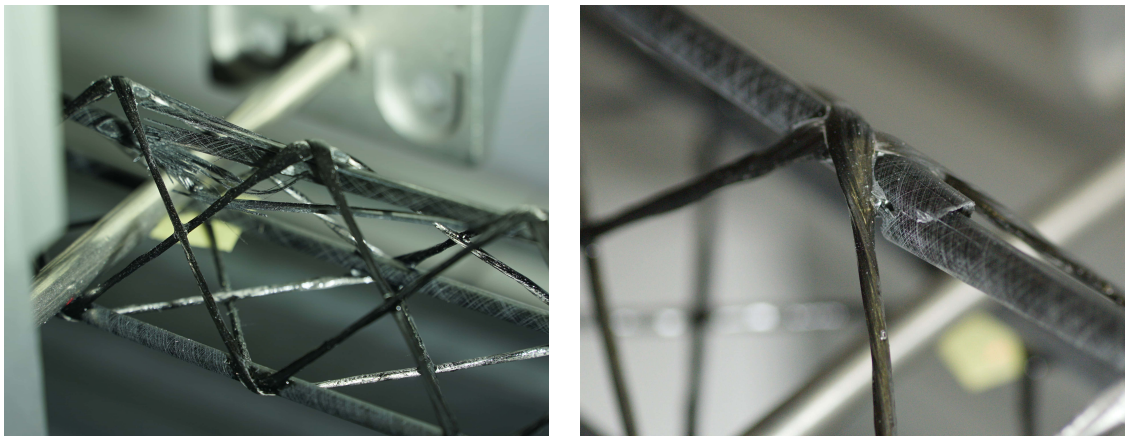

(a) (b)

Figure 5.14: Failure observed in chord members under axial compression: a) tube splitting; b) compression failure.

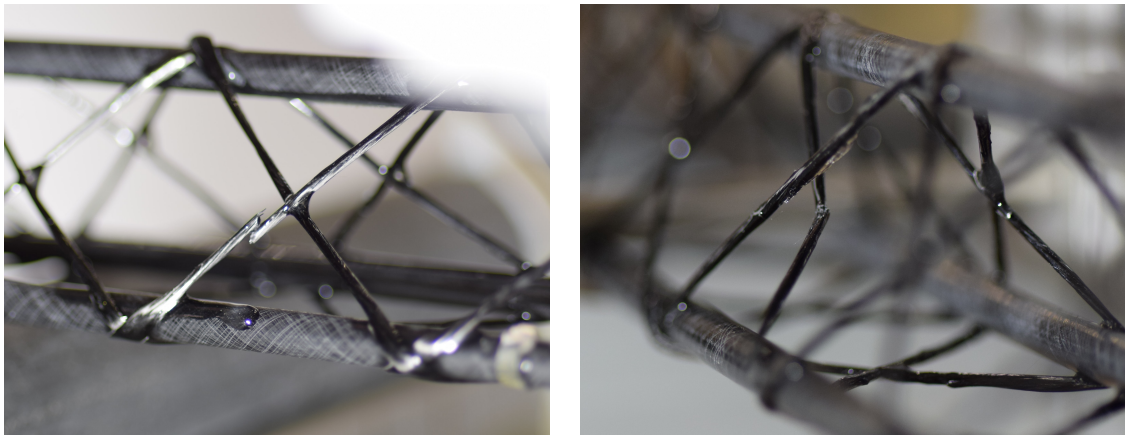

(a) (b)

Figure 5.15: Failure observed in shear members under axial compression: a) strut fracture; b) cross-point de-bond..

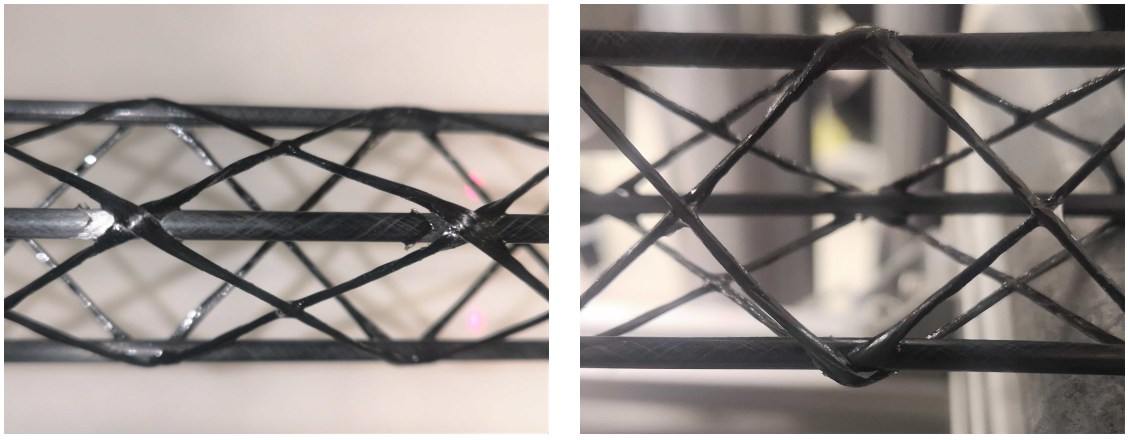

(a) (b)

Figure 5.16: Joint failure: a) shearing of upper joints; b) debonding of lower joint.

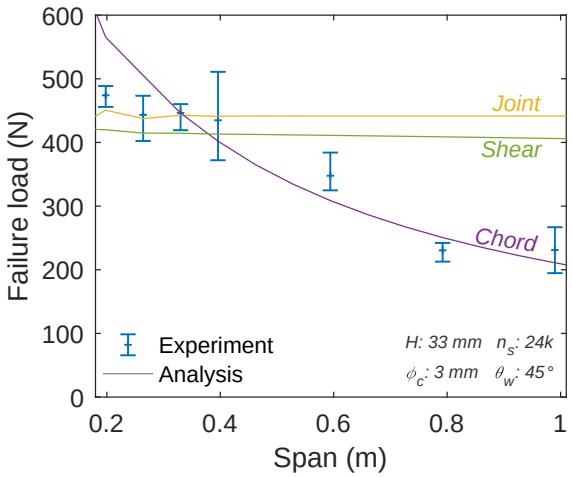

Figure 5.17: Failure predictions and experimental results of configuration H33_1 at varying spans. Error bars denote experimental range of three values.

tural performance. Stitching of the joints is a method that has been used by other researchers to improve joint performance. Several studies on the Isotruss® and Isobeam have used a Kevlar overwrap for both joint reinforcement and member consolidation [59, 65, 69]. While this has been shown to improve structural performance [60, 63], it appears to have been manually applied, significant increasing manufacturing labour requirements. Should joint stitching be investigated for the WrapToR technology, an automated process would be preferred.

In a small number of cases, failure occurred in a joint along a lower chord member, as is seen in Figure 5.16b. This mechanism is characterised by the peeling of a single shear member strand and only ever occurred along with other mechanisms. The mechanism likely occurs due to combined loading at the joint and is also dependant on more detailed joint geometry than is provided in the WrapToR analysis tool. The failure prediction methods developed here are therefore not capable of predicting this mechanism. While future work may require further investigation of this mechanism, it was deemed of minimal concern here due to its infrequent occurrence.

All other failure modes observed during testing were predicted using the maximum stress criteria detailed in Section 5.5. The predicted failure stresses seen in Figure 5.13 fell within 14% of the mean stress for all configurations (except H50_D5, discussed later) suggesting the utilised maximum stress criteria can provide a reasonable estimate of failure load. To accurately predict each specific mechanism, higher fidelity failure criteria would be required.

The failure prediction methods were assessed through a series of parameter sweeps that investigate how both the failure load and mode would be expected to vary across different truss configurations. Experimental results that fall within these parameter sweeps were compared to the predictions. In Figure 5.17, failure predictions for truss configuration H33_1 are plotted for a range of three-point

bending test spans. Plotted are predictions of chord and shear member compressive failure and failure due to joint shearing. Also plotted are the experimental results from testing of the truss configuration at seven spans. The analysis predicts that the truss span has minimal effect on the load at which both joint and shear member failure occurs, but has a substantial effect on the load at which chord member failure occurs. This can be explained by considering the chord members to primarily carry the beam bending load, and the shear members to carry the shear load. The shear load is independent of truss length, whereas the beam bending moments will increase with span. Analysis predicts that at spans lower than 0.4 m, failure load is independent of span and occurs due to compressive failure of the shear members. While shear member failure was observed in the tested shorter span trusses, joint failure was witnessed in a higher proportion of samples. When increasing above 0.4 m, failure is predicted to transfer into the chord members, and the critical load decreases; a trend that is observed within the experimental results. At spans above 0.4 m, failure predominately occurred due to chord member compression, however

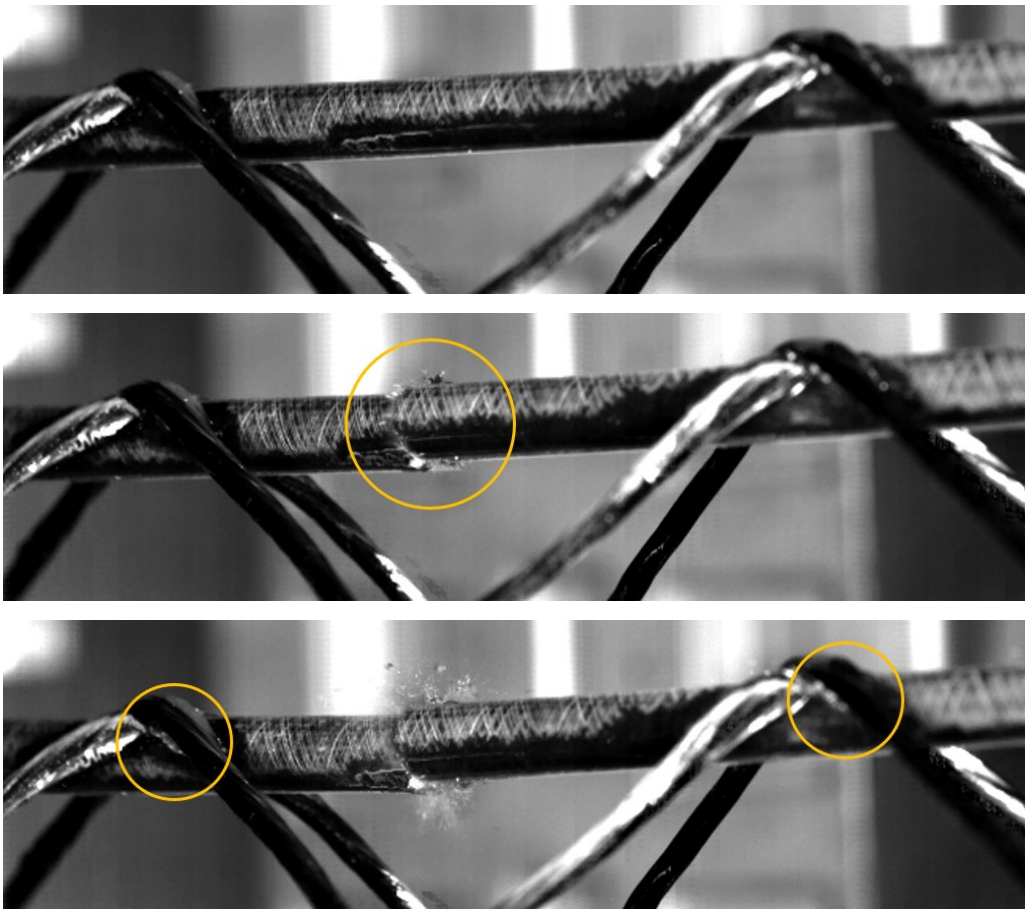

Figure 5.18: High speed video frames showing failure progression in H50_D5 truss. Sequence shows initial chord member failure followed by joint debonding. Failure features are highlighted.

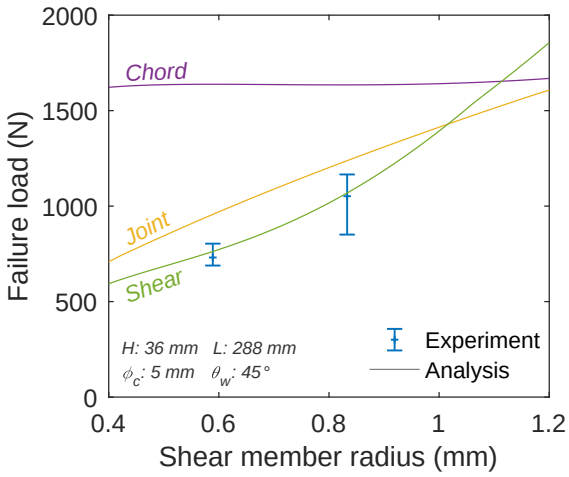

Figure 5.19: Failure predictions and experimental results of configurations H36_1 and H36_2 at 288 mm span with varying shear member radius. Error bars denote experimental range of three values.

in most samples, joint failure was also observed. While it is difficult to conclude that chord member failure occurred first in each of these samples, high-speed video footage was captured during testing of other configurations that showed failure initiating in the chord member. Still images taken from this high-speed video are displayed in Figure 5.18; note the appearance of the debonding fracture line (light grey) at the shear web to chord member interface in the third frame. As is seen in Table 5.4, H33_1 trusses tested at a span of 396 mm were seen to fail via all three mechanisms, suggesting the transition point predicted by the analysis is a reasonable approximation.

To investigate the effects of shear member radius on the failure predictions, the analysis was run for a range of shear member sizes while keeping all other parameters fixed to those of configurations H36_1 and H36_2. The results of this sweep are plotted in Figure 5.19, along with the experimental results of the two relevant configurations. Here, as would be expected, increasing shear member size is seen to increase shear member failure load. It also increases the load at which joint failure occurs; this is because within the model, joint area is directly affected by the shear member size. The two plotted experimental cases of truss configurations H36_1 and H36_2 were designed to target failure within the shear members. From Table 5.4, it is seen that failure in these samples occurred predominately in the shear members and also included some failure at the joints. In Figure 5.19, failure in these samples was predicted effectively by the analysis. A significant variance in the failure loads of H36_2 samples was observed due to two of the samples failing at a lower load via joint debonding. It was seen in Section 3.4, that the consistency of the joints is poor and that large variance in joint area exists. It is therefore possible that poorly formed joints caused this unexpected joint failure. These results highlight

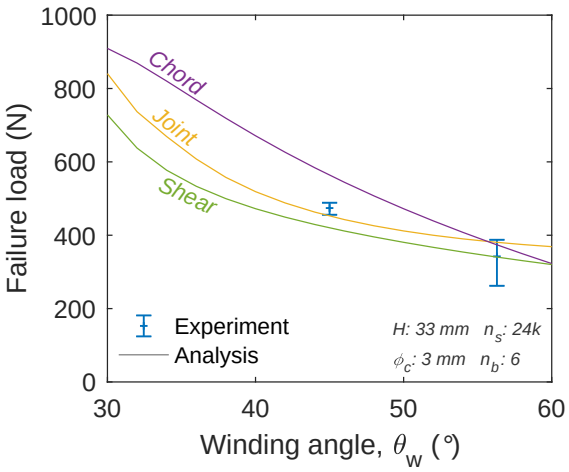

Figure 5.20: Failure predictions and experimental results of configurations H33_1 and H33_2 at a test span of 6 truss bays with varying winding angle. Error bars denote experimental range of four values.

the need to improve the consistency of the truss joints as it appears to have a direct effect on structural performance.

In Figure 5.20, failure predictions over a range of winding angles are shown for truss analyses where all other parameters are held constant at those for configurations H33_1 and H33_2. These analysis runs were all conducted with a span of 6 bays. Fixing the number of bays means that increasing the winding angle produces an increase in truss length. This increase in length, in-part, explains why the predicted chord member failure load decreases with increasing winding angle. Additional to this increase in overall truss length, the length of the chord members between supporting joints also increases with winding angle, resulting in larger internal moments. The unsupported length of the shear members also increases with the winding angle, causing the predicted failure load to decrease.

An unexpected result observed in Figure 5.20, is that joint failure load decreases with increasing winding angle. The winding angle has a positive effect on the joint area, and would therefore be expected to have a positive effect on the joint failure load. Inspection of the joint element forces predicted by the model revealed that the shear forces within the joints are higher at lower winding angles. As the shear members become more aligned to the chord members, the component of their axial force acting parallel to the chord member is increased. It is these components of the axial forces that generate the joint shear forces. The increase in joint shear forces outweighs the increase in joint area resulting in the observed drop in failure load.

The two configurations plotted in Figure 5.20 are H33_1 and H33_2 tested at spans of 198 and 297 mm, respectively. Both configurations predominately failed through the targeted mechanism of joint failure, but significant shear member failure was also witnessed. The analysis, however, predicts that shear member failure will

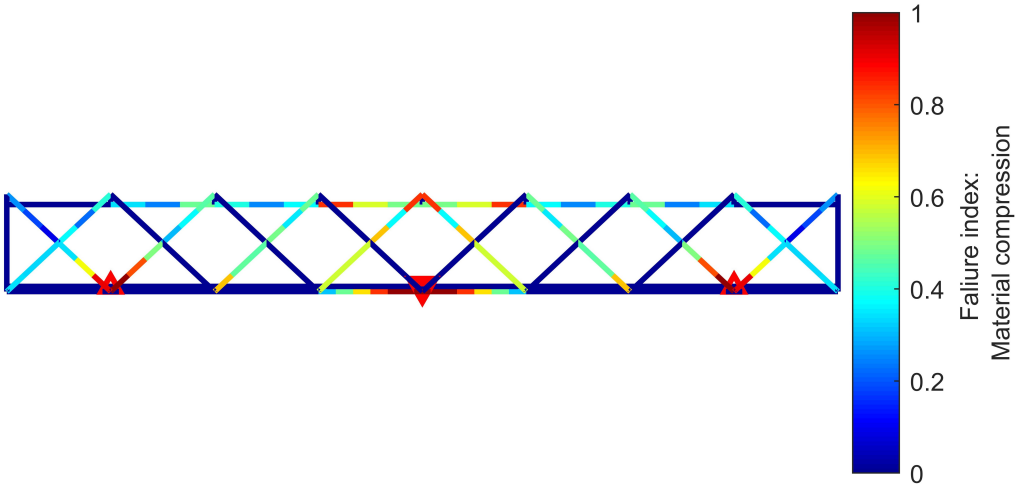

Figure 5.21: Contour plot showing failure indices in members due to material compression failure. Configuration H33_1 at 198 mm span. Red triangles denoted boundary condition and loading points.

be the critical mode in these test samples. This is similar to the results observed in Figure 5.17, where samples that predominately failed in the joints are predicted by the analysis to fail in the shear members. When inspecting the failure location predicted by the analysis tool, two equally critical regions are identified; these can be seen in the failure index contour plot in Figure 5.21. The first is located in the compressive shear member directly adjacent to the supports. Failure in this region was indeed witnessed in several truss samples. The second critical region is located on the lower truss surface close to the central loading points. During testing, no failure was observed in this region. The compressive stresses predicted in these lower shear members are primarily due to bending, as the axial forces experienced are relatively low. It was seen in Section 4.5.3.2, that validation of the models ability to predict shear member strains was difficult and that only the axial strain within the members could be assessed. It is therefore possible that the model does not produce accurate predictions of bending strain within the shear members. It is also possible that friction between the steel loading pin and the two truss load points restricts deformations at the truss centre and therefore reduces the bending moments in the lower shear members. Running the analysis with additional boundary conditions that fix the lateral translation of the two load points results in a substantial reduction of bending in the lower shear members.

The final parametric sweep of failure predictions looks at the effects of varying chord member diameter. In Figure 5.22, failure predictions are plotted at varying chord member diameter, with all other parameters fixed to those for configurations H50_D4 and H50_D5. Results here show that increasing chord member diameter is predicted to have a positive effect on both joint and member failure loads. The step-change observed at 5 mm diameter is due to the change in chord member wall

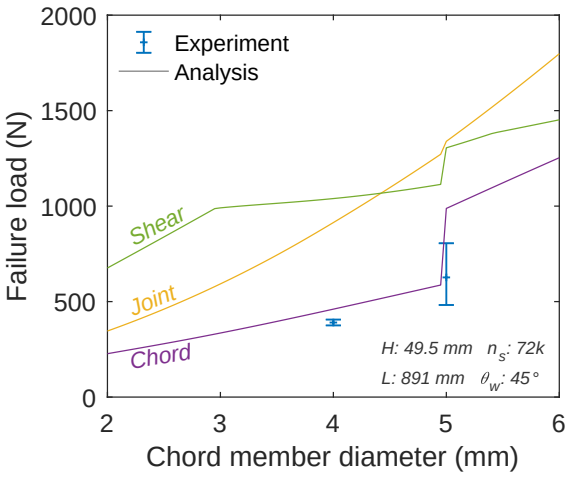

Figure 5.22: Failure predictions and experimental results of configurations H50_D4 and H50_D5 at a test span of 18 truss bays with varying chord member diameter. Note step change in results at 5 mm is due to thickness change of available tubes. Error bars denote experimental range of four values.

thickness. As was explained previously in Section 4.6, the pultrusions used for WrapToR truss manufacture were available at 0.5 mm wall thickness for diameters below 5 mm and at 1 mm for diameters of 5 mm or above. This step-change has a large effect on the shear and chord member failure predictions, but minimal effect on the joint failure. Predicted joint failure load increases with chord diameter due to its positive effect on joint area; a value that is not affected by the wall thickness.

Also plotted in Figure 5.22, are the test results of configurations H50_D4 and H50_D5. Both of these configurations were designed to target failure in the chord member tubes. For the 4 mm chord diameter configuration, H50_D4, all samples failed within the chord members with a mean failure load 14% lower than predicted. For the larger tube configuration, H50_D5, a large variance of both the failure load and mode was observed. A single H50_D5 sample failed in the chord member at 805 N (18% lower than predicted). All other samples failed at a substantially lower load due to a gradual collapse of the shear members. On inspection of the failed shear members, it was observed that they lacked rigidity and could be easily plastically deformed. Two possible explanations for this are given. Firstly, the shear members for these configurations are larger than in the other tested truss configurations and may have had a poorer level of consolidation. The results of the tow impregnation investigation in Section 2.5, did find worse consolidation in the larger shear members; however, the difference was not very large. The second potential reason is that a heating failure in the lab during the production of these trusses resulted in lower curing temperatures which may have led to a reduction in the shear member matrix properties. This result shows variability in the shear member performance and may highlight the need for more controllable curing methods.

5.7.3 Nonlinear response and buckling

Configuration H66_1 was designed to have long slender shear members that would be susceptible to buckling. It was originally tested during the tow twisting investigation in Section 3.6. Failure of the shear members was dominant in the samples; however, rather than a sudden change in shape that would be expected of column buckling, a gradual nonlinear softening of the structure was observed. In an attempt to model this softening response, the WrapToR analysis tool was updated to include considerations due to geometric nonlinearities. Linear eigenvalue buckling analysis was also added to the tool to see if it could be used to predict this failure mode and any other buckling behaviour that may occur. In this section, the results of the nonlinear and buckling analysis are compared to the experimental results of configuration H66_1.

In Figure 5.23, the observed experimental response of the H66_1 trusses are plotted alongside both the predicted response from the nonlinear analysis and the critical loading predicted by the eigenvalue buckling analysis. Nonlinear analysis results are plotted for two models: the standard eccentric model developed in Section 4.3, and a model in which the geometry is identical but where the connection between shear members at central cross-point is removed. For both models cases, the eigenvalue predictions appear to place the critical buckling load around the start of the nonlinear softening behaviour predicted by the nonlinear analysis. Further runs of the analysis for different truss configurations found this relationship between the eigenvalue and nonlinear analysis results to be consistent.

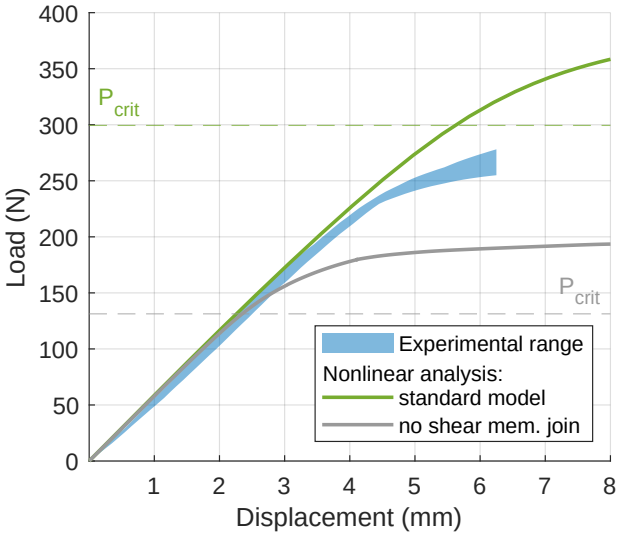

Figure 5.23: Comparison of H66_1 truss three-point bending response to predictions of nonlinear and eigenvalue buckling analysis. Experimental range combines responses of three tests. Dashed lines show critical loads, P_{crit}, predicted by eigenvalue analysis.

An instantaneous buckling is not observed in the shear members because they experience both axial compression and internal bending moments, meaning they do not behave as pure columns. The bending deformations cause the members to gradually loose axial stiffness, resulting in a loss of the overall truss stiffness. Even though the failure observed is not strictly buckling, the results in Figure 5.23 show that the linear eigenvalue buckling analysis approximates the beginning of the nonlinear region and therefore provides useful design information.

Both the nonlinear and eigenvalue analysis overpredict the load-carrying capability of truss configuration H66_1. There are several possible reasons for this overprediction. The WrapToR analysis tool uses a geometric model in which adjacent shear members intersect at the central cross-point. In reality the members cross over one another meaning they are, in effect, slightly pre-bent. This pre-bend is likely to promote the softening behaviour. Another possible reason is related to the flexural rigidity of the shear members being less than is modelled. The shear member modulus was determined through tensile testing of the members in Section 3.3, and the second moment of area was estimated through image analysis of sectional optical micrographs. The issue with this method is that it assumes a homogeneous distribution of the fibres throughout the shear member section. As was seen in Section 2.5, the fibre tends to be more densely packed at the centre of the shear member sections and that the outer region is mostly resin. It is therefore likely that the flexural rigidity of the shear members is lower than predicted, which would lower the load at which the softening effect occurs. Both of these possible sources of inaccuracy may also affect the linear analysis; however, perhaps the effects are less noticeable as the linear response is less dependant on bending deformations in the shear members. These additional geometric considerations should be incorporated during any future development of the analysis tool. A final possible reason for the observed inaccuracies is that material nonlinearities also occur which are not considered in the model.

Also plotted in Figure 5.23 is the response of an analysis case in which the connection between shear members at the central cross-point is removed. In the manufactured WrapToR trusses the connection at this cross-point is a small epoxy bond formed when two strands of wetted shear member tow make contact. Interesting to note is that in the initial linear phase of the response, the removal of the cross-point connection does not affect the truss stiffness. This observation is consistent to results of testing the model in Section 4.5: the connection of shear members at the cross-point has minimal effect on truss stiffness when using a linear model. Figure 5.23 however shows that the cross-point connection has a significant effect on the nonlinear and buckling behaviour where its removal drastically reduces the trusses load-carrying capability. This likely occurs because the connection at the

cross-points supports the compressive shear members at their centres and restricts their deformation. These results highlight that the cross-point connection plays a significant structural role. The formation of this cross-point connection during truss manufacture is a consequence of the process rather than a purposely designed feature. Due to its apparent structural role, further work may wish to give more formal consideration of how this connection is formed. This could include additional application of resin to the area or fibre reinforcement.

During testing of the configuration H66_1 trusses, large local deformations were observed, characterised by a bowing of the shear members. It was suspected that these large deformations were responsible for the nonlinear softening response as they reduce the shear members ability to resist axial loads. Similar such deformations were seen by Ju et al. [74] during testing of their GFRP truss concept where a nonlinear softening response was also observed. In Figure 5.24, the observed deformed truss shape is compared to both the deformation predicted by the nonlinear analysis and the first buckling analysis mode shape. From a qualitative assessment of the experimental and model deformations, two main similarities can be drawn.

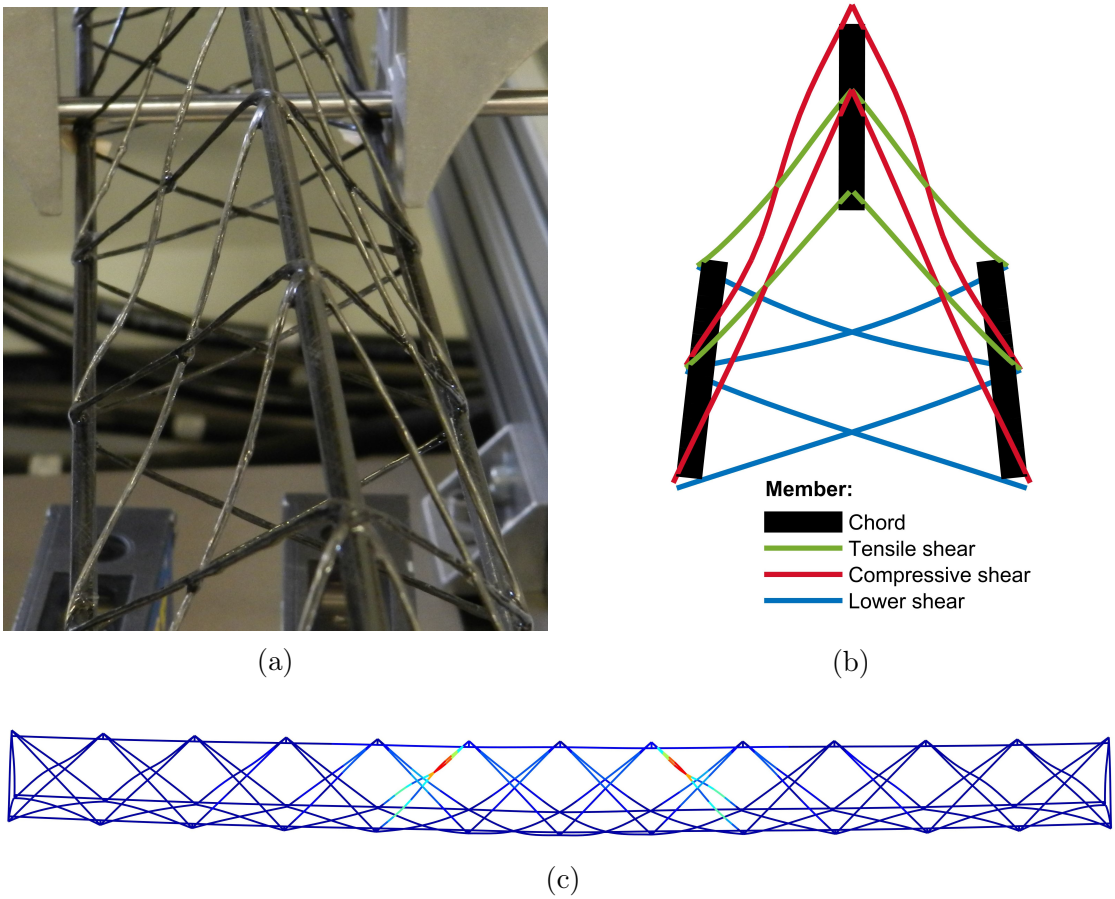

(a) (b)

(c)

Figure 5.24: Shear member deformations in H66_1 truss: a) experimental; b) nonlinear analysis predictions (only central bays displayed for clarity); c) eigenvalue analysis first mode shape.

Firstly, in all cases, the compressive shear members bow, forming an S-shape where the member below the cross-point bends in and above it bends out. Secondly, all cases show the lower shear members bowing out from the truss section. It is not possible to compare these local deformations quantitatively as the local member displacements were not measured during testing. The qualitative similarities do, however, suggest that the geometric nonlinearities captured by the model are, at least in part, responsible for the observed softening behaviour.

The buckling analysis results presented in this section only considered a single mode in which local buckling of the shear members is critical. As was shown in Figure 5.11, at least two other potential modes can occur. Local buckling of the chord members (Figure 5.11a) is predicted to be critical in trusses with higher chord member loading. While this buckling mode was not experimentally investigated here, analysis of the truss configurations at varying lengths finds that this mode is unlikely to occur as it is generally preceded by material compression failure. Global buckling (Figure 5.11c) is predicted when high aspect ratio trusses are loaded in axial compression. Global buckling was not experimentally investigated here because the work focused on the truss bending behaviour. It is however acknowledged that this mode will likely play an important role when assessing the compressive performance of the truss beams and will therefore require investigation during future work.

5.8 Conclusions

Within this chapter, the capabilities of the WrapToR truss analysis tool were extended to include failure predictions. Member and joint failure were predicted using maximum stress criterion. Nonlinear and buckling behaviour were modelled through implementation of incremental loading and linear eigenvalue analyses. Once developed, the predictive methods were validated against experimental results from testing of various truss configurations. The investigation conducted was primarily focused on failure of the trusses under flexural loading, however the predictive tools developed will be useful for analysing other loading scenarios.

During the experiments, various failure mechanisms were observed within the truss members, and sequential failure events made it difficult to identify the initial critical location. Member failure occurred exclusively within the axially compressed members, supporting the theory that tensile failure within the trusses is unlikely under flexural loading. The maximum stress criteria used to approximate member failure load were seen to provide reasonable predictions. These simple, non-interactive failure criteria would, however, need updating should future work aim to improve the accuracy of the failure predictions. Such improvements would require consideration of more detailed member geometry and stress interactions for each mechanism.

Joint failure predominately occurred along the upper chord members by what appeared to be a shearing of the tow from the tube. Maximum stress criteria again provided a reasonable estimate of the load at which this mechanism would occur. An additional, unexpected joint failure mechanism was observed that involved the peeling and subsequent fracture of a single tow strand. This mechanism highlighted the limitations of the current model as its simplistic representation of joint geometry and stress state make it incapable of predicting its occurrence. Prediction of this, and perhaps other joint failure mechanisms, would require development of a local model with more detailed considerations of joint topology. Such a model may also provide useful information about joint stiffness that could be used to improve the pre-failure analysis.

Nonlinear analysis was developed to investigate a previously observed softening behaviour in trusses with long slender members. The results showed the analysis predicts this softening behaviour, however the load at which it occurs was overpredicted. It was suggested that the experimentally observed softening occurs at lower loads due to geometric features that are not captured within the model. These features could be incorporated in future work to improve model accuracy. The nonlinear analysis was seen to have run times two orders of magnitude larger than the linear model, making it too computationally expensive to use within later optimisation studies. The coded buckling analysis, potentially offers a solution as results suggest it predicts the start of the nonlinear softening behaviour at a significantly lower run time. It should be noted here that while joint and member failure were validated against multiple test configurations, only one was used to validate the buckling and nonlinear analysis. Future work should therefore investigate other truss configurations that display nonlinear or buckling behaviour. Investigation of global buckling is highlighted as crucial for exploring the truss's potential as compression columns.

Results of both failure testing and nonlinear analysis show that the connection of the shear members at their central cross-point may have an important structural role. The formation of this connection has previously received little attention; therefore, exploring the benefits of reinforcing this bond is highlighted as a potential area of future research.

In earlier chapters inconsistency of both the shear member quality and the joint area were highlighted as an area of concern. In some test samples, this inconsistency is believed to have contributed to premature truss failure highlighting the need for future improvements in the manufacturing process focused on forming of both the shear members and the joints. Stitching of the joints to provide fibre reinforcement is one method suggested for consideration during future work. Any such modifications to the manufacturing process will need to consider the trade-off between structural gains and process complexity.

The work in this chapter aimed to develop simple failure prediction techniques for WrapToR trusses. While limitations in the developed methods exist, and the accuracy could be further improved, the results show that they provide a reasonable estimate that should be suitable for preliminary component design. With this in mind, the next chapter will use the developed analysis tools for structural optimisation of the WrapToR trusses.

Chapter 6

Optimisation

6.1 Introduction

To maximise the gains in structural efficiency offered by WrapToR trusses, it is crucial to select the most suitable combination of geometric parameters. Within the previous two chapters, analysis tools were developed to predict WrapToR truss deformations and failure. These tools are intended to facilitate informed truss design by determining whether a certain configuration meets a given set of stiffness and failure requirements. However, the developed tools can only assess the structural performance of a given truss configuration and are unable to select an efficient truss design for a given structural role. They can, however, be used with optimisation techniques to determine truss configurations that maximise structural efficiency.

Optimisation is a highly popular research area in which algorithms, known as optimisers, are used to minimise an objective function, often subject to a series of constraints. Optimisers are commonly used to find optimal solutions to design problems. In recent years, the field of optimisation has vastly benefited from substantial increases in computing power and as such optimisation algorithms are now commonly applied in a wide range of applications including, economics, chemistry, business, and engineering.

Within engineering, the use of optimisation for structural design is becoming ever more popular. However, structural design problems are generally not ideal candidates for computer optimisation for two main reasons. Firstly, underlying structural models often rely on computationally expensive FEA; this is particularly so if 3D elements or nonlinear analysis methods are used. Secondly, the design space for structural problems is generally vast, requiring large numbers of design variables to define any given structural solution [137]. The design space is broadened even further when using composite materials as, within the material itself, there are a practically limitless set of possibilities due to the selection of ply numbers and

orientations. Such difficulties have led to the development of optimisation algorithms specifically designed for structural problems [138].

Compared to that of large conventional structures, the design problem for a single WrapToR truss requires a relatively small number of design variables. For a prismatic, triangular section WrapToR truss, the geometry can be defined with just five variables. Additional to this, results in previous chapters have shown that usefully accurate predictions of truss performance can be made with computationally inexpensive models. The WrapToR truss therefore presents a highly suitable candidate for design via optimisation. This suitability for optimisation is not unique to the WrapToR truss and, as such, optimisation of other composite lattice structures has been explored within the literature. In Section 6.1.1, attempts by other researchers to use optimisation for design of composite lattice beams are discussed. Within the remainder of this chapter, the developed analysis tools will be used within an optimisation framework to determine truss designs that minimise mass for a given set of requirements. This work serves as an investigation into whether structural optimisation can be used for preliminary sizing of WrapToR trusses.

6.1.1 Optimisation of composite lattice beams

Many of the lattice beam technologies discussed earlier in Section 1.1.4.3 make great candidates for structural optimisation. Like the WrapToR truss, their geometric configurations can be characterised by varying a small number of well-defined parameters, such as member diameters, member orientations, and beam section radius. Additionally, the analysis methods used to predict their structural behaviour (outlined in Section 4.2) are relatively computationally inexpensive.

Ju et al. [120] conducted optimisation of their GFRP truss concept using the response surface methodology (RSM). Using RSM meant that rather than implementing their FEA model within an optimiser, the FEA model was used to create a surrogate model that approximates how variations in the design variables affect the problem constraints. This method was selected as the authors used a computationally expensive nonlinear FEA model to predict failure via nonlinear "yielding". No other failure mechanisms were considered during the optimisation, even though multiple other mechanisms would likely exist for the lattice beam technology.

Gurley et al. [76] used optimisation to maximise the stiffness of open-architecture composite structures (O-ACS) under four different loading scenarios. For the optimisation study, the O-ACS beam section diameter was fixed, the optimal helical angle was found using a genetic algorithm (GA), and the member diameters were found by determining the relative contributions of the members to overall beam stiffness and adjusting accordingly. The optimal beam configurations found using

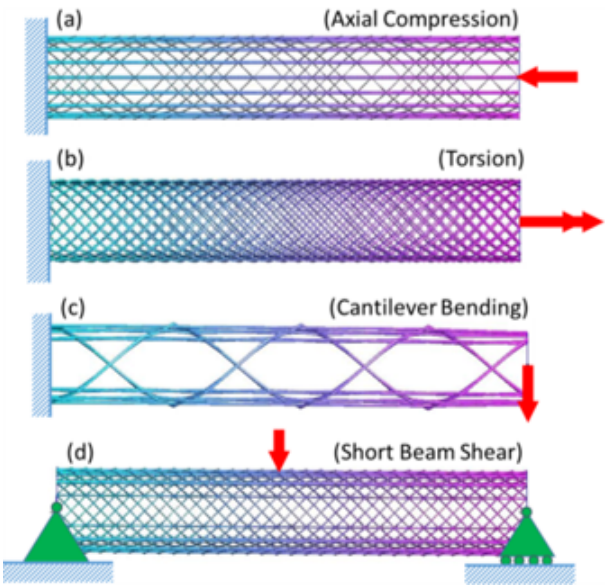

Figure 6.1: O-ACS configurations optimised for stiffness under various loading scenarios. Reproduced from [76].

this method (displayed in Figure 6.1) neatly demonstrated how the lattice beam configuration can be altered to maximise performance for different loading scenarios. The study results neatly demonstrate how the lattice beam configuration can be altered to maximise performance for different loading scenarios. However, as no failure constraints were applied during the optimisation, its use for practical structural component design is limited.

Woods et al. [82] performed multi-objective optimisation of WrapToR trusses using a GA to maximise flexural rigidity while minimising beam mass. For this study, a low-fidelity analysis tool that assumes two-force member behaviour was used for both stiffness and member stress prediction. This low-fidelity tool is the same as that used in Section 3.7. Failure was then predicted using Euler buckling formula and maximum stress criteria which were only partly validated. The analysis did not consider joint failure, and the two-force member assumption means that only axial stresses within the members were considered. The optimisation results were used to compare the trusses to commercially available composite beams and demonstrated large gains in structural efficiency.

For lattice beam structural design, the most practically useful optimisation framework would have the objective of minimising mass subject to constraints relating to stiffness, manufacturing capabilities, and a comprehensive set of failure mechanisms. As well as this, the accuracy of the implemented structural model would be sufficiently experimentally validated. All the presented studies to date are lacking in one or more of these areas. Within the following sections of this chapter, optimisation of WrapToR trusses is conducted under the suggested framework using a comprehensive set of constraints and well-validated models.

6.2 Problem definition

6.2.1 Algorithm

Matlab's in-built genetic algorithm (GA) was selected for the truss optimisation. Developed in the 1960s and 70s, genetic algorithms are heuristic optimisers that mimic natural selection processes [139]. They are most suited to non-convex optimisation problems in which many local optima may exist. They tend to require a larger number of evaluations to converge and are hence limited to problems with few design variables and computationally inexpensive objective and constraint functions. Other algorithms are available that are specifically designed for structural tasks, however, such algorithms are likely to be inappropriate for the WrapToR truss design problem due to the relatively low number of design variables. Additionally, Matlab's in-built GA is convenient for implementing discrete variable constraints.

The population size was set to 200, and the constraint tolerance to 1e-8. All other algorithm settings were kept at Matlab's default values. For each load case, the optimiser was run at least three times to ensure repeatable convergence. The average recorded run time for optimisation of a single load case was 17 minutes without buckling analysis enabled and 278 minutes with the buckling analysis enabled on a PC with 16 GB of RAM and a 2.6 GHz processor.

6.2.2 Design variables

Within the optimisation code, the truss geometry was defined using the five design variables displayed in Table 6.1. Note that the number of truss bays, n_b, is used as a design variable rather than the winding angle, θ_w. With the truss span constrained, it is simpler to define the number of bays and then calculate the winding angle rather than predetermining a possible set of winding angles for selection. The number of bays was specified as a discrete variable for which only even integers were permitted to ensure consistency of the loading configuration. For the optimisation work in this chapter, material properties were kept constant at those measured in Chapter 3, and hence material properties were not used as design variables.

The pultrusion tubes previously used for truss manufacture are available for purchase in a number of discrete sizes. For industrial applications, manufacturing of custom pultrusion tubes of any specified size would likely be possible. The optimisations were therefore run for the following two design variable scenarios:

- Discrete tube sizes: Only specific tube sizes are used based on sizes available from the current supplier.
- Continuous tube sizes: Tubes diameter and thickness can be set to any values within a reasonable continuous range.

Table 6.1: Optimisation design variables.

Design variable	Symbol	Units	Continuous/ discrete	Bounds	
				Lower	Upper
Height between chord centres	h	mm	continuous	15	160
Number of bays	n_b	-	discrete	2	28
Shear member diameter	$\varnothing_s$	mm	continuous	0.42	2
Chord tube diameter	$\varnothing_c$	mm	both	1	7
Chord tube thickness*	t_w	mm	both	0.5	2

**only a design variable in the continuous tube size case*

For the discrete tube size case, the tube's thickness is fixed, resulting in only four design variables. Tubes available from the current supplier have thicknesses of 0.5 mm for tube diameters of 4 mm and below, and 1 mm for diameters 5 mm and above.

In the WrapToR process, shear members are created by combining multiple fibre tows, meaning that, technically, only a discrete set of shear member diameters are achievable. However, as many combinations of different tow sizes exist, the possible selection is near-continuous and hence shear member diameter was set as a continuous variable.

Also displayed within Table 6.1 are the bounds set for each design variable. The bounds were set based on a combination of manufacturing limitations, supplier availability, and general intuition around the appropriate truss dimensions. For example, the smallest tube diameter available is 1 mm, the truss mandrel design is unlikely to permit manufacture of section heights below 15 mm, and section heights above 160 mm are likely to be excessive for the investigated load cases.

6.2.3 Objectives and constraints

As the purpose of the optimisation study was to maximise structural efficiency, truss mass per unit length (MUL) was the objective function. MUL was estimated using the analysis tool's mass estimation module, which is detailed in Appendix E.

Five constraints were applied relating to bending stiffness, failure, span, and geometric limitations. A minimum bending stiffness constraint was applied, with truss stiffness predicted using the analysis methods developed in Chapter 4. Similarly, a minimum failure load constraint was applied where failure under three-point bending was predicted using the analysis methods developed in Chapter 5. It was found that implementing the buckling analysis detailed in Section 5.5.4 within the optimiser increased the run time by an order of magnitude. It was also found that most of the optimised configurations were not critical in buckling. The buckling failure constraint was therefore left inactive for the initial optimisation to reduce the

runtime. The outputted optimal solution was then checked to see if buckling was critical and where it was, the optimisation was re-run with the buckling constraint applied. Both the stiffness and failure constraints were applied using Matlab's non-linear constraint function. The values used for the stiffness and failure constraints are detailed in the load cases presented in Section 6.2.4.

For all the load cases investigated, a three-point bending loading scenario was used. The span was set as a constraint by fixing it within the objective and constraint functions. Two further constraints related to ensuring feasible truss geometry were applied as linear inequality constraints. The first ensures that truss height is not less than the chord tube diameter and is defined in Equation 6.1. The second ensures chord tube thickness is less than the tube radius and is defined in Equation 6.2; note that this constraint only applies for continuous tube sizes.

$$h > \varnothing_c \tag{6.1}$$

$$t_c < \frac{\varnothing_c}{2} \tag{6.2}$$

6.2.4 Load cases

In Section 3.8, WrapToR trusses were experimentally compared to commercially available UD CFRP pultruded tubes. Results showed the truss to offer substantial increases in stiffness and load-carrying capability at a slightly reduced weight. However, the tested truss configuration (H33_1/S-T) was not optimised for that specific role, meaning even greater structural performance improvements are likely possible. Additionally, the truss configuration used did not provide an ideal comparison of structural efficiency as it was both much stronger and stiffer.

To address both of these issues, two load cases were investigated during the optimisation study, both of which are summarised in Table 6.2. In the first load case, the failure and stiffness constraints are set to the predicted stiffness and failure load for the H33_1 truss configuration. This first load case aims to show how optimisation can be used to improve structural efficiency compared to a non-optimised truss configuration. In the second load case the failure load and stiffness constraints are set to the experimentally determined values for the 8 mm pultruded tubes tested in Section 3.8. This second load case aims to determine the potential improvements in structural efficiency offered by the truss when compared to the pultruded tubes. As was the case in the previous experimental investigation, three-point bending was used at a test span of 0.396 m. Note that truss designs were required to have an even number of bays so that the loading configuration could be kept consistent, with the load being applied at the central lower truss joints.

Table 6.2: Summary of load cases investigated in optimisation study.

Load case	Failure load (N)	Bending stiffness (N/mm)	Span (m)	Constraint origin
1	402.0	91.0	0.396	Truss config. H33_1/S-T
2	198.8	14.8	0.396	8 mm pultruded tubes

6.2.5 Span sweeps

As has been seen from results in previous chapters, truss span affects the relative contributions of shear and bending loads within the truss beams. The span is therefore likely to have a significant effect on the optimised truss designs. Therefore, a series of optimisations were run over a sweep of truss spans to investigate how changing span would affect the optimised design. For the initial span sweep, the stiffness and failure requirements were kept the same as load case 1 while span was varied from 0.2 to 1.5 m in 0.1 m increments. To gain further insight into the results, two further sweeps were conducted in which either the stiffness or the failure constraint were removed. The three optimisation span sweeps conducted are summarised in Table 6.3.

Table 6.3: Span sweep constraint scenarios.

Constraint scenario	Failure load (N)	Bending stiffness (N/mm)	Span (m)
Failure & stiffness	402.0	91.0	0.2 - 1.5
Failure only	402.0	0	0.2 - 1.5
Stiffness only	0	91.0	0.2 - 1.5

6.3 Results

6.3.1 Load cases 1 & 2

In Table 6.4, optimised truss configurations for load case 1 are compared to the H33_1 truss that was previously tested in Section 3.8. The optimised truss configuration for the discrete tube size case offers a small mass saving of 4.2% when compared to the non-optimised H33_1 configuration. This optimised configuration is very similar to the H33_1 truss, with only small changes in three of the design variables. These results suggest that the tested H33_1 configuration provides a near-optimal solution for this particular load case. The H33_1 configuration was designed to be a compression strut within the Gamera human-powered helicopter. Whilst no optimisation was used when selecting this configuration, it was designed using analytical calculations, and as such, it is likely to have a sensible combination

of truss parameters. Within the previous chapter, the predicted and experimentally observed failure loads for this truss configuration were plotted over a range of spans in Figure 5.17. The results showed that for the H33_1 truss, a span of 0.396 m is a point within the design space at which the various failure modes' critical loads converge. This observation adds further evidence that this may be close to an optimum design as moving away from this point within the design space will likely trigger earlier failure.

For the continuous tube size optimisation, the greater design freedom results in a slightly larger mass saving of 5.8%. In this configuration, the optimiser has chosen to trade chord member material for increased height. Increasing height and increasing chord member size both positively affect the flexural rigidity, however, increasing the tube size comes with a greater mass penalty. It is therefore favourable to choose increased height over larger chord member tubes; providing the constraints allow for it.

Optimised truss configurations for load case 2 are displayed in Table 6.5. For these optimisations, the failure load and stiffness constraints were set at the experimentally observed values for the 8 mm pultrusion tubes tested in Section 3.8. The optimised trusses in Table 6.5 therefore show the potential improvements in structural efficiency offered by the WrapToR trusses when compared to UD CFRP tubes. Here the optimised trusses offer substantial improvements in efficiency with mass reduced by more than half for both the discrete and continuous tube size cases. Again, when going from discrete to continuous tube sizes, the optimiser chooses a configuration with a larger section height and smaller tube diameter. It is worth noting that the shear member diameter chosen by the optimiser is on the specified lower bound. This lower bound represents a 12k carbon tow shear member's diameter, which is a somewhat arbitrarily chosen boundary as tows are available in smaller sizes. It is therefore possible that further efficiency gains could be achieved by lowering this boundary.

For both load cases, the continuous tube size optimisations resulted in chord member thicknesses equal to the specified lower boundary of 0.5 mm. It is not surprising that the optimiser favours thinner tubes as, in general, thinner tubes are more efficient under bending. This lower bound was chosen as it was the lowest thickness available from the current supplier. Whilst it may be possible to lower this bound further, the minimum thickness of the UD tubes will likely be limited by transverse failure or shell buckling. Currently, neither of these failure modes are captured within the analysis methods and, therefore, further reduction of the tube thickness would require consideration of such modes. If transverse failure were found to be limiting, further work might wish to consider other configurations that feature transverse reinforcement, such as roll wrapped or pullwound tubes.

Table 6.4: Truss optimisation: load case 1 results.

Configuration	Height, h (mm)	No. of bays, n_b	Shear member diameter, $\varnothing_s$ (mm)	Chord diameter, $\varnothing_c$ (mm)	Chord thickness, t_c (mm)	Winding angle, θ_w (°)	MUL (g/m)	MUL % change
H33_1 / S-T truss	30.0	12	1.2	3.0	0.5	45.0	32.2	-
Optimised truss (discrete tubes)	29.2	16	1.0	3.0	0.5	37.6	30.9	-4.2
Optimised truss (continuous tubes)	32.1	20	1.0	2.5	0.5*	29.8	29.1	-5.8

**variable located at specified boundary.*

Table 6.5: Truss optimisation: load case 2 results.

Configuration	Height, h (mm)	No. of bays, n_b	Shear member diameter, $\varnothing_s$ (mm)	Chord diameter, $\varnothing_c$ (mm)	Chord thickness, t_c (mm)	Winding angle, θ_w (°)	MUL (g/m)	MUL % change
8 mm pultruded UD CFRP tube	-	-	-	-	-	-	38.0	-
Optimised truss (discrete tubes)	23.6	16	0.8*	2.0	0.5	44.1	18.0	-52.7
Optimised truss (continuous tubes)	25.2	18	0.8*	1.9	0.5*	39.1	17.8	-53.2

**variable located at specified boundary.*

6.3.2 Span sweeps

To gain insight into how the optimal truss design evolves across a range of spans, a series of optimisations were run at spans varying from 0.2 to 1.5 m using the load case 1 stiffness and failure constraints. To further investigate the results for this span sweep, optimisations were conducted for cases in which either the stiffness or the failure constraint were removed. Therefore, results in this section are presented for three constraint scenarios: one with both failure and stiffness constraints, one with only the failure constraint, and one with only the stiffness constraint.

In Figure 6.2, optimised truss MUL is plotted against span for the three constraint scenarios. As expected, the optimised truss MUL increases with span; this occurs because increasing the span results in larger bending moments, which require more material to withstand them. For the failure only scenario, MUL is much less sensitive to changes in span than the two scenarios involving stiffness constraints. The results in Figure 6.2 show that for optimisation with combined stiffness and failure constraints, the optimal designs at lower spans are primarily strength driven and at higher spans are primarily stiffness driven. The results also suggest that the design is driven by both the failure and stiffness constraints in the mid-span range.

Also highlighted in Figure 6.2 are the optimisation cases in which buckling was found to be critical and hence that had to be re-run with the buckling constraint active. Of the 28 relevant designs, only five were driven by failure via buckling. These five cases appear to be in the span region where the solution is driven by both stiffness and failure. It should be noted here that relative to the other failure mechanisms, the buckling analysis was poorly validated.

A series of parallel coordinate plots are displayed in Figure 6.3 that show how the optimised truss configurations change with span. Within these plots, each line represents a single optimised truss design. Plotted along a single line are a designs

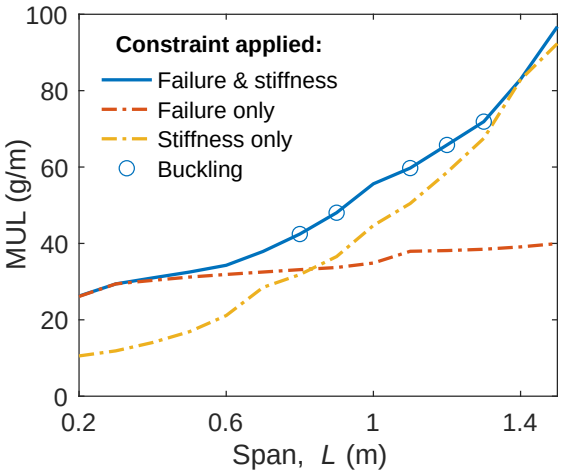

Figure 6.2: Optimised truss mass per unit length (MUL) at varying spans.

MUL and normalised values for its span and its design variables. Note here that the winding angle, θ_w is plotted instead of the number of bays, n_b, as it provides clearer physical interpretation of the geometric configuration. The design variables are normalised within the range of the lower and upper bounds specified in Table 6.1, meaning a normalised value of 0 represents a design variable on the lower permitted bound and of 1 on the upper bound. Winding angle, θ_w, is normalised within the range of 0-90° and span, L, 0-1.5 m.

Comparing the failure constrained designs of Figure 6.3a, with the stiffness constrained designs in Figure 6.3b, several significant differences are observed. Within the failure only constrained designs, a smaller section of the design space is utilised as the design variables appear less sensitive to changes in the span constraint. The smaller variation between optimal designs results in much more modest mass changes across the span range (as was seen in Figure 6.2). The sensitivity of the shear member diameter, $\varnothing_s$, is particularly low and only varies by about 5% of the available range. As the span increases the applied bending moment increases but the shear load remains constant. This means that as the span increases, more chord member material is prioritised over more shear member material.

Within the stiffness only constrained optimisations, trusses with much greater heights are selected. In Figure 6.3b, the height is seen to be highly sensitive to changes in the span constraint. Height increases rapidly with span and quickly reaches the specified upper bounds. Widening the allowed design space by increasing the upper bound on height would likely result in greater efficiencies. Additional to increasing height to meet the stiffness constraint, the optimal designs in Figure 6.3b also feature increasing member sizes as spans increases. The increasing of member sizes results in much greater masses at higher spans.

Designs given from optimisations using both stiffness and failure constraints are plotted in Figure 6.3c. Here the designs at lower spans are similar to those for the failure constrained case, and at the higher spans they are similar to the stiffness constrained case. This again shows that for this particular case, short span designs are driven by failure and longer spans by stiffness.

Interesting to note from the optimal designs in Figure 6.3 is that no obvious trends were observed for the selection of winding angle; which was seen to vary between 23 and 56°. Winding angle is calculated from the number of bays, n_b, which is a discrete design variable that is only permitted as an even integer. This effectively means that a limited discrete selection of winding angles is available for any given truss design. Additional to this, the winding angle, or number of bays, influences truss behaviour in multiples ways. The discrete nature of this parameter, coupled with complexity around how it influences structural behaviour, is perhaps responsible for the lack of observed trend.

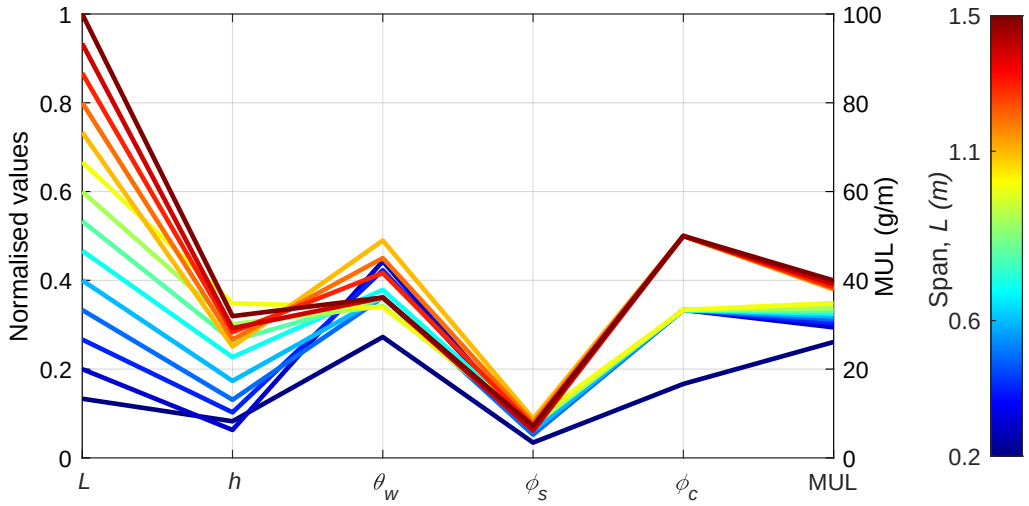

(a)

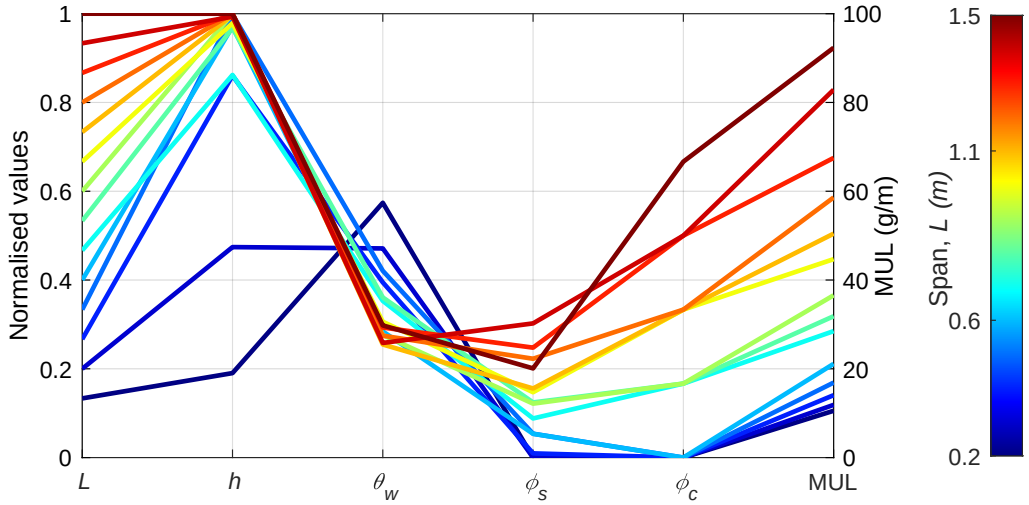

(b)

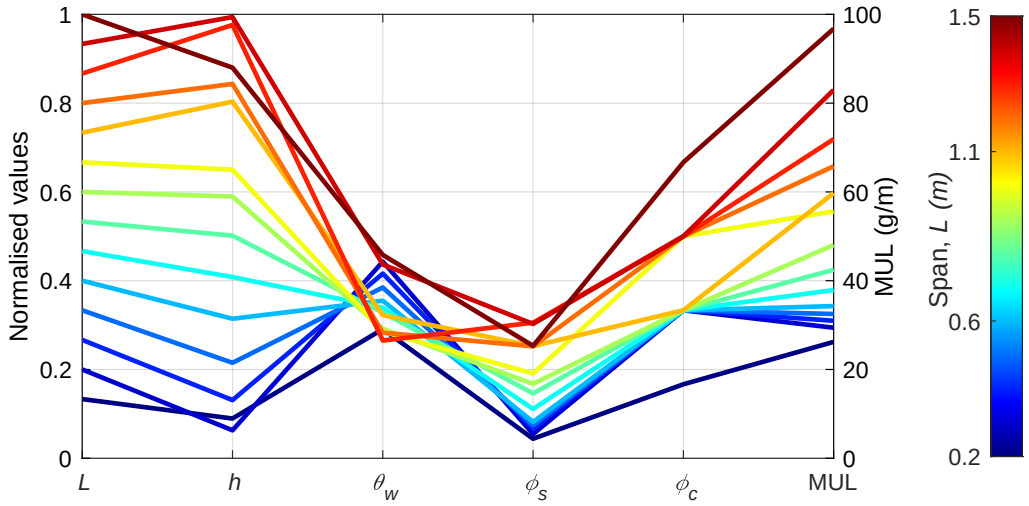

(c)

Figure 6.3: Parallel coordinate plots showing variation of optimal truss configuration across range of spans, L. Constraints used: a) failure only; b) stiffness only: c) failure and stiffness.

6.4 Conclusions and future work

Conducted within this chapter is a preliminary investigation into how optimisation techniques can be used within the design of WrapToR trusses. Analysis tools developed in previous chapters were embedded within a genetic algorithm (GA) to determine optimised truss designs for a series of load cases. This work aimed to demonstrate how optimisation can be used to maximise structural efficiency of the composite lattice beams.

When using optimisation to improve structural efficiency of a non-optimised truss configuration, modest mass reductions of 4 to 5% were observed. Study of the optimised configurations suggested that the original, non-optimised configuration was already well designed for the given load case. Optimisation was also used to determine a truss configuration that maximised structural efficiency compared to the UD CFRP tubes tested previously in Chapter 3. Results of this optimisation predict that truss configurations offering reductions in mass of over 50% are possible. Validation of this result could be conducted as part of future work where the optimised truss configuration is manufactured and tested.

Additional efficiency gains were achieved by allowing selection from a continuous choice of chord member tube sizes. Moving from discrete to continuous tube sizes essentially broadens the geometric design space in which the optimiser can operate. Future work may wish to investigate further expansions of the design space as a means of achieving even larger gains in structural efficiency. For example, in the current work, the number of chord members is fixed to 3, all of which use the same tube size. Allowing any number of chord members and different tube sizes would increase the design freedom. Extending the geometric design space to allow tapering trusses is also likely to provide structural benefits for cantilever and compression loading scenarios. Additional to expanding the geometric design space, future work should also investigate using various material choices. Allowing the optimiser to select properties from a set of given materials is another means to expand the design space and potentially increase structural efficiency. It has been suggested previously that high modulus carbon fibre could be structurally beneficial for composite lattice beams in which member buckling is of concern. Allowing selection of various fibre types (high strength, intermediate modulus, and high modulus) would be an efficient way to determine which is most suitable.

Truss configurations selected by the optimiser show that thinner chord member tubes are desirable for maximising efficiency. For the UD CFRP tubes used, the minimum thickness will likely be limited by transverse strength or shell buckling, neither of which are captured by the current failure prediction methods. Incorporating such modes into the optimisation could permit the use of thinner tubes and

improve efficiencies. Following this, the design space could be extended further to allow other chord member configurations, such as roll wrapped or pullwound tubes. Such radially reinforced tubes are likely to provide advantages over UD tubes, particularly when progressing to larger chord member diameters.

This chapter details the first optimisation study of a composite lattice beam using experimentally validated failure prediction methods that consider a reasonably comprehensive set of mechanisms. Initial results show great potential for optimisation techniques in WrapToR truss design. Expansion of the design space to increase potential gains in structural efficiency is suggested for future work. However, more design freedom will inevitably increase computational cost, and should therefore be coupled with informed restriction of the problem bounds.

Chapter 7

Conclusions & future Work

7.1 Summary of conducted work

The work within this thesis was split between two main themes: manufacturing and analysis. The analysis work was focused on developing tools that could predict structural behaviour. The manufacturing work focused on progressing the winding process so that trusses could be made efficiently and repeatably. The analysis and manufacturing themes were connected via characterisation work in which manufactured part quality was assessed, and structural models were validated. In Figure 7.1, a summary of the conducted work is given that shows the three themes, their related bodies of work, and how each are interconnected. The diagram also shows how each body of work feeds into the project aim of developing understanding and improving quality of WrapToR trusses. The key findings of the work are summarised below in Section 7.2, before discussion of potential future work in Section 7.3.

7.2 Key findings

Truss winding process automation

Previous to the work within this thesis, WrapToR trusses were manufactured using a manual hand-winding technique. This process is labour-intensive and imprecise, and is therefore unsuitable for industrial application. The initial work focused on automating the process through the design and manufacture of a three-axis truss winding machine. Production of the prototype machine demonstrated that the winding process could be automated using low-cost, mostly off-the-shelf electrical and mechanical components. Automating the winding process was a key objective for the thesis as it would help move the technology towards industrial application. Additional to meeting the objective, the automated process also provided a much more efficient and consistent method for producing trusses that were later structurally

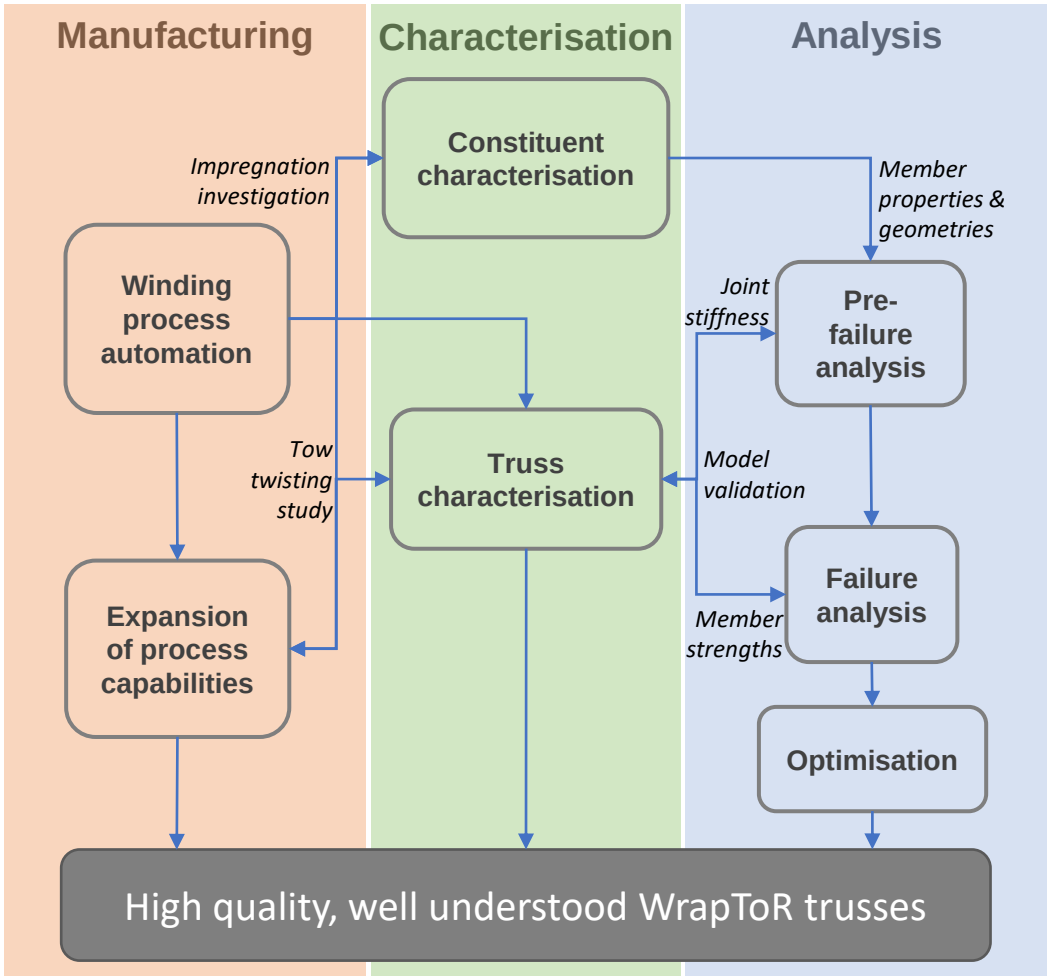

Figure 7.1: Summary of thesis work.

characterised. The parametrically generated mandrel design and winding program generator allowed new truss configurations to be made with accurate dimensions and minimal effort.

Structural benefits of tow twisting

Automating the process also enabled the manufacture of a new truss configuration in which the wound tow was twisted to form cylindrical shear members. It had been previously speculated that creating cylindrical members with circular sections would be structurally advantageous as it would improve their resistance to buckling. To test the hypothesis, trusses of both the previous non-twisted configuration and the new twisted configuration were manufactured and tested. Results showed that tow twisting improved the shear members' buckling resistance without degrading truss joint strength. Microscopic investigation of the member sections showed that tow twisting increased member minimum second moment of area by an average of 56%. Testing revealed that tow twisting increased truss load-carrying capability by 51% in a truss configuration susceptible to shear member buckling.

Manufacturing issues: impregnation and joint consistency

Whilst a significant improvement on the previously used hand-winding technique, the automated process does still present some issues. Inspection of the wound shear member's internal structure via optical microscopy revealed reasonably high void contents, varying between 5-7%. Additional to this, resin content decreased when larger shear member tow sizes were used. These issues are attributed to the processes's rudimentary impregnation method, in which tow is pulled through a resin bath and is left to cure without external pressure. Another region of variability in the manufactured trusses was the joints between the wound tow and the pultruded chord members. Measurement of the contact area between the impregnated tow and the pultruded tubes revealed large variability of the joint area. Furthermore, some anomalous test results in which trusses debonded well below the expected failure load were likely caused by poorly formed joints.

Bending behaviour is highly influenced by aspect ratio

Investigation of the truss mechanical response found that behaviour under bending loads is highly dependant on truss aspect ratio. Both the analysis and experimental results showed how at low aspect ratios, shear deformations in the truss beams significantly contribute to overall deflections. As aspect ratio increases, shear contributions become insignificant and bending deformations dominate the response. It was also shown that at very high aspect ratios (around 120), accurate predictions of truss bending deflections could be made using parallel axis theorem and considering only contributions from the chord members. At shorter, more realistic aspect ratios, this method is not appropriate.

Modelling behaviour at the joints is crucial

The analysis work in Chapter 4 demonstrated that it is necessary to model behaviour at the joints for accurate prediction of the truss stiffness response. The necessity of modelling joint behaviour was seen to be particularly important for low aspect ratio trusses in which shear deformations are significant. At higher aspect ratios where bending deformations dominate, the need to model the joint effects is less critical. The research highlighted two main reasons for the need to model joint effects. Firstly, joint eccentricity affects how forces are transferred between the members, meaning axial forces within the shear members impart bending moments in the adjacent chord members, and vice-versa. The second reason is that deformations occur within the joints, which contribute to the overall truss deformation.

Prediction of deformations, strains, and failure

Prior to work within this thesis, prediction of WrapToR truss behaviour relied on a low-fidelity model, based on matrix structural analysis (MSA) methods, in which the truss members were assumed to carry only axial loads. During testing in Chapter 3, this analysis method was seen to be inaccurate, particularly when predicting behaviour of lower aspect ratio trusses. Developed in Chapter 4 was a higher-fidelity model, again based on MSA methods, in which the truss members were treated as beam elements, capable of carrying axial, bending, and torsional loads. Through rigorous experimental validation, the higher-fidelity model was shown to accurately predict truss deformations and strains. Later, failure criteria were added to the model which were again experimentally validated. As would be expected, the model was somewhat less reliable at predicting failure than deformations and strains, but still provided a reasonable level of accuracy that would be useful for preliminary component design.

WrapToR trusses are highly efficient structures

Experimental comparison of WrapToR trusses with conventional pultruded UD CFRP tubes confirmed that at the length scales tested, the truss configuration provides large improvements in structural efficiency. The experimental comparison found that, when compare to 8 mm UD tubes, a non-optimised truss configuration offered a 9% reduction in mass, a stiffness increase of 537%, and an increase in failure load of 133%. For a more direct comparison of structural efficiency, optimisation was later used to find a truss configuration that minimised mass while providing stiffness and strength performance equivalent to the UD tubes. Given this task, the optimiser determined a truss configuration that is predicted to reduce mass by more than 50%. Whilst not yet experimentally validated, this result shows enormous potential for the WrapToR truss configuration. The ability to reduce structural mass by more than half could have profound consequences within engineering.

7.3 Future work

Work within this thesis has significantly improved understanding of the WrapToR truss's structural behaviour and manufacturing process. Being a very new concept, as are composite lattice beams in general, there is still great scope for further research. Identified within this section are the key areas of future work required to enable industrial application of the WrapToR truss technology. Note, many of the suggested areas apply to composite lattice beams in general.

Investigation of other loading scenarios

The work within this thesis has primarily focused on truss bending behaviour, specifically when loaded via three-point bending. It has been discussed that composite lattice beams, including the WrapToR truss, present great potential as compression columns. Investigation of the WrapToR trusses as compression columns is therefore identified here as a key area for future research. Other loading scenarios such as cantilever bending, or torsion are also of interest. Any such work should investigate the ability of the analysis tools developed within this thesis to predict structural response under different loading conditions. In addition to this, comparison to common structural configurations, both analytically and experimentally, would provide insight into the technology's potential under such load cases.

Improving understanding of truss joints

Analysis and experimental validation work demonstrated the importance of modelling behaviour of the truss joints. Within the models, joint eccentricity and deformations were captured by incorporating additional beam elements that represented the connection between the chord and shear members. For this low-fidelity method of modelling the joints, the joint elements' stiffness had to be approximated through empirical fitting with the truss testing data. A linear expression was then derived from the empirically fit values to approximate the joint stiffness for any given truss configuration. Future work should investigate developing a more robust methodology for determining the joint stiffness, probably by developing a higher fidelity model of the joints. A higher fidelity model would also be beneficial for predicting joint failure, which within this thesis was predicted using maximum stress criterion and a rudimentary area approximation.

As was concluded in Section 7.2, joint variability within the manufactured trusses was high. Improving the consistency of the joints is therefore identified as an area for future research. Methods for consideration include joint stitching, application of additional resin, and experimentation with tow tension. Any such modification to the process should consider any trade-offs between improved structural performance and increased labour requirements.

Further investigation of nonlinear and buckling behaviour

In an attempt to model experimentally observed nonlinear softening behaviour, the analysis was extended to include geometric nonlinearity considerations. While the nonlinear analysis appeared to capture the general softening trend, it was inaccurate at predicting the associated loading. Additional to this inaccuracy, the nonlinear

analysis presented significantly longer run times making it unsuitable for implementation within the optimisation study. Euler buckling analysis was used to circumvent this issue, which appeared to predict the onset of the nonlinear behaviour. Suggestions to improve the nonlinear analysis accuracy include incorporating a more detailed representation of the truss geometry at the shear member cross-point and refined consideration of the shear member sectional properties. Further experimental data from a range of truss configurations will also be required for more detailed validation of any developed models.

Alternative materials

Any technology offering solutions to current or future engineering challenges must firmly consider sustainability issues. Development of the WrapToR truss concept is intrinsically linked with the desire to reduce fossil fuel consumption through structural lightweighting. However, the current material choice of thermosetting polymer reinforced carbon presents a separate set of environmental issues related to disposability, recyclability, and embodied energy. Future work should investigate alternative material options. Thus far, the mindset adopted has considered the truss technology as a means to maximise structural performance by utilising high-performance materials within an efficient geometry. Perhaps an alternative mindset would be to use the efficient geometry to enable the use of lower-performance materials, such as natural fibres, that are more environmentally benign. However it is noted that much of the current generation of natural fibres have poor compressive properties. The use of thermoplastic matrix systems presents potential environmental and structural benefits. Switching from thermosetting to thermoplastic will require significant alterations to the current process to enable impregnation of the highly viscous matrix.

Design of truss connection methods

Efficient methods of connecting trusses, either to other structural components or other trusses, will be required for successful industrial adoption. Without efficient connection methods, the large mass benefits of using the trusses could be entirely offset by heavy joining components. Investigation of potential connection methods is therefore identified as a crucial next step in the technology's development. Additional to minimising weight, any method would ideally minimise the labour required to manufacture and attach any joining components.

Upscaling

Work within this thesis has demonstrated the enormous weight-saving potential of the WrapToR truss concept. However, the analytical and experimental work conducted has so far been focused on trusses of relatively small size and modest load-carrying capabilities. Future work must consider the technologies potential at larger length scales to extend the range of potential applications in which the technology can be used. Such work will require enlargement of the manufacturing process, assessment of larger truss performance, and investigation of model accuracy at larger scales. When moving to larger scale trusses, the use of UD chord members may require reconsideration, with radially reinforced tubes, such as roll-wrapped or pullwound, likely becoming more appropriate.

7.4 Potential applications

A key aim of the thesis was to develop the technology so that it could be industrially applied. However, little discussion of potential applications has yet been given. Based on the presented findings, briefly discussed within this section are some potential applications for the technology.

At the current tested scales, the trusses present fantastic potential as high aspect-ratio beam elements in highly weight critical, small-scale applications. One obvious candidate is small or lightly loaded unmanned aerial vehicles (UAVs); this includes multi-copter and fixed-wing concepts. Current work at the university is investigating using the truss concept to minimise quad-copter airframe mass. A prototype from this work is shown in Figure 7.2. One draw-back of the wound trusses in multi-copter applications is their poor impact resistance. Whilst currently untested, the exposed unidirectional truss members are likely to be prone to impact damage. Use is therefore likely to be more appropriate in applications where the trusses are less exposed, such as in fixed-wing UAVs, where they can be embedded within an aerodynamic skin. Fixed-wing high-altitude pseudo-satellite (HAPS) are a fairly new UAV concept designed to fly for days at a time in the stratospheric atmosphere to complement or replace traditional orbiting satellites. To achieve such a feat, these vehicles are highly mass critical and feature very high aspect ratio wings with relatively low loadings. HAPS therefore present an ideal candidate application for the WrapToR trusses.

Other researchers have identified the potential for composite lattice beams in large-aperture space structures, such as radio antenna and solar arrays. While the WrapToR truss presents a near-ideal structural solution for such applications, in its current form, the technology is inappropriate due to poor packing efficiencies.

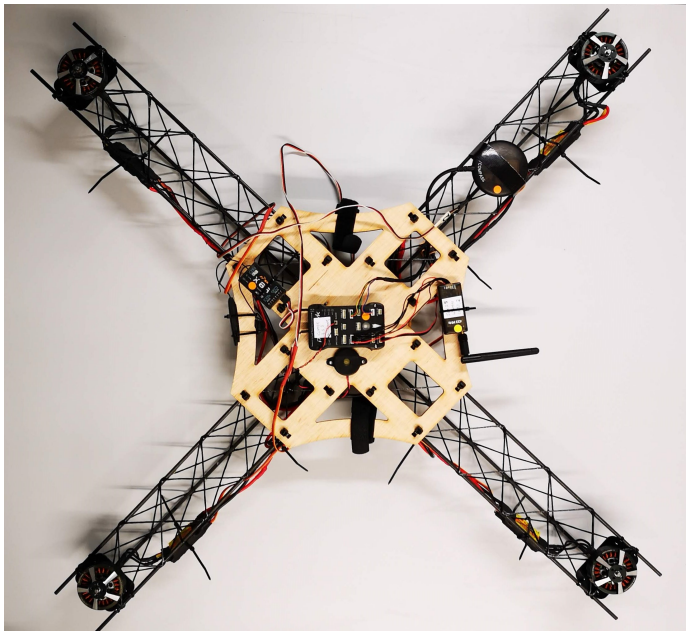

Figure 7.2: WrapToR truss quad-copter prototype.

Implementation of the technology in such applications would require significant alterations to the manufacturing process to enable in-orbit truss production.

If future work successfully demonstrates the truss technology's benefits at larger scales, many more potential applications become possible. Initial candidates would be mass critical applications, such as aircraft and spacecraft. Providing that the technology's mass reduction capabilities persist at larger scales, the truss technology could drastically reduce fuel burn and its associated environmental and economic costs when used in these applications.

Appendices

Appendix A

Derivation of shear and winding angle ratio

Shear member angle and winding angle are terms used to describe the orientation of the diagonal shear members. The subtle differences between the two is explained in Section 2.6 and in Equation 2.2 a mathematical relationship between the two is given. In this appendix the derivation of that relationship is detailed.

As is stated in Section 2.1.6, winding angle is a convenient term as it allows the following simple relationship relating truss height, H, and bay length, l:

$$\tan\theta_w = \frac{l}{H} \tag{A.1}$$

This relationship for winding angle can be drawn from the geometry displayed in Figure A.1b. For the shear member angle a similar relationship can be drawn if the parameter of extended height, H^*, is introduced. This parameter is depicted in Figure A.1a and gives the following relationship:

$$\tan\theta_s = \frac{l}{H^*} \tag{A.2}$$

To determine the extended height, an end view of the truss geometry is displayed in Figure A.2. Here, the length p is introduced such that:

$$H^* = H - \varnothing_c + 2p \tag{A.3}$$

Here p is given by:

$$\begin{aligned} p &= \frac{\varnothing_c}{2}\tan 60^\circ \\ &= \frac{\sqrt{3}}{2}\varnothing_c \end{aligned} \tag{A.4}$$

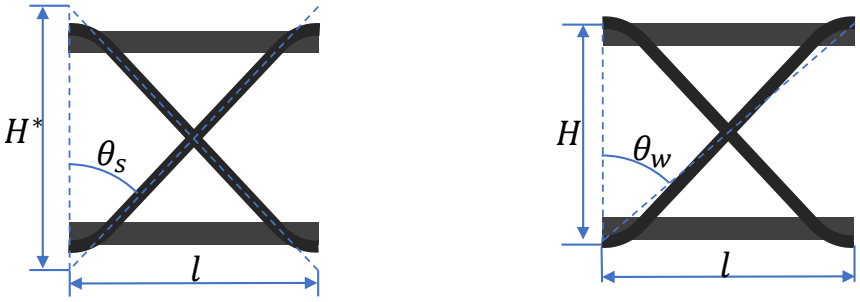

(a) (b)

Figure A.1: Face of individual truss bay depicting geometry of: a) shear member angle; b) winding angle.

Substituting Equation A.4 into Equation A.3 gives:

$$\begin{aligned} H^* &= H - \varnothing_c + \sqrt{3}\varnothing_c \\ &= H + \varnothing_c(\sqrt{3} - 1) \end{aligned} \tag{A.5}$$

Substituting Equation A.5 into Equation A.2 then gives:

$$\tan\theta_s = \frac{l}{H + \varnothing_c(\sqrt{3} - 1)} \tag{A.6}$$

Rearranging Equation A.1 and substituting into Equation A.6 gives:

$$\tan\theta_s = \frac{H\tan\theta_w}{H + \varnothing_c(\sqrt{3} - 1)} \tag{A.7}$$

Rearranging this gives the ratio of shear member and winding angle stated in Equation 2.2:

$$\frac{\tan\theta_s}{\tan\theta_w} = \frac{H}{H + \varnothing_c(\sqrt{3} - 1)} \tag{A.8}$$

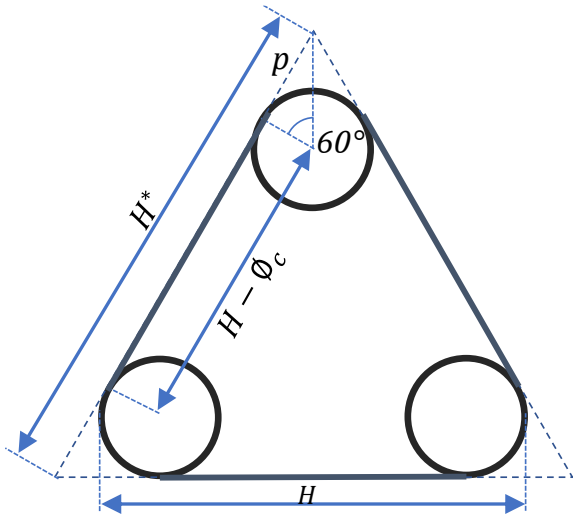

Figure A.2: Truss end view geometry.

Appendix B

Winding program generation

B.1 Introduction

This appendix details the operation of the bespoke g-code generating software written for winding of WrapToR trusses on the designed three-axes machine. The winding program generator (WPG) essentially uses information on truss geometry and process variables to produce a set of G-code commands that control the relative motion of the winders axes. In the winding program, each line of G-code (commonly referred to as a block) represents one linear movement of the machine's axes. The following notation and dimensions of movements for each of the machines three axes are used:

- Carriage translation, denoted by x and is defined in millimetres.
- Mandrel rotation, denoted by α and is defined in degrees.
- Tow twist denoted, by T and is defined in number of rotations.

During the project two variations of the WPG were written to produce g-code for both prismatic trusses and linearly tapering non-prismatic trusses. These two variants are detailed separately in the Sections B.3 and B.4. Summaries of the WPG operation for prismatic and tapered trusses are given in Figures B.1 and B.2, respectively.

B.2 Useful parameters

The key parameters used by the WPG are displayed in Tables B.1 and B.2. Parameters marked with an asterisk are calculated from the inputted parameters (the unmarked parameters).

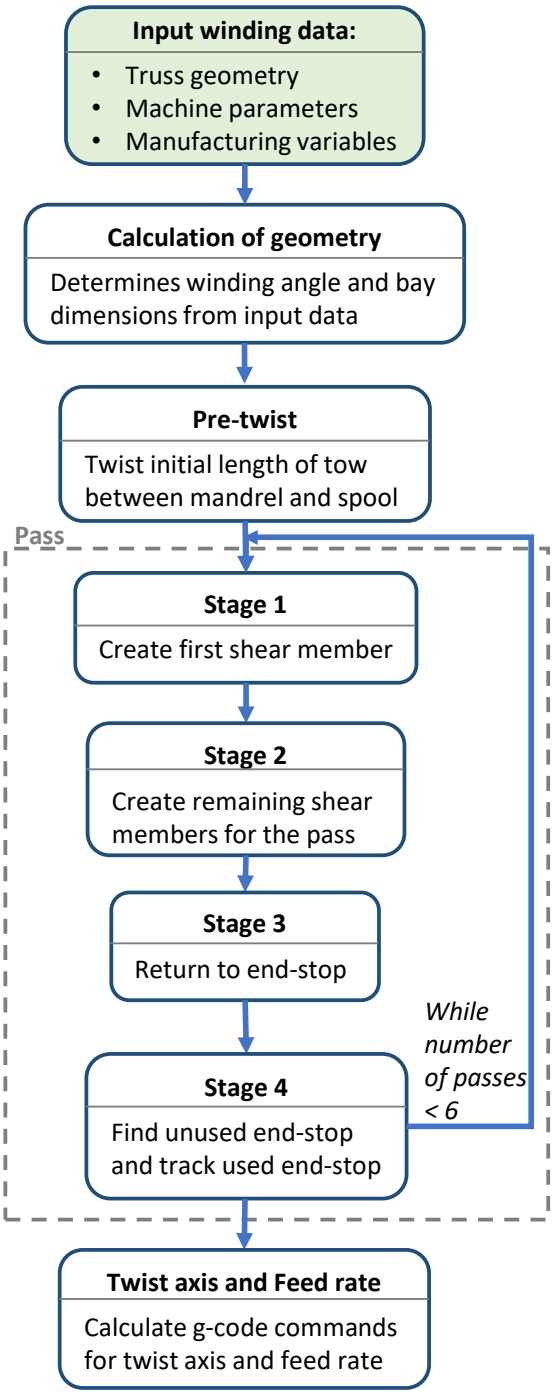

Figure B.1: Summary of operation of WPG for prismatic truss.

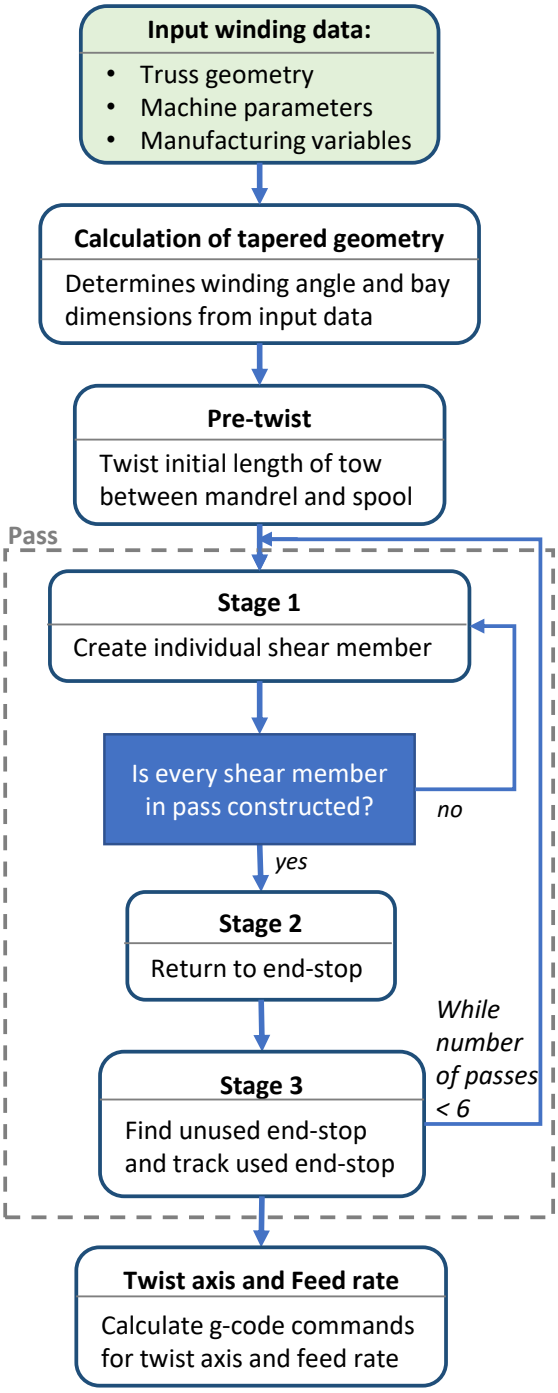

Figure B.2: Summary of operation of WPG for tapered truss.

Table B.1: Truss geometric parameters used for winding program generation.

Parameter	Symbol	unit
Level of twist	LoT	turns / mm
Winding angle	θ	degrees
Number of truss bays	n_b	-
Number of chord members	n_c	-
Chord diameter	$\varnothing_c$	mm
Angle between chord members*	α_c	degrees
Truss height*	H	mm
Truss height between centre of chord members	h	mm
Truss centre to outer of chord: truss radius*	R	mm
Truss centre to chord centre: inner truss radius*	r	mm
Truss length*	L	mm
Truss bay length*	l	mm

**values that are calculated from specified parameters*

Table B.2: Winding machine variables.

Parameter	Symbol	unit
Tow feed rate	F	mm / min
Distance of eyelet to truss centre	g	mm

B.3 Prismatic truss winding program generation

To wind a prismatic truss, the WPG uses the process of operation outlined in the flow diagram in Figure B.1. The first phase of the WPG is to take in information to allow it to produce a truss with specified geometry and manufacturing variables. The necessary input parameters required by the program are listed in Tables B.1 and B.2. Within Table B.1 all the parameters with an asterisk are not directly inputted and are calculated from the input parameters; the calculation of these parameters forms the second phase of the WPG. Once the truss geometry is determined, generation of the necessary g-code blocks for the winding program begins. The first block performs the function of twisting the initial tow that runs between the spool and the mandrel therefore requiring only a movement in the tow twisting axis. Once the pre-twist is completed, the WPG must then generate G-code for the first pass. A pass is defined as the movement from a departing end-stop at one end of the truss, to its concluding end-stop at the opposite truss end i.e. it is a movement from one end of the truss to the other. For a triangular section truss the number of passes required to complete the winding sequence is six. Each of the passes contains four movements, or stages. The first and second stages create all the shear members for their pass. The third and fourth stages perform the function of returning to an end-stop ready to commence the next pass. The following sections details the methodology used by the WPG to create G-code programs.

B.3.1 Calculation of geometry

The first step of the WPG is to use the given inputs to calculate the necessary truss geometric parameters. Within Table B.1 all the parameters marked with an asterisk are not directly inputted and are calculated from the inputted parameters. Any parameters not marked with an asterisk are given as an input. This section will detail how the WPG calculates the necessary parameters some of which are depicted in Figure B.3.

The angle between the chord members, α_c, is dependant solely on the number of chord members and is given by:

$$\alpha_c = \frac{2\pi}{n_c} \tag{B.1}$$

As the majority of trusses in this thesis had three chord members, the value of α_c was mostly 120°.

The distance between the truss centre and the centre of the chord members is referred to as the inner truss radius, r. This parameter is depicted in Figure B.3 and is calculated from the inputted height between the chord member centres, h, using:

$$r = \frac{h}{2\sin\alpha_c} \tag{B.2}$$

The truss radius, R, is then found from:

$$R = r + \frac{\varnothing_c}{2} \tag{B.3}$$

From the geometry in Figure B.3 the truss height, H, is seen to be equal to:

$$H = h + \varnothing_c \tag{B.4}$$

Truss bay length, l, can be found from the definition of winding angle given in Equation 2.1 in Section 2.1.6 such that:

$$l = H\sin\theta_w \tag{B.5}$$

Total truss length can then be found from the bay length, l, and the number of bays, n_b, using:

$$L = n_b\, l \tag{B.6}$$

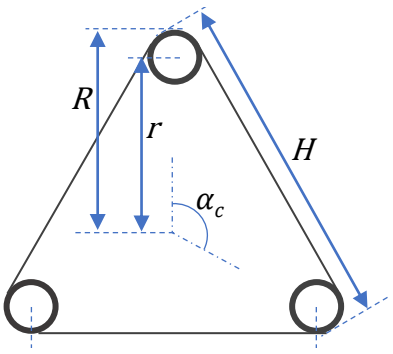

Figure B.3: Truss section view geometric features.

B.3.2 Pre-twisting

The first block of the program performs the function of twisting the initial tow that runs between the spool and the mandrel therefore requiring only a movement in the tow twisting axis. This pre-twist movement is determined by multiplying the initial tow length between the spool and the mandrel by the tow twist rate, T.

Following the pre-twist, the winding program makes the first pass across the length of the mandrel. Each pass creates one shear member in each truss bay. For any winding program the number of passes made along the mandrel is double the number of chord members. Therefore, a standard triangular section truss with three chord members will require six passes. Each pass consists of three or four movements which relate to four stages within the WPG.

B.3.3 Stage 1

The first stage relates to the initial movement away from the start point to create the first shear web member. This initial movement is depicted below in Figure B.4. The rotation of the first stage, α_1, is simply a rotation from one chord member to the next resulting in the creation of one shear member.

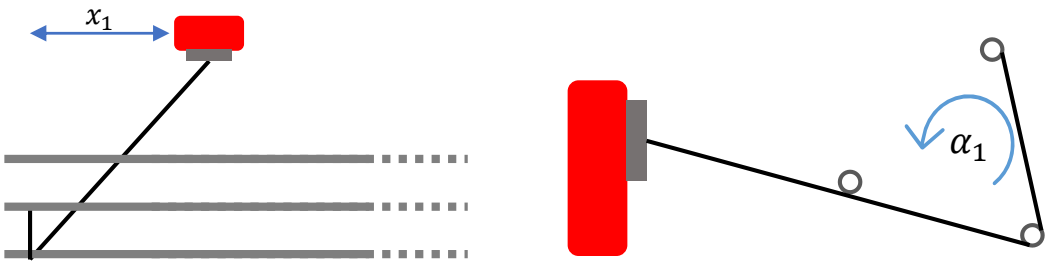

Figure B.4: Schematic of first movement: a) top view; b) side view.

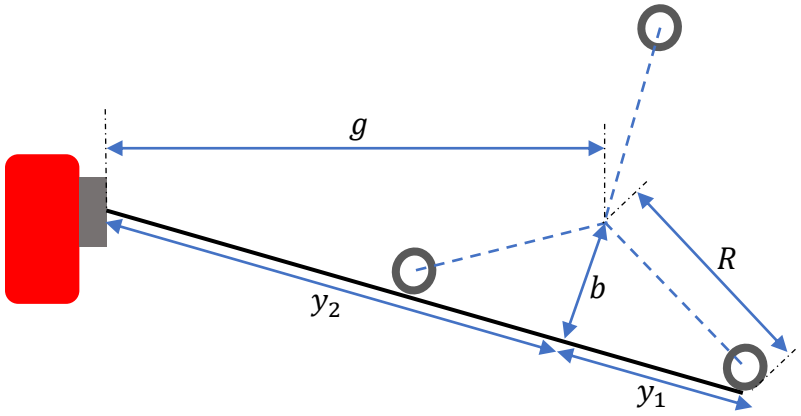

Figure B.5: Truss section view showing plane perpendicular to carriage translation axis.

$$\alpha_1 = \alpha_c = \frac{2\pi}{n_c} \tag{B.7}$$

Calculation of the first stage carriage translation, x_1, requires calculation of the distance from the eyelet to the initial departing chord member in the plane perpendicular to the carriage translation axis. This distance labelled y is formed of two components, y_1 and y_2 which are displayed in displayed in Figure B.5. These components are calculated using Equations B.8-B.11.

$$y_1 = \frac{h - \varnothing_c}{2} + \varnothing_c \cos\frac{\pi}{6} \tag{B.8}$$

Using Pythagoras the length b can be determined from:

$$b = y_1 \tan\frac{\pi}{6} \tag{B.9}$$

Again using Pythagoras' theorem y_2 is found as follows:

$$y_2 = \sqrt{g^2 - b^2} \tag{B.10}$$

Then:

$$y = y_1 + y_2 \tag{B.11}$$

By considering the geometry in the top view in Figure B.6, the first carriage translation motion can be found using Equation B.12.

$$x_1 = y \tan\theta_w \tag{B.12}$$

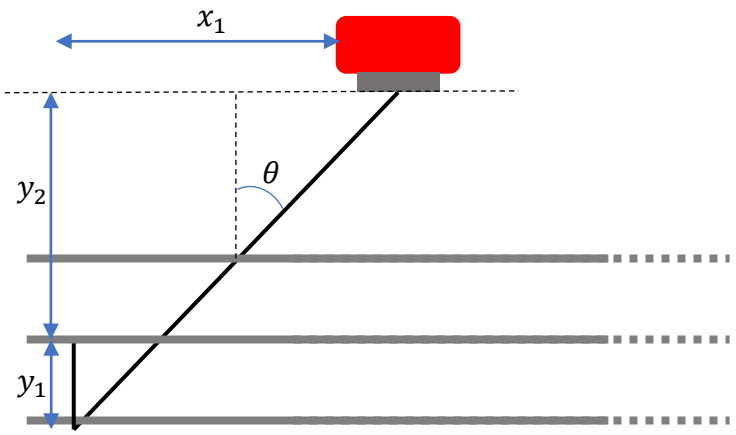

Figure B.6: Detailed top view of first movement.

B.3.4 Stage 2

The second stage creates the remaining shear members for the current pass and is depicted in Figure B.7. As the first stage created a single shear member in the first truss bay, the number of truss bays remaining for the pass is the total number of truss bays less one. The mandrel rotation and carriage translation for stage two are therefore given by:

$$\alpha_2 = (n_b - 1)\,\alpha_c \qquad \text{(B.13)} \qquad\qquad x_2 = (n_b - 1)\,L_u \qquad \text{(B.14)}$$

B.3.5 Stage 3

As is seen in Figure B.7, at the end of the second stage movement the delivery head has moved past the truss end. To hook the end-stop, allowing a reverse pass, the third stage moves the guide back to an end-stop while the mandrel is rotated by α_c. This movement is depicted in Figure B.8 and the corresponding mandrel rotation and carriage translation are determined from:

$$\alpha_3 = \alpha_c \qquad \text{(B.15)} \qquad\qquad x_3 = (L - x_1)\,l \qquad \text{(B.16)}$$

B.3.6 Stage 4

Before departing for the subsequent pass it is necessary to ensure that the current end stop has not been 'used', meaning a pass has not already departed from that end-stop resulting in a doubling up of the shear member wrap. To check whether the end-stop has been used, stage 4 contains an end-stop tracker that records which end-stops have been used. The flow diagram shown in Figure B.9 shows the operation of stage 4. Here it is seen that stage 4 only contains a movement if the end-stop reached at the end of stage 3 has already been used. On completion of stage 4

the next pass is commenced with the direction reversed. The four stages are then repeated until all the passes are completed.

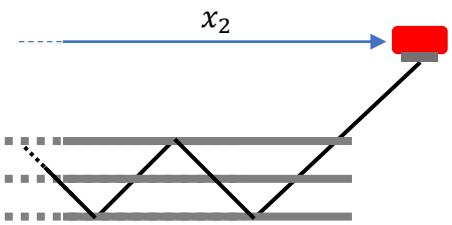

Figure B.7: Schematic of stage 2.

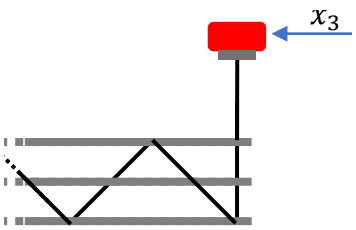

Figure B.8: Schematic of stage 3.

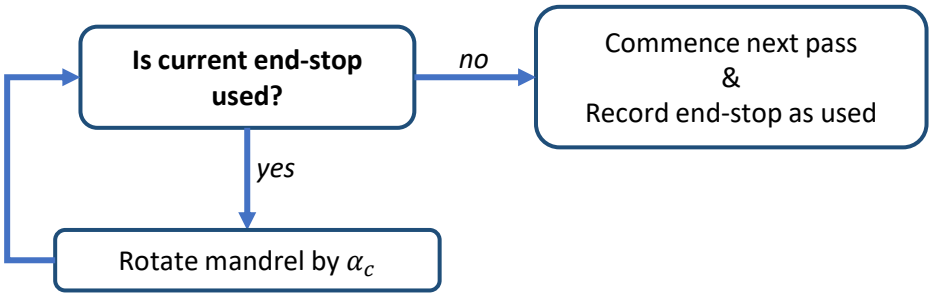

Figure B.9: Flow diagram of stage 4 operation.

B.3.7 Twist axis commands

Once the carriage translation and mandrel rotation axis movements have been determined it is then possible to calculate the twist axis movements that create a constant level of twist throughout the truss. The level of twist is the number of twists per unit length of tow, defined in twists / mm. To do this, first the length of tow fed out in each movement, δ, is determined from Pythagoras by:

$$\delta_n = \sqrt{x_n^2 + \left(\frac{\alpha_n}{\alpha_c} \cdot h\right)^2} \tag{B.17}$$

The number of revolutions of the twist axis for each movement, t_n, is then given by:

$$t_n = LoT \times \delta_n \tag{B.18}$$

B.3.8 Feed rate

Each G-code block must have a specified feed rate. The G-code interpreter used by the machines control board is designed to receive feed rate commands which relate to movements in a Cartesian space. For the winding process, control of the tow feed-out rate is desired. To achieve this, a feed rate converter module was written into the WPG which calculates the necessary G-code feed rate command to achieve a constant tow feed-out rate. The first step to this module is to determine the equivalent Cartesian length of each block; this is found by Pythagoras of the three axes:

$$\delta_{eq} = \sqrt{x^2 + \alpha^2 + t^2} \tag{B.19}$$

The feed rate command, f, for each block is then found by multiplying the desired tow feed out rate, F, by the ratio of equivalent Cartesian length to actual tow feed out length:

$$f = F \times \frac{\delta_{eq}}{\delta} \tag{B.20}$$

B.4 Tapered truss winding program generation

No modifications to the physical winding machine were required to allow the manufacture of tapered trusses, however significant alterations to the WPG were required. In the summaries in Figures B.1 and B.2, two main alterations to the code are seen for the winding of tapered trusses. Firstly, as the dimensions of the truss bays vary along the length, the relationship between the truss length, truss radius, number of truss bays, and winding angle is not trivial. Therefore, an extra step is required to determine the winding angle from given truss length, section dimensions, and number of bays. Once this is determined the geometry of each truss bay can be calculated. The calculation of tapered truss geometry was previously detailed in Section 2.3.1.

The second alteration is due to the change in length of each coincident shear member. This means that a single G-code instruction is required for the creation of each individual shear member. For winding of tapered trusses, stage 1 and 2 are combined into a single stage which is repeated continually until all the shear members are created. Stage 3 (returning to the end-stop) is then identical to that for a prismatic truss (Section B.3.5) as is the method for calculating the twist axis instructions and the feed rate (Sections B.3.7 and B.3.8).

B.4.1 Stage 1: Creation of each bay shear member

Once the geometry of each individual bay is determined using the methodology detailed in Section 2.3.1, it is then possible to generate the necessary G-code blocks to wind the tapered truss.

Stage 1 involves creating a shear member in each bay. As the bays change height and length, the generation of each shear member requires an individual block of g-code, meaning stage 1 involves n_b blocks per truss pass. Determining the blocks for each of these bays is achieved using similar formulations to stage 1 for the prismatic truss, however it is applied to every truss bay and has alterations to account for the taper. The mandrel rotational and carriage translation movements for each block are calculated separately and are therefore detailed in separate sections below.

B.4.1.1 Mandrel axis rotation

For a prismatic truss, the mandrel rotation for the creation of each shear member is constant. This is not the case for a tapered truss and therefore the change in mandrel rotation needs to be calculated for each bay. To determine the change in angle for each movement it is useful to define three variations of the mandrel angle, ω. This is the angle between:

- The line connecting the mandrel centre point and the machine eyelet
- The line connecting the mandrel centre point and foremost chord member

The three variations of the mandrel angle are displayed in Figure B.10. The first, ω_n, is the stated angle for no carriage translation. The second, ω_n^{fw} is the stated angle for a forward carriage movement (root to tip). The third, ω_n^{bk} is the stated angle for a backward carriage movement (tip to root).

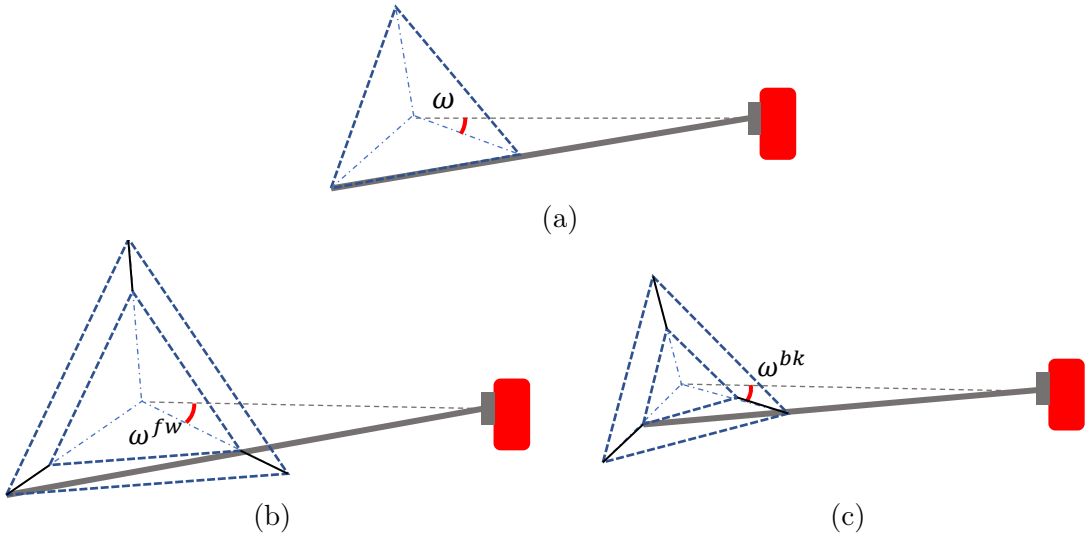

Figure B.10: Section view of tapered truss showing three variations of mandrel angle, a) ω; b) ω^{fw} ;c) ω^{bk}. Note tube thickness is omitted for clarity.

The mandrel angle for no carriage movement, ω, is displayed in Figure B.11 along with the geometric features that are required for its calculation. Here the length b is found using Equation B.9 . The angle φ is then found using the following equation, where g is the eyelet distance:

$$\sin \varphi_n = \frac{b_n}{g} \tag{B.21}$$

The mandrel angle can then be determined from:

$$\omega_n = \frac{\pi}{6} - \varphi_n \tag{B.22}$$

The mandrel angle for a forward carriage movement is determined by calculating the geometric features in Figure B.12. Note here that these geometric features have to be calculated at each bay and hence have the subscript, n. The method for calculating each of the features and ultimately the mandrel angle is detailed as follows.

The angle β can be determined using the following equation where y_1 is found using Equation B.8, and b found using Equation B.9:

$$\tan \beta_n = \frac{b_{n-1} - b_n}{y_{1,n-1} y_{1,n}} \tag{B.23}$$

The length k can then be found from:

$$k_n = r_n \sin\left(\frac{\pi}{6} + \beta_n\right) \tag{B.24}$$

Then, using trigonometry the two following relationships can be drawn:

$$\sin \varphi_n = \frac{k_n}{g} \qquad \text{(B.25)} \qquad\qquad \sin \rho_n = \frac{g \sin \varphi_n}{r_n} \tag{B.26}$$

When rearranging Equation B.26 to give ρ, the sine rule gives two possible solutions and the following must be used:

$$\rho_n = \pi - \sin^{-1} \frac{g \sin \varphi_n}{r_n} \tag{B.27}$$

The mandrel angle is then found from:

$$\omega_n^{fw} = \pi - \rho_n - \varphi_n \tag{B.28}$$

To calculate the mandrel angle going backward a similar method is used but the geometry calculations are altered to consider a backward movement. The geometric features that are used in the calculation of the backward mandrel angle are displayed in Figure B.13. For the backwards case, β is found using:

$$\tan \beta_n = \frac{b_n - b_{n+1}}{y_{1,n} + y_{1,n+1}} \tag{B.29}$$

The length k can then be found from:

$$k_n = r_{n+1} \sin\left(\frac{\pi}{6} + \beta_n\right) \tag{B.30}$$

Again, equation B.25 can be used to find the angle φ. ρ is then found from:

$$\rho_n = \pi - \sin^{-1} \frac{g \sin \varphi_n}{r_n} \tag{B.31}$$

The mandrel angle for a backward translation is then found from:

$$\omega_n^{bk} = \pi - \rho_n - \varphi_n \tag{B.32}$$

The mandrel rotation for each movement is then found from the angle between chord members, α_c, and the change in mandrel angle between two bays such that:

$$\alpha_n = \alpha_c + \omega_{n+1} - \omega_n \tag{B.33}$$

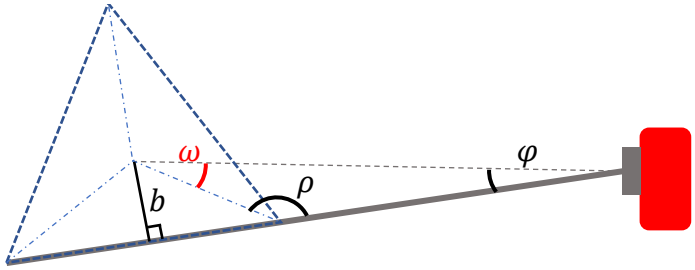

Figure B.11: Mandrel angle for movement with no carriage translation

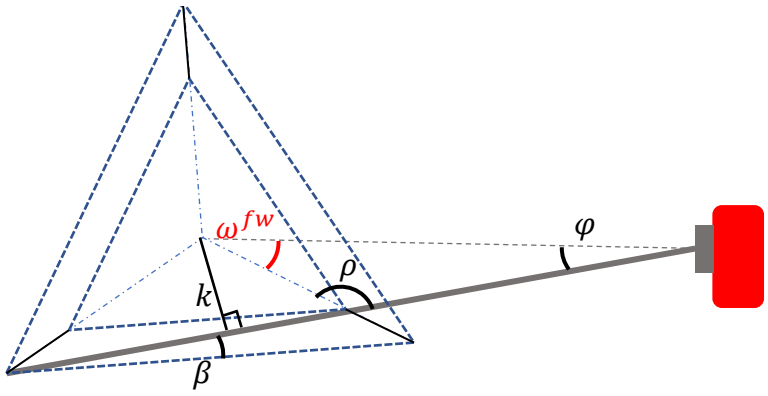

Figure B.12: Geometry for determining mandrel angle for a forward carriage movement.

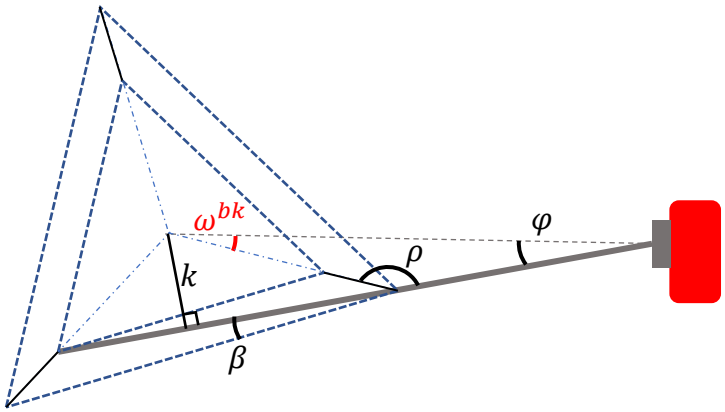

Figure B.13: Geometry for determining mandrel angle for a backward carriage movement.

B.4.1.2 Carriage translation

For the creation of each shear member a carriage translation movement must occur that places the tow at the correct winding angle between to the connecting chord members. Figure B.14 shows a schematic for the carriage translation when creating one shear member on a forward pass. By investigating the post movement geometry,

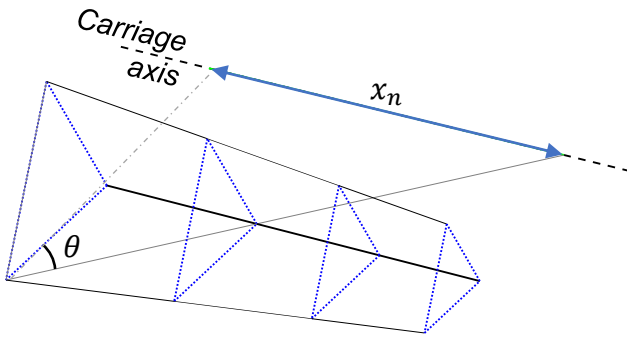

Figure B.14: Schematic showing the carriage translation for movement that generates one shear member, x_n.

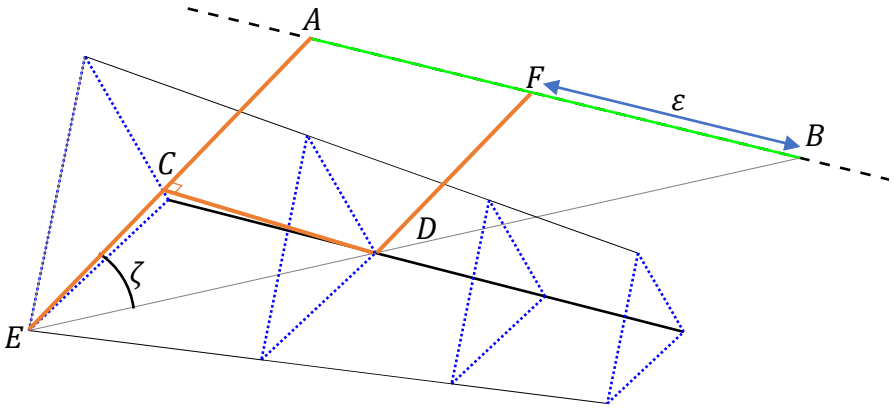

Figure B.15: Geometry for movement creating one shear web member, x_n.

it is possible to determine the carriage translation movement that will produce a shear member with the correct winding angle.

Figure B.15 shows the positioning of the mandrel, carriage, and tow following a movement to create one shear member. Here the length $|\vec{AB}|$ is the carriage translation, which can be determined by investigating the geometry on the plane ABE. The carriage translation length is divided into two parts: $\vec{AF}$ and $\vec{BF}$. $|\vec{AF}|$ is equal to the length of the bay and $\vec{BF}$ is the distance the eyelet travels past the bay end, referred to hereon as the overshoot distance, ε. Determination of the overshot distance is detailed below.

The carriage axis is parallel to the mandrel centre line, the lengths $|\vec{CD}|$ and $|\vec{AF}|$ are equal to the bay length parallel to the mandrel centre, i.e.:

$$|\vec{CD}| = |\vec{AF}| = l_{2D} \tag{B.34}$$

The length $|\vec{ED}|$ is then be found by:

$$|\vec{ED}| = \sqrt{l_{2d}^2 + (h_b + \delta_{2d})^2} \tag{B.35}$$

The angle between the vectors $\vec{AE}$ and $\vec{BE}$, ζ, is then found from:

$$\sin\zeta = \frac{|\vec{AE}|}{|\vec{BE}|} \tag{B.36}$$

As this angle is equal to the angle between the $\vec{DF}$ and $\vec{BD}$ all that is now needed to find the overshoot distance is the length $\vec{DF}$. This can be found through the geometry of a perpendicular plane parallel to the truss section that is displayed in Figure 14. From this sectional view it can be seen that the length $|\vec{DF}|$ is determined from:

$$\frac{|\vec{DF}|}{\sin\omega} = \frac{g}{\sin\rho} = \frac{r}{\sin\varphi} \tag{B.37}$$

The overshoot distance, ε, on a forward pass can then be calculated by:

$$\varepsilon = |\vec{DF}|\tan\zeta \tag{B.38}$$

The method for calculating the overshoot on a reverse pass uses the same method. The actual movement of the carriage translation axis is then found by determining the absolute position, $\bar{x}$, that the eyelet must be positioned at on completion of creating a shear member. For any bay n, this is given by:

$$\bar{x}_n = \varepsilon_n + \sum_{i=1}^{n} l_{3D,i} \tag{B.39}$$

The incremental movement of the carriage axis, x, which is used for the G-code instructions, is found using:

$$x_n = \bar{x}_n + \sum_{i=1}^{n-1} x_i \tag{B.40}$$

Appendix C

Manufactured truss configurations

On the following page, Table C.1 details all the prismatic truss configurations produced using the automated WrapToR winding machine. The truss configurations winding time and sample masses are then given in Table C.2.

Table C.1: All truss configurations produced using WrapToR winding machine.

Configuration ID	Truss height, H (mm)	Chord tube diameter, $\varnothing_s$ (mm)	Chord tube wall thickness, t_c (mm)	Shear member tow size	Winding angle, θ_w (°)	Shear member angle, θ_s (°)	Bay number, n_b	Level of twist (twists/mm)	Total length, L (mm)
S-F	33	3	0.5	24k	45	43.16	30	0	1000
S-T/H33_1	33	3	0.5	24k	45	43.16	30	0.0303	1000
L-F	66	4	0.5	24k	45	43.76	15	0	1000
L-T/H66_1	66	4	0.5	24k	45	43.76	15	0.0303	1000
H33_2	33	3	0.5	24k	56.31	54.59	30	0.0303	1000
H66_2	66	4	0.5	48k	45	43.76	15	0.05	1000
H99	99	5	1	96k	45	43.96	10	0.025	1000
H50_D4	49.5	4	0.5	72k	45	43.35	20	0.025	1000
H50_D5	49.5	5	1	72k	45	42.96	20	0.025	1000
Tower_1	95	3	0.5	24k	45	44.35	17	0.03	1715

Table C.2: Winding time and mass of all truss configurations.

Configuration ID	Number produced	Winding time (mm:ss)	Mass per unit length, MUL (g/m)	
			Mean	Standard deviation
S-F	5	04:26	33.0	0.55
S-T/H33_1	20	04:26	32.6	1.07
L-F	3	04:35	42.2	0.65
L-T/H66_1	3	04:35	41.2	0.36
H33_2	3	04:13	31.1	0.30
H66_2	3	04:35	56.2	1.10
H99	4	04:41	102.0	1.77
H49.5_4D	4	04:29	64.3	1.07
H49.5_5D	4	04:29	92.5	0.50
Tower_1	5	07:18	32.1	0.98

Appendix D

Linear regression of joint stiffness

In Section 4.5.1, a multiple linear regression was used to determine an expression relating the shear stiffness of the joint elements to variables that define the truss configurations. The shear stiffness values that the linear regressions aimed to approximate are those values displayed in Table 4.5. Detailed within this appendix are the statistics and rationale for selected linear expression. Statistics relating to the chosen linear expression are also further investigated. All linear regressions were conducted using Matlab's "fitlm" function. The following five defining truss parameters were identified as likely to influence the joint element shear stiffness:

- Chord member tube diameter, $\varnothing_c$
- Chord member wall thickness, t_w
- Shear member diameter, $\varnothing_s$
- Section height, H
- Winding angle, θ_w

Linear regressions were run using every possible combination of parameters to determine which of the five truss parameters have a significant influence on the joint shear stiffness. Table D.1 shows the the mean absolute percentage error (MAPE) and R^2 values of the linear models for all possible variable combinations. The chosen combination, highlighted in yellow, uses all variables excluding the chord member wall thickness. While the linear model using all variables has a slightly lower MAPE, it has a lower adjusted and predictive R^2 suggesting the model is significantly overfitted. This is unsurprising given the high number of variables relative to the number of data points. The selected linear model that uses four of the truss parameters still displays a certain level of overfitting; this is indicated by the its predictive R^2 value being significantly higher than its R^2 value. As is discussed in Section 4.5.1, testing of further truss configurations would be required to improve confidence in the model.

Table D.1: Assessment of fit of linear regressions for all possible combination of truss variables. Chosen variable selection highlighted in yellow.

Variables included in linear regression					Measures of fit			
Chord diameter, $\varnothing_c$	Chord thickness, t_c	Shear diameter, $\varnothing_s$	Section height, H	Winding angle, θ_w	MAPE (%)	R^2	R^2 (adjusted)	R^2 (predictive)
✓					44.9	0.13	-0.04	-0.95
	✓				43.6	0.19	-0.02	-1.01
✓	✓				39.7	0.29	-0.07	-1.48
		✓			39.5	0.17	0.01	-0.69
✓		✓			39.9	0.17	-0.24	-1.76
	✓	✓			41.8	0.20	-0.20	-1.95
✓	✓	✓			36.1	0.31	-0.37	-3.20
			✓		42.2	0.09	-0.09	-0.53
✓			✓		23.2	0.79	0.69	0.23
	✓		✓		18.2	0.84	-0.75	-0.15
✓	✓		✓		18.7	0.84	0.67	-0.94
		✓	✓		26.8	0.67	0.51	0.11
✓		✓	✓		17.1	0.84	0.68	0.21
	✓	✓	✓		13.7	0.87	0.75	0.57
✓	✓	✓	✓		13.7	0.87	0.62	-0.31
				✓	39.7	0.04	-0.15	-0.38
✓				✓	36.5	0.36	0.04	-1.15
	✓			✓	32.8	0.40	-0.10	-1.10
✓	✓			✓	29.8	0.41	-0.19	-1.41
		✓		✓	25.7	0.36	0.04	-0.72
✓		✓		✓	31.8	0.40	-0.21	-1.81
	✓	✓		✓	30.6	0.42	-0.16	-2.22
✓	✓	✓		✓	26.1	0.43	-0.70	-3.09
			✓	✓	40.1	0.10	-0.35	-0.83
✓			✓	✓	10.7	0.95	0.91	0.03
	✓		✓	✓	9.4	0.92	-0.84	-0.31
✓	✓		✓	✓	8.8	0.96	0.87	-0.93
		✓	✓	✓	23.1	0.74	0.48	-0.17
✓		✓	✓	✓	4.2	0.99	0.98	0.47
	✓	✓	✓	✓	9.1	0.97	0.90	-0.41
✓	✓	✓	✓	✓	3.8	0.99	0.96	-0.27

Table D.2: Chosen linear model coefficients and p-values

Related variable	Coefficient	Value	p-value (%)
Intercept	b_1	-64566	2.1
Chord diameter, $\varnothing_c$	b_2	22350330	1.4
Shear diameter, $\varnothing_s$	b_3	12233508	8.2
Section height, H	b_4	-403340	0.6
Winding angle, θ_w	b_5	1052	2.4

In Table D.2, the coefficients and p-values for each term in the final chosen linear model are displayed. Here all variables except for shear member diameter are seen to have a p-value below 5%, suggesting that they influence the shear stiffness to a high level of certainty. The shear member diameter term has a p-value of 8%, meaning it can not be confidently concluded to influence the shear stiffness. Again a higher level of confidence could be achieved through further testing.

Appendix E

Truss mass estimation

For the parametric sweeps in Section 4.6, and the optimisation study in Chapter 6, the ability to estimate truss mass was required. A simple mass estimation module was added to the analysis tool for this purpose. The mass calculation module uses the element lengths determined during geometric idealisation along with the element cross-sectional properties to determine member volume. The member volumes are then multiplied by member densities that were determined for the chord members in Section 3.2 and the shear members in Section 3.3. The densities used are summarised in Table E.1. Note here the chord member density was averaged across the three tube sizes.

To assess the accuracy of the mass estimation module, below in Table E.2, mass predictions for all the configurations manufactured are compared to the average measured values. The values in Table E.2 show that for all trusses of shear member sizes 24k or 48k the mass estimation has less than 4.5% error when compared to mean values. For configurations with larger shear member tow sizes the error is larger. This is particularly the case for the one configuration with a 96k shear member tow size: H99. The reason that the mass calculator is less accurate for the truss configurations with larger tow sizes is because of a drop in resin content when manufacturing with the larger tow sizes. This drop in resin content when using 72k or 96k tow was identified during the microscopy work in Section 2.5. While the mass calculator could have been adjusted to account for this drop in resin content, it is hoped that future manufacturing improvements will produce more consistent resin content across the range of tow sizes. For this reason the module was not altered to account for the resin content drop and it was accepted that for larger shear member sizes, a conservative estimate of mass is likely to be given.

Table E.1: Densities used for mass estimation.

Member type	Density (g/cm^3)
Chord	1.55
Shear	1.43

Table E.2: Comparison of estimated and mean measured sample mass. Configuration details are given in Appendix C.

Configuration	Shear member tow	MUL (g/m)		
		Sample mean	Estimation	% error
S-T/H33_1	24k	32.6	32.3	-0.8
L-T/H66_1	48k	41.2	39.4	-4.3
H33_2	24k	31.1	30.0	-3.5
H66_2	48k	56.2	53.9	-4.2
H99	96k	102.0	116.4	14.2
H50_D4	72k	64.3	68.0	5.7
H50_D5	72k	92.5	100.6	8.8
Tower_1	24k	32.1	31.8	-1.0

Appendix F

Joint area measurement methodology

Summarised in Section 3.4.2 is the method used to measure joint area in Wrap-ToR samples. In this appendix full detailing of the method and the accompanying mathematics is given.

The first step to measuring the joint area was acquiring samples in which the joints had failed, leaving a fracture surface that could be measured. Some joint samples were taken from full trusses that had failed at the joints during the failure tests detailed in Section 5.6. A majority of the samples, however, were manually sheared. This involved first cutting individual joints from a full truss using a diamond saw, leaving samples such as that seen in Figure F.1a. The shear member tow was then sheared from the chord tube by forcing it through a hole with a slightly larger diameter than the tube itself. This method is pictured in Figure F.1b

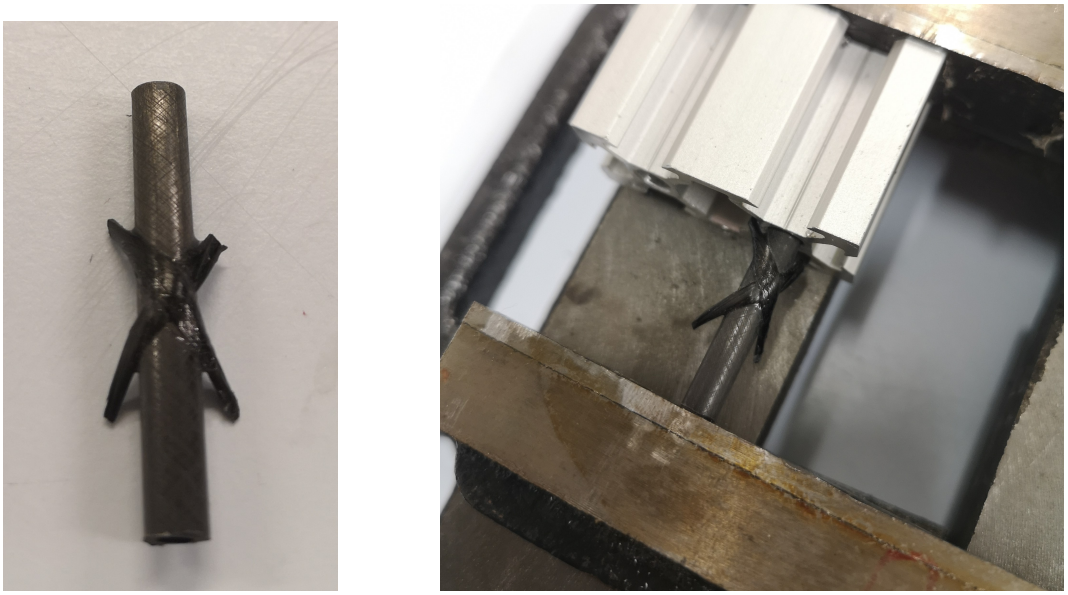

(a) (b)

Figure F.1: Acquisition of samples for joint area measurement: a) single joint cut from full truss; b) shearing of isolated joint.

The next step was capturing images of the exposed fracture surfaces. Due to the joints extending over halfway around the circumference of the tubes, two images of each joints were required to capture the whole joint. This means that analysing of each image relates to determining the area of a joint half. Images were captured with a Fujifilm X-T30 DLSR camera with an 18-55 mm f2.8-4 lens and a 16 mm macro extension. A green background was used for efficient detection during image processing. An example half joint image is displayed in Figure F.3a. Once captured, the images were manually cropped, and the joint regions were manually outlined using the image processing software GIMP. The joint region was outlined in red (RGB [1 0 0]), so that it could be easily detected using image analysis software. An example of a joint image with the joint region outlined is displayed in Figure F.3b. Further joint images for each configuration are displayed in Figures 2.25-2.28.

Following this, the manually processed images were fed into a custom-written MATLAB script. This script was designed to determine the area of the joint on the 3D tube surface from the inputted image, which is a 2D projection.

The script initially determines the tube boundary by detecting the colour difference between the dark tube and green background. From this, it calculates the tube centre line, or half diameter. This stage of the image analysis is displayed in Figure F.3c. Following this, the code identifies the manually outlined joint region. Using the determined tube boundaries and knowledge of the joint region, the script then creates a binary image that isolates the tube and joint regions. This binary image is seen in Figure F.3d.

Using the binary image, along with knowledge of the tube centre line position, the code then determines the tube surface area corresponding to each pixel in the joint region (the white pixels in Figure F.3d). For these calculations, the coordinate system seen in Figure F.3a is defined where the x and z-axis are in the image plane, with the latter running parallel to the tube length.

For each pixel in the joint region, the distance to the tube centre line is calculated and stored. As stated previously, each pixel in the image (2D projection) corresponds to an area on the 3D tube surface. A schematic, showing how an area in the projected 2D image relates to the area on the 3D tube surface is shown in Figure F.2a. Here the blue square shows the surface area corresponding to the red 2D projected area. The length of the corresponding surface area in the image z-axis, δz, will be equal to the length of the projected area as the tube does not curve along its length. The length of the corresponding area along the image x-axis will however be longer than the x-length of the pixel due to the tube curvature along this axis. The length on the tube surface, δs, corresponding to a projected length in the image x-axis, δx, can be found by considering the geometry in Figure F.2b. From this figure the following relationships can be drawn:

$$\sin\gamma = \frac{x}{r} \tag{F.1}$$

$$\sin(\gamma+\theta) = \frac{x+dx}{r} \tag{F.2}$$

where r is the tube radius. Rearranging these two equations to find the angles gives:

$$\gamma = \sin^{-1}\left(\frac{x}{r}\right) \tag{F.3}$$

$$\theta = \sin^{-1}\left(\frac{x+dx}{r}\right) - \gamma \tag{F.4}$$

Using these two equations the angle θ can be calculated. δs is then the arc length given by:

$$ds = \theta r \tag{F.5}$$

The surface area corresponding to each pixel is then found by multiplying the lengths δs and δx. Once the corresponding surface area of each pixel is determined, the total half joint surface area is found by summing for all pixels in the joint region.

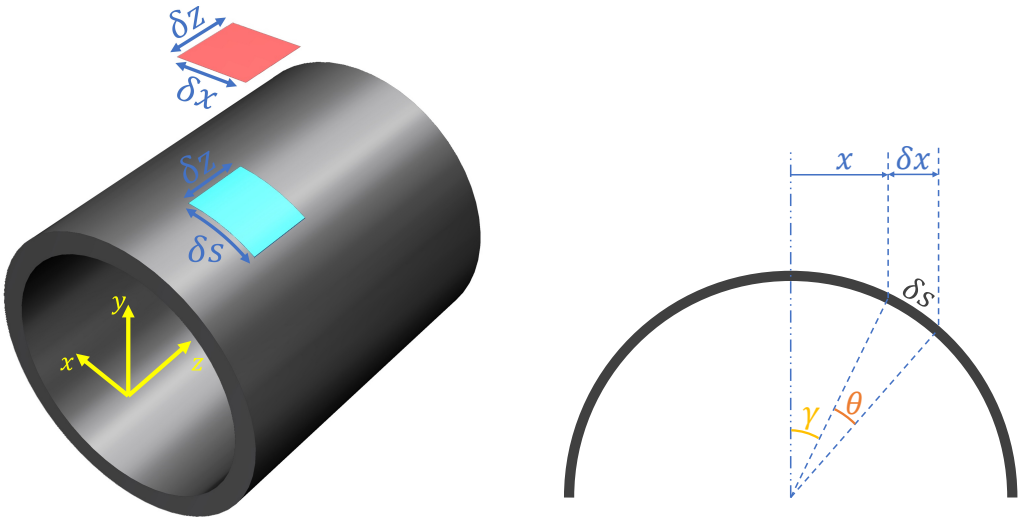

(a) (b)

Figure F.2: Schematics showing image area projection relationships: a) image projected area on tube surface; b) tube cross-sectional view showing how change in length along x-axis relates to change in arc length along tube surface.

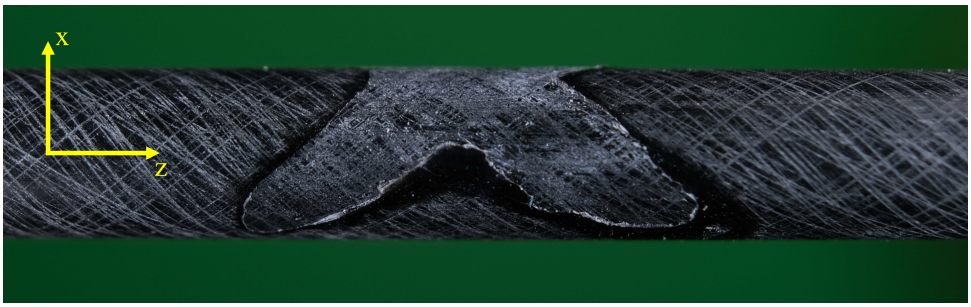

(a)

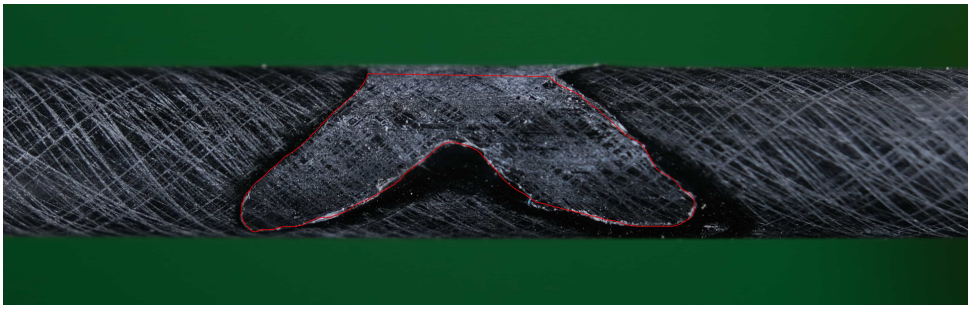

(b)

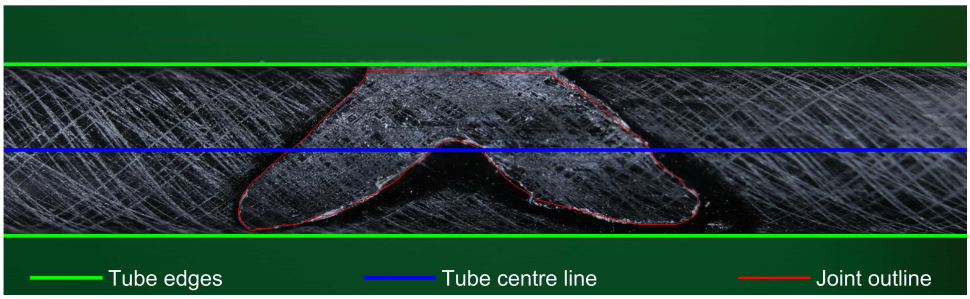

(c)

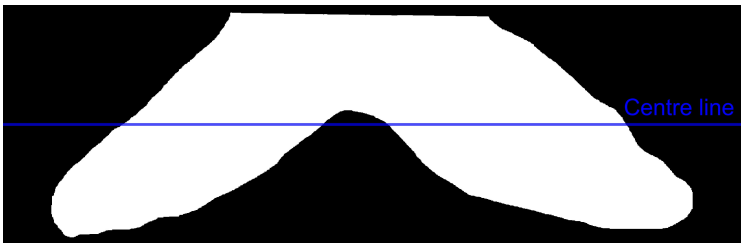

(d)

Figure F.3: Half joint image processing stages: a) cropped image; b) manual outlining of joint region; c) automated detection of tube edges and determination of tube centre line; d) isolation of tube and joint regions.

Below are examples images of the joint fracture surfaces used for estimating the joint area. Two example images are given per configuration. Note configurations are those detailed in Table 3.8. The red line in each image shows the manually outlined joint region.

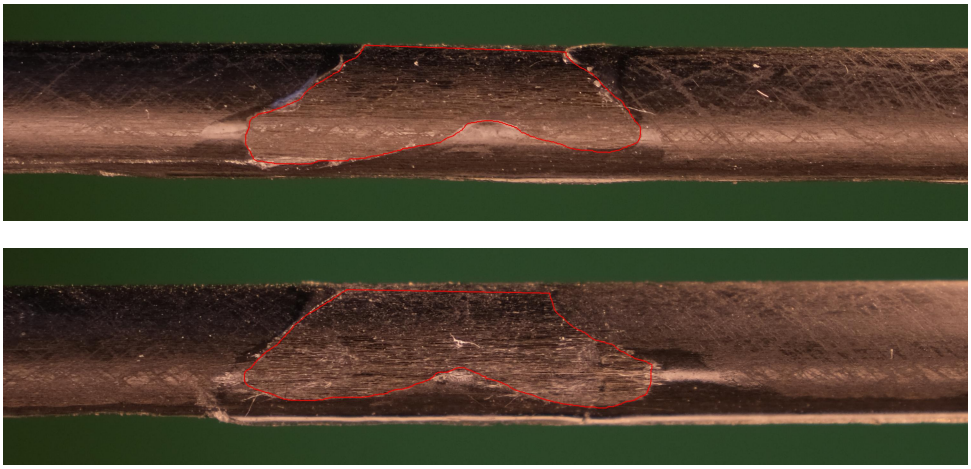

Figure F.4: Example half joint images for configuration 3_24k.

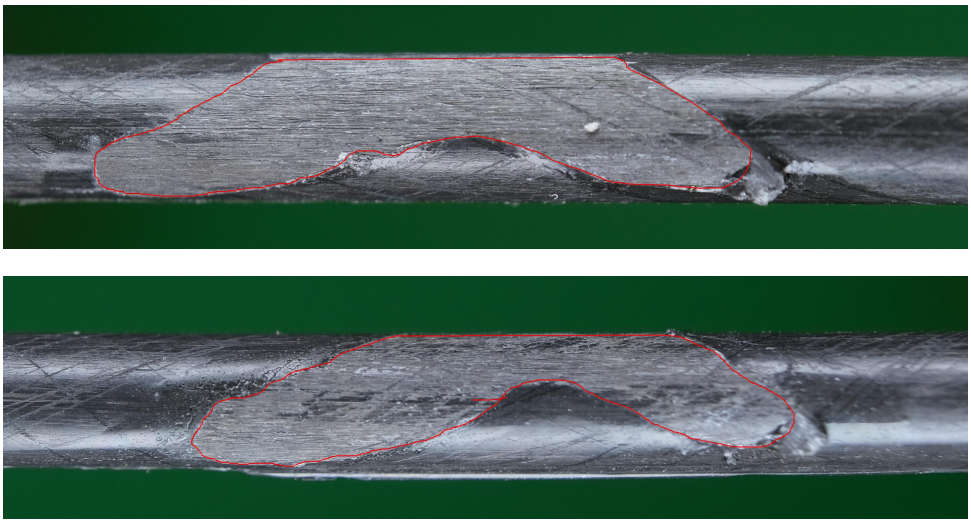

Figure F.5: Example half joint images for configuration 3_24k_56.3.

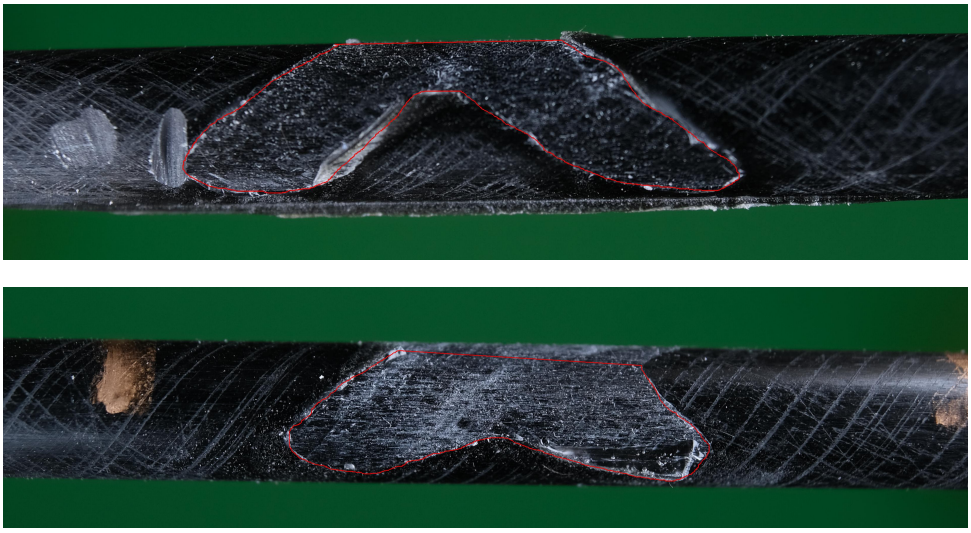

Figure F.6: Example half joint images for configuration 4_24k.

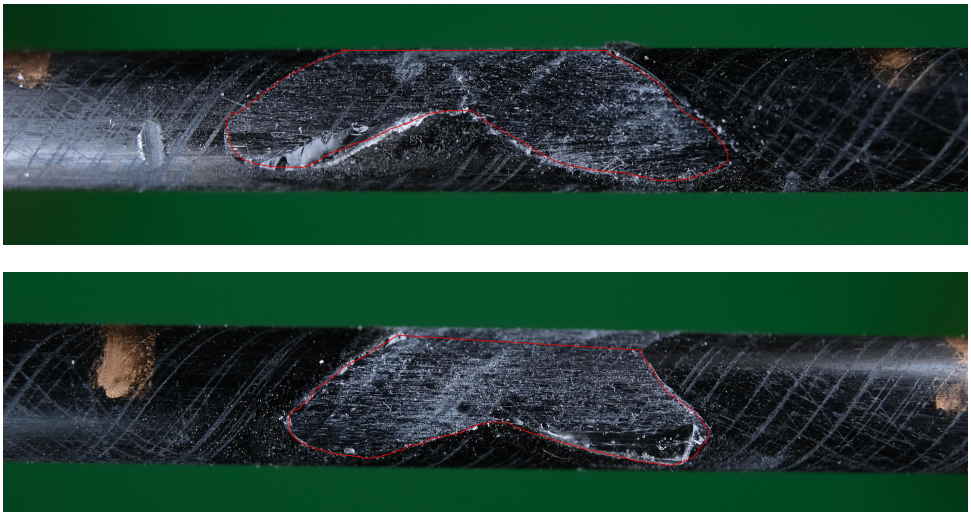

Figure F.7: Example half joint images for configuration 4_48k.

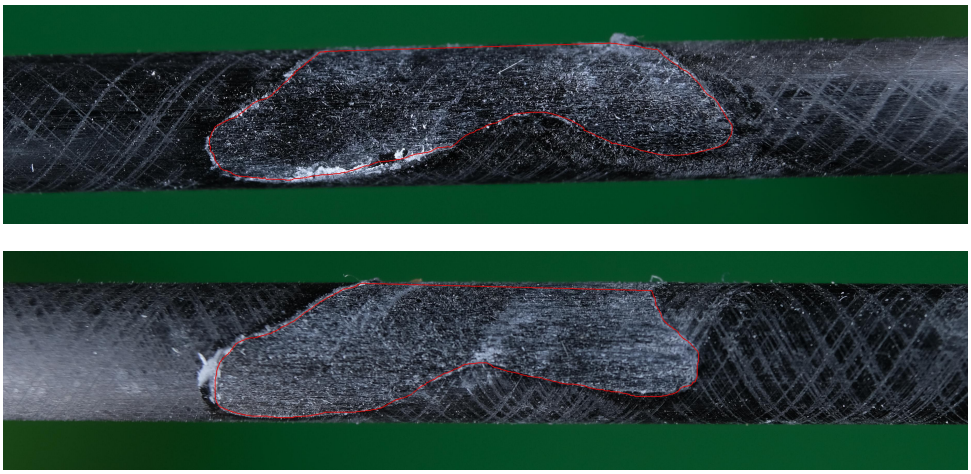

Figure F.8: Example half joint images for configuration 4_72k.

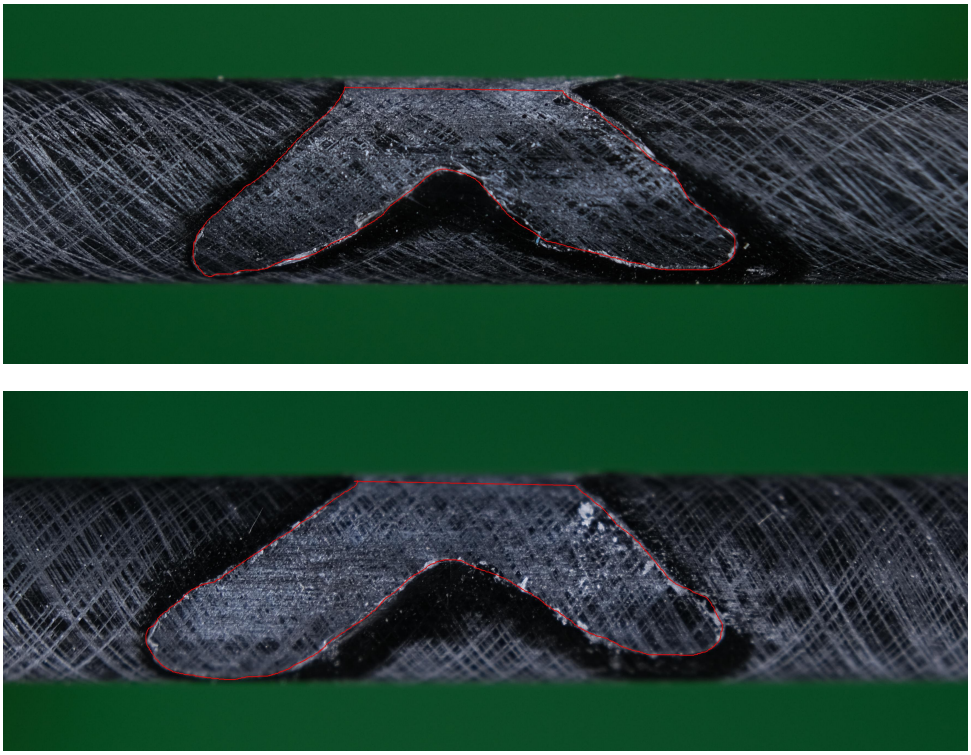

Figure F.9: Example half joint images for configuration 5_24k.

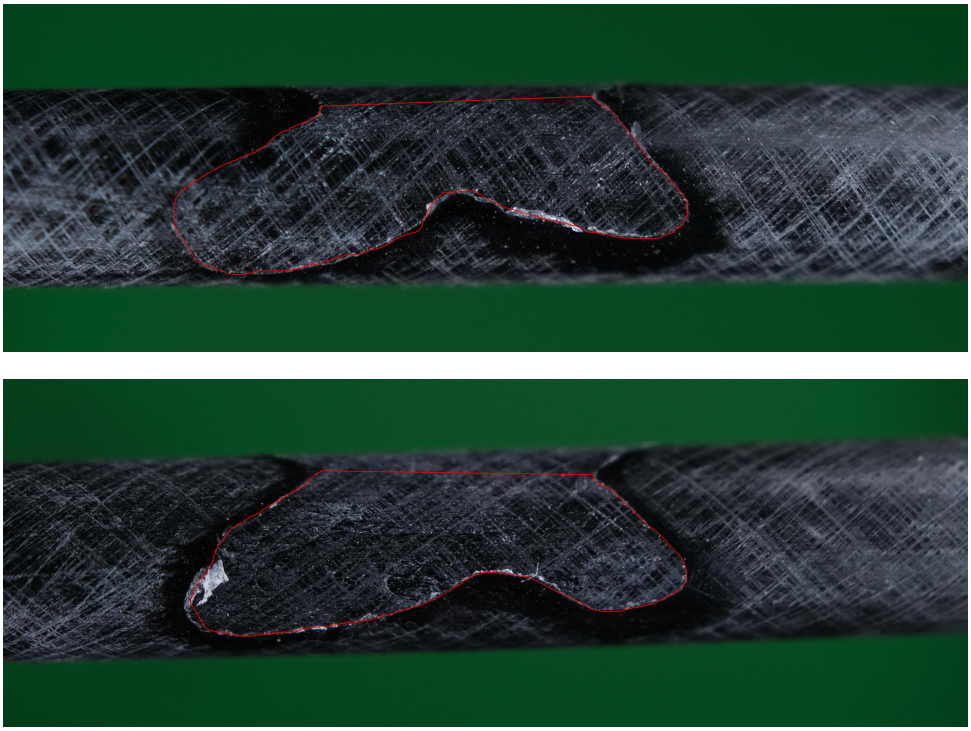

Figure F.10: Example half joint images for configuration 5_48k.

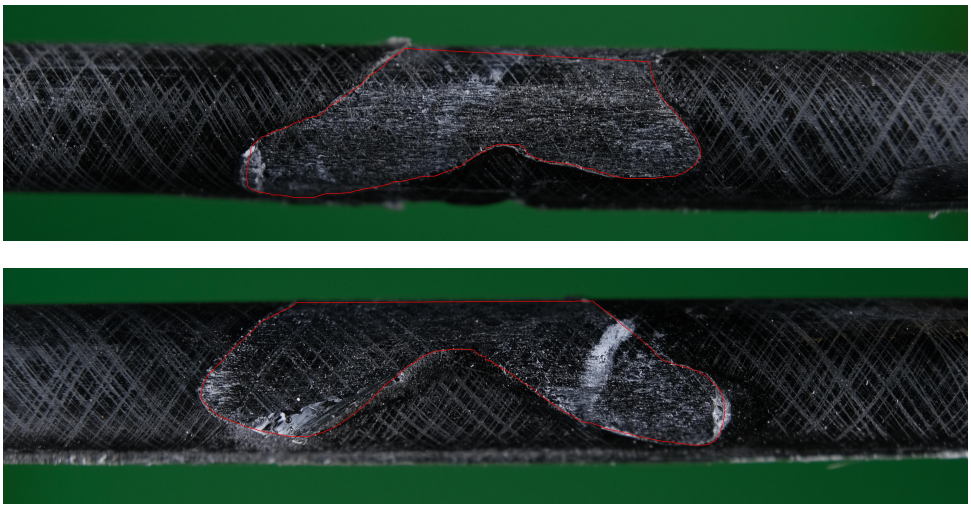

Figure F.11: Example half joint images for configuration 5_72k.

Appendix G

Joint area approximation

In Section 5.5, failure of the truss joints was predicted using the WrapToR analysis tool coupled with a geometric model of the joint area. In this appendix, this joint area model is fully detailed.

The model is based on predicting the flattened joint surface area as a cross-shape that is formed of two parallelograms. This cross shape is displayed in Figure G.1a where two parameters are introduced: the joint height, h_j and the spread tow width at the joint, w_t. The joint height is the length around the circumference of the tube that the joint region extends. To approximate the joint height a new parameter, the joint angle γ, is introduced. This is the angle around the tube that the joint extends and is depicted in G.1b. For a triangular section truss it may be intuitive that the joint angle would be 120°and that the joint would extend one-third of the way around the tube circumference. However, the formation of resin menisci (discussed and imaged in 3.4) means the joint actually extends further around the circumference than the expected 120°. Using the joint area measurement data from Section 3.4, the mean joint angle was found to be 227.3°. It should be noted here that while the joint angle would be expected to vary across truss configurations, only a small variance was observed between the eight configurations. For this reason, the

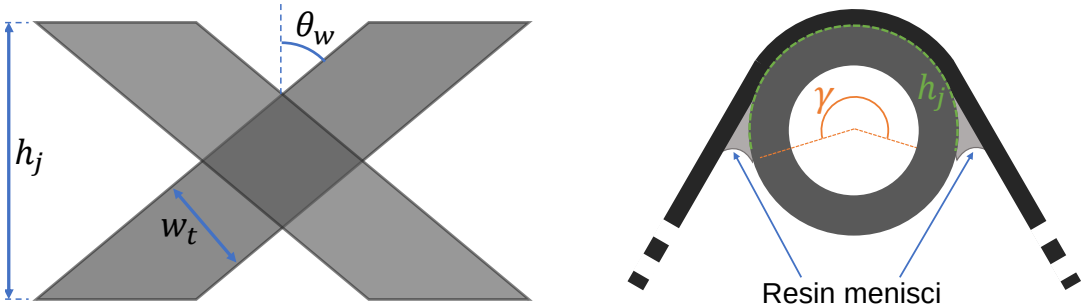

(a) (b)

Figure G.1: Joint area model schematics: a) cross-shape used to approximate joint region; b) joint section view showing joint angle.

mean measured value was used as a constant within the model. With the joint angle approximated, the joint height, is the arc length along the tube surface calculated by:

$$h_j = \gamma \times \frac{\varnothing_c}{2} \tag{G.1}$$

where γ is the joint angle in radians and $\varnothing_c$ is the tube diameter.

The width of the tow at the joint was assumed to be the tow diameter multiplied by a "spread factor". This factor represents how much the tow spreads out as it is compressed against the tube at the joint. This factor was determined using an empirical fit of the model to the measured joint area results found in Section 3.4. Through this empirical fit, a spread factor of 2.59 was found to give the smallest mean absolute percentage error (MAPE) of 6.9%.

With the joint height and the spread tow width defined, the area of the joint region cross-shape is calculated through geometric considerations. In Figure G.1a, the cross-shape is split into two constituent areas. The area of each of the two overlapping parallelograms is referred to as A_1. The rhombus formed where the two parallelograms intersect, is referred to as area A_2. The following summation therefore gives the total area of the joint:

$$A_j = 2A_1 - A_2 \tag{G.2}$$

An exception exists where Equation G.2, must be adjusted. This exception occurs when the height of the central rhombus, is greater that the joint height, h_j. This case, which is depicted in Figure G.2, could occur in trusses where the shear member diameter is large relative to the chord members. For this case, the additional area A_3 is introduced, and the total joint area is found from:

$$A_j = 2A_1 - (A_2 - 2A_3) \tag{G.3}$$

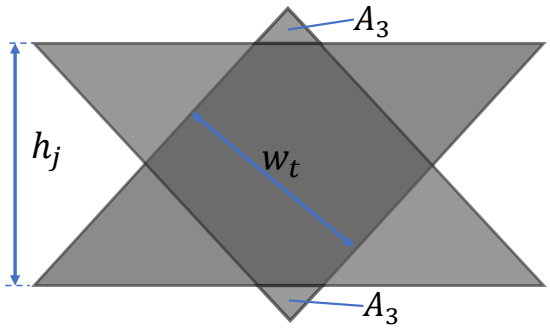

Figure G.2: Exception case to joint area model.

Bibliography

[1] D. I. Poll, "On the application of light weight materials to improve aircraft fuel burn - Reduce weight or improve aerodynamic efficiency?," *Aeronautical Journal*, vol. 118, no. 1206, pp. 903–934, 2014.

[2] H. W. Jones, "The Recent Large Reduction in Space Launch Cost," in *48th International Conference on Environmental Systems*, (Albuquerque, New Mexico), 2018.

[3] J. Knippers, E. Pelke, M. Gabler, and D. Berger, "Bridges with Glass Fibre–Reinforced Polymer Decks: The Road Bridge in Friedberg, Germany," *Structural Engineering International*, vol. 20, pp. 400–404, 11 2010.

[4] P. M. Weaver and M. F. Ashby, "The optimal selection of material and section-shape," *Journal of Engineering Design*, vol. 7, no. 2, pp. 129–150, 1996.

[5] M. F. Ashby, "Overview No. 92: Materials and shape," *Acta Metallurgica Et Materialia*, vol. 39, pp. 1025–1039, 6 1991.

[6] N. Buckney, A. Pirrera, and P. Weaver, "Structural efficiency measures for sections under asymmetric bending," *Journal of Mechanical Design, Transactions of the ASME*, vol. 137, no. 1, 2015.

[7] P. M. Weaver and M. F. Ashby, "Material limits for shape efficiency," *Progress in Materials Science*, vol. 41, no. 1-2, pp. 61–128, 1997.

[8] W. Chen and E. Lui, *Handbook of Structural Engineering*. New York, NY: CRC Press, 1997.

[9] D. R. Sherman, "Latticed Structures: State-of-the-Art Report," *Journal of the Structural Division*, vol. 120, no. 11, pp. 2197–2230, 1976.

[10] International Association for Shell and Spatial Structures (IASS) Working Group on Spatial Steel Structures., "Analysis, design and realization of space frames.," 1984.

[11] M. Ashby, "The properties of foams and lattices," *Philosophical Transactions of the Royal Society A: Mathematical, Physical and Engineering Sciences*, vol. 364, pp. 15–30, 1 2006.

[12] S. Krenk and J. Høgsberg, *Statics and Mechanics of Structures*. Dordrecht: Springer Netherlands, 2013.

[13] M. J. Salkind and G. S. Holister, "Applications of Composite Materials," tech. rep., American Society for testing and Materials, Tallahassee, 1972.

[14] *IsoTruss Industries LLC*. www.IsoTruss.com, [Accessed: 09/01/21].

[15] V. V. Vasiliev and A. F. Razin, "Anisogrid composite lattice structures for spacecraft and aircraft applications," *Composite Structures*, vol. 76, no. 1-2, pp. 182–189, 2006.

[16] J. Xiong, L. Ma, L. Wu, B. Wang, and A. Vaziri, "Fabrication and crushing behavior of low density carbon fiber composite pyramidal truss structures," *Composite Structures*, vol. 92, pp. 2695–2702, 10 2010.

[17] R. Hizam, A. C. Manalo, W. Karunasena, and Y. Bai, "Behaviour of pultruded GFRP truss system connected using through-bolt with mechanical insert," *Composites Part B: Engineering*, vol. 168, pp. 44–57, 7 2019.

[18] Y. Bai and C. Zhang, "Capacity of nonlinear large deformation for trusses assembled by brittle FRP composites," *Composite Structures*, 2012.

[19] D. Zhang, Q. Zhao, Y. Huang, F. Li, H. Chen, and D. Miao, "Flexural properties of a lightweight hybrid FRP-aluminum modular space truss bridge system," *Composite Structures*, vol. 108, pp. 600–615, 2 2014.

[20] N. Minsch, M. Müller, T. Gereke, A. Nocke, and C. Cherif, "Novel fully automated 3D coreless filament winding technology," *Journal of Composite Materials*, vol. 52, no. 22, pp. 3001–3013, 2018.

[21] N. Minsch, M. Müller, T. Gereke, A. Nocke, and C. Cherif, "3D truss structures with coreless 3D filament winding technology," *Journal of Composite Materials*, vol. 53, pp. 2077–2089, 6 2019.

[22] T. W. Murphey and W. F. Davidson, "High Strain Composite Folding Truss Structures," in *2018 AIAA Spacecraft Structures Conference*, (Reston, Virginia), American Institute of Aeronautics and Astronautics, 1 2018.

[23] V. V. Vasiliev, V. A. Barynin, and A. F. Razin, "Anisogrid composite lattice structures - Development and aerospace applications," *Composite Structures*, vol. 94, no. 3, pp. 1117–1127, 2012.

[24] S. Huybrechts, S. Hahn, and T. Meink, "Grid stiffened structures: a survey of fabrication, analysis and design methods," in *12th International Conference on Composite Materials*, pp. 1–10, 1999.

[25] V. V. Vasiliev, V. A. Barynin, and A. F. Rasin, "Anisogrid lattice structures - Survey of development and application," *Composite Structures*, vol. 54, pp. 361–370, 11 2001.

[26] H. L. Fan, F. H. Meng, and W. Yang, "Sandwich panels with Kagome lattice cores reinforced by carbon fibers," *Composite Structures*, vol. 81, no. 4, pp. 533–539, 2007.

[27] H. Fan, D. Fang, L. Chen, Z. Dai, and W. Yang, "Manufacturing and testing of a CFRC sandwich cylinder with Kagome cores," *Composites Science and Technology*, vol. 69, pp. 2695–2700, 12 2009.

[28] H. Zhang, F. Sun, H. Fan, H. Chen, L. Chen, and D. Fang, "Free vibration behaviors of carbon fiber reinforced lattice-core sandwich cylinder," *Composites Science and Technology*, vol. 100, pp. 26–33, 8 2014.

[29] S. Huybrechts and S. W. Tsai, "Analysis and behavior of grid structures," *Composites Science and Technology*, vol. 56, pp. 1001–1015, 1 1996.

[30] T. S. Jang, J. Rhee, B. S. Hyun, H. S. Seo, T. Y. Kim, and J. K. Seo, "A study on grid-stiffened multi-functional composite structures with radiation spot shielding," *Aerospace Science and Technology*, vol. 54, pp. 330–339, 7 2016.

[31] Y. Mo, G. Cheng, B. Wang, and X. Wang, "The effects of delamination deficiencies on compressive properties of composite grid-stiffened structures," *Mechanics of Advanced Materials and Structures*, vol. 25, pp. 901–916, 8 2018.

[32] C. Zhao, M. J. Donough, B. G. Prusty, and J. Xiao, "Influences of ply waviness and discontinuity on automated fibre placement manufactured grid stiffeners," *Composite Structures*, vol. 256, 1 2021.

[33] D. Han and S. W. Tsai, "Interlocked Composite Grids Design and Manufacturing," *Journal of Composite Materials*, vol. 37, pp. 287–316, 2 2003.

[34] Y. H. Lee, B. K. Lee, I. Jeon, and K. J. Kang, "Wire-woven bulk Kagome truss cores," *Acta Materialia*, vol. 55, no. 18, pp. 6084–6094, 2007.

[35] B.-C. Lee, K.-W. Lee, J.-H. Byun, and K.-J. Kang, "The compressive response of new composite truss cores," *Composites Part B: Engineering*, vol. 43, pp. 317–324, 3 2012.

[36] L. Che, G. d. Xu, T. Zeng, S. Cheng, X. w. Zhou, and S. c. Yang, "Compressive and shear characteristics of an octahedral stitched sandwich composite," *Composite Structures*, vol. 112, no. 1, pp. 179–187, 2014.

[37] H. Kim, B. H. Cho, H. K. Hur, and K. J. Kang, "A composite sandwich panel integrally woven with truss core," *Materials and Design*, vol. 65, pp. 231–242, 1 2015.

[38] L. Dong and H. Wadley, "Mechanical properties of carbon fiber composite octet-truss lattice structures," *Composites Science and Technology*, vol. 119, pp. 26–33, 11 2015.

[39] G. Zhang, L. Ma, B. Wang, and L. Wu, "Mechanical behaviour of CFRP sandwich structures with tetrahedral lattice truss cores," *Composites Part B: Engineering*, vol. 43, pp. 471–476, 3 2012.

[40] W. Huang, Z. Fan, W. Zhang, J. Liu, and W. Zhou, "Impulsive response of composite sandwich structure with tetrahedral truss core," *Composites Science and Technology*, vol. 176, pp. 17–28, 2019.

[41] B. Wang, L. Wu, L. Ma, Y. Sun, and S. Du, "Mechanical behavior of the sandwich structures with carbon fiber-reinforced pyramidal lattice truss core," *Materials and Design*, vol. 31, pp. 2659–2663, 5 2010.

[42] S. Yin, L. Wu, L. Ma, and S. Nutt, "Pyramidal lattice sandwich structures with hollow composite trusses," *Composite Structures*, vol. 93, pp. 3104–3111, 11 2011.

[43] J. Xiong, R. Ghosh, L. Ma, H. Ebrahimi, A. Hamouda, A. Vaziri, and L. Wu, "Bending behavior of lightweight sandwich-walled shells with pyramidal truss cores," *Composite Structures*, vol. 116, pp. 793–804, 9 2014.

[44] Y. Hu, W. Li, X. An, and H. Fan, "Fabrication and mechanical behaviors of corrugated lattice truss composite sandwich panels," *Composites Science and Technology*, vol. 125, pp. 114–122, 3 2016.

[45] J. Xiong, L. Ma, A. Vaziri, J. Yang, and L. Wu, "Mechanical behavior of carbon fiber composite lattice core sandwich panels fabricated by laser cutting," *Acta Materialia*, vol. 60, pp. 5322–5334, 8 2012.

[46] J. Mei, J. Liu, and J. Liu, "A novel fabrication method and mechanical behavior of all-composite tetrahedral truss core sandwich panel," *Composites Part A: Applied Science and Manufacturing*, vol. 102, pp. 28–39, 11 2017.

[47] M. Eichenhofer, J. I. Maldonado, F. Klunker, and P. Ermanni, "ANALYSIS OF PROCESSING CONDITIONS FOR A NOVEL 3D-COMPOSITE PRODUCTION TECHNIQUE," in *20th International Conference on Composite Materials*, (Copenhagen), 2015.

[48] M. Eichenhofer, J. C. Wong, and P. Ermanni, "Continuous lattice fabrication of ultra-lightweight composite structures," *Additive Manufacturing*, vol. 18, pp. 48–57, 12 2017.

[49] T. George, V. Deshpande, and H. Wadley, "Hybrid carbon fiber composite lattice truss structures," *Composites Part A: Applied Science and Manufacturing*, vol. 65, pp. 135–147, 10 2014.

[50] T. George, V. S. Deshpande, K. Sharp, and H. N. Wadley, "Hybrid core carbon fiber composite sandwich panels: Fabrication and mechanical response," *Composite Structures*, vol. 108, no. 1, pp. 696–710, 2014.

[51] S. Yin, L. Wu, L. Ma, and S. Nutt, "Hybrid truss concepts for carbon fiber composite pyramidal lattice structures," *Composites Part B: Engineering*, vol. 43, pp. 1749–1755, 6 2012.

[52] S. Yin, L. Wu, and S. Nutt, "Stretch–bend-hybrid hierarchical composite pyramidal lattice cores," *Composite Structures*, vol. 98, pp. 153–159, 4 2013.

[53] Q. Wu, Y. Gao, X. Wei, D. Mousanezhad, L. Ma, A. Vaziri, and J. Xiong, "Mechanical properties and failure mechanisms of sandwich panels with ultralightweight three-dimensional hierarchical lattice cores," *International Journal of Solids and Structures*, vol. 132-133, pp. 171–187, 2 2018.

[54] Q. Wu, A. Vaziri, M. E. Asl, R. Ghosh, Y. Gao, X. Wei, L. Ma, J. Xiong, and L. Wu, "Lattice materials with pyramidal hierarchy: Systematic analysis and three dimensional failure mechanism maps," *Journal of the Mechanics and Physics of Solids*, vol. 125, pp. 112–144, 4 2019.

[55] R. Schütze, "Lightweight carbon fibre rods and truss structures," *Materials & Design*, vol. 18, pp. 231–238, 1997.

[56] D. Jensen, M. Redford, and L. Francom, "On the structural efficiency of three-dimensional isogrid designs," *37th Structure, Structural Dynamics and Materials Conference*, pp. 1704–1710, 1996.

[57] L. R. Francom and D. W. Jensen, "Three-dimensional iso-tross structure," 7 1999.

[58] T. Weaver and D. W. Jensen, "Mechanical characterization of a graphite/epoxy IsoTruss," *Jorunal of Aerospace Engineering*, vol. 13, no. January, pp. 23–35, 2000.

[59] M. E. Rackliffe, D. W. Jensen, and W. K. Lucas, "Local and global buckling of ultra-lightweight IsoTruss® structures," *Composites Science and Technology*, vol. 66, pp. 283–288, 2 2006.

[60] S. M. Hansen and D. W. Jensen, "Influence of Consolidation and Interweaving on Compression Behavior of IsoTruss Structures," *Design and Nature II*, 2004.

[61] Q. Sui, C. Lai, and H. Fan, "Buckling analyses of double-shell octagonal lattice truss composite structures," *Journal of Composite Materials*, vol. 52, pp. 1227–1237, 4 2018.

[62] Q. Sui, H. Fan, and C. Lai, "Failure analysis of 1D lattice truss composite structure in uniaxial compression," *Composites Science and Technology*, 2015.

[63] C. Lai, J. Wang, C. Liu, H. Fan, B. Xu, and K. Wu, "A flexible tooling and local consolidation process to manufacture 1D lattice truss composite structure," *Composites Science and Technology*, vol. 113, pp. 63–70, 2015.

[64] Q. Sui, C. Lai, and H. Fan, "Fundamental frequency of IsoTruss tubular composite structures," *Archive of Applied Mechanics*, vol. 87, pp. 2011–2024, 12 2017.

[65] D. W. Jensen and K. B. Hinds, "Shear-Dominated Bending Behavior of Carbon / Epoxy Composite Lattice IsoBeam Structures," in *20th International Conference on Composite Materials*, 2015.

[66] M. J. Jensen, A. D. Howcroft, and D. W. Jensen, "Design of an IsoTruss aircraft strut," in *SAMPE 2011 - Long Beach CA - May 23-26 / 2011*, (Long Beach CA), 2011.

[67] D. W. Jensen and R. R. Blake, "COMPRESSION AND;-FLEXURE OF GRAPHITE/EPOXY ISOTRUSS-REINFORCED CONCRETE," in *SAMPE 1999 - Long Beach CA - May 23-27 / 1999*, pp. 23–27, 1999.

[68] L. D. Winkel, D. W. Jensen, and D. K. Darooka, "PARAMETRIC INVESTIGATION OF CANTILEVERED ISOTRUSS™ BEAMS SUBJECTED TO AXIAL COMPRESSION," in *SAMPE 2001 - Long Beach CA - May 6-10 / 2001*, (Long Beach CA), 2001.

[69] D. H. A. D. Jensen, M J; Jensen, "Continuous Manufacturing of Cylindirical Composite Lattice Structures," in *International Conference on Textile Composites (TEXCOMP10)*, 2010.

[70] D. W. Jensen, "Using External Robots Instead of Internal Mandrels to Produce Composite Lattice Structures," in *International Conference on Textile Composites (TEXCOMP10)*, 2010.

[71] A. R. Gurley, "Design and Analysis of Optimal Braided Composite Lattice Structures," 2014.

[72] R. M. Brougton, D. J. Branscomb, and D. G. Beale, "Minimal weight compsoites using open structure," 2015.

[73] D. Branscomb, D. Beale, and R. Broughton, "New Directions in Braiding," *Journal of Engineered Fibers and Fabrics*, vol. 8, p. 155892501300800, 6 2013.

[74] S. Ju, D. Z. Jiang, R. A. Shenoi, and J. Y. Xiao, "Flexural properties of lightweight FRP composite truss structures," *Journal of Composite Materials*, vol. 45, no. 19, pp. 1921–1930, 2011.

[75] B. A. Asay and D. W. Jensen, "BENDING BEHAVIOR OF CARBON/EPOXY COMPOSITE ISOBEAM STRUCTURES," in *SAMPE 2016 - Long Beach CA - May 23-26 / 2016*, (Long Beach CA), 2016.

[76] A. Gurley, D. Beale, R. Broughton, and D. Branscomb, "The Design of Optimal Lattice Structures Manufactured by Maypole Braiding," *Journal of Mechanical Design*, vol. 137, no. 10, p. 101401, 2015.

[77] Q. P. McAllister, J. Senne, and A. Romanyszyn, "Development of a Continuous Advanced Composite Truss Printing System," in *3rd AIAA Spacecraft Structures Conference*, (Reston, Virginia), pp. 1–18, American Institute of Aeronautics and Astronautics, 1 2016.

[78] R. P. Hoyt, J. Cushing, J. Slostad, and G. Jimmerson, "TRUSSELATOR: On-Orbit Fabrication of High-Performance Composite Truss Structures," in *AIAA SPACE 2014 Conference and Exposition*, (Reston, Virginia), pp. 1–10, American Institute of Aeronautics and Astronautics, 8 2014.

[79] R. P. Hoyt, J. Slostad, J. Cushing, and T. Moser, "In-Space Manufacturing of Constructable ™ Long-Baseline Sensors using the Trusselator ™ Technology," in *AIAA SPACE 2016*, no. September, (Reston, Virginia), p. 5244, American Institute of Aeronautics and Astronautics, 9 2016.

[80] B. Berry, G. Bowen-Davies, K. Gluesenkamp, Z. Kaler, J. Schmaus, W. Staruk, E. Weiner, and B. K. Woods, "Design optimization of Gamera II: A human powered helicopter," *Annual Forum Proceedings - AHS International*, vol. 1, no. January 2012, pp. 646–664, 2012.

[81] B. Woods, B. Otto Berry, and V. Bohdan Stavnychyi, "Continuous Wound Composite Truss Structures," 2013.

[82] B. K. Woods, I. Hill, and M. I. Friswell, "Ultra-efficient wound composite truss structures," *Composites Part A: Applied Science and Manufacturing*, vol. 90, pp. 111–124, 11 2016.

[83] S. Peters, *Composite FIlament Winding*. ASM Internationl, 2011.

[84] H. L. Giacoletto, "The art of filament winding," *Reinforced Plastics*, vol. 46, no. 10, pp. 30–31, 2002.

[85] L. Sorrentino, E. Anamateros, C. Bellini, L. Carrino, G. Corcione, A. Leone, and G. Paris, "Robotic filament winding: An innovative technology to manufacture complex shape structural parts," *Composite Structures*, vol. 220, pp. 699–707, 7 2019.

[86] W. Polini and L. Sorrentino, "Winding Trajectory and Winding Time in Robotized Filament Winding of Asymmetric Shape Parts," *Journal of Composite Materials*, vol. 39, pp. 1391–1411, 8 2005.

[87] S. Ratner, A. Weinberg, and G. Marom, "Neat Uhmwpe Filament Wound Composites by Crosslinking Compaction," *Advanced Composites Letters*, vol. 12, p. 096369350301200, 9 2003.

[88] P. Lehtiniemi, K. Dufva, T. Berg, M. Skrifvars, and P. Järvelä, "Natural fiber-based reinforcements in epoxy composites processed by filament winding," *Journal of Reinforced Plastics and Composites*, vol. 30, pp. 1947–1955, 12 2011.

[89] T. Sofi, S. Neunkirchen, and R. Schledjewski, "Path calculation, technology and opportunities in dry fiber winding: a review," *Advanced Manufacturing: Polymer & Composites Science*, vol. 4, pp. 57–72, 7 2018.

[90] S. V. Hoa, *Principles of the Manufacturing of Composite Materials*. DEStech Publications, 2009.

[91] R. Funck and M. Neitzel, "Improved thermoplastic tape winding using laser or direct-flame heating," *Composites Manufacturing*, vol. 6, no. 3-4, pp. 189–192, 1995.

[92] Y. M. Toso, P. Ermanni, and D. Poulikakos, "Thermal phenomena in fiber-reinforced thermoplastic tape winding process: Computational simulations and experimental validations," *Journal of Composite Materials*, vol. 38, no. 2, pp. 107–135, 2004.

[93] F. Henninger and K. Friedrich, "Thermoplastic filament winding with online-impregnation. Part A: process technology and operating efficiency," *Composites Part A: Applied Science and Manufacturing*, vol. 33, pp. 1479–1486, 11 2002.

[94] J. C. Wong, J. M. Blanco, and P. Ermanni, "Filament winding of aramid/PA6 commingled yarns with in situ consolidation," *Journal of Thermoplastic Composite Materials*, vol. 31, pp. 465–482, 4 2018.

[95] N. Wiegand and E. Mäder, "Commingled Yarn Spinning for Thermoplastic/Glass Fiber Composites," *Fibers*, vol. 5, p. 26, 7 2017.

[96] G. Lubin, *Handbook of Composites*. Springer US, 1982.

[97] V. V. Vasiliev, A. A. Krikanov, and A. F. Razin, "New generation of filament-wound composite pressure vessels for commercial applications," *Composite Structures*, vol. 62, no. 3-4, pp. 449–459, 2003.

[98] D. B. Miracle and S. L. Donaldson, eds., *ASM Handbook Volume 21: Composites*. ASM Internationl, 2001.

[99] J. Xu, H. Yang, M. Liu, J. Tian, and B. Liu, "Research on winding trajectory planning for elbow pipe based on industrial robot," *The International Journal of Advanced Manufacturing Technology*, vol. 93, pp. 537–545, 10 2017.

[100] J. Scholliers and H. Van Brussel, "Computer-integrated filament winding: computer-integrated design, robotic filament winding and robotic quality control," *Composites Manufacturing*, vol. 5, pp. 15–23, 3 1994.

[101] A. D. Reddy, R. R. Valisetty, and L. W. Rehfield, "Continuous filament wound composite concepts for aircraft fuselage structures," *Journal of Aircraft*, vol. 22, pp. 249–255, 3 1985.

[102] J. Jones, L. F. Kawashita, B. C. Kim, and S. R. Hallett, "Analysis of novel hybrid joints for composite struts," in *18th European Conference on Composite Materials (ECCM 18)*, pp. 1–11, 2018.

[103] F. H. Abdalla, S. A. Mutasher, Y. A. Khalid, S. M. Sapuan, A. M. Hamouda, B. B. Sahari, and M. M. Hamdan, "Design and fabrication of low cost filament winding machine," *Materials and Design*, vol. 28, no. 1, pp. 234–239, 2007.

[104] S. Mutasher, N. Mir-nasiri, and L. E. E. C. Lin, "Small-Scale Filament Winding Machine for Producing Fiber Composite Products," *Journal of Engineering Science and Technology*, vol. 7, no. 2, pp. 156–168, 2012.

[105] D. Cohen, "Influence of filament winding parameters on composite vessel quality and strength," *Composites Part A: Applied Science and Manufacturing*, vol. 28, no. 12, pp. 1035–1047, 1997.

[106] P. Mertiny and F. Ellyin, "Influence of the filament winding tension on physical and mechanical properties of reinforced composites," *Composites Part A: Applied Science and Manufacturing*, vol. 33, no. 12, pp. 1615–1622, 2002.

[107] ASTM, "ASTM D3916-08: Standard Test Method for Tensile Properties of Pultruded Glass-Fiber-Reinforced."

[108] ASTM, "ASTM D4018-17: Standard Test Methods for Properties of Continuous Filament Carbon and Graphite Fiber Tows."

[109] Y. Shen, D. Branscomb, and S. Adanur, "Effect of joint stiffness on torsional stiffness of open lattice composite structures," *Journal of Industrial Textiles*, p. 152808371988181, 10 2019.

[110] D. W. Jensen and L. Francom, "Three-dimensional iso-truss structure," 2000.

[111] Y. Shen and D. J. Branscomb, "A general approach to fast prototype the topology of braided structures," *International Journal of Engineering Science*, 2018.

[112] R. Schütze and H. C. Goetting, "Adaptive Lightweight CFRP Strut for Active Vibration Damping in Truss Structures," *Journal of Intelligent Material Systems and Structures*, vol. 7, pp. 433–440, 7 1996.

[113] B. Asay and D. W. Jensen, "Composite lattice beam," 2019.

[114] N. K. Naik and V. Madhavan, "Twisted impregnated yarns: Elastic properties," *The Journal of Strain Analysis for Engineering Design*, vol. 35, pp. 83–91, 2 2000.

[115] M. Shioya, T. Itoh, T. Kunugi, and A. Takaku, "Variation of Longitudinal Modulus with Twist for Yarns Composed of High Modulus Fibers," *Textile Research Journal*, vol. 71, pp. 928–936, 10 2001.

[116] N. Salkind, *Encyclopedia of Research Design*. California, United States: SAGE Publications, Inc., 2010.

[117] K. D. Potter, M. R. Wisnom, M. V. Lowson, and R. D. Adams, "Innovative approaches to composite structures," *The Aeronautical Journal*, vol. 102, pp. 107–111, 1998.

[118] A. Kassimali, *Matrix Analysis of Structures*. Global Engineering: Christopher M. Shortt, second ed., 2000.

[119] K. Finnegan, G. Kooistra, H. N. G. Wadley, and V. S. Deshpande, "The compressive response of carbon fiber composite pyramidal truss sandwich cores," *International Journal of Materials Research*, vol. 98, pp. 1264–1272, 12 2007.

[120] S. Ju, R. Shenoi, D. Jiang, and A. Sobey, "Multi-parameter optimization of lightweight composite triangular truss structure based on response surface methodology," *Composite Structures*, vol. 97, pp. 107–116, 3 2013.

[121] W. McGuire, R. H. Gallagher, and R. D. Ziemain, *Matrix Structural Analysis*. Wiley, second ed., 1999.

[122] J. Przemieniecki, *Theory of Matrix Structural Analysis*. McGraw-Hill Inc.,US, 1968.

[123] R. Talreja and C. V. Singh, *Damage and Failure of Composite Materials*. Cambridge: Cambridge University Press, 2012.

[124] T. Ramesh and Varna Janis, *Modeling Damage, Fatigue and Failure of Composite Materials*. Elsevier, 2016.

[125] M. Hinton, A. Kaddour, and P. Soden, *Failure Criteria in Fibre-Reinforced-Polymer Composites : The World-Wide Failure Exercise*. Amsterdam: Elsevier, 2004.

[126] Toray, "Torayca® T800H technical data sheet No. CFA-007."

[127] Toray, "Torayca® T1000G technical data sheet No. CFA-008."

[128] Hexcel, "HexPly® 8552 product data sheet."

[129] U. G. Wegst and M. F. Ashby, "The structural efficiency of orthotropic stalks, stems and tubes," *Journal of Materials Science*, vol. 42, pp. 9005–9014, 11 2007.

[130] I. S. Plitov and A. N. Polilov, "Rational dimensions of segments of bamboo stems and composite tubes subjected to compression, flexure, and torsion," *Journal of Machinery Manufacture and Reliability*, vol. 44, pp. 239–248, 5 2015.

[131] A. A. Smerdov, "Failure of composite tubes in the Chinese lantern mode under a weight-type load," *Mechanics of Composite Materials*, vol. 35, pp. 223–226, 5 1999.

[132] I. Djordjevic, D. Sekulic, and M. Stevanovic, "Non-linear elastic behavior of carbon fibres of different structural and mechanical characteristic," *Journal of the Serbian Chemical Society*, vol. 72, no. 5, pp. 513–521, 2007.

[133] J. L. Meek, *Computer Methods in Structural Analysis*. E & F SPON, 1st ed., 1991.

[134] P. Wriggers, *Nonlinear Finite Element Methods*. Springer-Verlag Berlin Heidelberg, 2010.

[135] D. Gay, S. V. Hoa, and S. W. Tsai, *Composite Materials: Design and Applications*. CRC Press, 2002.

[136] A. FERREIRA, *MATLAB Codes for Finite Element Analysis*, vol. 157 of *Solid Mechanics and its Applications*. Dordrecht: Springer Netherlands, 2009.

[137] R. T. Haftka and J. Sobieszczanski-Sobieski, "Structural Optimization: History," in *Encyclopedia of Optimization*, no. 2, pp. 3834–3836, Boston, MA: Springer US, 2008.

[138] K. Svanberg, "The method of moving asymptotes—a new method for structural optimization," *International Journal for Numerical Methods in Engineering*, vol. 24, pp. 359–373, 2 1987.

[139] J. H. Holland, *Adaptation in Natural and Artificial Systems : An Introductory Analysis with Applications to Biology, Control, and Artificial Intelligence*. Cambridge: MIT Press, 1992.